

Award Number: W81XWH-13-1-0130

TITLE: Understanding Selective Downregulation of c-Myc Expression through Inhibition of General Transcription Regulators in Multiple Myeloma

PRINCIPAL INVESTIGATOR: Dr. Charles Lin

CONTRACTING ORGANIZATION:

Dana-Farber Cancer Institute, Inc.
Boston, MA 02115-6013

REPORT DATE: December 2015

TYPE OF REPORT: Final Report

PREPARED FOR: U.S. Army Medical Research and Materiel Command
Fort Detrick, Maryland 21702-5012

DISTRIBUTION STATEMENT: Approved for Public Release;
Distribution Unlimited

The views, opinions and/or findings contained in this report are those of the author(s) and should not be construed as an official Department of the Army position, policy or decision unless so designated by other documentation.

REPORT DOCUMENTATION PAGE				<i>Form Approved</i> <i>OMB No. 0704-0188</i>	
Public reporting burden for this collection of information is estimated to average 1 hour per response, including the time for reviewing instructions, searching existing data sources, gathering and maintaining the data needed, and completing and reviewing this collection of information. Send comments regarding this burden estimate or any other aspect of this collection of information, including suggestions for reducing this burden to Department of Defense, Washington Headquarters Services, Directorate for Information Operations and Reports (0704-0188), 1215 Jefferson Davis Highway, Suite 1204, Arlington, VA 22202-4302. Respondents should be aware that notwithstanding any other provision of law, no person shall be subject to any penalty for failing to comply with a collection of information if it does not display a currently valid OMB control number. PLEASE DO NOT RETURN YOUR FORM TO THE ABOVE ADDRESS.					
1. REPORT DATE December 2015		2. REPORT TYPE Final		3. DATES COVERED 15 Jun 2013 - 30 Sep 2015	
4. TITLE AND SUBTITLE Understanding Selective Downregulation of c-Myc Expression through Inhibition of General Transcription Regulators in Multiple Myeloma				5a. CONTRACT NUMBER	
				5b. GRANT NUMBER W81XWH-13-1-0130	
				5c. PROGRAM ELEMENT NUMBER	
6. AUTHOR(S) Dr. Charles Lin E-Mail: Charles_lin@dfci.harvard.edu				5d. PROJECT NUMBER	
				5e. TASK NUMBER	
				5f. WORK UNIT NUMBER	
7. PERFORMING ORGANIZATION NAME(S) AND ADDRESS(ES) Dana-Farber Cancer Institute 450 Brookline Ave. Boston, MA 02115-5450				8. PERFORMING ORGANIZATION REPORT	
9. SPONSORING / MONITORING AGENCY NAME(S) AND ADDRESS(ES) U.S. Army Medical Research and Materiel Command Fort Detrick, Maryland 21702-5012				10. SPONSOR/MONITOR'S ACRONYM(S)	
				11. SPONSOR/MONITOR'S REPORT NUMBER(S)	
12. DISTRIBUTION / AVAILABILITY STATEMENT Approved for Public Release; Distribution Unlimited					
13. SUPPLEMENTARY NOTES					
14. ABSTRACT Through analysis of the chromatin and transcriptional landscape of Multiple Myeloma (MM) and other tumors, this project has endeavored to provide an explanatory mechanism for how treatment with inhibitors of chromatin regulators can selectively target oncogene transcription, and to understand how chromatin and transcription are altered to promote tumorigenesis. Here we report the discoveries that BET bromodomains are required to communicate enhancer mediated pro-inflammatory signal dependent transduction (Brown et al., 2014), that translocations of the <i>IgH</i> enhancer to the <i>MYC</i> locus in MM expose both enhancer driven and MYC/E2F driven regulatory programs to BET bromodomain inhibition (Fulciniti et al., in preparation), and that master transcription factors co-operate with one another and BET bromodomains to establish oncogenic state in MM and other tumors (Lin et al., Nature in press). In anticipation of clinical drug resistance to BET bromodomain inhibition, we identified an epigenetic mechanism of resistance in which hyper-phosphorylation of BET bromodomains enables tumor cells to recruit these proteins to chromatin independent of bromodomain activity (Shu et al., Nature in press). These efforts have yielded insights into the dynamic transcriptional control of oncogenic cell state, the development of novel and extendable experimental and computational approaches, and therapeutic insights into the consequences of systemic <i>in vivo</i> BET bromodomain inhibition.					
15. SUBJECT TERMS Multiple myeloma, chromatin, computational biology					
16. SECURITY CLASSIFICATION OF:			17. LIMITATION OF ABSTRACT	18. NUMBER OF PAGES	19a. NAME OF RESPONSIBLE PERSON
a. REPORT U	b. ABSTRACT U	c. THIS PAGE U			USAMRMC
			UU	112	19b. TELEPHONE NUMBER (include area code)

Table of Contents

	<u>Page</u>
Introduction.....	2
Keywords.....	2
Key Research Accomplishments.....	3
Impact.....	8
Changes/Problems.....	9
Products.....	9
Participants and other collaborating organizations.....	10
Special reporting requirements.....	11
Appendices.....	12

Introduction: Multiple Myeloma (MM) is an aggressive and incurable plasma cell malignancy often characterized by IgH Enhancer/*MYC* (IgH/*MYC*) translocations that drive excess levels of the c-Myc oncoprotein. Recently, the Bradner laboratory has shown that inhibition of the general transcriptional co-activator BRD4 with a selective chemical probe (JQ1) leads to dramatic down regulation of c-Myc expression and cell death in MM cell lines (Delmore et al., 2011). In other tumors, BRD4 inhibition does not lead to down regulation of the IgH/*MYC* translocation gene, but rather causes the selective down regulation of other key cancer genes (Dawson et al., 2011; Ott et al., 2012; Zuber et al., 2011). BRD4 is a BET (bromodomain and extra-terminal) family protein (Filippakopoulos et al., 2010) that binds to acetyl-lysine residues on histones and other chromatin associated factors. BRD4 is a key co-activator of the elongation factor P-TEFb and has been shown to co-activate transcription through co-operative interactions with master regulator transcription factors (Huang et al., 2009). P-TEFb is required for the transcription elongation of essentially all active genes (Rahl et al., 2010) suggesting a general role for BRD4 in broadly co-activating transcription. Thus, it is unexpected based on current paradigms of mammalian transcriptional regulation and chromatin structure, how inhibition of BRD4 can selectively inhibit the transcriptional activity of oncogenes in tumors. Currently, small molecule inhibitors of BRD4 (including derivatives of JQ1) are in FDA Phase I clinical trials, with recent reports of positive clinical response (AACR 2014). As such, it is imperative to understand how BRD4 regulates gene expression and the mechanisms by which inhibition of BRD4 leads to dramatic effects at a small subset of genes in a cell type specific manner. This study is focused on understanding mechanisms of JQ1 activity and resistance in MM and other tumors as it is critical for understanding both how chromatin regulators function in cancer and how general transcriptional regulator inhibitors can achieve selective effects against cancer.

Keywords: Chromatin, Transcription, Multiple Myeloma, *MYC*, Therapeutics, Gene Regulation

Key Research Accomplishments - *To explore the mechanisms by which inhibition of BRD4 leads to selective effects on oncogene transcription, we have undertaken the following aims:*

Major goals and accomplishments

Aim 1. To map BRD4 onto the transcriptional and epigenomic landscape of MM

Status: Completed

Reported in Loven et al., Cell 2013; Chapuy et al., Cancer Cell 2013, Fulciniti et al., submitted

Using genome wide ChIP-Seq (chromatin immunoprecipitation coupled to high throughput sequencing) approaches, we have mapped the comprehensive transcriptional and epigenomic landscape of MM in steady state and in response to treatment with increasing doses of JQ1. Given that BRD4 was present at all active promoters and enhancers, it was unclear how inhibition of such a broad co-factor could yield highly specific results. In several JQ1 sensitive cell lines, we integrated global BRD4 occupancy data with comprehensive chromatin landscapes and found that BRD4 was disproportionately found at only a handful of large enhancer domains that spanned tens of kilobases and were also highly occupied by all other chromatin and transcriptional co-activators. On the whole, these “super-enhancers” made up only 3% of the cell’s enhancers, but encompassed 40% of all enhancer bound co-activators. In each tumor, super enhancers associated with key oncogenic genes, driving the not only continued cancer cell growth, but also genes specifying tumor cell identity itself.

The discovery and characterization of super-enhancers first published in this work (Loven et al., 2013) and its companion paper (Whyte et al., 2013) have now been extended and further studied in more than 40 publications. Data from this study has been curated and made publically available on the Epigenome gateway browser in the “Multiple Myeloma Epigenome Portal” (<http://epigenomegateway.wustl.edu/browser/>). Consequently, we have developed and made openly available analysis software that can quantify normalized factor occupancy genome wide to identify and rank super-enhancers, genomic regions of asymmetric chromatin co-activator loading (<https://github.com/BradnerLab/pipeline>). These methods have been used by more than 100 laboratories and have been incorporated into online databases including dbSuper (<http://bioinfo.au.tsinghua.edu.cn/dbsuper/>).

In subsequent work, we have employed this chromatin mapping framework in patient MM samples to investigate changes to the enhancer landscape of MM induced by the primary tumor microenvironment and have identified candidate primary tumor specific super-enhancers. We have also integrated a new chromatin mapping technique (ATAC-Seq) that identifies putative cis-regulatory elements from small cell samples (Buenrostro et al., 2013). These approaches have been extended to profile transcription factor occupancy in the MM.1S cell line (Figure 1), and also to profile chromatin landscapes in other MM cell lines (Fulciniti et al., in preparation). Here we have identified distinct regulatory axes governed by BRD4 and the cell cycle promoting transcription factor E2F and have incorporated this theme into our study of BRD4 cooperation with other transcriptional regulators (Aim 3). Finally, in collaboration with others, we have extended these approaches into other tumor model systems including Non Hodgkin’s lymphoma (Chapuy et al., 2013), triple negative breast cancer (Shu et al., Nature in press), and medulloblastoma (Lin et al., Nature in press).

Aim 2. To examine the kinetic, transcriptional response to BET bromodomain inhibition

Status: Completed and extended with new objectives

Reported in Loven et al., Cell 2013; Chapuy et al., Cancer Cell 2013; Anand et al., Cell 2013; Brown et al., Molecular Cell 2014; Fulciniti et al., in preparation

From data generated in Aim 1, we hypothesized that asymmetric occupancy of chromatin regulators including BRD4 at oncogene driving super-enhancers might explain their sensitivity to chromatin co-activator inhibition. We have mapped JQ1 induced changes in gene expression and RNA Pol II genomic occupancy in both a time and concentration dependent manner in MM and other disease model systems (Anand et al., 2013; Brown et al., 2014; Chapuy et al., 2013; Loven et al., 2013). These data consistently show that BET bromodomain inhibition by JQ1 treatment leads to a global decrease in transcriptional activity, specifically a decrease in elongating RNA Pol II. This inhibition of transcription is most pronounced at super-enhancer proximal target genes and is supported at the chromatin level by evidence that both BRD4 and the active kinase subunit of the elongation P-TEFb are preferentially lost at super-enhancer loci upon JQ1 treatment. In MM, JQ1 treatment leads to rapid downregulation of *MYC* and other super-enhancer associated oncogenes. Interestingly in diffuse large B-cell lymphoma (DLBC), super-enhancers associate with different oncogenes and thus JQ1 treatment does not preferentially downregulate *MYC* transcription. Instead, in DLBCL, super-enhancers associate with other prominent B-cell factors including *BCL6* and *PAX5* that are strongly downregulated upon JQ1 treatment (Chapuy et al., 2013). In all profiled systems, inhibition of chromatin and transcriptional regulators including BET bromodomains (BRD4), the BAF complex (BRG1) and transcriptional kinases (CKD7) caused a selective inhibition of transcription at super-enhancer driven oncogenes as compared to other genes (Chapuy et al., 2013; Chipumuro et al., 2014; Kwiatkowski et al., 2014; Loven et al., 2013; Shi et al., 2013).

We next sought to explore the consequences BRD4 inhibition during dynamic cell state transitions. Previously, we had quantified BRD4 inhibition response in static, steadily growing tumor cell models. However, MM and other tumor cell states are often maintained through aberrant oncogenic signaling, necessitating an understanding of the role of BRD4 in stimulus coupled signal transduction response. *In vivo*, MM tumors exist in a pro-inflammatory environment in the bone marrow that is supported through increased NF- κ B signaling and transcriptional activity (Demchenko and Kuehl, 2010). NF- κ B transcription factors are known to directly interact with BRD4 (Huang et al., 2009) and we hypothesized that activation of NF- κ B transcriptional response subsequent to pro-inflammatory stimulation requires BRD4 activity. Since *in vitro* immortalized MM cell line models fail to fully articulate *in vivo* inflammatory response, we utilized the well characterized NF- κ B responsive primary human endothelial cell system to investigate basic mechanisms of signal dependent BRD4 function.

Treatment of endothelial cells with pro-inflammatory stimuli caused NF- κ B to localize to the nucleus leading to transcriptional response and phenotypic cell state transition from resting to inflamed and activated endothelium. Surprisingly we found that NF- κ B activation resulted in a rapid and comprehensive remodeling of the chromatin co-activator landscape, with more than 50% of all BRD4 bound super-enhancers redistributing to sites of newly acquired NF- κ B binding. In inflammatory stimulated endothelial cells co-treated with JQ1, NF- κ B still enters the nucleus and binds chromatin. However, BRD4 fails to redistribute to these sites of NF- κ B binding, thus blocking super-enhancer formation and consequently abrogating NF- κ B directed pro-inflammatory transcriptional response.

These data suggest a crucial role for BRD4 in dynamic cell state transitions where it communicates signals from signaling pathway terminal transcription factors to RNA Pol II. Further, JQ1 inhibited transcription of NF- κ B directed *de novo* super-enhancer target genes an order of magnitude more than genes associated with resting endothelial super-enhancers at

baseline. This observation suggests that *in vivo* cell populations undergoing dynamic cell state transitions in response to cell signaling are most likely to be affected by JQ1. Results from this study of BRD4 and NF- κ B dynamics were published in *Molecular Cell* (Brown et al., 2014) and is included in the appendices of this report.

Aim 3. To explore the contribution of cooperative binding and disproportionate load by BRD4 to transcriptional response

Status: completed

Reported in Fulciniti et al., in preparation; Lin et al., Nature in press

The initial description of super-enhancers in MM revealed additional features of super-enhancers with potential utility in characterizing tumor epigenomes. Super-enhancers differ from typical enhancers in their underlying sequence composition, their response to perturbation, and their ability to drive high levels of transcription at target genes. Towards a mechanistic understanding of these features, we have now developed experimental and computational approaches to map transcription factor binding sites within super-enhancer loci using data derived from a combination of H3K27ac ChIP-Seq to map super-enhancers and ATAC-Seq to precisely identify high-resolution transcription factor binding sites. From this data we are able to computationally reconstruct enhancer gene regulatory networks and predict transcription factor regulated gene expression programs. Applying these methods to MM cells, we observed that many cell type specific transcription factors in MM were regulated by a super-enhancer and also bound to super-enhancers. These auto-regulatory patterns established a core regulatory circuitry in which a small number of transcription factors are super-enhancer associated, and in turn bind to and regulate super-enhancers (Figure 2). Analysis of core regulatory circuitry in MM and normal cd19+ plasma cells revealed many shared plasma cell transcription factors including XBP1 and IRF family factors. Differential analysis revealed the glucocorticoid receptor transcription factor as present only in the circuitry of MM cells. As MM are primarily treated with dexamethasone (a glucocorticoid receptor agonist), these data support a central role for glucocorticoid receptor signaling in driving MM oncogenesis and suggest that core circuitry network approaches accurately describe tumor cell identity.

We have also used methodology developed from this effort to elucidate core transcriptional regulatory circuitry in other poorly classified tumors. In collaboration with the German cancer research institute (DKFZ), we have deployed chromatin enhancer mapping and core regulatory circuitry inference methods to elucidate cellular origins of different medulloblastoma subgroups. Medulloblastoma is clinically classified into 4 different subgroups, each with different molecular pathologies. However, the cellular origins of individual subgroups are poorly understood. Here the use of core regulatory circuitry inference has elucidated the developmental and cellular origins of the previously uncharacterized Group 4 medulloblastoma. A manuscript describing these results has been submitted to *Nature* and is currently in revision (Lin et al., *Nature* in press).

Currently we are extending these chromatin profiling and computational approaches across a large number of hematopoietic lineage derived normal and tumor cell populations. To date H3K27ac ChIP-Seq in primary patient MM samples has proven technically challenging. Although ATAC-Seq is able to identify transcription factor binding sites in primary samples, it fails to adequately map super-enhancers, necessitating H3K27ac mapping approaches. To overcome technical challenges with ChIP-Seq, we are implementing the newly developed iChIP methodology that is able to produce ChIP-Seq equivalent data from small (< 1 million cell) patient samples (Lara-Astiaso et al., 2014).

Finally, analysis of the transcription factor occupancy in relation to BRD4 in MM has suggested new therapeutic strategies to target the disease. Previously we reported the concomitant inhibition of MYC and E2F activity in multiple myeloma (MM) upon treatment with the BET bromodomain inhibitor JQ1 (Delmore et al., 2011). BET bromodomains (BETs) are transcriptional co-activators that occupy active promoters and enhancers, but are asymmetrically localized to a small number of “super-enhancer” domains. JQ1 treatment results in disproportionate displacement of BETs from super-enhancers leading to potent and selective downregulation of super-enhancer target genes, including MYC which is > 90% depleted after 6 hours.

In contrast, E2F protein levels are relatively unperturbed by JQ1 treatment. Instead, JQ1 treatment inhibits the expression of super-enhancer driven upstream regulators of E2F including the MYC and CCND2. In tumors where MYC is not super-enhancer associated, JQ1 treatment fails to directly downregulate E2F activity. These observations suggest that the MYC translocation status of MM plays a key role in determining the sensitivity of E2F activity to BET inhibition. They also suggest an unexplored collaboration between MYC, E2F, and BETs in maintenance of MM.

In both MYC translocated and non MYC translocated MM, we mapped the global occupancy patterns of E2F1 and its dimerization partner DP1. We next utilized chemical and genetic perturbations to investigate the functional consequences of E2F depletion singly or in combination with JQ1 *in vitro* and *in vivo*. Across MM, we demonstrate that E2F activity is required for tumor growth both *in vitro* and *in vivo*, as depletion results in G1 arrest (Figure 3a,b). We find surprisingly that DP1, the dimerization partner of E2F1, is required for tumor growth, and that DP1 expression negatively correlates with patient outcome. Global chromatin analysis reveals distinct regulatory axes for E2F and BETs, with E2F predominantly localized to active gene promoters and BETs disproportionately found at super-enhancers (Figure 3 c-j). As MYC activates E2F, translocations of *MYC* to the *IgH* enhancer place both super-enhancer and E2F driven genes under BET control. Consequently BET inhibition is synergistic with E2F depletion only in non-*IgH/MYC* translocated MM (Figure 3k).

Our results implicate E2F as a dependency in MM and expose a vulnerability to BET inhibition imparted by *IgH/MYC* translocations. In non *IgH/MYC* translocated MM, E2F inhibition is synergistic with JQ1 treatment. These observations suggest targeting of E2F as promising therapeutic strategy in MM. A manuscript describing these results is currently under preparation for 2015 submission.

Summary of reported accomplishments: During this reporting period, data from these aims have been prepared in the following manuscripts.

- 1) Brown et al., Molecular Cell 2014
- 2) Lin et al., Nature in press
- 3) Fulciniti et al., in preparation
- 4) Wolf et al., Trends in Cell Biology 2014
- 5) Shu et al., Nature in press

Opportunities for training and professional development: The work described in these aims was performed in collaboration with clinicians, molecular biologists, and computational biologists. Through collaborative interactions, I have gained knowledge and experience in the clinical management of cancer and translational research approaches. Conversely, I have been able to train several molecular biologists in computational bioinformatics.

Professional development during this reporting period include the presentation of invited seminars at the Dana-Farber Cancer Institute, Broad Institute, Memorial Sloan Kettering Cancer Institute, Baylor College of Medicine, and the National Institutes of Health.

Dissemination of results to communities of interest: In addition to the aforementioned public presentations, work from these aims was presented to disease advocacy groups and disease stakeholders at the Dana-Farber Cancer Institute, the Leukemia and Lymphoma Society, and the Multiple Myeloma Research Foundation. Work from these aims was also accepted for presentation as an oral abstract at the American Society of Hematology annual meeting in December 2015. Emerging themes and concepts on oncogenic transcription regulation by the transcription factor MYC were also presented in a peer reviewed review article (Wolf et al., 2014).

Future plans: I have accepted and transitioned to an Assistant Professor tenure track research faculty appointment at the Baylor College of Medicine Department of Molecular and Human Genetics. Continuing research priorities from my fellowship work include submission and revision of results in Fulciniti et al., and the preparation of a manuscript on transcription factor networks in MM and other hematopoietic malignancies.

Impact:

The discovery and characterization of super-enhancers first published in this work (Loven et al., 2013) and its companion paper (Whyte et al., 2013) have now been extended and further studied in more than 40 publications. Data from this study has been curated and made publically available on the Epigenome gateway browser in the “Multiple Myeloma Epigenome Portal” (<http://epigenomegateway.wustl.edu/browser/>). Consequently, we have developed and made openly available analysis software that can quantify normalized factor occupancy genome wide to identify and rank super-enhancers, genomic regions of asymmetric chromatin co-activator loading (<https://github.com/BradnerLab/pipeline>). These methods have been used by more than 100 laboratories and have been incorporated into online databases including dbSuper (<http://bioinfo.au.tsinghua.edu.cn/dbsuper/>).

The discovery of BET bromodomain regulation of inflammatory signaling has prompted additional pre-clinical research on therapeutic strategies to target chromatin and transcription regulation in vascular disease by pharmaceutical companies developing BET bromodomain inhibitors for the clinic (Tensha Therapeutics & Glaxosmithkline).

Finally, the work described in this report encompasses several high impact manuscripts describing the transcriptional role of BET bromodomain proteins and the transcriptional and chromatin consequences of their inhibition. These manuscripts have been cited in the design and implementation of Phase I and Phase 2 clinical trials of BET bromodomain inhibitors. In many of these trials, BET bromodomain inhibition has demonstrated numerous instances of objective response including several complete responses. Trials for these compounds in multiple myeloma are ongoing and will likely report outcomes in 2016.

Changes and Problems:

We have experienced technical challenges in profiling chromatin in primary MM patient samples. This is largely due to the low cellularity of MM tumor samples, and sample preservation techniques that impede chromatin extraction. Additionally, we failed to clonally evolve MM cell lines that were resistant to BET bromodomain inhibition. To overcome these problems, we have first orthogonally extended our approaches to other tumor systems as a way to prototype new analytical methods. We have also extended work in MM cell line models and *in vivo* xenograft models in collaboration with other MM researchers. Finally we are in the process of applying new low cell requirement chromatin profiling techniques including the newly developed iChIP methodology that is able to produce ChIP-Seq equivalent data from small (< 1 million cell) patient samples (Lara-Astiaso et al., 2014).

There are no other significant changes and problems to report.

Products:

Publications: During this reporting period, data from these aims have been prepared in the following manuscripts.

- 1) Brown et al., Molecular Cell 2014
- 2) Lin et al., Nature in press
- 3) Fulciniti et al., in preparation
- 4) Wolf et al., Trends in Cell Biology 2014
- 5) Shu et al., Nature in press

Presentations: During this reporting period, this work was presented in invited seminars at the Dana-Farber Cancer Institute, Broad Institute, Memorial Sloan Kettering Cancer Institute, Baylor College of Medicine, and the National Institutes of Health.

Conferences: During this reporting period, this work was presented at conference poster proceedings at the Keystone Symposium on Epigenetics and Cancer and at the AACR meeting "MYC: From biology to therapy". Work from these aims was also accepted for presentation as an oral abstract at the American Society of Hematology annual meeting in December 2015.

There are no other significant products to report.

Participants and Other Collaborating Organizations:

Name:	<i>Jonathan Brown, M.D.</i>
Project Role:	<i>Instructor</i>
Researcher Identifier	N/A
Nearest person month worked:	9
Contribution to Project:	<i>Dr. Brown contributed experimental analysis and direction as part of a collaboration reported in Brown et al., 2014.</i>
Funding Support:	<i>Dr. Brown is supported by the NIH-K08 HL105678, The Watkins Discovery Research Award and The Harris Family Award</i>

Name:	<i>Alexander Federation, Ph.D.</i>
Project Role:	<i>Graduate Student</i>
Researcher Identifier	N/A
Nearest person month worked:	4
Contribution to Project:	<i>Dr. Federation provided computational analysis as part of a collaboration reported in Aim 2 and in Lin et al., Submitted 2015</i>
Funding Support:	<i>Dr. Federation is supported by a Leukemia and Lymphoma Society SCOR, the National Science Foundation, and NIH grants 1R01 CA176745-01 and P01 CA109901</i>

Name:	<i>Mariateresa Fulciniti Ph.D.</i>
Project Role:	<i>Instructor</i>
Researcher Identifier	N/A
Nearest person month worked:	12
Contribution to Project:	<i>Dr. Fulciniti provided experimental analysis as part of a collaboration reported in Aims 1 and Aim 2.</i>
Funding Support:	<i>Dr. Fulciniti is supported by NIH PO1-CA078378, and RO1CA050947</i>

There are no other significant participants or collaborating organizations.

Special reporting requirements: There are no special reporting requirements to report

Appendices:

1. Figure Legends

Figure 1 Transcription factor and chromatin landscape of multiple myeloma:

a) A heatmap showing the pairwise similarities between spatial occupancy patterns of various transcription factors, chromatin regulators, and chromatin modifications in the MM1.S multiple myeloma cell line. Individual factors are hierarchically clustered to group spatially similar binding profiles.

Figure 2 Transcription regulatory circuitry of multiple myeloma:

a) Schematic showing methodology of constructing transcription factor networks. For each super-enhancer associated transcription factor a regulatory IN and OUT degree are calculated. For any transcription factor (TF_a) The IN degree represents the number of other super-enhancer associated transcription factors that binds to the super-enhancer of TF_a . The OUT degree represents the number of super-enhancers bound by the transcription factor TF_a .

b) Network of the most highly interconnected super-enhancer associated transcription factors in the multiple myeloma cell line MM1.S. Each node represents a super-enhancer associated transcription factor. Each edge represents binding of a transcription factor to the super-enhancer of another transcription factor.

c) Comparative network analysis of various hematopoietic lineage derived cells. Each comparison shows a rank ordered bar plot of the largest changes in total regulatory degree (IN + OUT) for each cell type comparison. At each transition, transcription factors with significant changes in total regulatory degree are highlighted.

Figure 3 E2F and BET bromodomains establish distinct oncogenic regulatory axes in multiple myeloma:

a) A panel of MM cell lines were infected with either scrambled (pLKO.1) or DP1-targeted shRNA and selected with puromycin for 72 hours. DP1 mRNA levels and cell growth were then evaluated by qPCR and Thymidine uptake respectively. The results are presented as mRNA (gray line) or cell growth (black bars) changes from cells infected with pLKO.1. Data are shown as the mean values \pm s.d. of triplicates.

b) *In vivo* evaluation of the effects of DP1 knockdown on MM cells. Growth curve assess tumor size after injection of MM.1S cells transduced with DP1-specific shRNA or scrambled control vectors subcutaneously into the right posterior flank region of SCID mice. Data are shown as the mean values \pm s.d.

c) Gene tracks showing RNA Pol II, H3K4me3, E2F1, and DP1 occupancy at the *E2F1* gene loci

d) Gene tracks showing BRD4, H3K27ac, E2F1, and DP1 occupancy at the *BCL-xL* gene loci. The *BCL-xL* intronic super-enhancer (SE) is annotated.

e,f) Pie charts showing the fraction of active promoters and enhancers bound by E2F1 and DP1

g) Scatter plot showing the contribution of BRD4 enhancer regulation and E2F promoter regulation for all active genes in MM1.S. The y-axis shows enhancer BRD4 signal and the x-axis shows promoter E2F signal. Units are in reads per million.

h) Venn diagram showing the overlap of high BRD4 SE regulated genes and high E2F promoter regulated genes.

i,j) Functional enrichment categories for high BRD4 SE regulated genes (i) and high E2F promoter regulated genes (j)

k) Isobologram of anti-E2F peptide and JQ1 treatment effects on cell proliferation.

2. References.

- Anand, P., Brown, J.D., Lin, C.Y., Qi, J., Zhang, R., Artero, P.C., Alaiti, M.A., Bullard, J., Alazem, K., Margulies, K.B., *et al.* (2013). BET bromodomains mediate transcriptional pause release in heart failure. *Cell* *154*, 569-582.
- Brown, J.D., Lin, C.Y., Duan, Q., Griffin, G., Federation, A.J., Paranal, R.M., Bair, S., Newton, G., Lichtman, A.H., Kung, A.L., *et al.* (2014). NF-kappaB Directs Dynamic Super Enhancer Formation in Inflammation and Atherogenesis. *Molecular cell*.
- Buenrostro, J.D., Giresi, P.G., Zaba, L.C., Chang, H.Y., and Greenleaf, W.J. (2013). Transposition of native chromatin for fast and sensitive epigenomic profiling of open chromatin, DNA-binding proteins and nucleosome position. *Nature methods* *10*, 1213-1218.
- Chapuy, B., McKeown, M.R., Lin, C.Y., Monti, S., Roemer, M.G., Qi, J., Rahl, P.B., Sun, H.H., Yeda, K.T., Doench, J.G., *et al.* (2013). Discovery and characterization of super-enhancer-associated dependencies in diffuse large B cell lymphoma. *Cancer cell* *24*, 777-790.
- Chipumuro, E., Marco, E., Christensen, C.L., Kwiatkowski, N., Zhang, T., Hatheway, C.M., Abraham, B.J., Sharma, B., Yeung, C., Altabef, A., *et al.* (2014). CDK7 Inhibition Suppresses Super-Enhancer-Linked Oncogenic Transcription in MYCN-Driven Cancer. *Cell* *159*, 1126-1139.
- Dawson, M.A., Prinjha, R.K., Dittmann, A., Giotopoulos, G., Bantscheff, M., Chan, W.I., Robson, S.C., Chung, C.W., Hopf, C., Savitski, M.M., *et al.* (2011). Inhibition of BET recruitment to chromatin as an effective treatment for MLL-fusion leukaemia. *Nature* *478*, 529-533.
- Delmore, J.E., Issa, G.C., Lemieux, M.E., Rahl, P.B., Shi, J., Jacobs, H.M., Kastiris, E., Gilpatrick, T., Paranal, R.M., Qi, J., *et al.* (2011). BET bromodomain inhibition as a therapeutic strategy to target c-Myc. *Cell* *146*, 904-917.
- Demchenko, Y.N., and Kuehl, W.M. (2010). A critical role for the NFkB pathway in multiple myeloma. *Oncotarget* *1*, 59-68.
- Filippakopoulos, P., Qi, J., Picaud, S., Shen, Y., Smith, W.B., Fedorov, O., Morse, E.M., Keates, T., Hickman, T.T., Felletar, I., *et al.* (2010). Selective inhibition of BET bromodomains. *Nature* *468*, 1067-1073.
- Huang, B., Yang, X.D., Zhou, M.M., Ozato, K., and Chen, L.F. (2009). Brd4 coactivates transcriptional activation of NF-kappaB via specific binding to acetylated RelA. *Molecular and cellular biology* *29*, 1375-1387.
- Kwiatkowski, N., Zhang, T., Rahl, P.B., Abraham, B.J., Reddy, J., Ficarro, S.B., Dastur, A., Amzallag, A., Ramaswamy, S., Tesar, B., *et al.* (2014). Targeting transcription regulation in cancer with a covalent CDK7 inhibitor. *Nature* *511*, 616-620.
- Lara-Astiaso, D., Weiner, A., Lorenzo-Vivas, E., Zaretsky, I., Jaitin, D.A., David, E., Keren-Shaul, H., Mildner, A., Winter, D., Jung, S., *et al.* (2014). Immunogenetics. Chromatin state dynamics during blood formation. *Science* *345*, 943-949.
- Loven, J., Hoke, H.A., Lin, C.Y., Lau, A., Orlando, D.A., Vakoc, C.R., Bradner, J.E., Lee, T.I., and Young, R.A. (2013). Selective inhibition of tumor oncogenes by disruption of super-enhancers. *Cell* *153*, 320-334.
- Ott, C.J., Kopp, N., Bird, L., Paranal, R.M., Qi, J., Bowman, T., Rodig, S.J., Kung, A.L., Bradner, J.E., and Weinstock, D.M. (2012). BET bromodomain inhibition targets both c-MYC and IL7R in high-risk acute lymphoblastic leukemia. *Blood*.
- Rahl, P.B., Lin, C.Y., Seila, A.C., Flynn, R.A., McCuine, S., Burge, C.B., Sharp, P.A., and Young, R.A. (2010). c-Myc regulates transcriptional pause release. *Cell* *141*, 432-445.
- Shi, J., Whyte, W.A., Zepeda-Mendoza, C.J., Milazzo, J.P., Shen, C., Roe, J.S., Minder, J.L., Mercan, F., Wang, E., Eckersley-Maslin, M.A., *et al.* (2013). Role of SWI/SNF in acute leukemia maintenance and enhancer-mediated Myc regulation. *Genes & development* *27*, 2648-2662.
- Whyte, W.A., Orlando, D.A., Hnisz, D., Abraham, B.J., Lin, C.Y., Kagey, M.H., Rahl, P.B., Lee, T.I., and Young, R.A. (2013). Master transcription factors and mediator establish super-enhancers at key cell identity genes. *Cell* *153*, 307-319.
- Wolf, E., Lin, C.Y., Eilers, M., and Levens, D.L. (2014). Taming of the beast: shaping Myc-dependent amplification. *Trends in cell biology*.

Zuber, J., Shi, J., Wang, E., Rappaport, A.R., Herrmann, H., Sison, E.A., Magoon, D., Qi, J., Blatt, K., Wunderlich, M., *et al.* (2011). RNAi screen identifies Brd4 as a therapeutic target in acute myeloid leukaemia. *Nature* 478, 524-528.

3. Attachments

- a) Brown et al., Molecular Cell 2014**
- b) Lin et al., Nature in press**
- c) Wolf et al., Trends in Cell Biology 2014**
- d) Shu et al., Nature in press**

NF- κ B Directs Dynamic Super Enhancer Formation in Inflammation and Atherogenesis

Jonathan D. Brown,^{1,6} Charles Y. Lin,^{2,6} Qiong Duan,^{1,3,6} Gabriel Griffin,⁴ Alexander J. Federation,² Ronald M. Paranal,² Steven Bair,² Gail Newton,⁴ Andrew H. Lichtman,⁴ Andrew L. Kung,^{2,5} Tianlun Yang,³ Hong Wang,¹ Francis W. Lusciuskas,⁴ Kevin J. Croce,¹ James E. Bradner,^{2,*} and Jorge Plutzky^{1,*}

¹Cardiovascular Division, Brigham and Women's Hospital, Harvard Medical School, Boston, MA 02115, USA

²Department of Medical Oncology, Dana Farber Cancer Institute, Harvard Medical School, Boston, MA 02115, USA

³Cardiovascular Division, Xiangya Hospital, Central South University, 410078 Changsha, Hunan, PR China

⁴Center for Excellence in Vascular Biology, Department of Pathology, Brigham and Women's Hospital, Harvard Medical School, Boston, MA 02115, USA

⁵Department of Pediatrics, Columbia University Medical Center, New York, NY 10032, USA

⁶Co-first author

*Correspondence: james_bradner@dfci.harvard.edu (J.E.B.), jplutzky@rics.bwh.harvard.edu (J.P.)

<http://dx.doi.org/10.1016/j.molcel.2014.08.024>

SUMMARY

Proinflammatory stimuli elicit rapid transcriptional responses via transduced signals to master regulatory transcription factors. To explore the role of chromatin-dependent signal transduction in the atherogenic inflammatory response, we characterized the dynamics, structure, and function of regulatory elements in the activated endothelial cell epigenome. Stimulation with tumor necrosis factor alpha prompted a dramatic and rapid global redistribution of chromatin activators to massive de novo clustered enhancer domains. Inflammatory super enhancers formed by nuclear factor-kappa B accumulate at the expense of immediately decommissioned, basal endothelial super enhancers, despite persistent histone hyperacetylation. Mass action of enhancer factor redistribution causes momentous swings in transcriptional initiation and elongation. A chemical genetic approach reveals a requirement for BET bromodomains in communicating enhancer remodeling to RNA Polymerase II and orchestrating the transition to the inflammatory cell state, demonstrated in activated endothelium and macrophages. BET bromodomain inhibition abrogates super enhancer-mediated inflammatory transcription, atherogenic endothelial responses, and atherosclerosis in vivo.

INTRODUCTION

Precise control of inflammation is essential for host defense. Defense against pyogenic infection requires rapid activation of tissue and circulating leukocytes and their recruitment by activated endothelium. However, inflammation is also integral to the pathophysiology of many common and life-threatening illnesses. Acute, high-grade inflammation accompanying sepsis features

systemic inflammatory cell activation and contributes to multi-system organ failure and death (Medzhitov et al., 2012). Chronic, low-grade inflammation is a pathogenic feature of autoimmune disorders as well as highly prevalent and morbid conditions such as diabetes mellitus and atherosclerosis (Libby et al., 2011). As such, there is a pressing need to dissect inflammatory signaling for the elucidation of pathologic mechanisms of disease and the identification of targeted therapeutic interventions.

In inflammation, a primary mode of bidirectional cellular communication involves one set of cells releasing cytokines to activate surface receptors on effector cells. Transduced signals converge on activation and translocation of inflammatory transcription factors (Barnes and Karin, 1997). A central pathway common to the interaction between activated leukocytes and endothelium is tumor necrosis factor alpha (TNF- α)-mediated signal transduction to nuclear factor-kappa B (NF- κ B)—a family of master regulatory, proinflammatory transcription factors canonically defined by the p50/p65 heterodimer (Baltimore, 2011). Following entry into the nucleus, NF- κ B binds to DNA *cis*-regulatory elements at enhancers and promoters, prompting proinflammatory transcription (Pierce et al., 1988).

Genome-bound nuclear NF- κ B interacts with transcriptional coactivators to stimulate transcription at multiple steps including the remodeling of chromatin as well as the initiation and elongation of RNA polymerase II (RNA Pol II; Barboric et al., 2001; Kaikonen et al., 2013; Natoli, 2009). NF- κ B recruits and interacts with defined chromatin regulators including histone acetyltransferases (P300), histone deacetylases, and epigenetic reader proteins, such as BRD4 (Ashburner et al., 2001; Huang et al., 2009; Zhong et al., 2002). Through these interactions, NF- κ B engages in crosstalk with chromatin remodeling machinery.

BRD4 is a member of the bromodomain and extraterminal domain (BET) family of transcriptional coactivators and elongation factors (BRD2, BRD3, BRD4, and BRDT; Dey et al., 2000; LeRoy et al., 2008). At active genes, BET bromodomains recruit the positive transcription elongation factor complex (P-TEFb; Jang et al., 2005; Yang et al., 2005), and chromatin remodeling factors including the SWI/SNF complex (Shi et al., 2013) via molecular recognition of polyacetylated histone tails (Mujtaba et al.,

2007). Mechanistically, TNF- α or lipopolysaccharide (LPS) stimulation promotes direct acetylation of the p65 subunit (Lys310) of NF- κ B by P300 (Chen et al., 2001), promoting a direct interaction with BRD4 through twin acetyl lysine-recognizing bromodomains (Huang et al., 2009). This interaction is needed for productive NF- κ B transactivation (Huang et al., 2009), suggesting a central role for BRD4 in inflammatory transcriptional signaling.

Prior research from our group and others has identified that BET bromodomains localize genome-wide to promoter and enhancer regions (Anand et al., 2013; Chapuy et al., 2013; Lovén et al., 2013; Nicodeme et al., 2010). The majority of enhancer-bound BRD4 is found within a small number of massive enhancer regions termed super enhancers (SE). Like locus control regions or stretch enhancers, SEs concentrate chromatin-bound coactivators to genes essential for specialized cellular function (i.e., immunoglobulin production in plasma cells), and lineage specification (i.e., germinal center differentiation; Chapuy et al., 2013; Lovén et al., 2013; Parker et al., 2013; Whyte et al., 2013). Disruption of SE function by a first acetylated lysine-competitive small molecule BET bromodomain inhibitor from our group known as JQ1 (Filippakopoulos et al., 2010) suggests the mutability of these large chromatin structural elements (Chapuy et al., 2013). However, the role of SEs in the control of dynamic cell state transitions remains unknown. Recently, BET bromodomain inhibition has been shown to abrogate global, maladaptive transcriptional programs during sepsis and heart failure, implicating BRD4 in stress-induced cell state transitions (Anand et al., 2013; Nicodeme et al., 2010). These data provided a rationale for investigating the collaborative roles of NF- κ B and BRD4 in regulating SEs during proinflammatory activation.

The endothelium is critical to the initiation and propagation of inflammation. Endothelial cells (ECs) prompt leukocyte recruitment, adhesion, and trafficking into tissues, thus mediating responses essential for many inflammatory disorders, including atherogenesis, in which activation of ECs is pathogenic (Gimbrone et al., 1990; Ley et al., 2007). Despite these important roles in disease, global studies of chromatin structure and function in vascular endothelium have to date not been undertaken. In this study, we investigate the role of BRD4 in determining the inflammatory activation of ECs through NF- κ B and SE formation. Here, we provide evidence that EC activation by the archetypal proinflammatory stimulus TNF- α rapidly deploys NF- κ B to enhancers and promoters genome-wide, where it recruits BRD4. Through the recruitment of BRD4, NF- κ B establishes new SEs coincident with the surprising, rapid redistribution of BRD4 away from endothelial resting state SEs. Newly established NF- κ B SEs are proximal to and drive canonical genes of the inflammatory response in ECs, including key effectors of chemotaxis, adhesion, migration, and thrombosis. BRD4 depletion from chromatin through small molecule BET bromodomain inhibition impedes NF- κ B-directed SE reorganization. The failure to form proinflammatory SEs preferentially suppresses SE-dependent proinflammatory gene transcription, translating into functional suppression of key TNF- α -induced endothelial responses of leukocyte rolling, adhesion, and transmigration. In vivo, we find that BET bromodomain inhibition suppresses atherogenesis—a pathogenic process predicated on inflammatory endothelial activation. Together, these data establish BET bromodomain-containing

proteins as key effectors of the integrated mammalian inflammatory response through their rapid, dynamic, global reorganization of SEs during NF- κ B activation and suggest SE targeting during inflammatory cell state transitions as a therapeutic approach.

RESULTS

p65 and BRD4 Establish Super Enhancers during Proinflammatory Stimulation

To explore the role of NF- κ B, BRD4, and SEs in the acute inflammatory activation of ECs, we activated NF- κ B in primary human umbilical vein ECs with TNF- α , a canonical proinflammatory stimulus, for one hour. As expected, TNF- α resulted in NF- κ B nuclear translocation (Figures 1A and 1B), a rapid change in EC state characterized by increased monocyte adhesion (Figure 1C), and induction of adhesion molecule gene expression including E-selectin (*SELE*) and vascular cell adhesion molecule (*VCAM1*; Figure 1D; Ley et al., 2007). The recognized capacity of BRD4 to bind acetylated NF- κ B (Huang et al., 2009), suggests a coactivator role for the BET family in the robust p65-mediated EC inflammatory response observed. We therefore used chromatin immunoprecipitation coupled with high-throughput genome sequencing (ChIP-seq) to define p65 and BRD4 genomic occupancy in ECs before and following acute proinflammatory activation.

In TNF- α -stimulated ECs, p65 enrichment was evident at promoters (17.5%), intragenic (45.8%), and intergenic regulatory sequences (36.7%; Figures 1E and 1F). Striking colocalization of BRD4 and p65 was observed by global enrichment alignment and binding site motif analysis (Figure 1F; Figure S1A available online). TNF- α treatment prompts dynamic colocalization of p65 and BRD4 to enhancer and promoter regions marked by H3K27ac, which are significantly enriched for p65 consensus sequences (Figure S1A; Matys et al., 2006). At the exemplary *VCAM1* locus, TNF- α stimulation of resting ECs for one hour increased p65 occupancy at both promoters and upstream enhancer elements marked by acetylated chromatin (H3K27ac; Figure 1G). Coincident with these events, we identified recruitment of exceptionally high levels of BRD4 at discrete hyperacetylated enhancer elements (Figures 1F and 1G; Figure S1B), consistent with the formation of de novo SEs (SEs). Focal BRD4 colocalization with p65 was observed at each discrete peak, with complete concordance. Comparable evidence is provided at the *SELE* locus, where TNF- α stimulation recruits p65 and high levels of BRD4 to a gene regulatory region completely devoid of p65 and BRD4, augmenting regional hyperacetylation (Figure S1C). The dramatic remodeling of these loci in one hour in TNF- α stimulated ECs corroborates the robust transcriptional activation of these canonical EC inflammatory gene products (Figure 1D). Notably, typical enhancers are found at most other EC genes as exemplified by endothelial tyrosine kinase (*TEK*) and serpin peptidase inhibitor clade H1 (*SERPINH1*), where the levels of p65 and BRD4 are an order of magnitude lower compared to the *VCAM1* or *SELE* SE; and TNF- α does not induce mRNA expression (Figure 1H; Figures S1D and S1E).

To assess the genome-wide distribution of SEs during the EC inflammatory cell state transition, we characterized and compared the enhancer landscape in resting and TNF- α -activated

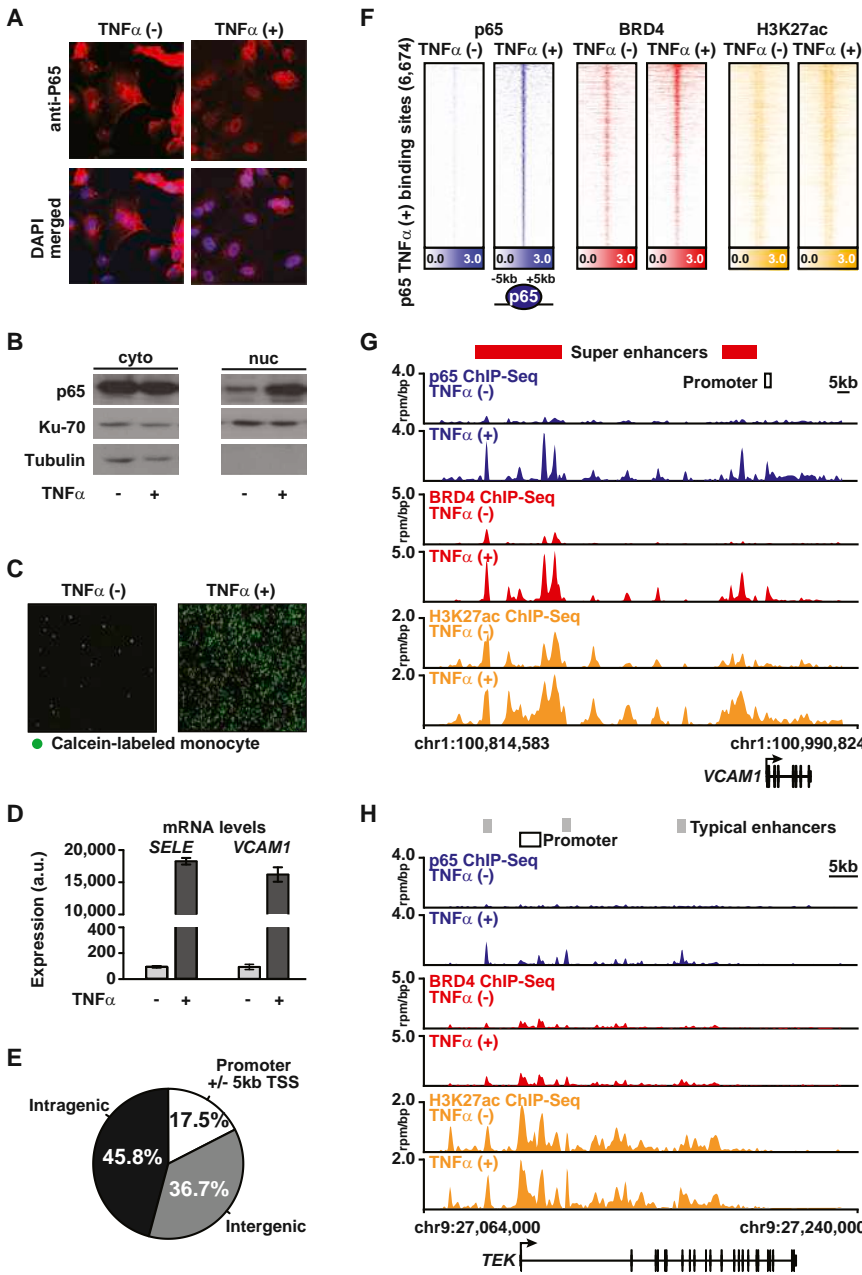


Figure 1. p65 and BRD4 Genome Binding during Proinflammatory Activation in ECs

(A) Images of ECs \pm TNF- α stained for p65 (red) or DAPI (blue) (25 ng/ml, 1 hr). (B) Western blot for p65, Ku-70, and tubulin in cytosolic (left) and nuclear (right) protein fraction lysates in ECs \pm TNF- α . (C) Images showing adhesion of calcein-labeled THP-1 monocytes to ECs \pm TNF- α (25 ng/ml, 3 hr). (D) Bar plots showing cell count normalized expression levels of *SELE* and *VCAM1* in ECs \pm TNF- α (25 ng/ml, 3 hr). Error bars represent SEM. (E) Pie chart of p65 binding site distribution in EC genome in TNF- α (+). (F) Heatmap of p65 (blue), BRD4 (red), and H3K27ac (yellow) levels in resting ECs and after TNF- α (25 ng/ml, 1 hr). Each row shows \pm 5kb centered on p65 peak. Rows are ordered by max p65 in each region. ChIP-seq signal (rpm/bp) is depicted by color scaled intensities. (G and H) Gene tracks of ChIP-seq signal for p65, BRD4, and H3K27ac at the *VCAM1* and *TEK* gene loci in untreated (top) or TNF- α (+) (bottom) ECs. The y axis shows ChIP-seq signal (rpm/bp). The x axis depicts genomic position with TNF- α gained typical enhancers (TE, gray) and SEs (SE, red) and promoter regions (white) marked. See also [Figure S1](#).

p65 total binding signal and density at SE loci when compared to either typical enhancer regions or active gene transcriptional start sites ([Figure 2E](#); [Figure S2D](#)). As exemplified by the *VCAM1* SE locus and also observed globally, ECs feature dense clustering of multiple regulatory transcription factor binding sites known to be involved in EC proinflammatory responses including p65, p50, ETS1/2, and transcription factor 3/4 (TCF3/4; [Figure 2F](#); [Figure S2E](#); [De Val et al., 2008](#); [Masckauchán et al., 2005](#)). In contrast, typical enhancer sites typified by the *TEK* locus possess a much lower density of these motifs ([Figure 2G](#); [Figure S2E](#)).

ECs using BRD4 ChIP-seq data sets. When ranked by increasing BRD4 enrichment, 347 and 271 SEs were identified in resting and TNF- α -activated ECs, respectively. These SEs comprised \sim 7% of the total number of discrete EC enhancer loci ([Figure 2A](#); [Figure S2A](#)), but represented more than one-fourth of the total amount of enhancer size and more than one-third of enhancer-bound BRD4 ([Figures 2A](#) and [2B](#)). Compared to typical enhancers, SE loci are significantly larger in DNA length, total BRD4 signal, and signal density and share less overlap between resting and TNF- α -activated ECs ([Figure 2C](#); [Figures S2A](#) and [S2B](#)). Following TNF- α stimulation, the absolute change in BRD4 total signal and density at SEs was greater compared to typical enhancers ([Figure 2D](#); [Figure S2C](#)). We observed higher

To dissect the temporal relationship between p65 and BRD4 localization to enhancers, we next performed time-ranging chromatin binding studies. ChIP for p65 and BRD4 followed by real-time PCR centered on the most prominent NF- κ B binding site in the 5' *VCAM1* and *CCL2* SEs revealed enrichment of p65 five minutes after TNF- α stimulation, with peak occupancy detected by 30 min ([Figure 2H](#); [Figure S2F](#)). BRD4 recruitment followed the identical temporal pattern of recruitment at these sites. Inhibition of NF- κ B phosphorylation and function by I κ B kinase inhibition (BAY 11-7082, "BAY") ([Pierce et al., 1997](#)) completely abrogated TNF- α -induced p65 and BRD4 accumulation at both NF- κ B sites at all time points, while also suppressing *VCAM1* gene induction ([Figure S2G](#)). As expected,

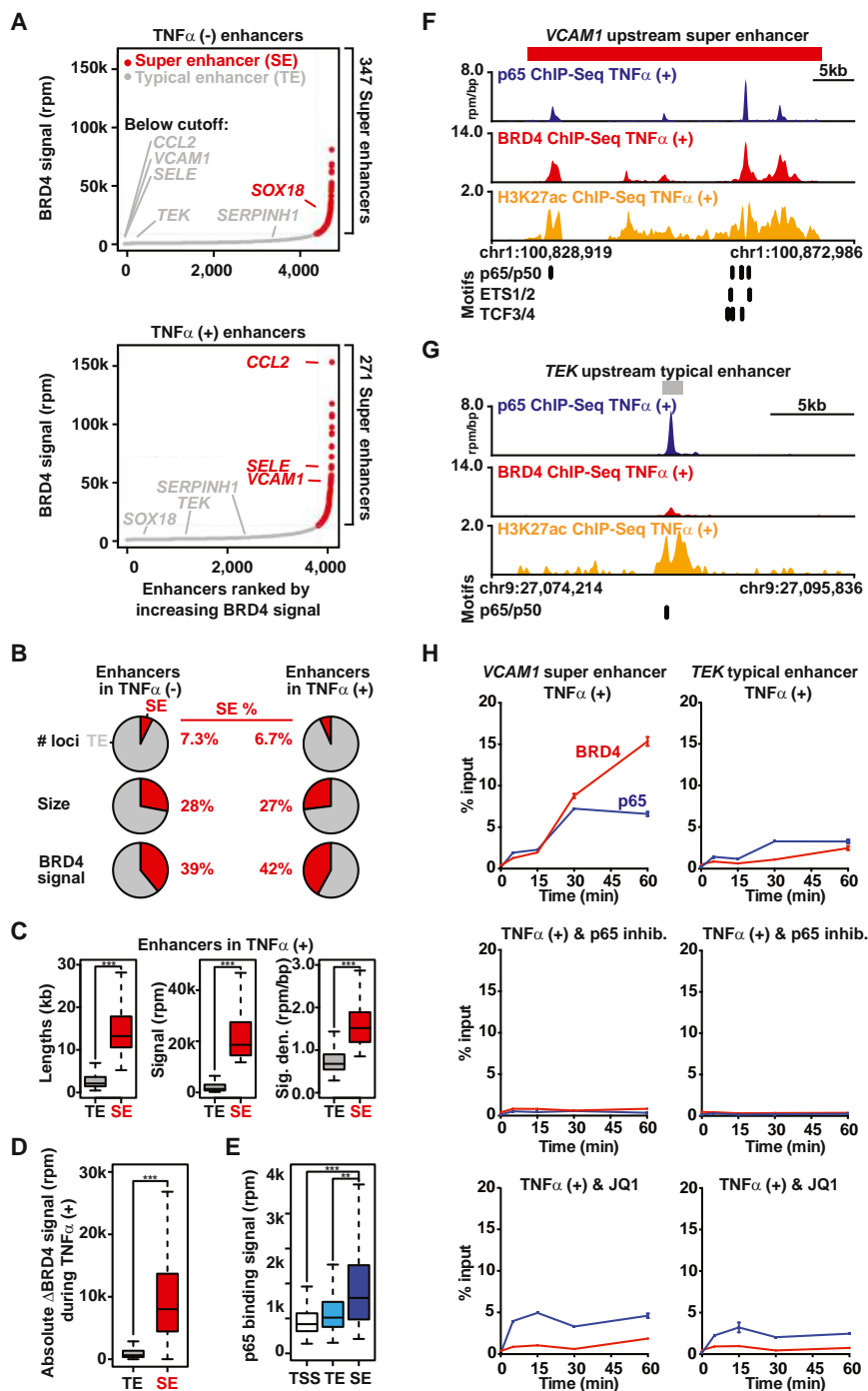


Figure 2. p65 and BRD4 Establish Super Enhancers during Proinflammatory Stimulation

(A) Ranked plots of enhancers defined in resting (top) or TNF- α (+) (bottom) ECs ranked by increasing BRD4 signal (units: rpm). Enhancers are defined as regions of BRD4 ChIP-seq binding not contained in promoters. The cutoff discriminating TEs from SEs is shown as a dashed line. Genes associated with enhancers that are considered typical or super are colored gray and red, respectively.

(B) Pie charts displaying characteristics of TE and SE regions including number of loci, size, and BRD4 signal.

(C) Boxplots of median enhancer length (kb), signal (rpm), and density (rpm/bp) in TNF- α -gained enhancers. Significance of the difference between distributions determined using a two-tailed t test. *** $p < 1 \times 10^{-10}$.

(D) Boxplot of absolute change in BRD4 signal in response to TNF- α measured at all enhancers in TNF- α (-) and TNF- α (+). Significance of the difference between distributions determined using a two-tailed t test. *** $p < 1 \times 10^{-10}$.

(E) Boxplot of p65 binding signal (rpm) at all active gene promoters (TSS), TEs, and SEs in TNF- α -treated ECs. Significance of the difference between distributions determined using a two-tailed t test. ** $p < 1 \times 10^{-5}$, *** $p < 1 \times 10^{-10}$.

(F and G) Schematic of transcription factor motif binding sites at the *VCAM1* SE (red box; F) or *TEK* TE (gray box; G) loci in ECs treated with TNF α . (H) Line plots of kinetic ChIP-PCR showing enrichment (percent input normalized to time 0) of p65 and BRD4 at an NF- κ B binding site in the *VCAM1* (left) SE and *TEK* TE (right) in ECs treated with TNF- α (25 ng/ml; 0, 5, 15, 30, 60 min). The effect of cotreatment with vehicle (top), BAY (NF- κ B inhibitor, middle), and JQ1 (bottom) is shown. See also Figure S2.

NF- κ B Provokes Rapid Global Redistribution of BRD4 at Super Enhancers

We next explored the dynamics and function of SEs in inflammation in both ECs and macrophages. One hour following TNF- α stimulation, we observed the formation of pronounced, prototypical SEs at canonical inflammatory genes, such as the *CCL2* chemokine (Figure 3A). There, a density of upstream

and intragenic enhancer elements was identified, characterized by regional hyperacetylation (H3K27ac) and peaks of BRD4 enrichment coinciding with focal p65 binding sites (Figure 3A). Functionally, rapid SE formation was associated with recruitment of RNA Pol II (Figure 3A) and marked transcriptional activation (Figure S3A). These data provide a demonstration that the canonical proinflammatory stimulus TNF- α rapidly induces de novo formation of SEs established by p65 at proinflammatory

and intragenic enhancer elements was identified, characterized by regional hyperacetylation (H3K27ac) and peaks of BRD4 enrichment coinciding with focal p65 binding sites (Figure 3A). Functionally, rapid SE formation was associated with recruitment of RNA Pol II (Figure 3A) and marked transcriptional activation (Figure S3A). These data provide a demonstration that the canonical proinflammatory stimulus TNF- α rapidly induces de novo formation of SEs established by p65 at proinflammatory

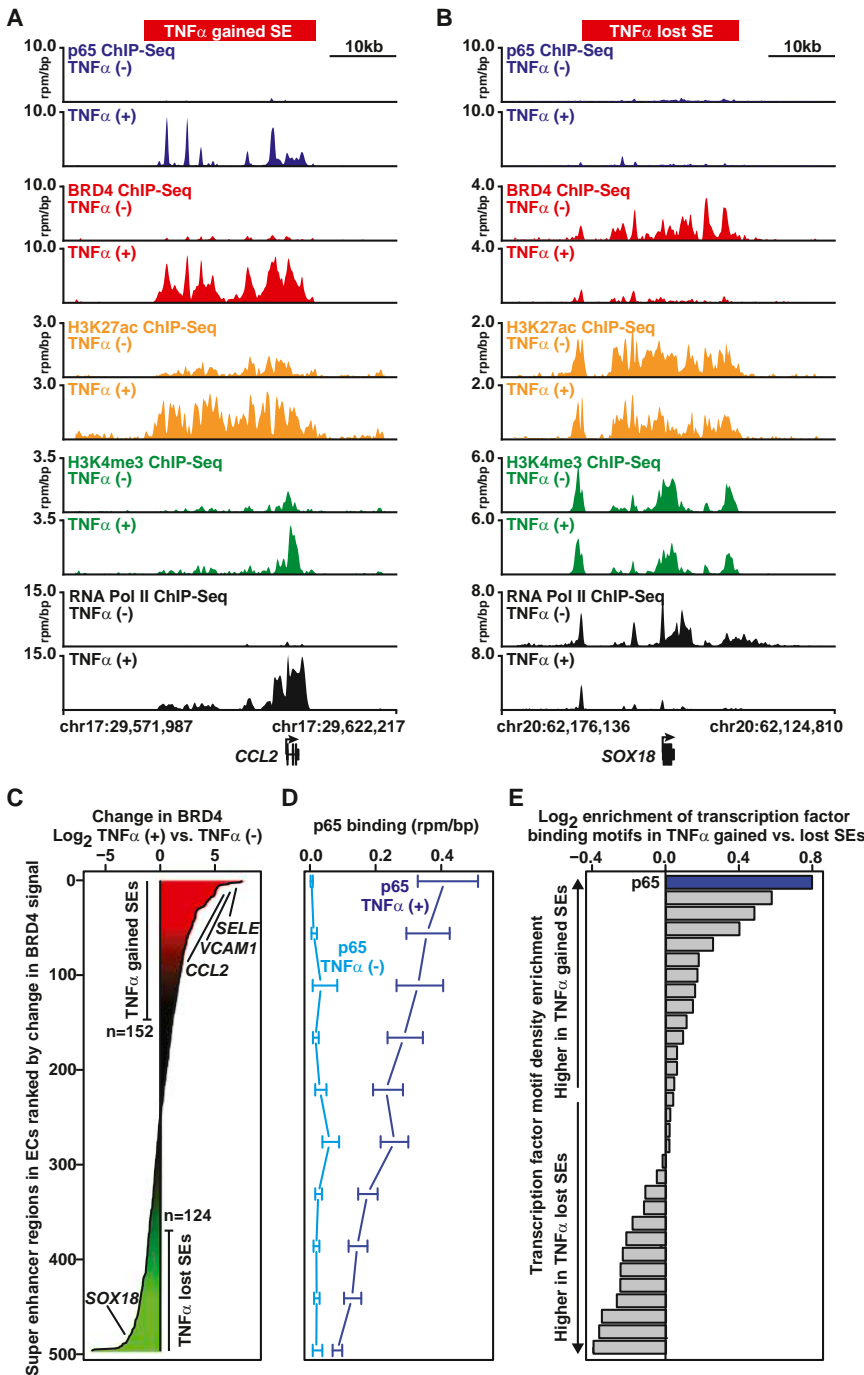


Figure 3. NF- κ B Provokes Rapid, Global Redistribution of BRD4

(A and B) Gene tracks of ChIP-seq signal (rpm/bp) for p65, BRD4, H3K27ac, H3K4me3, and RNA Pol II at the *CCL2* gene (A) or *SOX18* (B) locus in TNF α (-) (top) and TNF α (+) (bottom) ECs.

(C) All genomic regions containing a SE in TNF α (-) and TNF α (+) ECs are shown ranked by log₂ change in BRD4 signal (treated versus untreated). The x axis shows the log₂ fold change in BRD4 signal. Change in BRD4 levels at SEs is colored by intensity of change (green to red).

(D) Line plot showing the median levels of p65 binding (rpm/bp) at SEs in either TNF α (-) light blue or TNF α (+) dark blue conditions. SEs were ranked by change in BRD4 and binned (50/bin). The median p65 level was calculated in each bin. Error bars represent 95% confidence intervals (CI) of the median determined by empirical resampling.

(E) Horizontal bar plot showing the ratio of transcription factor motif density between TNF α -gained and TNF α -lost SEs. Twenty-one transcription factors are displayed whose motifs occur more frequently than expected based on dinucleotide background model. The transcription factor motifs are ranked by log₂ fold change in density between TNF α -gained versus TNF α -lost SEs. See also [Figure S3](#).

at the *SOX18* locus, accompanied by characteristic BRD4 occupancy and evident enrichment for RNA Pol II throughout the gene body. In the inflammatory EC state, TNF α fails to drive NF- κ B to the *SOX18* locus, RNA Pol II enrichment is markedly diminished and transcription is muted ([Figure 3B](#); [Figure S3A](#)). Only 1 hour following TNF α stimulation, BRD4 is effectively depleted, despite persistent hyperacetylation (H3K27ac) of the *SOX18* SE ([Figure 3B](#)).

To explore the relevance of changes in SEs provoked by proinflammatory activation across the genome, a systematic analysis of dynamic alterations in SE formation was undertaken. BRD4 enrichment was selected here as a preferred marker for SE identity owing to a concern that H3K27ac, or other more biochemically stable enhancer modifications (such as H3K4me1/2), may lag behind

target genes, also including *VCAM1* and *SELE* ([Figures 1G](#) and [S1C](#)).

Unexpectedly, the enrichment of BRD4 at inflammatory EC SEs was associated with the rapid, reciprocal depletion of BRD4 at resting EC SEs. ECs grown in culture feature 347 canonical SEs, including SEs associated with genes critical for noninflammatory EC function, such as the *SOX18* transcription factor implicated in vasculogenesis ([Matsui et al., 2006](#)). In such resting ECs, regional enrichment for H3K27ac is observed

BRD4 redistribution globally in a dynamic cell state change, as above at the *SOX18* locus. We identified a dramatic redistribution of genomic BRD4 occupancy following TNF α stimulation ([Figure 3C](#)). Differential enhancer analysis revealed an evident global balance in chromatin-associated BRD4, but importantly TNF α stimulation resulted in the reclassification of multiple enhancers from typical enhancer to SE (N = 152) and from SE to typical enhancer (N = 124; [Figure 3C](#)). Gains in BRD4 occupancy were strongly and directly associated with site-specific

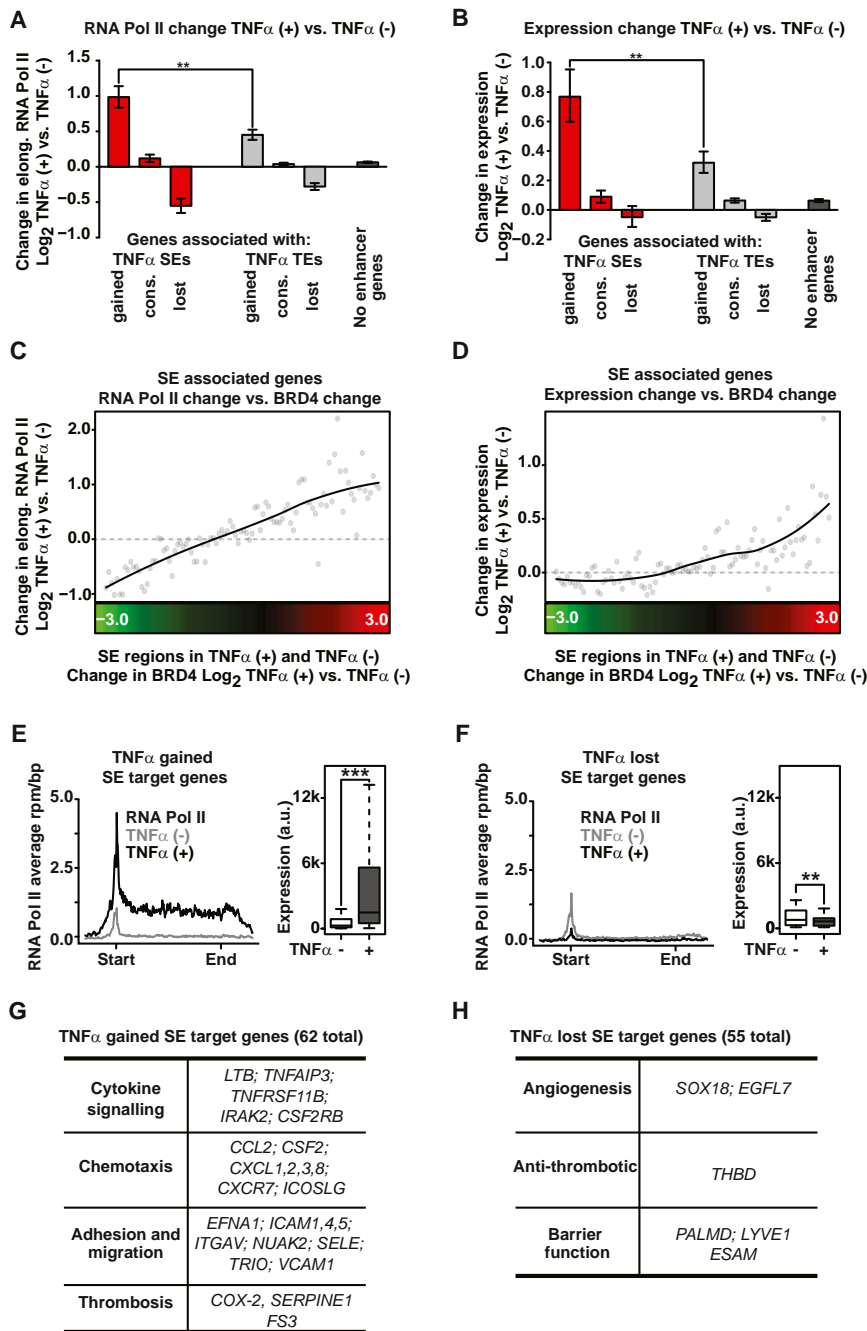


Figure 4. NF- κ B-Formed Super Enhancers Drive Proinflammatory Transcription

(A and B) Bar plot of average change in elongating RNA Pol II (A) or mRNA expression (B) at genes associated with TNF- α -gained, TNF- α -lost, or TNF- α -conserved SEs (red), TEs (gray), and no enhancers (black). Error bars represent 95% CI of the mean determined by empirical resampling. Significance of the difference between distributions determined using a two-tailed t test. ** $p < 1 \times 10^{-5}$, *** $p < 1 \times 10^{-10}$.

(C and D) Change in elongating RNA Pol II in the gene body region of genes (C, y axis) or change in mRNA levels (D, y axis) are plotted ranked by change in BRD4 at proximal SEs (x axis). Dots represent median change sampled across 50 evenly distributed bins with a loess fitted line overlaid. Change in BRD4 levels at proximal SEs are colored by intensity of change (green to red).

(E and F) Metagene representations of average RNA Pol II ChIP-seq signal (gray, untreated; black, TNF- α treated) in units of rpm/bp at a meta composite of target genes of SEs that are gained (E) or lost (F) in response to TNF- α treatment. Boxplots of cell count normalized expression levels are shown to the right of each metagene in arbitrary units for genes with associated SEs (gray, untreated; black, TNF- α treated) that are gained (E) or lost (F) in response to TNF- α treatment. Significance of the difference between distributions determined using a two-tailed t test. ** $p < 1 \times 10^{-5}$, *** $p < 1 \times 10^{-10}$.

(G and H) Table showing the functional categories of selected genes that are targets of SEs gained (G) or lost (H) in response to TNF- α treatment. See also Figure S4.

sites in TNF- α -gained SEs as a causal event in BRD4 SE redistribution during inflammatory activation (Figure 3E), akin to comparable “stretch enhancers” as described by Francis Collins and colleagues (Parker et al., 2013).

NF- κ B-Formed Super Enhancers Drive Proinflammatory Transcription

To assess the consequences of SE redistribution on transcriptional output, we integrated genome-wide ChIP-seq data

increases in p65 binding occupancy genome-wide (Figure 3D). As expected, TNF- α -gained SEs are characterized by coordinate increases in BRD4 and H3K27ac enrichment at regions of increased p65 occupancy, which correlates directly with SE formation (Figures 3C and S3B). Consistent with the SOX18 regulatory region, lost SEs are defined by a significant reduction of BRD4 occupancy following TNF- α stimulation that is disproportionate to minimal changes in p65 and modest reductions in H3K27ac (Figures 3D and S3C). Finally, the p65 motif was found at much higher density in TNF- α -gained versus TNF- α -lost SEs in ECs, further suggesting p65 direct binding to clustered

with cell count-normalized, array-based absolute gene expression profiling measurements obtained before and 1 hour after TNF- α stimulation. Compared to typical and conserved enhancer regions, the gain or loss of SEs provoked by TNF- α resulted in the largest changes to RNA Pol II occupancy and expression of adjacent genes (Figures 4A and 4B). This global relationship was also evident when specifically comparing the change in the levels of SE constituent BRD4 versus change in nearby gene elongating RNA Pol II levels and expression (Figures 4C and 4D). Those genes positioned near TNF- α -gained SEs, which also feature BRD4 enrichment at their promoters

suggestive of promoter-enhancer communication, demonstrated marked induction of transcriptional initiation, elongation, and gene expression (Figure 4E; Figure S4A). Functional classification of TNF- α -gained SE marked genes reveals known drivers of key functional facets of EC inflammatory responses: cytokine signaling, chemotaxis, adhesion and migration, and thrombosis (Figure 4G; Figure S4F). In contrast, the reciprocal loss of BRD4 at resting EC SEs resulted in a proportionate decrease in transcription and expression of nearby genes (Figures 4A, 4B, and 4F), such as *THBD* and genes involved in angiogenesis and endothelial barrier function (Figure 4H; Figure S4G). Notably, the cohort of lost SE genes featured marked decreases in transcriptional initiation and elongation by RNA Pol II enrichment metagene analysis in advance of changes in promoter modification (H3K4me3 enrichment; Figure S4B). Genes with conserved enhancers show minimal change in expression and serve pathways that govern homeostatic function in ECs (Figures 4A and 4B; Figure S4H). Globally, this chromatin restructuring results in a strong induction of proinflammatory SE driven transcription compared to typical enhancer associated genes. The 62 TNF- α -gained, SE-associated genes comprise only \sim 8% of all genes with >2 -fold increase in mRNA expression, but account for \sim 60% of the total increase in upregulated gene expression and \sim 20% of the increase in cellular mRNA within 3 hr of TNF- α stimulation (Figures S4C–S4E). These data provide discrete examples and global evidence of dynamic, functional remodeling of enhancer factors even preceding the structural decommissioning of abandoned enhancers.

NF- κ B-Formed Super Enhancers Drive Proinflammatory Gene Expression in a BET Bromodomain-Dependent Manner

Disruption of SEs by disrupting enhancer factors, such as BRD4, has been observed to selectively influence the expression of genes associated with SEs (Lovén et al., 2013). In cancer, we have observed that competitive displacement of BET bromodomains from nuclear chromatin provokes coordinated inhibition of the MYC transcriptional program, often associated with downregulation of MYC itself (Chapuy et al., 2013; Delmore et al., 2011; Zuber et al., 2011). Using a chemical genetic approach, we assessed the role of BET bromodomains in the rapid transcriptional response of SE-associated, proinflammatory genes in TNF- α -stimulated ECs. Small molecule probes, such as the BET bromodomain inhibitor JQ1, are particularly appealing in the study of dynamic processes, because they offer precise temporal perturbation of the biological system (Frye, 2010; Strausberg and Schreiber, 2003). We therefore performed a dynamic, genome-wide analysis of BET bromodomain inhibition on inflammatory SE integrity, global chromatin structure, gene expression, and EC postinflammatory function.

First, we characterized the effect of JQ1 on EC chromatin structure and function immediately following TNF- α exposure. ECs were treated with JQ1 (500 nM) to displace BET bromodomains, then stimulated with TNF α for 1 hour. Chromatin from treated and untreated ECs was subjected to ChIP-seq for promoters (H3K4me3), enhancers (H3K27ac), RNA Pol II, the p65 transcription factor, and the BRD4 coactivator. At the *SELE* locus, BET inhibition had no effect on TNF- α -mediated recruit-

ment of p65 (Figures 5A and 5B). However, JQ1 depleted BRD4 resulting in abrogated *SELE* expression assessed by decreased RNA Pol II enrichment (Figure 5A and cell surface protein levels assessed by flow cytometry (Figure S5E). Comparable observations are evident at the *CCL2* and *IRAK2* loci, where BET inhibition selectively displaces BRD4 leading to impaired transcription induction and elongation by RNA Pol II (Figures S5A and S5B).

Global analysis of TNF- α -stimulated ECs revealed preferential loss of BRD4 at TNF- α -gained SEs compared to typical enhancers, with minimal effect on TNF- α -induced p65 binding or H3K27ac levels (Figure 5B). TNF- α -gained SEs possessed a diminished capacity to drive proinflammatory transcription initiation and elongation in the presence of the BRD4 inhibitor, JQ1 (Figure 5C), and these dynamic effects on RNA Pol II enrichment were independent of alterations in promoter modification by differential metagene analysis of H3K4me3 enrichment at the transcriptional start sites (Figure S5C). Functionally, preferential JQ1-induced loss of transcription at TNF- α -gained SE-associated genes culminated in more potent suppression of their proinflammatory gene expression program relative to genes driven by typical enhancers (Figure 5C; Figure S5D). Treatment of ECs with TNF- α and JQ1 suppressed the maximal mRNA induction of SE-associated genes (*FS3*, *CCL2*, *VCAM1*) at a lower concentration of JQ1 and to a greater degree compared to TE-associated genes (*LOX*, *TEK*, *NLRP1*; Figure 5D). Together, these data support a model in which BET bromodomains mediate dynamic and immediate inflammatory EC response gene transcription, by facilitating chromatin-dependent signal transduction from NF- κ B to RNA Pol II.

To determine whether JQ1 transcriptional effects resulted from specific engagement of BETs at nuclear chromatin, we spatially localized the JQ1 molecule genome-wide using a new biotechnology called Chem-seq (Anders et al., 2014). This technique maps the interactions of small molecules with chromatin in the human genome, in this instance by using a retrievable synthetic derivative of JQ1 (biotin-JQ1). Notably, despite high levels of acetylated H3K27ac at enhancers, we detected no biotin-JQ1 occupancy with Chem-seq at *SELE* and other SEs (Figure 5E; Figures S5F and S5G) in resting ECs. Rather, at these loci, biotin-JQ1 binding to chromatin perfectly colocalized with BRD4 spatially and temporally following TNF- α -stimulation. Genome-wide analysis demonstrated a dose-dependent relationship between biotin-JQ1 localization and the decrease in genomic BRD4 occupancy, not H3K27ac, in ECs treated with TNF- α + JQ1 compared to TNF- α alone (Figures 5F and 5G). Taken together, these data reveal that JQ1 directly targets BRD4 during proinflammatory activation in ECs. Preferential loss of BRD4 at inflammatory SEs by BET bromodomain inhibition serves mechanistically to underscore the observed selective effects on transcription.

To assess the generalizability of these observations, we tested whether the BRD4-dependent formation of proinflammatory SEs is relevant for other immune effector cells. We integrated robust, publically available acetyl-histone data (H4K12ac) with RNA Pol II ChIP-seq data in LPS-stimulated macrophages (Nicodeme et al., 2010), to map SEs and explore the effect of BET inhibition on enhancer-mediated transcriptional signaling. H4K12ac is a

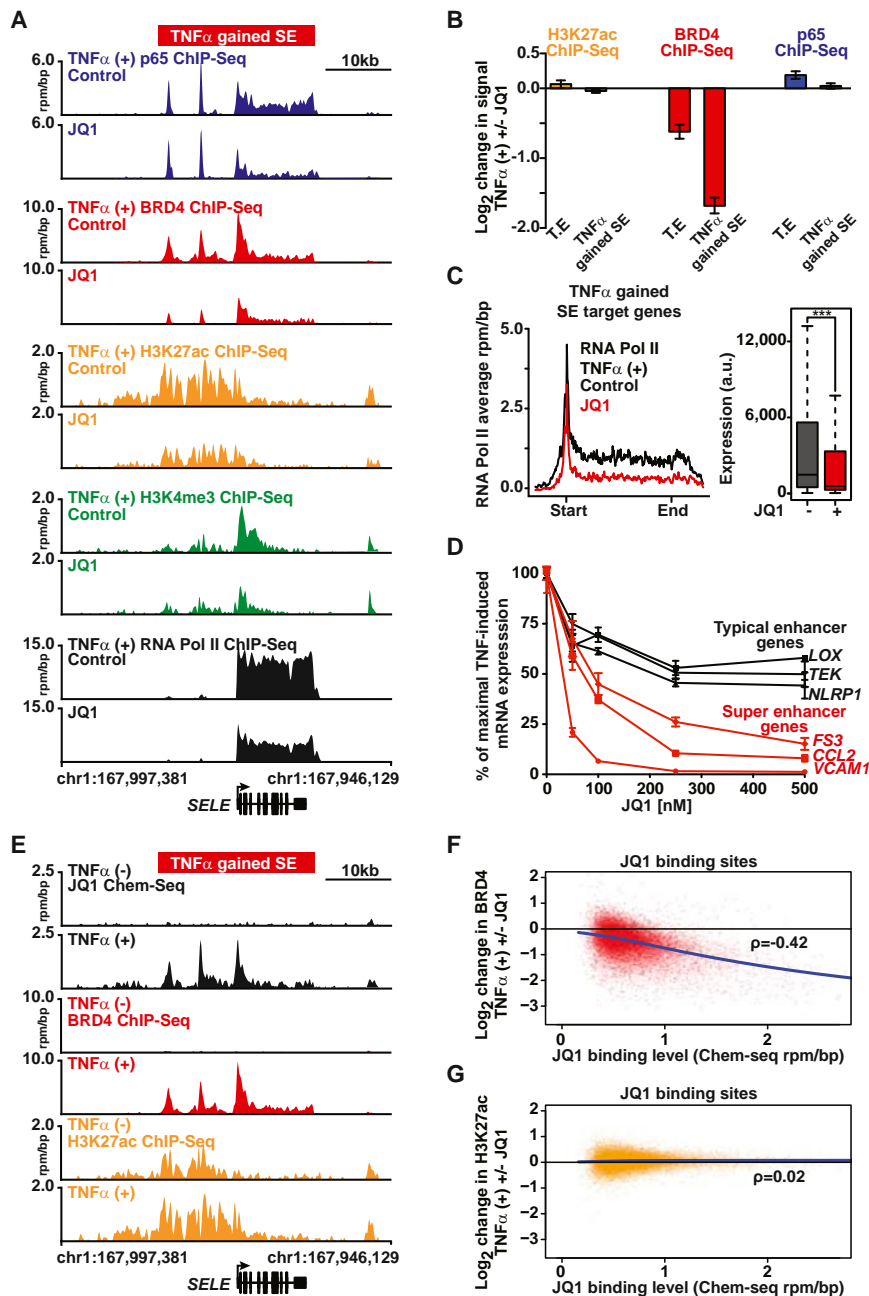


Figure 5. NF- κ B-Formed Super Enhancers Drive Proinflammatory Gene Expression in a BET Bromodomain-Dependent Manner

(A) Gene tracks of ChIP-seq signal (rpm/bp) for p65, BRD4, H3K27ac, H3K4me3, and RNA Pol II at the *SELE* locus in TNF- α -treated ECs cotreated with vehicle (top) or JQ1 (bottom).

(B) The mean log₂ fold change in H3K27ac (yellow), BRD4 (red), and p65 (blue) ChIP-seq signal in TNF- α -treated cells \pm JQ1 at either TEs or SEs gained in response to TNF- α treatment. Error bars represent 95% CI of the mean determined by empirical resampling.

(C) Metagene representations of average RNA Pol II ChIP-seq signal (black, TNF- α treated; red, JQ1 treated) in units of rpm/bp at a meta composite of target genes of SEs gained in response to TNF- α treatment. Boxplots (right) show cell count normalized expression levels in TNF- α (25 ng/ml, 3 hr) treated ECs \pm JQ1. Significance of the difference between distributions determined using a two-tailed t test. *** $p < 1 \times 10^{-10}$.

(D) Line plots of mRNA levels (qRT-PCR) of three representative genes associated with TEs (*LOX*, *TEK*, *NLRP1* in black) and SEs (*FS3*, *CCL2*, *VCAM1* in red) in response to TNF- α and JQ1 (50, 100, 250, 500 nM). The mRNA levels from TNF- α + VEH (10 ng/ml, 3 hr)-treated ECs were set to 100%. Results displayed as the percent reduction from maximum. Error bars represent SEM. Representative results from two independent experiments are shown.

(E) Gene tracks from Chem-seq (JQ1) and ChIP-seq (BRD4, H3K27ac) data sets of the *SELE* SE locus (rpm/bp) for JQ1, BRD4, and H3K27ac from TNF- α (-) or TNF- α (+)-stimulated ECs.

(F and G) Scatter plot of JQ1 genome-wide binding levels on the x axis compared to the log₂ change in BRD4 (F) or H3K27ac (G) ChIP-seq signal on the y axis. The change in BRD4 and H3K27ac signal was determined comparing TNF- α + JQ1 versus TNF- α .

See also Figures S5 and S6.

histone mark defining active enhancers that can be used to identify SEs in the absence of specific enhancer coactivator data (Hnisz et al., 2013; Whyte et al., 2013).

Large gains of histone acetylation were identified in macrophages following LPS stimulation at the *Irf2* proinflammatory gene locus (Figure S6A). LPS treatment provoked an immediate increase in promoter and intergenic acetylation, accompanied by an increase in RNA Pol II enrichment throughout the gene body. Globally, SE analysis identified 122 gained SEs following LPS treatment near proinflammatory genes involved in cytokine signaling, cell adhesion, and chemotaxis (Figures S6B and S6C). Unlike inflammatory ECs, the target genes induced and associ-

ated with proinflammatory SEs in macrophages are largely distinct from those found in ECs (Figure S6D). Transcription at SE-associated genes was more strongly induced by LPS compared to genes controlled by typical enhancers, as revealed by composite analysis of RNA Pol II enrichment and elongation (Figures S6E and S6F). As in activated ECs, BET bromodomain inhibition in macrophages preferentially suppressed transcription of genes driven by proinflammatory SEs as compared to genes controlled by typical enhancers (Figures S6G and S6H). The *Irf2* locus provides an exemplary illustration of the effect of BET bromodomain inhibition using the structurally analogous I-BET inhibitor (Nicodeme et al., 2010), on depletion of RNA Pol II enrichment (Figure S6A). Collectively, these data from ECs and macrophages demonstrate that proinflammatory SEs drive proinflammatory gene activation in a cell context specific manner.

BET Bromodomain Inhibition Suppresses Leukocyte Rolling, Adhesion, and Transmigration in Endothelium

In response to proinflammatory stimuli, endothelial-leukocyte interactions follow a sequential cascade involving leukocyte chemoattraction, their slow rolling, and subsequent firm adhesion to ECs, culminating in leukocyte endothelial transmigration into tissue (Ley et al., 2007). To explore a phenotypic effect of SE disruption by BET bromodomain inhibition, we tested the functional effects of JQ1 on leukocyte rolling across TNF- α -activated endothelium in vivo. C57Bl/6 mice were pretreated with JQ1 (50 mg/kg) 12 hours before TNF- α injection. As depicted with intravital microscopy of leukocyte rolling in the cremaster postcapillary venule, BET bromodomain inhibition significantly reduced the leukocyte rolling flux (15.8 versus 7.5, $p < 0.01$; Figure 6A) and the number of leukocyte rollers/minute (42.8 versus 25.14, $p < 0.05$; data not shown), without changing systemic white blood cell count or shear stress (Figure S7A). BET bromodomain inhibition also shifted the distribution of leukocyte velocity and increased mean velocity (2.89 μ m/s versus 3.91 μ m/s, $p < 0.01$), consistent with an effect on E-selectin-mediated slow rolling (Figures 6B and 6C).

Next, we examined firm adhesion of the human monocytic cell line (THP1) to activated ECs in vitro. TNF- α -stimulated ECs had significantly increased numbers of attached THP1 cells (Figure 6D). JQ1 pretreatment of ECs suppressed THP1 adhesion to TNF- α -activated ECs by 70% (Figures 6D and 6E). Similarly, siRNA inhibition of BRD4 expression in ECs recapitulated JQ1's effects on THP1 adhesion to ECs (Figures 6F and 6G). Lastly, we tested BET bromodomain inhibitor effects on leukocyte transmigration in a parallel-plate flow chamber. TNF- α stimulation of ECs resulted in transmigration of 67% of human neutrophils (Figure 6H). Pretreatment of ECs with JQ1 prior to TNF- α stimulation reduced neutrophil transmigration in a concentration-dependent manner (Figure 6H). In kinetic studies of transcription response of TNF- α -stimulated ECs, JQ1 demonstrated prolonged inhibitory effects on expression of SE-associated genes (*SELE*, *VCAM1*, *CXCL8*, *CCL2*) over 48 hr (Figures 6I–6L). These data establish BET bromodomain inhibition as a functional suppressor of the phenotypic features of EC proinflammatory activation.

BET Bromodomain Inhibition Suppresses Atherogenesis in Hypercholesterolemic Mice

Proinflammatory activation of ECs is a seminal, early event in atherogenesis, a process driven by vascular inflammation that also involves monocytes/macrophages and precedes atherosclerosis (Cybulsky et al., 2001). The transcriptional and functional effects of BET bromodomain inhibition in ECs prompted us to examine their role in atherogenesis using the well-established low-density lipoprotein (LDL) receptor-deficient (*Ldlr*^{-/-}) mouse model. Vehicle-treated mice fed a cholesterol-enriched diet (10 weeks) developed atherosclerosis, as measured by oil red O staining (Figure 7A). Once-daily JQ1 treatment (50 mg/kg) reduced aortic plaque area by 40% (Figure 7A). Notably, there was no difference in LDL and high-density lipoprotein cholesterol between the vehicle and JQ1 treatment groups (168 versus 164 mg/dL and 56 versus 59 mg/dL, respectively; total cholesterol 911 versus 1,349 mg/dl; see also Table S6.). Early atherosclerotic lesions are comprised of macrophages

(98%–99%) with lesser amounts of T lymphocytes (1%–2%). Mac-3 staining demonstrated that JQ1 treatment significantly lowered total macrophage staining area, CD4-positive T lymphocytes, and levels of VCAM1 protein (Figures 7B–7D). Oil red O staining of en face thoracoabdominal aortas revealed decreased atherosclerotic plaque beyond the aortic root (Figures 7E and 7F). Soluble VCAM1 and ICAM1 levels were also significantly reduced in JQ1-treated animals compared to vehicle (Figures S7B and S7C), suggesting an effect of BET bromodomain inhibition on systemic proinflammatory activation in vivo. We next tested whether BET bromodomain inhibition mitigated the activation of proadhesion pathways in aortic endothelium, which occurs during the first 10 weeks of exposure to an atherogenic diet. In ex vivo aortic adhesion assays, the aortas harvested from animals (6 weeks on diet) treated with JQ1 supported less adhesion of fluorescently labeled monocytes (Figures S7D and S7E). These data demonstrate BET inhibition significantly decreased atherogenesis and accumulation of inflammatory cells in a well-characterized murine model of atherosclerosis.

DISCUSSION

The inflammatory response underlies numerous chronic diseases. NF- κ B is a master regulatory transcription factor in several dominant inflammatory signaling cascades, which cooperate with chromatin-associated regulatory complexes to direct inflammatory transcription (Natoli, 2009). Enhancer-bound NF- κ B arises following nuclear translocation in a manner influenced by pioneer transcription factors (Kaikkonen et al., 2013; Natoli, 2009; Ostuni et al., 2013) and a preestablished topology that places distal enhancer regions and target genes in spatial proximity (Jin et al., 2013). Here, we explore the role of chromatin in terminal signal transduction from NF- κ B to RNA polymerase, specifically at massive regulatory regions.

Super or stretch enhancers represent less than 5% of the enhancers in a cell, yet they use almost half of all enhancer coactivator proteins (Lovén et al., 2013; Parker et al., 2013; Whyte et al., 2013) and are highly transcribed, producing large amounts of enhancer RNA that may itself facilitate target gene activation (Hnisz et al., 2013; Kaikkonen et al., 2013). The SE landscape is remarkably cell-type specific, driving expression of the genes that define and maintain cell identity in different tissues and cell lineages. The present study demonstrates that NF- κ B engages most endothelial enhancers following proinflammatory activation, yet significant BRD4 recruitment to form de novo SEs is restricted to a subset of these enhancer regions. NF- κ B-directed SE formation causes global reorganization of the BRD4 SE landscape and induces the transcription of many canonical proinflammatory endothelial genes. Whereas previous studies have studied the importance of SEs in the maintenance of cell identity (Whyte et al., 2013), here we describe de novo SE formation as a mechanism by which stimulus-coupled master regulatory transcription factors such as NF- κ B can coordinate a rapid transcriptional response that drives a dynamic change in cell state.

This study of kinetic transcriptional response during the inflammatory cell state transition in ECs unexpectedly identified a rapid loss of SEs upon cytokine stimulation. As orchestrated

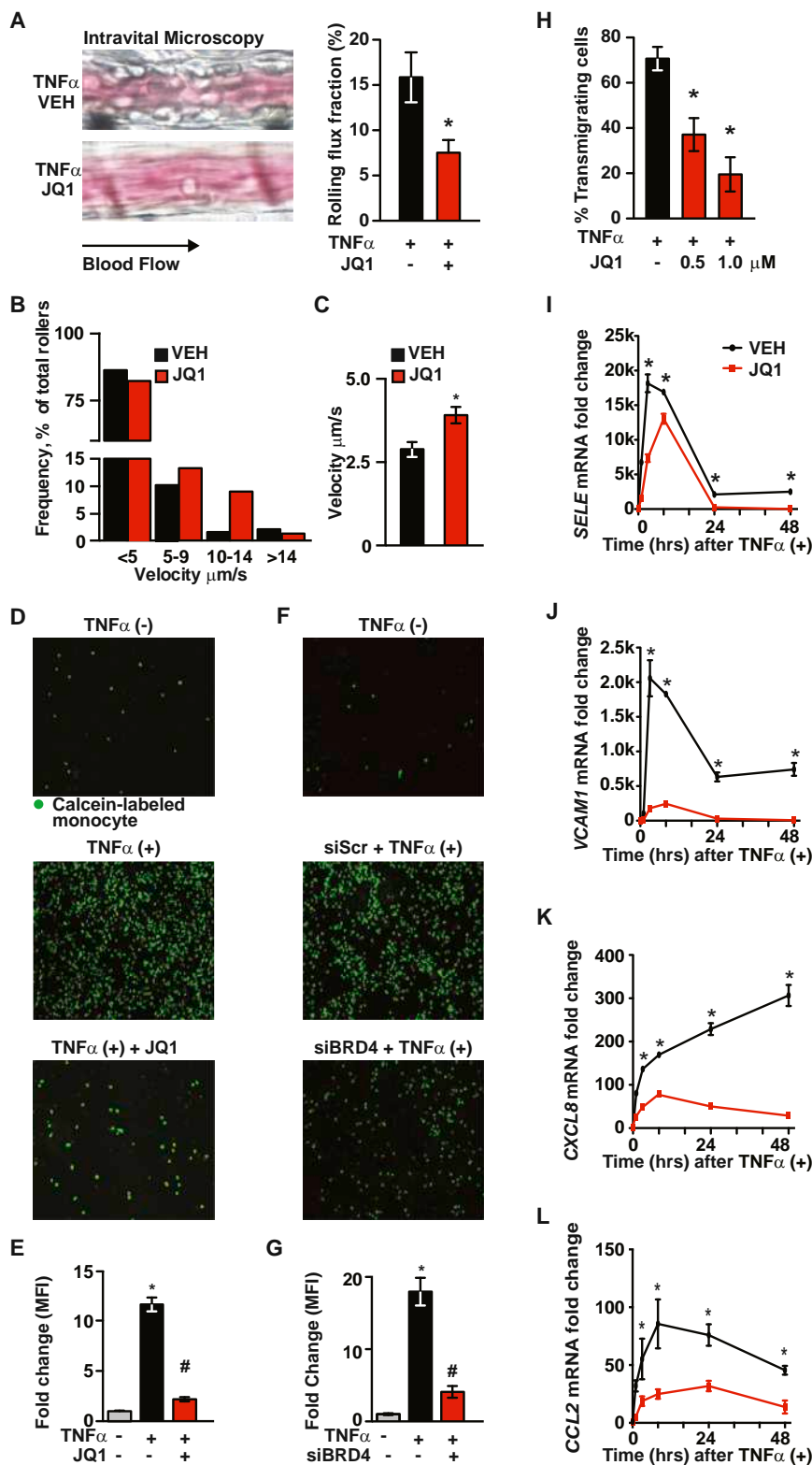


Figure 6. Phenotypic Consequences of BET Bromodomain Inhibition in Endothelium

(A) Intravital microscopy image (left) and bar plot quantification (right) of leukocyte flux fraction in the cremaster postcapillary venule after TNF- α (2 hr, n = 7/group) in VEH- or JQ1-treated samples. Error bars represent SEM. The statistical significance of the difference between JQ1- and VEH-treated samples was determined using a two-tailed t test. *p < 0.05.

(B) Velocity distribution of leukocytes measured in (A).

(C) Bar plot showing mean leukocyte velocity in cremaster postcapillary venule in TNF- α (+) animals \pm BET bromodomain inhibition. Error bars represent SEM.

(D and F) Representative fluorescence microscopy images showing adhesion of calcein-labeled THP1 cells to (D) ECs pretreated with JQ1 then activated with TNF α (4 hr) as well as (F) TNF- α -treated ECs after siRNA knockdown of BRD4.

(E and G) Bar plots showing quantification of fluorescence from (D) and (F).

(H) Bar plots showing quantification of transmigrating neutrophils on TNF- α -activated EC monolayers. Results pooled from three independent experiments. Data represent mean \pm SEM. The statistical significance of the difference between JQ1- and VEH-treated samples was determined using a two-tailed t test. *p < 0.05.

(I-L) Line plots of mRNA levels (qRT-PCR) for (I) SELE, (J) VCAM1, (K) CXCL8, and (L) CCL2 measured after stimulation of ECs with TNF- α (12.5 ng/ml; 1, 3, 8, 24, 48 hr) \pm JQ1 (500 nM).

The statistical significance of the difference between samples was determined using a two-tailed t test. *p < 0.05 in TNF- α (+) versus TNF- α (-); #p < 0.05 in JQ1 versus VEH. Data represent mean \pm SEM of fold change versus 0 hr. See also Figure S7.

by the master regulatory inflammatory transcription factor NF- κ B, SE formation comes at the immediate expense of SEs associated with active transcription of genes in unstimulated

for enhancer output, converting typical enhancers into SEs, thereby driving rapid and robust induction of inflammatory transcription.

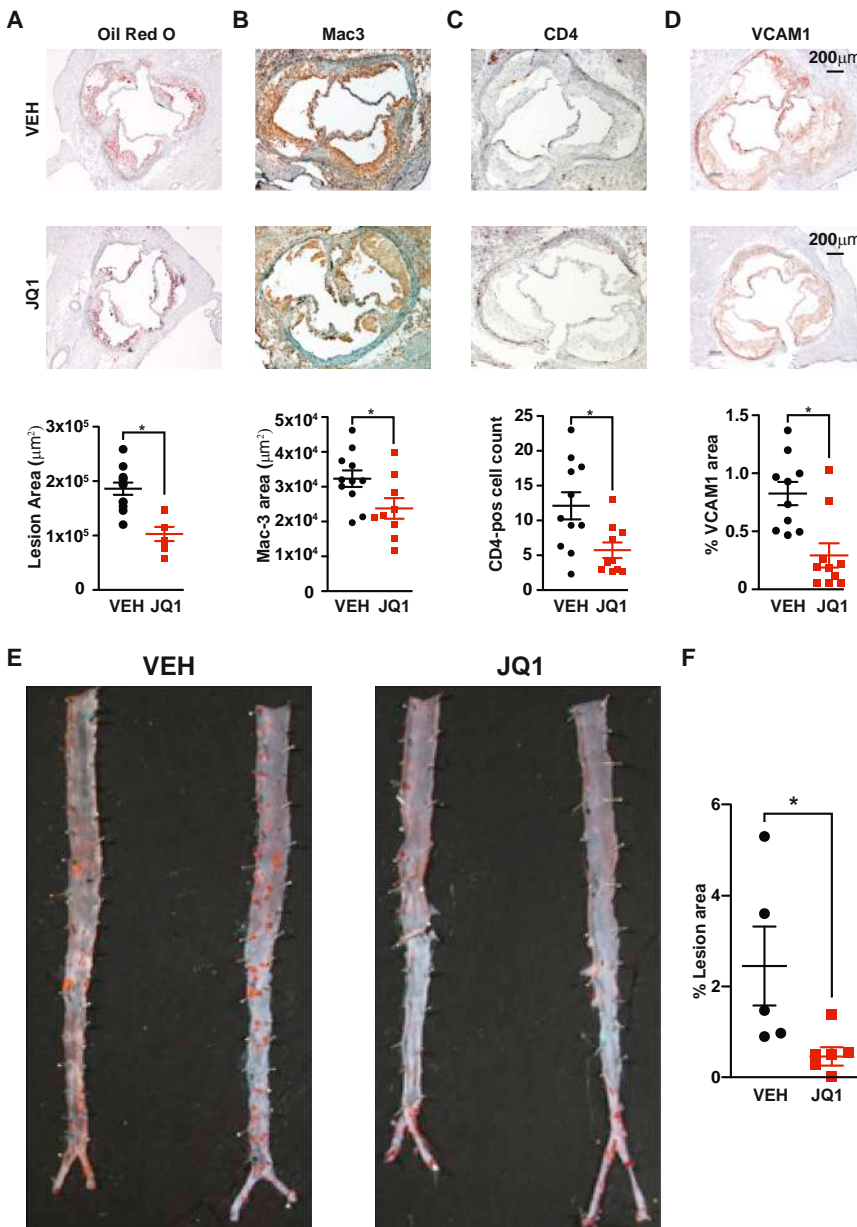


Figure 7. BET Bromodomain Inhibition Suppresses Atherogenesis in *Ldlr*^{-/-} Mice

(A–D) Photomicrographs of aortic root sections from *Ldlr*^{-/-} animals treated with VEH or JQ1 stained for (A) oil red O, (B) Mac-3, (C) CD-4, or (D) VCAM1. Quantification of staining is shown below. Results represent mean \pm SEM. The statistical significance of the difference between JQ1- and VEH-treated samples was determined using a two-tailed t test. * $p = 0.002$ for (A); and * $p < 0.05$ for (B)–(D).

(E) Oil red O staining of en face aortas prepared from cohort in (A)–(D).

(F) Quantification of lesion area (%) between VEH- and JQ1-treated en face aortas. The statistical significance of the difference between JQ1- and VEH-treated samples was determined using a two-tailed t test. * $p < 0.05$.

See also [Figure S7](#).

may influence the pathogenesis of inflammatory diseases. Changes in eRNA levels by NF- κ B-directed BRD4 SE formation may also be an important factor in proinflammatory transcription in ECs, but await future study. Further granularity on dynamic enhancer remodeling will accompany progress in genome-wide enhancer detection and assignment.

In many disease settings, the degree of the host inflammatory response is a key determinant of severity ([Medzhitov et al., 2012](#)). Here we show small molecule BET bromodomain inhibition (JQ1) significantly attenuated endothelial activation during acute inflammation in vitro and ex vivo, as revealed by suppression of TNF- α induced leukocyte rolling, adhesion and transmigration. Finally, in a hypercholesterolemic murine model of atherosclerosis, in which EC proinflammatory activation is a seminal early event, 10-week treatment with JQ1 suppressed cardinal histopathologic

In our previous studies, genes with the highest occupancy of BRD4 at their proximal SEs were the most selectively downregulated by BET bromodomain inhibition ([Chapuy et al., 2013](#); [Lovén et al., 2013](#)). However, these studies characterized effects on cells at ground state, where stable, preestablished SEs predominate. During cell state transitions, such as the present study of EC and macrophage activation, we observe potent and selective effects on up-regulated genes associated with de novo SEs. Preferential disruption of dynamic SEs by BET bromodomain inhibition abrogates the induction of inflammatory transcription. The direct relationship between BRD4 enrichment and transcription suggests that modulating BRD4 levels at enhancers

features of atherogenesis. These data in vascular endothelial activation establish a critical and early role for BET bromodomains in dynamic enhancer remodeling. They describe a mechanism for rapid inflammatory gene activation by NF- κ B-mediated formation of SEs. Taken in the context of prior research in macrophage activation, spermatogenesis, and myocyte hypertrophy ([Anand et al., 2013](#); [Delmore et al., 2011](#); [Matzuk et al., 2012](#); [Nicodeme et al., 2010](#)), these data support a model where localization of BET bromodomains to chromatin facilitates cell state transitions. The existence of BET bromodomain inhibitors provides, then, a broad opportunity for inflammatory gene control through modulation of chromatin structure and function.

EXPERIMENTAL PROCEDURES

Animal Models

LDL receptor knockout mice (4 weeks old) on a C57Bl/6 background were purchased from Jackson Laboratories. Mice were fed an atherogenic diet (Clinton/Cybulsky Rodent Diet, D12108 with 1.25% cholesterol, Research Diets) for 10 weeks. While on the diet, the animals were treated with vehicle (DMSO) or JQ1 (50 mg/kg) by intraperitoneal injection, once daily (N = 10/group). Oil red O staining was used to quantify atherosclerotic plaque lesion area in the aortic root. Macrophage (Mac-3) and T lymphocyte (CD-4) accumulation was assessed in the aortic root, and the total staining area was analyzed using computer-assisted imaging analysis. For CD-4 cells, total cell numbers were counted. Whole aorta from the left subclavian artery to the iliac bifurcation, was used for en face preparation and stained with oil red O. All protocols concerning animal use were approved by the Harvard Medical School Institutional Animal Care and Use Committee and conducted in accordance with the NIH Guide for the Care and Use of Laboratory Animals. All studies were performed in C57Bl/6J mice (Jackson Laboratories), maintained in a pathogen-free facility with standard light/dark cycling and ad libitum access to food and water.

Reagents and Cell Culture

ECs from pooled human umbilical cords were cultured in M199 medium supplemented with 20% fetal bovine serum (FBS), 0.1% heparin, 50 μ g/ml endothelial cell growth factor (Biomedical Technologies), penicillin/streptomycin on gelatin-coated tissue culture plates. U937 cells (ATCC) were maintained in RPMI with 10% FBS and antibiotics. For transendothelial migration (see below), human umbilical vein ECs (subculture 2) were grown on fibronectin-coated glass coverslips (5 mg/ml; BD Biosciences) and treated with JQ1 (500 nM) or vehicle (DMSO) for 1 hr before TNF- α stimulation (10 ng/ml, 4 hr). Recombinant human TNF- α was obtained from PeproTech. JQ1 was dissolved in DMSO at a concentration of 50 mg/ml. Working stocks of JQ1 were prepared by diluting 1:10 in 10% beta-cyclodextrin solution (Filippakopoulos et al., 2010). Animals were treated at 50 mg/kg once daily by intraperitoneal injection.

ChIP-Seq and Data Analysis

ChIP was performed in ECs in the presence or absence of TNF- α (1 hr, 25 ng/ml) and JQ1 (3 hr pretreatment, 500 nM). Specific antibodies and detailed methods are described in the [Supplemental Experimental Procedures](#). ChIP was carried out as described elsewhere (Lovén et al., 2013). All ChIP-seq data sets were aligned using Bowtie (version 1.0.0; Langmead et al., 2009) to build version NCBI36/HG18 of the human genome or build version NCBI37/MM9 of the mouse genome. Enhancers and super enhancers were mapped as described elsewhere (Lovén et al., 2013). Additional details are provided in the [Supplemental Experimental Procedures](#).

ACCESSION NUMBERS

The GEO (<http://www.ncbi.nlm.nih.gov/geo>) accession numbers for all ChIP-seq and Chem-seq data (including microarray data) and aligned and raw data reported in this work are GSE53998 and GSE54000, respectively.

SUPPLEMENTAL INFORMATION

Supplemental Information includes Supplemental Experimental Procedures, seven figures, and six tables and can be found with this article online at <http://dx.doi.org/10.1016/j.molcel.2014.08.024>.

AUTHOR CONTRIBUTIONS

J.D.B., C.Y.L., Q.D., J.E.B., and J.P. designed research. J.D.B. and Q.D. performed in vitro and in vivo endothelial function studies with assistance from G.G., G.N., A.H.L., F.W.L., K.C. J.D.B. and C.Y.L. performed ChIP studies and analyzed ChIP data. A.J.F. developed motif analysis code. A.L.K. treated mice with JQ1 for atherogenesis studies. J.D.B., C.Y.L., J.E.B., and J.P. wrote manuscript.

ACKNOWLEDGMENTS

We are grateful to R. Young, P. Rahl, T. Graf, and C. Van Oevelen for stimulating discussions; M. Berkeley, Z. Herbert, and the late E. Fox (DFCI Microarray Core) for assistance with microarray experiments; and T. Volkert, J. Love, and S. Gupta at the Whitehead Genome Core for assistance with genome sequencing. This research was supported by NIH-K08 HL105678, The Watkins Discovery Research Award and The Harris Family Award (to J.D.B.); US Department of Defense CDMRP CA120184 (to C.Y.L.); Sarnoff Cardiovascular Research Foundation (to G.G. and S.B.); NIH PO1 HL36028 (to F.W.L. and A.H.L.); NIH-K08 HL086672-3 and Watkins Family Foundation (to K.C.); NIH-K08 CA128972, the Burroughs-Wellcome Fund, the Damon-Runyon Cancer Research Foundation, the Richard and Susan Smith Family Foundation, and the Next Generation Award (to J.E.B.); and the Neissa Foundation and NHLBI P01 HL048743 (to J.P.). J.E.B. is the scientific founder of Tensha Therapeutics, which is clinically translating drug-like derivatives of the JQ1 chemical probe of BET bromodomains used in this study as cancer therapeutics. As such, the Dana-Farber Cancer Institute and J.E.B. have been granted minority equity in Tensha.

Received: March 19, 2014

Revised: July 7, 2014

Accepted: August 20, 2014

Published: September 25, 2014

REFERENCES

- Anand, P., Brown, J.D., Lin, C.Y., Qi, J., Zhang, R., Artero, P.C., Alaiti, M.A., Bullard, J., Alazem, K., Margulies, K.B., et al. (2013). BET bromodomains mediate transcriptional pause release in heart failure. *Cell* 154, 569–582.
- Anders, L., Guenther, M.G., Qi, J., Fan, Z.P., Marineau, J.J., Rahl, P.B., Lovén, J., Sigova, A.A., Smith, W.B., Lee, T.I., et al. (2014). Genome-wide localization of small molecules. *Nat. Biotechnol.* 32, 92–96.
- Ashburner, B.P., Westerheide, S.D., and Baldwin, A.S., Jr. (2001). The p65 (RelA) subunit of NF- κ B interacts with the histone deacetylase (HDAC) corepressors HDAC1 and HDAC2 to negatively regulate gene expression. *Mol. Cell. Biol.* 21, 7065–7077.
- Baltimore, D. (2011). NF- κ B is 25. *Nat. Immunol.* 12, 683–685.
- Barboric, M., Nissen, R.M., Kanazawa, S., Jabrane-Ferrat, N., and Peterlin, B.M. (2001). NF- κ B binds P-TEFb to stimulate transcriptional elongation by RNA polymerase II. *Mol. Cell* 8, 327–337.
- Barnes, P.J., and Karin, M. (1997). Nuclear factor- κ B: a pivotal transcription factor in chronic inflammatory diseases. *N. Engl. J. Med.* 336, 1066–1071.
- Chapuy, B., McKeown, M.R., Lin, C.Y., Monti, S., Roemer, M.G., Qi, J., Rahl, P.B., Sun, H.H., Yeda, K.T., Doench, J.G., et al. (2013). Discovery and characterization of super-enhancer-associated dependencies in diffuse large B cell lymphoma. *Cancer Cell* 24, 777–790.
- Chen, L.F., Fischle, W., Verdin, E., and Greene, W.C. (2001). Duration of nuclear NF- κ B action regulated by reversible acetylation. *Science* 293, 1653–1657.
- Cybulsky, M.I., Iiyama, K., Li, H., Zhu, S., Chen, M., Iiyama, M., Davis, V., Gutierrez-Ramos, J.C., Connelly, P.W., and Milstone, D.S. (2001). A major role for VCAM-1, but not ICAM-1, in early atherosclerosis. *J. Clin. Invest.* 107, 1255–1262.
- De Val, S., Chi, N.C., Meadows, S.M., Minovitsky, S., Anderson, J.P., Harris, I.S., Ehlers, M.L., Agarwal, P., Visel, A., Xu, S.M., et al. (2008). Combinatorial regulation of endothelial gene expression by ets and forkhead transcription factors. *Cell* 135, 1053–1064.
- Delmore, J.E., Issa, G.C., Lemieux, M.E., Rahl, P.B., Shi, J., Jacobs, H.M., Kastriitis, E., Gilpatrick, T., Paranal, R.M., Qi, J., et al. (2011). BET bromodomain inhibition as a therapeutic strategy to target c-Myc. *Cell* 146, 904–917.
- Dey, A., Ellenberg, J., Farina, A., Coleman, A.E., Maruyama, T., Sciortino, S., Lippincott-Schwartz, J., and Ozato, K. (2000). A bromodomain protein,

- MCAP, associates with mitotic chromosomes and affects G(2)-to-M transition. *Mol. Cell. Biol.* **20**, 6537–6549.
- Filippakopoulos, P., Qi, J., Picaud, S., Shen, Y., Smith, W.B., Fedorov, O., Morse, E.M., Keates, T., Hickman, T.T., Felletar, I., et al. (2010). Selective inhibition of BET bromodomains. *Nature* **468**, 1067–1073.
- Frye, S.V. (2010). The art of the chemical probe. *Nat. Chem. Biol.* **6**, 159–161.
- Gimbrone, M.A., Jr., Bevilacqua, M.P., and Cybulsky, M.I. (1990). Endothelial-dependent mechanisms of leukocyte adhesion in inflammation and atherosclerosis. *Ann. N Y Acad. Sci.* **598**, 77–85.
- Hnisz, D., Abraham, B.J., Lee, T.I., Lau, A., Saint-André, V., Sigova, A.A., Hoke, H.A., and Young, R.A. (2013). Super-enhancers in the control of cell identity and disease. *Cell* **155**, 934–947.
- Huang, B., Yang, X.D., Zhou, M.M., Ozato, K., and Chen, L.F. (2009). Brd4 coactivates transcriptional activation of NF- κ B via specific binding to acetylated RelA. *Mol. Cell. Biol.* **29**, 1375–1387.
- Jang, M.K., Mochizuki, K., Zhou, M., Jeong, H.S., Brady, J.N., and Ozato, K. (2005). The bromodomain protein Brd4 is a positive regulatory component of P-TEFb and stimulates RNA polymerase II-dependent transcription. *Mol. Cell* **19**, 523–534.
- Jin, F., Li, Y., Dixon, J.R., Selvaraj, S., Ye, Z., Lee, A.Y., Yen, C.A., Schmitt, A.D., Espinoza, C.A., and Ren, B. (2013). A high-resolution map of the three-dimensional chromatin interactome in human cells. *Nature* **503**, 290–294.
- Kaikkonen, M.U., Spann, N.J., Heinz, S., Romanoski, C.E., Allison, K.A., Stender, J.D., Chun, H.B., Tough, D.F., Prinjha, R.K., Benner, C., and Glass, C.K. (2013). Remodeling of the enhancer landscape during macrophage activation is coupled to enhancer transcription. *Mol. Cell* **51**, 310–325.
- Langmead, B., Trapnell, C., Pop, M., and Salzberg, S.L. (2009). Ultrafast and memory-efficient alignment of short DNA sequences to the human genome. *Genome Biol.* **10**, R25.
- LeRoy, G., Rickards, B., and Flint, S.J. (2008). The double bromodomain proteins Brd2 and Brd3 couple histone acetylation to transcription. *Mol. Cell* **30**, 51–60.
- Ley, K., Laudanna, C., Cybulsky, M.I., and Nourshargh, S. (2007). Getting to the site of inflammation: the leukocyte adhesion cascade updated. *Nat. Rev. Immunol.* **7**, 678–689.
- Libby, P., Ridker, P.M., and Hansson, G.K. (2011). Progress and challenges in translating the biology of atherosclerosis. *Nature* **473**, 317–325.
- Lovén, J., Hoke, H.A., Lin, C.Y., Lau, A., Orlando, D.A., Vakoc, C.R., Bradner, J.E., Lee, T.I., and Young, R.A. (2013). Selective inhibition of tumor oncogenes by disruption of super-enhancers. *Cell* **153**, 320–334.
- Masckauchán, T.N., Shawber, C.J., Funahashi, Y., Li, C.M., and Kitajewski, J. (2005). Wnt/ β -catenin signaling induces proliferation, survival and interleukin-8 in human endothelial cells. *Angiogenesis* **8**, 43–51.
- Matsui, T., Kanai-Azuma, M., Hara, K., Matoba, S., Hiramatsu, R., Kawakami, H., Kurohmaru, M., Koopman, P., and Kanai, Y. (2006). Redundant roles of Sox17 and Sox18 in postnatal angiogenesis in mice. *J. Cell Sci.* **119**, 3513–3526.
- Matys, V., Kel-Margoulis, O.V., Fricke, E., Liebich, I., Land, S., Barre-Dirrie, A., Reuter, I., Chekmenev, D., Krull, M., Hornischer, K., et al. (2006). TRANSFAC and its module TRANSCOMP: transcriptional gene regulation in eukaryotes. *Nucleic Acids Res.* **34**, D108–D110.
- Matzuk, M.M., McKeown, M.R., Filippakopoulos, P., Li, Q., Ma, L., Agno, J.E., Lemieux, M.E., Picaud, S., Yu, R.N., Qi, J., et al. (2012). Small-molecule inhibition of BRDT for male contraception. *Cell* **150**, 673–684.
- Medzhitov, R., Schneider, D.S., and Soares, M.P. (2012). Disease tolerance as a defense strategy. *Science* **335**, 936–941.
- Mujtaba, S., Zeng, L., and Zhou, M.M. (2007). Structure and acetyl-lysine recognition of the bromodomain. *Oncogene* **26**, 5521–5527.
- Natoli, G. (2009). Control of NF- κ B-dependent transcriptional responses by chromatin organization. *Cold Spring Harb. Perspect. Biol.* **1**, a000224.
- Nicodeme, E., Jeffrey, K.L., Schaefer, U., Beinke, S., Dewell, S., Chung, C.W., Chandwani, R., Marazzi, I., Wilson, P., Coste, H., et al. (2010). Suppression of inflammation by a synthetic histone mimic. *Nature* **468**, 1119–1123.
- Ostuni, R., Piccolo, V., Barozzi, I., Polletti, S., Termanini, A., Bonifacio, S., Curina, A., Prosperini, E., Ghisletti, S., and Natoli, G. (2013). Latent enhancers activated by stimulation in differentiated cells. *Cell* **152**, 157–171.
- Parker, S.C., Stitzel, M.L., Taylor, D.L., Orozco, J.M., Erdos, M.R., Akiyama, J.A., van Bueren, K.L., Chines, P.S., Narisu, N., Black, B.L., et al.; NISC Comparative Sequencing Program; National Institutes of Health Intramural Sequencing Center Comparative Sequencing Program Authors; NISC Comparative Sequencing Program Authors (2013). Chromatin stretch enhancer states drive cell-specific gene regulation and harbor human disease risk variants. *Proc. Natl. Acad. Sci. USA* **110**, 17921–17926.
- Pierce, J.W., Lenardo, M., and Baltimore, D. (1988). Oligonucleotide that binds nuclear factor NF- κ B acts as a lymphoid-specific and inducible enhancer element. *Proc. Natl. Acad. Sci. USA* **85**, 1482–1486.
- Pierce, J.W., Schoenleber, R., Jesmok, G., Best, J., Moore, S.A., Collins, T., and Gerritsen, M.E. (1997). Novel inhibitors of cytokine-induced I κ B α phosphorylation and endothelial cell adhesion molecule expression show anti-inflammatory effects in vivo. *J. Biol. Chem.* **272**, 21096–21103.
- Shi, J., Whyte, W.A., Zepeda-Mendoza, C.J., Milazzo, J.P., Shen, C., Roe, J.S., Minder, J.L., Mercan, F., Wang, E., Eckersley-Maslin, M.A., et al. (2013). Role of SWI/SNF in acute leukemia maintenance and enhancer-mediated Myc regulation. *Genes Dev.* **27**, 2648–2662.
- Strausberg, R.L., and Schreiber, S.L. (2003). From knowing to controlling: a path from genomics to drugs using small molecule probes. *Science* **300**, 294–295.
- Whyte, W.A., Orlando, D.A., Hnisz, D., Abraham, B.J., Lin, C.Y., Kagey, M.H., Rahl, P.B., Lee, T.I., and Young, R.A. (2013). Master transcription factors and mediator establish super-enhancers at key cell identity genes. *Cell* **153**, 307–319.
- Yang, Z., Yik, J.H., Chen, R., He, N., Jang, M.K., Ozato, K., and Zhou, Q. (2005). Recruitment of P-TEFb for stimulation of transcriptional elongation by the bromodomain protein Brd4. *Mol. Cell* **19**, 535–545.
- Zhong, H., May, M.J., Jimi, E., and Ghosh, S. (2002). The phosphorylation status of nuclear NF- κ B determines its association with CBP/p300 or HDAC-1. *Mol. Cell* **9**, 625–636.
- Zuber, J., Shi, J., Wang, E., Rappaport, A.R., Herrmann, H., Sison, E.A., Magoon, D., Qi, J., Blatt, K., Wunderlich, M., et al. (2011). RNAi screen identifies Brd4 as a therapeutic target in acute myeloid leukaemia. *Nature* **478**, 524–528.

Medulloblastoma regulatory circuitries reveal subgroup-specific cellular origins

Charles Y. Lin^{1*®}, Serap Erkek^{2,3*}, Yiai Tong⁴, Linlin Yin⁵, Alexander J. Federation¹, Marc Zapatka⁶, Parthiv Haldipur⁷, Daisuke Kawauchi³, Thomas Risch⁸, Hans-Jörg Warnatz⁸, Barbara C. Worst³, Bensheng Ju⁹, Brent A. Orr¹⁰, Rhamy Zeid¹, Donald R. Polaski¹, Maia Segura-Wang², Sebastian M. Waszak², David T.W. Jones³, Marcel Kool³, Volker Hovestadt⁸, Ivo Buchhalter¹¹, Laura Sieber³, Pascal Johann³, Stefan Gröschel¹², Marina Ryzhova¹³, Andrey Korshunov¹⁴, Wenbiao Chen⁵, Victor V. Chizhikov¹⁵, Kathleen J. Millen^{7,16}, Vyacheslav Amstislavskiy⁹, Hans Lehrach⁸, Marie-Laure Yaspo⁸, Roland Eils^{11,17}, Peter Lichter⁶, Jan O. Korbel², Stefan M. Pfister^{3,18#}, James E. Bradner^{1#} and Paul A. Northcott^{3,4#}

¹Dana Farber Cancer Institute (DFCI), Medical Oncology, Boston, MA, USA

²European Molecular Biology Laboratory (EMBL), Genome Biology Unit, Heidelberg, Germany

³German Cancer Research Center (DKFZ), Division of Pediatric Neurooncology, Heidelberg, Germany

⁴St. Jude Children's Research Hospital, Developmental Neurobiology, Memphis, TN, USA

⁵Department of Molecular Physiology & Biophysics, Vanderbilt University School of Medicine, Nashville, TN, USA

⁶German Cancer Research Center (DKFZ), Division of Molecular Genetics, Heidelberg, Germany

⁷Center for Integrative Brain Research, Seattle Children's Research Institute, Seattle, WA, USA

⁸Max Planck Institute for Molecular Genetics, Department of Vertebrate Genomics, Berlin, Germany

⁹St. Jude Children's Research Hospital, Department of Bone Marrow Transplantation & Cellular Therapy, Memphis, TN, USA

¹⁰Department of Pathology, St. Jude Children's Research Hospital, Memphis, TN

¹¹German Cancer Research Center (DKFZ), Division of Theoretical Bioinformatics, Heidelberg, Germany

¹²NCT Heidelberg, Department of Translational Oncology, Heidelberg, Germany

¹³NN Burdenko Neurosurgical Institute, Department of Neuropathology, Moscow, Russia

¹⁴Clinical Cooperation Unit Neuropathology, German Cancer Research Center (DKFZ), and Department of Neuropathology University Hospital, Heidelberg, Germany

¹⁵Department of Anatomy and Neurobiology, University of Tennessee Health Sciences Center, Memphis, TN, USA

¹⁶Department of Pediatrics, Genetics Division, University of Washington, Seattle, WA, USA

¹⁷Institute of Pharmacy and Molecular Biotechnology and BioQuant, University of Heidelberg

¹⁸University of Heidelberg, Department of Pediatrics, Heidelberg, Germany

*These authors contributed equally to this study

#Co-senior authorship

®Current affiliation: Baylor College of Medicine, Department of Molecular and Human Genetics, Houston, TX, USA

Manuscript correspondence:

Paul A. Northcott, Ph.D.

Assistant Member, Department of Developmental Neurobiology
St. Jude Children's Research Hospital
262 Danny Thomas Place
Mailstop 325
Memphis, TN 38105
paul.northcott@stjude.org
www.stjude.org/northcott
901-595-2816 (P)
901-595-7478 (F)

James E. Bradner, M.D.

Associate Professor
Dana-Farber Cancer Institute
Harvard Medical School
Boston, MA
james_bradner@dfci.harvard.edu
<http://bradner.dfci.harvard.edu>
617-632-3352 (P)

Stefan M. Pfister, M.D.

Division Head, Division of Pediatric Neurooncology
German Cancer Research Center (DKFZ)
Im Neuenheimer Feld 280
D-69120 Heidelberg, Germany
S.Pfister@dkfz-heidelberg.de
+49.62 21.42-4618 (P)
+49.62 21.42-4639 (F)

Summary (151 words):

Medulloblastoma is a highly malignant paediatric brain tumour, often inflicting devastating consequences on the developing child. Genomic studies have revealed four distinct molecular subgroups with divergent biology and clinical behaviour. An understanding of the regulatory circuitry governing the transcriptional landscapes of medulloblastoma subgroups, and how this relates to their respective developmental origins, is currently lacking. Using H3K27ac and BRD4 ChIP-Seq, coupled with tissue-matched DNA methylation and transcriptome data, we describe the active *cis*-regulatory landscape across 28 primary medulloblastoma specimens. Analysis of differentially regulated enhancers and super-enhancers reinforced inter-subgroup heterogeneity and revealed novel, clinically relevant insights into medulloblastoma biology. Computational reconstruction of core regulatory circuitry identified a master set of transcription factors, validated by ChIP-Seq, that are responsible for subgroup divergence and implicate candidate cells-of-origin for Group 4. Our integrated analysis of enhancer elements in a large series of primary tumour samples reveals insights into *cis*-regulatory architecture, unrecognized dependencies, and cellular origins.

Introduction (391 words):

Medulloblastoma is a highly malignant paediatric brain tumour classified into four biologically and clinically distinct molecular subgroups¹⁻³. The present clinical approach to medulloblastoma involves maximal safe surgical resection, cytotoxic chemotherapy, and cranio-spinal radiation, which together are associated with profound morbidity in the developing child, underscoring the need for new subgroup-specific therapeutic insights.

Transcriptional diversity amongst WNT, SHH, Group 3, and Group 4 subgroup medulloblastomas is partially explained by active and discriminatory signaling pathways, such as the Wntless/WNT and Sonic hedgehog/SHH developmental cascades inherent to WNT and SHH medulloblastomas, respectively. Somatic alterations of driver genes including *MYC* (Group 3), *KDM6A* (Group 4), *GFI1/GFI1B* (Group 3 and Group 4), and others contribute further to subgroup divergence⁴⁻¹⁰. Recurrent targeting of genes involved in chromatin modification has been the most consistent theme to emerge from recent next-generation sequencing (NGS) studies^{6,11,12}, strongly suggesting deregulation of the epigenome as a critical step during medulloblastoma pathogenesis. However, this hypothesis has yet to be substantiated and knowledge pertaining to how the medulloblastoma epigenome influences subgroup-specific transcriptional programs remains in its infancy. Recent analysis of DNA methylation in medulloblastoma corroborated transcriptional differences in subgroups and enumerated novel mechanistic insights into gene regulation¹³. Still, a detailed analysis of the *cis*-regulatory epigenome of this disease has not been undertaken.

Enhancers are *cis*-acting regulatory elements that serve as sites of recruitment for transcription factors (TFs) and chromatin-associated regulatory complexes, which together signal to RNA polymerase to regulate target gene expression¹⁴. Massive catalogues of genome-wide enhancers have been developed by large consortia such as ENCODE^{15,16} and Roadmap¹⁷, dramatically advancing our understanding of enhancer-gene regulation across a comprehensive spectrum of cell lines and tissues from different species. These resources empower our understanding of the complex cartography of the human regulatory landscape, provide testable hypotheses regarding disease-risk association, contribute evolutionary inferences, and establish robust analytical techniques. To deeply characterize the active *cis*-regulatory circuitry of a single disease entity, here medulloblastoma, we performed high-resolution chromatin immunoprecipitation with sequencing (ChIP-Seq) for active enhancers (H3K27ac) in 28 primary tumour specimens and three established cell lines, collectively accounting for all known molecular subgroups. Our approach to studying enhancers genome-wide in a large set of primary tissue samples led to a regulatory explanation for subgroup transcriptional diversity, previously unrecognized subgroup-specific dependencies and firm insights into medulloblastoma cellular origins, in particular for the poorly characterized and aggressive Group 3 and Group 4 subgroups.

Results: (2,784 words):

The enhancer landscape of primary medulloblastoma

Recent publications of large-scale efforts to annotate active regulatory elements genome-wide in human tissues (e.g. through DNase I hypersensitivity, H3K27ac and BRD4 ChIP-Seq), have focused on immortalized or malignant cell lines and normal human tissues for cataloguing active enhancers^{15,17}. Discrete disease entities have been

under-represented in these comprehensive surveys, including medulloblastoma, with only a single long-term culture cell line (D721; first reported in 1997) included amongst 125 cell types initially studied by ENCODE¹⁶. Further, cancer cell lines often exhibit drastic genomic and transcriptional divergence from their corresponding primary tumour tissues. This is exemplified in Non-Hodgkin's lymphoma where our prior epigenomic analyses identified greater likeness between primary tumour samples and normal lymphoid tissues than between tumours and cell lines¹⁸. Given the apparent limitations of using cell lines to faithfully study the tumour epigenome, and the recognized subgroup-dependent heterogeneity of medulloblastoma, we collected a series of 28 treatment-naïve, fresh-frozen medulloblastoma specimens for studying the active enhancer landscape by H3K27ac ChIP-Seq (Figure 1a, b; Extended Data Figure 1a, b).

The cohort was selected to be inclusive of all four medulloblastoma subgroups (Supplemental Table S1; WNT, n=3, SHH, n=5, Group 3, n=9, Group 4, n=11). Three additional Group 3 cell lines (MED8A, D425, and HD-MB03) were also included in our experimental workflow. Using MACS¹⁹ to identify significantly enriched H3K27ac peaks, we inferred 78,516 medulloblastoma enhancers, effectively saturating the medulloblastoma enhancer landscape (Extended Data Figure 1e). These regions of promoter distal H3K27ac enrichment mainly (~80%) covered introns and intergenic regions (Extended Data Figure 1c). Parallel ChIP-Seq was performed for *Bromodomain Containing 4* (BRD4), an enhancer-associated transcriptional coactivator^{18,20}, in 27/31 cases. Enrichment of H3K27ac and BRD4 ChIP-Seq signals was highly correlated at putative enhancer loci (Pearson correlation, $r=0.949$), confirming that the selected regions are indeed active enhancers (Figure 1c)^{18,20}. In agreement with this result, H3K27ac peaks showed a high degree of overlap with H3K4me1 but not H3K27me3 peaks, consistent with the definition of active enhancers (Extended Data Figure 1d). Furthermore, regions enriched for H3K27ac were strongly anti-correlated with DNA methylation (Pearson correlation, $r=-0.577$; Figure 1d). Finally, strand-specific RNA-Seq data generated from the same cohort detected short, unspliced, bidirectional RNA transcripts overlapping H3K27ac peaks (Figure 1e), in accordance with recently described enhancer RNAs (eRNAs), known also to arise from active enhancers²¹. Active enhancers exhibited a modest statistical enrichment for overlap with focal amplifications and deletions identified in published Group 3 and Group 4 copy-number data⁸, suggesting that these gene-regulating elements are altered in the disease ($P=0.028$ for amplifications, $P=0.016$ for deletions, see Supplementary Methods; Extended Data Figure 1f). Comparison of predicted medulloblastoma enhancers with those reported using analogous methods employed by the ENCODE and Roadmap Epigenomics Projects revealed 19,850 novel regulatory regions, indicative of potentially cerebellar cell type- or medulloblastoma-specific enhancers in our dataset (Figure 1f, g). Importantly, primary medulloblastoma enhancer landscapes exhibited poor overlap and correlation with those generated from medulloblastoma cell lines (Extended Data Figure 1g, h), further emphasizing the importance of studying the epigenome in primary tumours.

ANOVA identified sets of enhancers differing according to known molecular subgroup, revealing 20,406 differentially active enhancers (26% of all inferred enhancers; Figure 2a, b). The remaining 74% ($n=58,110$) displayed varied activity across subgroups, suggesting either ubiquitous activity of e.g. 'housekeeping' genes or a general role in medulloblastoma or cerebellar identity (Figure 2a; Supplemental Table S2). K-means clustering of differentially regulated enhancers delineated six distinct medulloblastoma enhancer classes, including one for each subgroup (i.e. WNT, SHH, Group 3 and Group 4) as well as WNT-SHH and Group 3-Group 4 shared classes (Figure 2b, c). Group 3

and Group 4 subgroups are known to exhibit some degree of transcriptional similarity²²⁻²⁴, consistent with the enhancer clustering results. In contrast, WNT and SHH subgroups tend to be mostly dissimilar from a transcriptional perspective, and thus a common subset of shared enhancers between these groups was unexpected.

Subgroup-specific oncogenicity revealed through enhancer/gene assignments

We next sought to assign enhancer elements to target genes, a process typically hindered by the fact that the majority of enhancer/promoter interactions occur over extensive and highly variable genomic distances²⁵. To overcome these challenges, we leveraged sample-matched RNA-Seq gene expression data to identify putative enhancer/gene interactions that are (i) contained in the same topologically associated domain (TAD²⁶) and (ii) exhibit strong positive correlations between enhancer H3K27ac signal and gene expression ($\rho > 0.6$ and FDR < 0.05 , Extended Data Figure 2). TADs are megabase-scale genomic regions of interacting chromatin that form a fundamental unit of genome structure. This approach assigned 8,775 enhancers (43% of all differential enhancers) to at least one protein-coding target gene (Supplemental Table S3). The majority (44%) of inferred target genes were assigned to a single enhancer, but in many cases, several enhancers were predicted to converge on the regulation of a single gene (Figure 2d). Likewise, 73% of enhancers were assigned to only a single gene target (Figure 2e). Our computational method of defining enhancer/gene assignments proved to be most effective when considering differentially regulated enhancers, with $>85\%$ of assigned genes targeted by an enhancer active in only 1-2 subgroups (Figure 2f). To validate the robustness of our methods, we used 4C-Seq²⁷ to query Group 3-specific enhancer/promoter interactions for enhancers showing conserved activity in both primary Group 3 tumours and cell lines. This approach confirmed enhancer/promoter interactions for both *SMAD9* and *TGFBR1* in the Group 3 cell line HD-MB03 – a low-passage line that is more molecularly faithful to primary Group 3 tumours than older models^{13,28} – substantiating our approach (Figure 2g and Extended Data Figure 2j).

Medulloblastoma subgroup ‘signature’ genes have been well described using array-based expression profiling methods²³, discriminating the most highly differentially expressed genes between subgroups. Enhancer/gene assignments derived from coupling H3K27ac ChIP-Seq with RNA-Seq produced a refined ‘lens’ for investigating subgroup-related diversity in medulloblastoma, implicating themes previously undisclosed through transcriptional data alone. For example, enhancers regulating *ALK*, a receptor tyrosine kinase frequently altered in a variety human cancers²⁹, were found to be highly active in the WNT subgroup and explained the largely WNT-specific expression pattern detected by RNA-Seq and confirmed by immunohistochemical staining of primary patient samples (n=49; P=1.35e-5, Fisher's exact test; Figure 2h-k). Although further investigations into a potential oncogenic role for *ALK* in WNT subgroup medulloblastoma will be required, *ALK* inhibitors currently FDA approved for the treatment of NSCLC (i.e. crizotinib and ceritinib) may serve as a rational therapeutic option for this patient subgroup.

In contrast to WNT patients (who almost universally survive with current treatment regimens), and SHH patients (who represent rational candidates for SHH pathway inhibitors such as SMO inhibitors), rational target-based treatment options remain scarce for Group 3 and Group 4 patients. As such, additional insights are needed to direct

future mechanistic and translational research. Functional pathway analysis (see Supplementary Methods) performed on differential enhancer/gene target assignments identified transcriptional regulators of neuronal development in the Group 4 functional annotation, whereas Group 3 enhancer target genes prominently included thematic pathways associated with TGF β signaling (Extended Data Figure 3). A differential analysis performed on the union of the top 1,000 enhancers in both Group 3 and Group 4 revealed enhancers regulating TGF β pathway components as a divergent functional axis separating Group 3 and Group 4 (Extended Data Figure 3b,c). Notably, we uncovered a ~450kb focal amplification at the *ACVR2A* locus in one Group 3 sample that encompassed both the gene and the upstream enhancer regions (Extended Data Figure 3d). In this sample, enhancers regulating TGF β pathway components exhibited increased H3K27ac versus other Group 3 tumours (Extended Data Figure 3e). These data, combined with our prior observations that TGF β receptor genes are recurrently amplified in Group 3⁸, further suggest TGF β signaling as a putative oncogenic driver in this subgroup.

Medulloblastoma super-enhancers define subgroup identity

In multiple tumour types, super-enhancers (SEs), broad spatially co-localized enhancer domains³⁰⁻³³, have recently been shown to drive oncogenes, genes required for maintenance of tumour cell identity, and genes associated with cell type-specific functions. To determine whether SEs might play an essential role in establishing subgroup-specific identity, we undertook a systematic mapping of SEs across all 28 medulloblastoma samples (Figure 3a). Massive (>50kb) SE domains were identified at the cerebellar-specific TFs, *ZIC1* and *ZIC4*^{34,35} (Figure 3b, c), and at 70% of a queried set of established medulloblastoma driver genes and chromatin modifiers implicated in cancer, including *GLI2*, *MYC*, *OTX2* and others⁸ (Extended Data Figure 4a).

To identify subgroup-specific SEs, we identified the union of all enhancer regions in a given subgroup and ranked them by average H3K27ac enrichment across all samples in that subgroup. Subgroup SEs were identified from this meta-H3K27ac signal using previously established methods³³, resulting in ~3,000 distinct SE containing loci with ~600-1,100 SEs identified per subgroup (Figure 3a, d, Supplemental Table S4). Compared to typical enhancers, SEs showed higher occupancy of BRD4 and greater enhancer signal dynamic range between subgroups (Extended Data Figure 4b-d). Targets of differential enhancers contained within SEs (i.e. SE target genes) included a large fraction of established medulloblastoma signature genes (32%; Supplemental Table S3), as well as novel candidates, including *NKD1/NKD2* (WNT subgroup), *PCNT* (SHH subgroup), *HLX* (Group 3), and *SNCAIP* (Group 4) (Figure 3d-f). Medulloblastoma SEs were inferred to regulate known Cancer Gene Census genes, including the aforementioned *ALK* in WNT, *SMO* and *NTRK3* in SHH, *LMO1*, *LMO2*, and *MYC* in Group 3, and *ETV4* and *PAX5* in Group 4, among others (Supplemental Table S3). Furthermore, several actionable, SE-regulated genes were revealed in our analysis including kinases (*NTRK1*, *SGK1*) and chromatin modifying enzymes (*PNMT*, *HDAC4*) (Supplemental Table S5).

Unbiased hierarchical clustering of SEs across all primary medulloblastoma samples was sufficient to recapitulate transcriptional subgroupings using no prior knowledge of subgroup status, suggesting that SEs might play a pivotal role in driving subgroup identity (Figure 3a). As shown with all enhancer elements (Extended Data Figure 1g,h), SEs from established Group 3 medulloblastoma cell lines clustered with one another, but

failed to show similarity to primary Group 3 samples or samples from any other subgroup.

To experimentally validate the activity of medulloblastoma subgroup-specific SEs, we synthesized twenty-two unique SE loci (size range, 1.1-2.1kb) and evaluated them using Tol2 transposon-mediated zebrafish transgenesis (see Supplementary Methods)³⁶. Enhancer constructs (together with *in vitro* transcribed transposase RNA) were injected into one-cell-stage zebrafish eggs and developing embryos were visualized for GFP reporter activity at 24 hours post fertilization. These *in vivo* reporter assays resulted in a validation rate of 45% (10/22), with all reproducibly active enhancer constructs showing specific activity in the zebrafish CNS (Figure 4a-g; Extended Data Figure 5). We used TF ChIP-Seq data for HLX, LHX2, and LMX1A – all of which are highly expressed and SE-regulated in Group 3 and/or Group 4 (Figure 3d and data not shown) – to enable precise definition of enhancer coordinates (based on TF occupancy) prior to selecting regions to be tested in zebrafish reporter assays (Figure 4j). This may explain the exceptionally high *in vivo* validation rate we observed in zebrafish, which is remarkable considering human enhancer sequences were chosen without any strict consideration of sequence conservation. These experiments confirmed zebrafish hindbrain-specific activity for an SE mapping ~90kb upstream of *MYC* that is commonly active in WNT and Group 3 and inferred to regulate *MYC* expression (Figure 4f, i, j). This SE was not found in other common human cancers (Figure 4i), or in seventy-seven different primary tissues included in Roadmap, suggesting that this novel and validated *MYC* SE is highly specific to the developing hindbrain and/or medulloblastoma (Extended Data Figure 5g). Importantly, identified *MYC* upstream SEs clearly demarcate a focal amplification hotspot in published Group 3 medulloblastoma copy-number data⁸ (Figure 4i), strongly implicating these SEs in the oncogenic regulation of *MYC*. Collectively, these *in vivo* validation data further substantiate our highly integrative approach for the identification of enhancers and SEs, and inference of their target genes.

SE-regulated TFs implicate Group 4 cellular origins

Among subgroup-specific SE target genes, we observed an enrichment of TFs involved in neuronal development ($P \sim 0.0001$, Fisher's exact test; Extended Data Figure 6a). Overall, subgroup-specific TFs displayed similar patterns of expression, enhancer motif enrichment, and overlap of target genes (Extended Data Figures 6 & 7). TFs were also enriched in subgroup-specific SE targets as compared to subgroup-specific non-SE targets ($P \sim 0.002$, Fisher's exact test), consistent with prior observations in other cancers that SEs regulate key TFs required for tumour cell identity and maintenance^{18,20,31}. Given evidence in embryonic stem cells that pluripotency master regulator TFs (OCT4, SOX2, and NANOG) are driven by SEs and themselves bind to and establish SEs³³, we hypothesized that a *reverse* analysis of SEs in medulloblastoma might enable a *de novo* reconstruction of tumour identity-defining TFs and their associated regulatory circuitry, thereby providing novel insights into medulloblastoma origins.

Pursuant to this idea, we proposed a set of criteria for TF inclusion into the core regulatory circuitry of medulloblastoma: (i) the TFs are SE-regulated and (ii) the TFs themselves bind to SEs of one another (Figure 5a). For each SE-regulated TF, these criteria can be quantified through a measurement of the *in* and *out* degree of regulation, whereby the *in degree* represents the total number of SE-regulated TFs that bind to a TF's SE, and the *out degree* represents the total number of other TF SEs bound by a given TF (Figure 5a, b). Regulatory circuitry reconstruction across all SE-associated TFs

in medulloblastoma identified cliques of TFs with similar patterns of *in/out* degree, strong interconnectivity via motif binding, and higher likelihoods of pairwise protein/protein interaction and motif co-occurrence at enhancers (Supplementary Methods, Figure 5c, Extended Data Figure 8). This reconstruction creates for the first time a core regulatory circuitry blueprint for each subgroup, and implicates specific sets of TFs in establishing medulloblastoma subgroup identity (Figure 5c). Importantly, ChIP-Seq for the homeodomain TFs HLX (Group 3 network), LMX1A (Group 4 network), and LHX2 (shared Group 3/Group 4 network) performed on select Group 3 and Group 4 primary samples (n=4) largely validated the computationally derived regulatory networks constructed for these subgroups (Figure 5c-f, Extended Data Figures 8-9).

Cellular origins for WNT and SHH medulloblastomas have been experimentally established using mouse models genetically engineered to aberrantly activate the WNT and SHH signaling pathways, respectively, in distinct hindbrain stem/progenitor cells during development³⁷⁻⁴⁰. The origins of Group 3 and Group 4 medulloblastoma, however, are unknown and yet essential to define as these tumours account for ~60% of all diagnoses, lack targeted therapies, and are frequently associated with a poor clinical outcome secondary to current standard of care².

Cell identity is most essentially defined by the activity of master regulator TFs. As such, we hypothesized that the regulatory SE regions governing endogenous expression of candidate master TFs and embedded in the core regulatory circuitry of medulloblastoma subgroups might inform cellular origins of the disease via their cell type-specific expression and activity. During early cerebellar development, *Lmx1a*, *Eomes*, and *Lhx2* – master regulator Group 4 TFs deduced from core regulatory circuitry analysis (Figure 5c) – exhibit overlapping spatiotemporal restricted expression in the nuclear transitory zone (NTZ; Figure 6a, b), an assembly point for immature deep cerebellar nuclei (DCN). DCN residing in the NTZ at this time point are predominantly glutamatergic projection neurons that originate from earlier progenitors of the upper rhombic lip (uRL), a transient germinal zone producing progenitors with distinct cellular fates, including DCN and cerebellar granule neurons⁴¹. Immunofluorescence microscopy confirmed compartmentalized expression of *Lmx1a*, *Eomes*, and *Lhx2* that was notably distinct from *Atoh1* expression, the latter marking the early external granule layer (EGL) at this developmental stage (e13.5; Figure 6b).

Both LMX1A enhancer activity and expression are highly discriminatory for Group 4, nominating this TF as a master regulator of the Group 4 transcriptional program (Figure 3d, 5d; Extended Data Figure 9). Indeed, LMX1A ChIP-Seq performed on Group 4 primary samples verified >90% of predicted target genes inferred through motif-driven computational analyses (Extended Data Figures 8-9). LMX1A is a LIM-homeodomain TF previously shown to function as a critical regulator of cell-fate decisions in the uRL and essential for normal cerebellar development⁴². Spontaneous *Lmx1a* loss-of-function null mutations are causative in *dreher* mice, resulting in profound cerebellar phenotypes typified by premature regression of the RL, reduced choroid plexus, and cerebellar hypoplasia predominantly affecting the posterior vermis (Figure 6c)⁴³. To further investigate the molecular targets associated with *dreher* cerebellar phenotypes, we microdissected uRL from wild-type and *dreher* (*dr^d/dr^d*) mice at e13.5 and delineated transcriptional differences through expression array profiling. Strikingly, SE-regulated TFs contained in Group 3/Group 4 regulatory circuitry (Figure 5c) were among the most differentially expressed genes in *dreher* uRL compared to controls, especially *Eomes* and *Barhl1*, both exhibiting significantly reduced expression (Figure 6d-f). Collectively,

these phenotypic and molecular data further support Lmx1a as a master regulator TF in both the cerebellar uRL and in Group 4 medulloblastoma, implicating the uRL compartment and its derivate precursors as putative cells-of-origin for Group 4.

Discussion (457 words):

We describe the active medulloblastoma enhancer landscape across a series of 28 fresh-frozen, treatment-naïve tissue samples and three cultured cell lines, to our knowledge representing the largest such dataset for any single cancer entity. Our data reveal drastic divergence between primary tumour and tumour cell line material and uncover considerable *cis*-regulatory element heterogeneity between subgroups of the disease that would be overlooked and unsubstantiated in series limited to just a few cases.

Clinically relevant medulloblastoma subgroups are principally defined based on their underlying transcriptional profiles. Differentially regulated medulloblastoma enhancers and SEs are here shown to recapitulate these subgroups, and importantly extend our understanding of this disease to inferences regarding cell specification and actionable tumour dependencies. Biological themes and signaling networks extracted from transcriptional data have served as the primary source of annotation for medulloblastoma subgroups, with WNT and SHH subgroups characterized by activation of their respective signaling pathways, and Group 3 and Group 4 recognized for their GABAergic and glutamatergic expression phenotypes, respectively. Although these data provide a functional and phenotypic annotation of medulloblastoma, they fail to articulate the cell of origin and developmental identity of individual subgroups. Using a reverse analysis of the medulloblastoma chromatin landscape starting at the level of differentially-regulated enhancers and SEs, we have reconstructed and experimentally validated the core regulatory circuitry inherent to medulloblastoma subgroups, inferring master transcriptional regulators responsible for subgroup-specific divergence. The majority of these master regulator TFs were not previously implicated in medulloblastoma development, nor were they visible amongst transcriptionally-derived gene sets dominated by aberrant signaling and overwhelming phenotypic signatures. Through tracing the spatiotemporal activity of a subset of Group 4 master TFs, these studies identified DCN of the cerebellar NTZ, or plausibly their earlier precursors originating from the uRL, as putative cells-of-origin for this large subgroup of patients. Together these approaches establish a framework for the inference of tumour cell of origin through enhancer core regulatory circuitry mapping.

Understanding the cellular origins of cancer has broad implications for the understanding and treatment of the disease⁴⁴. Numerous cancers, especially those of the immune compartment are treated through targeting of the lineage (e.g. anti-B cell therapies)^{45,46}. As medulloblastoma is believed to originate from cell populations that normally exist ephemerally during development, targeting the aberrant persistence of tumour cells from these lineages may represent a novel therapeutic strategy with minimal effect on the normal tissue compartment. Moreover, elucidation of core regulatory circuitry implicates upstream signaling dependent regulators of master TFs, their co-activators, and their downstream effectors as potential subgroup-specific targets for rational therapeutic intervention. These insights demonstrate the critical importance of epigenetic analyses of primary tumours as opposed to cell line model systems and highlight the broad utility of core regulatory circuitry mapping especially in poorly characterized and clinically heterogeneous malignancies.

Methods Summary (254 words):

All patient material included in this study was collected after receiving informed consent from the patients and/or their families. Medulloblastoma samples were collected at first resection, before adjuvant chemotherapy or radiotherapy. Subgroup assignments were made using the Illumina 450K DNA methylation array as described⁴⁷. Chromatin extraction and library preparation for ChIP-Seq of H3K27ac, BRD4, HLX, LHX2, and LMX1A were performed at ActiveMotif (Carlsbad, CA) using proprietary protocols. Alignment and filtering of ChIP-Seq data was performed as described⁷. H3K27ac enhancer peaks were called using MACS¹⁹. Peaks were classified as being subgroup-specific or as common enhancers by first calculating H3K27ac enrichment on the merged peaks followed by ANOVA and k-means clustering. Target gene identification of enhancers was performed as described⁴⁸ by correlating H3K27ac enrichment at the enhancers with expression levels of genes located in the same TAD²⁶ as the enhancers. Candidate gene(s) showing the highest statistically significant (FDR<0.05) correlations were selected as the putative target(s) of the enhancer. Gene Ontology/Pathway analysis of enhancer/gene targets was performed using the ClueGO plugin for cytoscape⁴⁹. SEs were called using ROSE2 (<https://github.com/BradnerLab/pipeline>)⁵⁰ and subgroup specificity of SEs was assigned via ranking average H3K27ac signal across the subgroups. Medulloblastoma core regulatory circuitry analysis was performed using the COLTRON (<https://pypi.python.org/pypi/coltron>) which calculated inward and outward degree regulation of SE-regulated TFs. *In vivo* reporter assays for validating enhancers were tested in one-cell-stage zebrafish embryos as described in the Supplementary Methods. Endogenous expression of candidate TFs was determined by querying the Allen Brain Atlas Data Portal (<http://developingmouse.brain-map.org>) or by immunofluorescence microscopy performed on the murine embryonic hindbrain (e13.5).

Acknowledgements

S.E. is a recipient of Human Frontiers Science Program long-term postdoctoral fellowship (LT000432/2014). SMW received funding through a SNSF Early Postdoc Mobility Fellowship (P2ELP3_155365) and an EMBO Long-Term Fellowship (ALTF 755-2014). CYL is supported by a US Department of Defense CDMRP CA120184 postdoctoral fellowship. PAN is a V Foundation V Scholar in Childhood Cancer Research. We thank Creative Science Studios (<http://www.creativesciencestudios.com/>) for assistance with artwork.

Author Contributions

PAN, JEB, and SMP conceived and co-led the study. CYL and SE performed all bioinformatics related to the analysis of medulloblastoma enhancers and super-enhancers. YT, LY, DK, BCW, BJ, and WC validated subgroup-specific enhancers *in vivo*. CYL and AJF constructed medulloblastoma regulatory circuitry networks. MZ, SW, RZ, MS-W, DTWJ, MK, VH, and IB provided informatics and general scientific support. PH, VVC, and KJM performed the developmental studies with *dreher* and WT mouse embryonic cerebella. TR, H-JW, VA, HL, and M-LY conducted RNA-Seq data generation and enhancer RNA analysis. BAO performed ALK staining on medulloblastoma TMAs. LS, PJ, and SG performed 4C-Seq experiments. MR and AK provided medulloblastoma tissue samples. RE, PL, JOK, SMP, JEB, and PAN provided institutional support and project supervision. CYL, SE, SMP, JEB, and PAN prepared the figures and wrote the manuscript.

Author information

Short-read sequencing data have been deposited at the European Genome-Phenome Archive (EGA, <http://www.ebi.ac.uk/ega/>) hosted by the EBI, under accession number EGAS00001000215. Reprints and permissions information is available at www.nature.com/reprints. The authors declare no competing financial interests. Readers are welcome to comment on the online version of this article at www.nature.com/nature. Correspondence and requests for materials should be addressed to P.A.N. (paul.northcott@stjude.org), J.E.B. (james_bradner@dfci.harvard.edu), and S.M.P. (s.pfister@dkfz-heidelberg.de).

Figure Legends

Figure 1. The enhancer landscape of primary medulloblastoma.

- (a) Experimental workflow for studying enhancers and super-enhancers in primary medulloblastomas.
- (b) H3K27ac ChIP-Seq data across all 28 primary medulloblastoma samples from our series showing a highly active enhancer at the *OTX2* locus, especially in Group 3 and Group 4 subgroups.
- (c) Scatter plot comparing the enrichment (\log_2) of H3K27ac signal versus BRD4 signal at medulloblastoma enhancers ($n=78,516$) as determined by ChIP-Seq.
- (d) Scatter plot comparing the enrichment (\log_2) of H3K27ac signal versus DNA methylation at medulloblastoma enhancers ($n=78,516$) as determined by ChIP-Seq and WGBS, respectively.
- (e) RNA-Seq data showing Group 3-specific enhancer RNA (eRNA) expression (lower left) overlapping a Group 3-specific *MYC* enhancer (upper left) in a subset of Group 3 and Group 4 medulloblastomas. *MYC* gene expression (RPKM) is also shown for the same subset of cases (lower right).
- (f) Venn diagram showing the overlap of medulloblastoma enhancers with those reported by ENCODE and Roadmap.
- (g) Pie chart summarizing the results presented in (f).

Figure 2. Differentially regulated enhancers and enhancer/gene assignments in medulloblastoma subgroups.

- (a) ANOVA classification of medulloblastoma enhancers displayed as a pie chart.
- (b) Pie chart showing the distribution of differentially regulated enhancers among medulloblastoma enhancer classes.
- (c) K-means clustering of differentially regulated medulloblastoma enhancers ($n=20,406$).
- (d) Bar plot showing the proportion of enhancer/gene assignments to N enhancers.
- (e) Bar plot displaying the proportion of enhancer/gene assignments to N genes.
- (f) Bar plot summarizing the proportion of enhancer/gene assignments to N subgroups.
- (g) 4C-Seq validation of *SMAD9* enhancer/promoter interaction in Group 3.
- (h) H3K27ac data highlighting a WNT-specific enhancer inferred to regulate *ALK*.
- (i) Scatter plot correlating sample-matched gene expression (RPKM, x-axis) of *ALK* with H3K27ac enrichment (\log_2 ; y-axis) for the WNT-specific enhancer shown in (h).
- (j) *ALK* expression (\log_2 RPKM) across medulloblastoma subgroups ($n=140$ samples). Error bars represent standard deviation (s.d.) of the mean.

- (k) Immunohistochemical validation of ALK expression in WNT medulloblastoma patients as determined by staining a medulloblastoma tissue microarray (n=49 patient samples).

Figure 3. Medulloblastoma super-enhancers define subgroup-specific identity.

- (a) Unsupervised hierarchical clustering of primary medulloblastomas and cell lines using H3K27ac signal calculated at all SEs identified in each individual sample.
- (b) Meta tracks of H3K27ac ChIP-Seq signal for the *ZIC1/ZIC4* SE locus. Expression (mean RPKM) for both *ZIC4* (left) and *ZIC1* (right) is displayed as bar graphs to the right of each H3K27ac track with error bars representing s.d. of the mean (n = 140 samples).
- (c) Line plot showing the enhancer rank for the *ZIC1/ZIC4* SE locus across all samples according to subgroup.
- (d) Ranked plots of enhancers defined across composite H3K27ac landscapes of WNT, SHH, Group 3, and Group 4 medulloblastomas. Enhancers are ranked by increasing group average H3K27ac signal (rpm). The cut-off discriminating typical enhancers (TEs) from super-enhancers (SEs) is shown as a dashed line. Select genes associated with SEs in each subgroup are highlighted and shaded according to enhancer class specificity.
- (e) Line plots showing the enhancer rank for candidate SE loci across all samples according to subgroup. Examples of subgroup-specific SEs (*NKD2* (WNT), *PCNT* (SHH), *HLX* (Group 3), *SNCAIP* (Group 4)) are shown.
- (f) Meta tracks of H3K27ac ChIP-Seq signal across medulloblastoma subgroups for the loci described in (e). The y-axis shows ChIP-Seq signal (rpm/bp) for each individual sample (shaded regions) with the average signal across the group shown in a line. The x-axis depicts genomic position with SE boundaries demarcated as rectangles. Bar graphs shown to the right of each H3K27ac track summarize the expression (mean RPKM) of the relevant candidate genes as determined by RNA-Seq with error bars representing s.d. of the mean (n = 140 samples).

Figure 4. *In vivo* validation of Group 3 and Group 4 medulloblastoma super-enhancers.

- (a-f) Representative bright-field and fluorescence images of embryos (1 dpf) injected with individual enhancer-containing Tol2 vectors. Lateral views (60x) show GFP reporter expression in the whole body and dorsal views show GFP expression in the CNS (120x). White arrows indicate the locations of GFP signal. CNS, central nervous system; HB, hindbrain; MB, midbrain; CB, cerebellum; TC, telencephalon; RE, retina; OP, olfactory placode; TG, trigeminal ganglion.
- (g) Summary of zebrafish reporter assays.
- (h) Heatmap summarizing *MYC* copy-number data derived from a published series of Group 3 medulloblastoma SNP6 profiles (n=168).
- (i, j) Identification of a medulloblastoma-specific SE driving *MYC* expression. H3K27ac ChIP-Seq (upper panels) data revealed a shared WNT/Group 3 enhancer inferred to regulate *MYC* expression that was not found in other common human cancers (i, lower panel) and occupied by SE-regulated TFs *HLX*, *LHX2*, and *LMX1A* as determined by TF ChIP-Seq (j, lower panel).

Figure 5. Super-enhancers define medulloblastoma regulatory circuitry.

- (a) Methodology for inferring transcriptional regulatory circuitry driven by medulloblastoma SEs.

- (b) Heatmap of all SE-associated TFs in medulloblastoma (rows) clustered by similarity of IN/OUT regulatory degree. Regulatory degree in each subgroup is shaded (units of normalized total degree). Selected TFs with similar subgroup-specific patterns of regulatory degree are annotated on the left.
- (c) Subgroup-specific regulatory circuitry. Nodes are TFs associated with an SE in a subgroup-specific context. Edges indicate co-regulating TFs as defined by enrichment of TF binding motifs in respective regulatory regions. Edges validated by TF ChIP-Seq are coloured according to their respective subgroup association.
- (d) TF and H3K27ac ChIP-Seq meta tracks for the SE-regulated TFs *LMX1A*, *LHX2*, *HLX*, and *EOMES*. Locations of SEs inferred to regulate each of the respective TFs are highlighted as rectangles at the top of the panel.
- (e) Medulloblastoma subgroup distribution of shared, co-bound peaks for master regulatory TFs analysed by ChIP-Seq. TF binding is quantified as area under curve per peak (AUC/peak) in units of rpm. Differences in the means of the distributions is quantified by a Welch's two-tailed *t* test (N.S. $p > 0.1$, ** $p < 1e^{-6}$).
- (f) Summary of predicted versus validated regulatory circuitry for master SE-regulated TFs identified in Group 3 and Group 4.

Figure 6. Master regulator transcription factors implicate Group 4 cellular origins.

- (a) In situ hybridization data obtained from the Allen Brain Developing Mouse Atlas showing highly localized expression of Group 4 master TFs *Lmx1a*, *Eomes*, and *Lhx2* in the embryonic cerebellum at e13.5. Red arrows indicate common, highly specific focal expression in cells of the nuclear transitory zone (NTZ). *Atoh1* expression is shown at the same developmental time-point to serve as a marker of the external granule layer (EGL).
- (b) Immunofluorescence microscopy for the same TFs shown in (a) performed on sagittal sections of the e13.5 murine cerebellum. Red arrows confirm highly localized expression of *Lmx1a*, *Eomes*, and *Lhx2* in cells populating the NTZ. *Atoh1* staining is shown at the same developmental time-point to serve as a marker of the EGL.
- (c) H&E-stained cerebellar sections (sagittal) isolated from wild-type and *dr^l/dr^l* (*Lmx1a^{-/-}*) embryos at multiple developmental time points. The rhombic lip (RL; demarcated by yellow boxes), choroid plexus (CP), and cerebellum (CB) are dramatically affected in *Lmx1a^{-/-}* embryos.
- (d) Immunofluorescence microscopy confirming loss of *Eomes* expression in the NTZ and RL of *Lmx1a^{-/-}* embryos during cerebellar development.
- (e) Summary of differentially expressed TFs in the e13.5 RL of *Lmx1a^{-/-}* embryos compared to wild-type controls. Expression of TFs belonging to Group 4 regulatory circuitry are shaded green and the identity of the most significantly reduced TFs are labelled. Error bars represent standard error of the mean, $n = 3$ for each mouse.
- (g) Boxplot depicting specific down-regulation of Group 4 regulatory circuitry-associated TFs in *Lmx1a^{-/-}* embryos. Differences in the means of the distributions is quantified by a Welch's two-tailed *t* test (N.S. $p > 0.1$, ** $p < 1e^{-6}$).

Extended Data Figure 1 (accompanies Figure 1): Enhancer landscape of primary medulloblastoma.

- (a) H3K27ac ChIP-Seq data showing a highly active enhancer at the *NEUROD1* locus across all 28 primary medulloblastoma samples from our series.
- (b) Scatter plots showing Pearson correlation of H3K27ac peaks called using either sample-matched WGS or whole cell extract (WCE) sequences as background for two samples from our series.
- (c) Saturation analysis showing the number of discrete enhancer regions identified as a function of increasing sample number (top), or the fraction of newly gained discrete enhancer regions as a function of increasing sample number (bottom). Error bars represent 95% confidence intervals obtained from 1,000 permutations of sample order.
- (d) Pie chart showing the genomic distribution of enhancer elements in medulloblastoma.
- (e) Heatmaps of ChIP-Seq data showing the scaled read densities for H3K27ac, BRD4, H3K4me1, and H3K27me3 in regions located \pm 5kb from Group 3-specific H3K27ac (top panel) and H3K27me3 peak midpoints (bottom panel).
- (f) Histograms showing the fractional overlap of enhancers with focal amplifications (top) or focal deletions (bottom) in Group 3 and Group 4 medulloblastoma samples. The blue distributions represent expected fractional overlap generated from 10,000 random simulations. The red line depicts the actual observed fractional overlap with empirical p-value noted.
- (g) Scatter plot correlating average H3K27ac enrichment in Group 3 cell lines with average H3K27ac enrichment in Group 3 primary medulloblastomas. Enrichments are calculated for peaks called in primary Group 3 samples.
- (h) Venn diagram showing the overlap between H3K27ac peaks called for primary Group 3 medulloblastomas and Group 3 medulloblastoma cell lines.

Extended Data Figure 2 (accompanies Figure 2): Enhancer/gene assignments in medulloblastoma.

- (a) Meta H3K27ac ChIP-Seq tracks of the Group 3-specific enhancers (E1 and E2) in the TAD containing *ATP10A*, *GABRB3*, and *GABRA5*.
- (b) Zoom in meta H3K27ac ChIP-Seq tracks of enhancer E1 from (a).
- (c-e) Scatter plots correlating sample-matched gene expression (\log_2 RPKM, x-axis) of *ATP10A* (c), *GABRB3* (d), and *GABRA5* (e) with H3K27ac enrichment (\log_2 ; y-axis) for the Group 3-specific enhancer shown in (b).
- (f) Zoom in meta H3K27ac ChIP-Seq tracks of enhancers E2 from (a).
- (g-i) Scatter plots correlating sample-matched gene expression (\log_2 RPKM, x-axis) of *ATP10A* (g), *GABRB3* (h), and *GABRA5* (i) with H3K27ac enrichment (\log_2 ; y-axis) for the Group 3-specific enhancer shown in (f). j, 4C-Seq validation of *TGFBR1* enhancer/promoter interaction in a Group 3 cell line.

Extended Data Figure 3 (accompanies Figure 2): Enhancer-driven TGF β activity in Group 3 medulloblastoma.

- (a) Functional annotation of target genes assigned to subgroup-specific enhancers based on their significant overlap with gene sets annotated in Gene Ontology (GO Biological Process) and pathway databases (KEGG, Reactome).
- (b) Waterfall plot discriminating the top 1,000 Group 3 and Group 4 subgroup-specific enhancers as defined by total H3K27ac signal. The distribution of assigned targets in Group 3, Group 4, and shared Group 3-4 targets are shown below the waterfall.
- (c) Convergence of Group 3-specific enhancers on TGF β pathway genes. Subgroup-specific enhancers are summarized as nodes according to their

respective medulloblastoma enhancer class – Group 3, Group 4, and shared Group 3/Group 4 – with edges representing individual enhancer/TGF β pathway gene assignments.

- (d) Amplification of the TGF β type II receptor, *ACVR2A*, in a Group 3 medulloblastoma from the ChIP-Seq cohort (MB-4M23). Log₂ read depth data (tumour versus matched germline) derived from WGS data for this case is shown (upper panel). Highly active H3K27ac enhancer peaks overlapping the amplified *ACVR2A* locus are shown for the same case (lower panel).
- (e) Bar plot showing the difference in H3K27ac enhancer signal between MB-4M23 (*ACVR2A*-amplified Group 3 sample) and all other Group 3 samples. Bar plot shows H3K27ac log₂ fold change at all enhancers regulating TGF β component genes. Enhancers are ranked by increasing change in H3K27ac. Error bars represent standard error of the mean fold change.

Extended Data Figure 4 (accompanies Figure 3): Features of medulloblastoma super-enhancers.

- (a) Heatmap showing the SE association of known medulloblastoma driver genes and chromatin modifiers. Genes with called differential SEs are shaded black, whereas genes with proximal SEs (within 100kb of TSS) are shaded grey, according to their respective subgroup.
- (b) Bar plot of enhancer signal cross sample variance (y-axis) displayed as a fraction of the mean for SE enhancer constituents (left, black) or TE enhancer constituents (right, grey) identified in each medulloblastoma subgroup.
- (c) Boxplots of H3K27ac (left, blue) or BRD4 (right, red) enhancer signal at SEs or typical enhancers (TE) in their active group-specific context or in their inactive group context (e.g. for SEs or TEs present in Group 3, active group context includes all Group 3 samples and inactive group context includes all other samples). Differences in the means of the distributions is quantified by a Welch's two-tailed *t* test (***) $p < 1e^{-9}$.
- (d) Dot plots of average H3K27ac enhancer signal in the constituents of SEs (left) or TEs (right) for enhancer constituents identified in WNT, SHH, Group 3, or Group 4 samples, respectively. Error bars represent standard deviation of the mean across all samples in a subgroup.
- (e) Bar plot showing the number of SE regions assigned to individual enhancer classes in medulloblastoma.

Extended Data Figure 5 (accompanies Figure 4): *In vivo* validation of Group 3 and Group 4 medulloblastoma super-enhancers.

- (a-e) Representative bright-field and fluorescence images of embryos (1 dpf) injected with individual enhancer-containing Tol2 vectors. Lateral views (60x) show GFP reporter expression in the whole body and dorsal views show GFP expression in the CNS (120x). White arrows indicate the locations of GFP signal. CNS, central nervous system; HB, hindbrain; MB, midbrain; CB, cerebellum; TC, telencephalon; RE, retina; OP, olfactory placode; TG, trigeminal ganglion. For a-d, meta tracks of H3K27ac ChIP-Seq signal across medulloblastoma subgroups for the cloned enhancer region are shown.
- (f) Pie chart showing the fraction of all tested medulloblastoma enhancer regions that demonstrate any CNS localized reporter activity.
- (g) Heatmap showing H3K27ac enrichment at the +/- 250kb region flanking the medulloblastoma *MYC* SE described in Figure 4 (SE #2; panels f, h-j) across 77 Epigenome Roadmap tissues. Each row represents a single tissue. Each column

represents a region of the *MYC* gene desert locus. Black shaded regions indicate the presence of H3K27ac enrichment. The samples are ordered by similarity of H3K27ac enrichment pattern. Notable clusters of mesoderm (MESO.), epithelial (EPI.), blood, brain, or GI lineage derived samples are noted. The cloned enhancer reporter region described in Figure 4 (panels f, h-j) is depicted as a vertical line and shows overlap with only 4/77 H3K27ac Epigenome Roadmap samples.

Extended Data Figure 6 (accompanies Figure 5): Pathways regulated by super-enhancer associated transcription factors in medulloblastoma.

- (a) Functional pathways regulated by SE-associated TFs in medulloblastoma.
- (b) Heatmap of select subgroup-specific TFs showing their expression (left columns) and enhancer motif enrichment (right columns). Enhancer motif enrichment was calculated at differential enhancer elements in the respective enhancer classes.

Extended Data Figure 7 (accompanies Figure 5): Medulloblastoma subgroup-specific transcription factors and their associated target genes.

- (a-d) Network of subgroup-specific TFs and their predicted target genes for WNT (a), SHH (b), Group 3 (c) and Group 4 (d) subgroups. Nodes represent subgroup-specific TFs. In each subgroup, node size is scaled and shaded according to the expression level of the TF and node font is scaled and shaded according to the number of inferred target genes (i.e. OUT degree). TF target genes are shown in red font scaled according to the number of TFs predicted to target that gene (i.e. IN degree).

Extended Data Figure 8 (accompanies Figure 5): Super-enhancers define medulloblastoma regulatory circuitry.

- (a-d) Scatter plots of IN (x-axis) and OUT (y-axis) regulatory degree for SE-associated TFs in each medulloblastoma subgroup.
- (e-h) TF interaction networks for each medulloblastoma subgroup. Nodes represent the top 50% of SE-associated TFs in each subgroup as ranked by total degree (counter clockwise). Each node is colored by total degree and predicted binding interactions with other TF SEs are shown as edges. For Group 3 and Group 4 networks, edges validated by TF ChIP-Seq binding are colored.
- (i-l) Position weight matrices showing the top statistically enriched motif identified for each transcription factor at the top 10,000 bound enhancers in each subgroup.
- (m) Pie charts showing the fraction of predicted edges in each Group 3 and Group 4 TF networks that are validated by the presence of the respective TF ChIP-Seq binding at the enhancer.
- (n) Boxplot of protein-protein interaction frequency (y-axis) calculated from STRING database for pairs of SE-associated TFs showing patterns of subgroup-specific SE co-regulation (left) or randomized pairs (right).

Extended Data Figure 9 (accompanies Figure 5): LMX1A, EOMES, and LHX2 are master transcriptional regulators of Group 4 medulloblastoma.

Network involving LHX2, LMX1A, and EOMES TFs and target genes inferred based on the presence of the respective TF motifs in Group 4-specific enhancers. Target genes are colored according to their validation status based on LMX1A and LHX2 ChIP-Seq, with genes arranged in the center of the network inferred to be targeted by all three master TFs. For visualization purposes, these

common targets are displayed with a larger font size compared to the genes in the surrounding network.

Supplementary Tables:

Supplemental Table S1: List of primary medulloblastoma samples included in the study, including their subgroup affiliation, patient demographic and clinical information, and availability of supporting NGS data.

Supplemental Table S2: Genomic coordinates of common and differentially-regulated enhancers identified in medulloblastoma.

Supplemental Table S3: Target gene assignments of differentially-regulated enhancers and their overlap with SEs, cancer gene and drug target databases, and published medulloblastoma signature genes.

Supplemental Table S4: Genomic coordinates of medulloblastoma SEs.

Supplemental Table S5: SE-associated target genes and their overlap with multiple databases.

Supplemental Table S6: Genomic coordinates of all medulloblastoma SEs and their subgroup-specificity.

Supplementary Methods:

Identifying super-enhancer constituents for reporter assays. We sought to identify candidate Group 3 and Group 4 super-enhancer constituents for validation by reporter assays. We identified candidate Group 3 and Group 4 super-enhancer constituents by first locating nucleosome free “valleys” in the H3K27ac data using an algorithm adapted from Ramsey et al., 2010⁵¹. Valleys that showed strong evidence of TF ChIP-Seq binding for respective Group 3 (HLX and LHX2) and Group 4 (LHX2 and LMX1A) TFs were selected and manually curated for validation in reporter assays. Based on restrictions for DNA synthesis and cloning, candidate reporter regions of roughly +/- 1kb flanking the valley center were used (Figure 4 and Extended Data Figure 5)

Zebrafish in vivo enhancer assays. All experiments involving zebrafish (*Danio rerio*, AB strain) were approved by the Vanderbilt Institutional Animal Care and Use Committee, Nashville, TN. Microinjection was done as described Ni et al 2012⁵². Briefly, a mixture of individual enhancer-containing vector DNA (25µg/ml) and transposase RNA (25µg/ml) was injected into zebrafish zygotes (1 nl/zygote). The injected embryos were cultured in 0.3x Danieau’s solution at 28.5°C. After 24 hours, the embryos were examined for EGFP expression under a fluorescent dissecting microscope (Zeiss Discovery V12) to determine the stereotypic expression pattern conferred by the enhancer. The total number of embryos injected with the construct and the number of embryos with the stereotypical EGFP pattern were determined to calculate the frequency of the pattern. Embryos were dechorionated and imaged using a Zeiss AxioCam HRC digital camera. At a minimum, ~150-200 embryos were injected per reporter construct and assays were repeated 2-3 times per construct to confirm reproducibility.

Immunofluorescence microscopy. Spatial protein expression of medulloblastoma_{G4}-specific transcription factors in e13.5 cerebella was determined by IHC. PFA-fixed frozen tissues were sectioned (12µm thickness) and processed without antigen retrieval steps. The antibodies used here are Tbr2 (1:100, Abcam, ab23345), Lmx1a (1:100, Novus Biologicals, NBP1-81303), Atoh1 (1:500, Abcam, ab105497) and appropriate secondary antibodies conjugated with Alexa fluorophores (1:400, Invitrogen). The images were captured by an epifluorescence microscopy.

Medulloblastoma tissue microarrays (TMAs). The molecular subgroup of 49 medulloblastoma samples on tissue microarrays were determined as previously described¹⁰. Immunohistochemistry was performed using clone ALK01 (#790-2918, Ventana) with appropriate secondary reagents. Individual tumors were scored positive in the presence of cytoplasmic immunoreactivity for ALK1, whereas the tumor was considered negative in the absence of immunoreactivity.

Phenotypic analysis of Dreher (*Lmx1a*^{-/-}) embryos.

All mouse (*Mus musculus*) experiments were done in accordance with the guidelines laid down by the Institutional Animal Care and Use Committee (IACUC), of Seattle Children’s Research Institute, Seattle, WA. *Lmx1a*^{+/-} mice were crossed and the day of plug was taken as e0.5. WT and *Lmx1a*^{-/-} embryos were dissected out between e12.5 and e17.5 and subsequently fixed in 4% paraformaldehyde (PFA) for 2-6 hours. The fixed embryos were washed in PBS and incubated in 30% sucrose overnight. The following day, embryos were frozen in optimum cutting temperature (OCT) compound. Mid-sagittal cryo-sections of the cerebellum at 11 microns were taken. H&E staining and Immunohistochemistry were performed as described previously⁵³. Briefly, cryosections

were incubated at room temperature for 1 hour after which they were subjected to heat-mediated antigen retrieval. All sections were blocked using 5% serum containing 0.35% triton X, and then incubated with the primary antibody (Eomes (Tbr2); #14-4875, ebioscience, Mouse, 1:200), overnight. The following day fluorescent dye labelled secondary antibodies (Alexa fluor 488, 1:1000, Molecular probes, Grand Island, NY, USA) were used. Sections were counter stained using DAPI (4',6-diamidino-2-phenylindole) (Vector laboratories). All images were captured at room temperature. H&E stained sections were imaged as done using Hamamatsu Nanozoomer whole slide scanner. All confocal images were captured using Zeiss LSM Meta and Zen 2009 software.

Collection of patient material and cell lines. An Institutional Review Board ethical vote (Ethics Committee of the Medical Faculty of Heidelberg) was obtained according to ICGC guidelines (<http://www.icgc.org>), along with informed consent for all participants. No patient underwent chemotherapy or radiotherapy before surgical removal of the primary tumour. Tumour tissues were subjected to neuropathological review for confirmation of histology and for tumour cell content >80%. The ChIP-Seq cohort was established based on tissue availability and availability of orthogonal data types (e.g. WGS, RNA-Seq) and patient metadata (e.g. molecular subgroup). Medulloblastoma cell lines were cultured at 37 °C with 5% CO₂. D425_Med (D425; a gift from D. D. Bigner) and MED8A cells (from the authors' own stocks; T. Pietsch) were cultured in DMEM with 10% FCS (Life Technologies). HD-MB03 cells²⁸ were grown in RPMI-1640 with 10% FCS (Life Technologies). All cells were regularly authenticated and tested for mycoplasma (Multiplexion, Heidelberg, Germany).

ChIP-Sequencing. H3K27ac, BRD4, H3K27me3, H3K4me1, LMX1A, LHX2, and HLX ChIP-Seq were performed at ActiveMotif (Carlsbad, CA) using antibodies against H3K27ac (AM#39133, Active Motif), BRD4 (#A301-985A, Bethyl Laboratories), H3K27me3 (#07-449, Millipore), H3K4me1 (AM#39298, ActiveMotif), LMX1A (#AB10533, Millipore), LHX2 (#sc-19344, Santa Cruz), and HLX (#HPA005968, Sigma). Libraries were sequenced on the Illumina HiSeq 2000 platform using 2 × 101 cycles according to the manufacturer's instructions. Alignment, and downstream processing of ChIP-Seq data was performed as described⁶.

RNA-sequencing and transcriptome read alignment. RNA was extracted from fresh frozen tissue samples using the AllPrep DNA/RNA/Protein Mini kit (Qiagen) including DNase I treatment on column. All samples were subjected to quality control on a Bioanalyzer instrument. RNA sequencing libraries were prepared from 10 µg of total RNA. Strand-specific RNA sequencing was performed following a protocol described previously^{50,51}. Sequencing was carried out with 2x51 cycles on a HiSeq 2000 instrument (Illumina). All reads were aligned to the human reference genome (1000 genomes version of human reference genome hg19/GRCh37) using BWA (v 0.5.9-r16). Aligned reads were converted to the SAM/BAM format using SAMtools. Gene annotation was based on Ensembl v70 (Homo sapiens).

4C-Seq. 4C samples were prepared from Group 3 medulloblastoma cell line HD-MB03 using the method as described^{27,54}. DpnII was used as the primary restriction enzyme and Csp6I as the secondary restriction enzyme in template generation. Sample libraries for SMAD9 and TGFBR1 were amplified using the primers, SMAD9_F: TTATCCAGGCAAGGAAGATC, SMAD9_R: ATTACCTCATCTGCAAACCC, TGFBR1_F: CATTCTTTCTCCCATGATC, and TGFBR1_R: ACACAATCTTGGGTGTTTTT,

respectively. Amplified libraries were multiplexed, spiked with 40% PhiX viral genome and sequenced on Hiseq 2000. Reads were mapped to human genome (hg19) using Bowtie (v 1.0.0)⁵⁵.

Identification of enhancer RNA candidates. Forward and reverse RNA transcription based on directional RNA sequencing data was quantified in 3 kb windows upstream and downstream of enhancer peaks that were based on H3K27ac ChIP-Seq data, resulting in four RNA expression values for each enhancer region: (L_fwd) forward transcription left of enhancer peak, (R_fwd) forward transcription right of enhancer peak, (L_rev) reverse transcription left of enhancer peak, and (R_rev) reverse transcription right of enhancer peak. We calculated the “directionality index” D, a measure of the directionality of transcription inside an enhancer region, with D ranging from 0 to 1, by $D = |R_fwd - L_rev| / (R_fwd + L_rev)$ as described before²⁵, with low D values representing bidirectional eRNA transcription. For correlation of eRNA transcription values with corresponding gene expression values, we calculated eRNA transcription values in 3 kb windows upstream and downstream of enhancer peaks by $eRNA_transcription = (R_fwd + L_rev) / 2$.

Genomic coordinates and gene annotation. All coordinates in this study were based on human reference genome assembly hg19, GRCh37 (ncbi.nlm.nih.gov/assembly/2758/). Gene annotations were based on genecode annotation release 19 (gencodegenes.org/releases/19.html).

Calculating read density. We calculated the normalized read density of a ChIP-Seq dataset in any genomic region using the Bamliquidator (version 1.0) read density calculator (<https://github.com/BradnerLab/pipeline/wiki/bamliquidator>). Briefly, ChIP-Seq reads aligning to the region were extended by 200bp and the density of reads per base pair (bp) was calculated. The density of reads in each region was normalized to the total number of million mapped reads producing read density in units of reads per million mapped reads per bp (rpm/bp).

Plotting meta representations of ChIP-Seq signal. To compactly display medulloblastoma H3K27ac ChIP-Seq signal at individual genomic loci and across subgroups, we developed a simple meta representation (Figure 1e and others). For all samples within a group, ChIP-Seq signal is smoothed using a simple spline function and plotted as a translucent shape in units of rpm/bp. Darker regions indicate regions with signal in more samples. An opaque line is plotted and gives the average signal across all samples in a group.

Peak finding and classification. H3K27ac peak finding was performed using MACS²³ with a p-value threshold of 1e-9, and with other settings as default parameters. Peak finding for each medulloblastoma was performed separately and as a control background for each H3K27ac ChIP-Seq sample, its matched genomic DNA was used. The SPOT statistic⁵⁶, a measure of read fraction found in enriched regions developed by the ENCODE consortium, was used to quantify H3K27ac enrichment quality. Primary medulloblastoma datasets had a median SPOT score of 0.62 which was equivalent to cell line data and on par with primary human data generated in the Epigenome ROADMAP. Afterwards, H3K27ac peaks were merged into a single coordinate file. Peaks which can not be identified in at least two primary medulloblastomas and contained completely within the region surrounding ± 1 kb TSS were excluded from any further analysis. This resulted in final combined and filtered peak set (n=78516).

H3K27ac enrichments were calculated on the final peak set using the following formula: $\log_2\left(\frac{(\text{Cnt}_{\text{ChIP}}/\text{LSize}_{\text{ChIP}} * \min(\text{LSize}_{\text{ChIP}}, \text{LSize}_{\text{cnt}})) + \text{pscnt}}{((\text{Cnt}_{\text{cnt}}/\text{LSize}_{\text{cnt}} * \min(\text{LSize}_{\text{ChIP}}, \text{LSize}_{\text{cnt}})) + \text{pscnt})}\right)$, where Cnt_{ChIP} denotes the total number of reads mapping to the enhancer coordinate in ChIP sample, $\text{LSize}_{\text{ChIP}}$ is the total library size for the ChIP sample, Cnt_{cnt} is the total number of reads mapping to the enhancer coordinate in the control genomic DNA, $\text{LSize}_{\text{cnt}}$ is the total library size for the control sample, and pscnt is a constant number (pscnt=8), which was used to stabilize enrichments based on low read counts. (Peaks showing statistically significant differential H3K27ac enrichment across medulloblastoma subgroups were determined using ANOVA and the ones with $\text{FDR} < 0.01$ were preserved after multiple testing correction. From the resulting peak-set, peaks having 1.5 (\log_2) fold change difference across any medulloblastoma subgroup comparison were called as “subgroup specific” enhancers (n=20,406). Peaks that do not fulfill these criteria were referred as “common” enhancers (n=58,110). Subgroup specific enhancers were further clustered using k means, with k=6 into 6 groups as “SHH”, “WNT”, “Group4”, “WNT-SHH”, “Group3-Group4”, and “Group3” (Figure 2).

Coverage of medulloblastoma enhancers in the genome. Genome was classified into regions as exon, intron, intergenic and promoter (region surrounding $\pm 1\text{kb}$ transcriptional start sites) by following the hierarchy promoter > exon > intron > intergenic. Then, medulloblastoma enhancers were intersected with these defined elements and fraction covered by each element was calculated.

Enhancer saturation analysis. To better understand whether our enhancer profiling adequately captured the primary medulloblastoma enhancer landscape, we performed a saturation analysis. We measured the total number of discrete regions and the fraction of novel regions gained by increasing sample number. This was performed across 1,000 permutations of the 28 medulloblastoma samples to establish 95% confidence intervals (Extended Data Figure 1e).

Comparison of H3K27ac with BRD4 occupancy and DNA methylation at enhancers. Enrichment values for H3K27ac at enhancers were calculated as the ratio between library size normalized read counts for H3K27ac ChIP and its sample matched genomic DNA control. The formula used for the enrichment calculation is as follows: $\log_2\left(\frac{(\text{Cnt}_{\text{ChIP}}/\text{LSize}_{\text{ChIP}} * \min(\text{LSize}_{\text{ChIP}}, \text{LSize}_{\text{cnt}})) + \text{pscnt}}{((\text{Cnt}_{\text{cnt}}/\text{LSize}_{\text{cnt}} * \min(\text{LSize}_{\text{ChIP}}, \text{LSize}_{\text{cnt}})) + \text{pscnt})}\right)$, where Cnt_{ChIP} denotes the total number of reads mapping to the enhancer coordinate in ChIP sample, $\text{LSize}_{\text{ChIP}}$ is the total library size for the ChIP sample, Cnt_{cnt} is the total number of reads mapping to the enhancer coordinate in the control genomic DNA, $\text{LSize}_{\text{cnt}}$ is the total library size for the control sample, and pscnt is a constant number (pscnt=8), which was used to stabilize enrichments based on low read counts. To compare BRD4 enrichment with H3K27ac enrichment at the enhancers, BRD4 enrichments were calculated in the same way as H3K27ac enrichments. DNA methylation values at enhancers were determined by calculating the average DNA methylation of all medulloblastoma samples where DNA methylation data is available¹⁷.

Comparison of H3K27ac occupancy with H3K4me1, H3K27me3 and BRD4 occupancy. We generated ChIP-seq data for H3K4me1 and H3K27me3 for only three Group 3 medulloblastomas (MB-1M21, MB-4M23, and MB-4M26). Therefore, comparison of H3K27ac occupancy with H3K4me1, H3K27me3 and BRD4 (Extended Data Figure 1d) was done using the data from only these three Group 3 samples. To analyze the occupancy of the marks at H3K27me3 enriched regions, we called H3K27me3 peaks using MACS. ChIP-seq reads covering each base pair either in the region $\pm 5\text{ kb}$ around

Group 3-specific enhancer midpoints (Extended Data Figure 1d top panel) or in the region ± 5 kb around H3K27me3 peak midpoints (Extended Data Figure 1d bottom panel) were quantified. Read coverage was averaged in 100-bp windows along the regions and the values were scaled to arrange between 0 -1. Resulting values were represented as heatmaps.

Comparison of H3K27ac peak calling using whole genome sequencing or whole cell extract backgrounds. We repeated H3K27ac peak finding (running MACS with a p-value threshold of $1e-9$, and with other settings as default parameters) for the two medulloblastomas (MB12 and MB200) using their input chromatin as the backgrounds instead of using their matched whole genome sequencing. Resulting set of peaks identified using whole chromatin extract were compared to the ones identified using whole genome sequencing in scatter plots in Extended Data Figure 1b.

Comparison of medulloblastoma H3K27ac enhancers with published H3K27ac data. ENCODE¹⁵ H3K27ac peaks were downloaded from http://ftp.ebi.ac.uk/pub/databases/ensembl/encode/integration_data_jan2011/byDataType/e/peaks/jan2011/histone_macs/optimal/hub/ and all peaks were merged into a single coordinate file. Regarding ROADMAP data^{54,55}, all available H3K27ac alignment files were downloaded and peak finding on individual samples was performed using MACS²³. All ROADMAP H3K27ac peaks were as well merged into a single coordinate file. Resulting peaks from both ENCODE and ROADMAP were intersected with medulloblastoma H3K27ac peaks (with a minimum 50% overlap criteria) (Figure 1f, g).

Comparison of medulloblastoma H3K27ac enhancers with CNV data. To determine the overlap of enhancer loci with CNVs, medulloblastoma enhancer loci were intersected with focal amplifications and deletions obtained from⁸. To determine the statistical significance of the overlap, we performed 10,000 random simulation whereby CNV locations were randomly permuted across the genome without overlap using the bedtools shuffle utility (<http://bedtools.readthedocs.org>) and excluding regions found in the ENCODE¹⁵ blacklist (<https://sites.google.com/site/anshulkundaje/projects/blacklists>). This distribution of random overlaps was used to calculate an empirical p-value of the observed overlap significance (Extended Data Figure 1f).

Quantification of gene expression and assignment of subgroup specific expression. Expression values in rpkm were calculated using “qCount” function of Bioconductor package “quasR” (<http://www.bioconductor.org/packages/release/bioc/html/QuasR.html>). Genes showing differential gene expression across four medulloblastoma subgroups were determined using ANOVA (FDR less than 1%). Then, subgroup specific assignment of gene expression was done by performing a post-hoc test (using “glht” function of R package “multcomp”⁵⁶).

Identification of enhancer target genes. For each enhancer, topology-associated domain (TAD)³¹ which it belongs to was identified. Then, genes with transcriptional start sites falling into the same TAD were determined. We filtered nearby genes for protein coding status, as eRNAs and other enhancer associated ncRNAs are likely to emanate from enhancers and obfuscate distal target genes. Correlation tests (Spearman's rank correlation coefficient) for H3K27ac enrichment of the enhancer and expression level of genes which are in the same TAD were performed. After repeating this procedure for each enhancer, all p-values obtained via correlation tests were combined and corrected

for multiple testing globally using Bioconductor package “qvalue” (<http://www.bioconductor.org/packages/release/bioc/html/qvalue.html>). Correlations with a FDR less than 5% were preserved. For each enhancer, gene whose expression best correlates with the H3K27ac enrichment of the enhancer was selected as the potential target gene. For the cases where the difference between spearman correlation coefficients for the best and second best correlating genes were less than 0.1, the second best correlating gene was also selected as another potential target gene. Identification of enhancer target genes was performed for subgroup specific and common enhancers separately. After getting final gene lists for targets of subgroup specific and common enhancers, genes which are identified as targets both for subgroup specific and common enhancers were removed from common enhancer target gene list.

Classification of enhancer targets according to enhancer regulation. Genes regulated by differential enhancers were classified into categories depending on the number of differential enhancers they are targeted by (Figure 2d). As mentioned in “identification of enhancer targets” part, to assign the enhancers to their targets with highest probability, in the final list of enhancer target genes, number of genes per enhancer was restricted to 2 genes having the highest correlation coefficient. However, to evaluate the number of genes targeted by each enhancer overall, enhancers were classified into categories depending on the number of genes they target by including all the genes targeted by enhancers (satisfying FDR<0.05 criteria) (Figure 2e). Furthermore, genes were classified according their regulation by differential enhancers specific to different number of medulloblastoma subgroups (Figure 2f). This is basically done using the 6 category of differential enhancers defined by k-means clustering (Figure 2c). Differential enhancer categories which are shared between the subgroups such as “WNT-SHH” and “Group3-Group4” are attributed to regulation by enhancers specific to two subgroups.

Overlap of target genes with regulatory information from literature. medulloblastoma signature genes were defined to be the genes regulated differentially in 4 medulloblastoma subgroups²⁸. To be conservative on the signature genes, for each medulloblastoma subgroup, top 100 genes differentially regulated in the respective subgroups were included in the analysis. Resulting gene list were compared to the genes regulated by medulloblastoma subgroup specific enhancers and super-enhancers. Comparison to cancer genes was performed using the gene list provide in cancer gene census (<http://cancer.sanger.ac.uk/cancergenome/projects/census>). Target genes were overlapped with consensus TFs provided⁵⁷. Inference whether the target genes we identified was druggable was done by intersecting target genes with the genes provided in the drug gene interaction database (<http://dgidb.genome.wustl.edu/>) by using “Expert curated” option in the source trust level category of the interactions. All information showing the overlap of target genes with gene lists from literature can be found in Supplemental Table S3.

Pathway analysis. Functional characterization of enhancer/gene assignments was conducted using the ClueGO plugin for cytoscape⁴⁸. Subgroup-specific enhancer gene targets or SE-regulated TFs were queried against a compendium of gene sets from GO (Biological Process), KEGG, and REACTOME to identify processes/pathways that were significantly enriched in tested gene lists from our dataset. Analyses were performed using the GO Term Fusion option in ClueGO and only processes/pathways with a *P*-value < 0.05 (right-sided hypergeometric test) following *P*-value correction (Bonferroni

step down) were visualized. Manual trimming of ClueGO output was performed to remove processes/pathways affiliated with only a single gene set.

Functional comparison of Group 3 and Group 4 enhancers. To identify subgroup specific enhancers and their associated functional pathways, we performed a differential enhancer analysis⁵⁷ on Group 3 and Group 4 enhancers. We first took the union of the top 1,000 enhancer in Group 3 and Group 4 as defined by total H3K27ac signal (area under the curve). We next ranked all enhancer regions by the log₂ fold change in H3K27ac (Extended Data Figure 3b). Differential enhancer target genes as previously defined were depicted under associated enhancers. Visual inspection revealed a number of TGFβ pathway components associated with Group 3 specific enhancers. We visualized this by identifying all enhancer regulated TGFβ pathway components (obtained from KEGG, REACTOME, and GO Biological Process databases) and depicting their specific regulation by Group 3, Group 4, or Group 3-4 differential enhancers (Extended Data Figure 3c).

Comparing enhancer acetylation at TGFβ pathway components in ACVR2A amplified vs. non-amplified Group 3 tumors. We identified a focal amplification of the TGFβ pathway receptor gene ACVR2A in the Group 3 medulloblastoma sample MB-4M23. Whole genome sequencing log₂ read depth ratio is plotted in Extended Data Figure 3d. We hypothesized that in MB-4M23, amplification of ACVR2A leads to increased TGFβ pathway activity, including the increased H3K27ac at enhancers regulating TGFβ pathway components. We identified all Group 3 enhancers regulating TGFβ pathway components and compared the median enhancer normalized H3K27ac signal in MB-4M23 vs. all other Group 3 medulloblastomas. Extended Data Figure 3e shows all enhancers ranked by their log₂ fold change in H3K27ac for MB-4M23 vs. other Group 3 samples. The standard error of the mean was calculated for the fold change and is displayed as error bars in Extended Data Figure 3e.

Nucleosome free region (NFR) identification. H3K27ac data for the samples within the same subgroup was combined. Nucleosome free regions per subgroup were identified by feeding these combine datasets to HOMER software (<http://homer.salk.edu/homer/ngs/index.html>) using “findPeaks” function with the option “-nfr”.

Enrichment of TFs at subgroup-specific enhancers. TF binding sites obtained from TRANSFAC⁵⁸ and detected at NFRs using FIMO⁵⁹ were overlapped with NFRs located within each class of differentially regulated enhancers. For each TF, contingency tables showing the number of NFRs overlapping and non-overlapping with the respective TF were constructed. Significance of enrichment of TFs in NFRs of differentially regulated enhancers was determined using Chi-squared test. Resulting p-values were corrected for multiple testing (FDR<0.01). TF enrichments were calculated as the ratio between observed counts over expected counts. To represent TF enrichments as a heatmap (Extended Data Figure 6b), for each class of enhancers, 4-5 TFs showing the highest enrichments were selected.

Linking subgroup-specific enhancers with TFs. For each of differentially regulated enhancers in the classes of WNT, SHH, Group 3 and Group 4, NFRs belonging to each subgroup were overlapped with the respective subgroup-specific enhancers targeting at least one gene. Overlapping NFRs were intersected with TF binding sites having top 20th

percentile enrichment scores in the respective subgroup-specific enhancers and differentially expressed in the same subgroup. For each TF, NFRs having the top 10th percentile number of binding sites were identified as sites occupied by the respective TF. Then, resulting NFRs were linked back to enhancers they are located, which enabled the linking of TFs having binding sites in the respective enhancers with the target genes of the enhancers. TF regulatory networks for each subgroup (Extended Data Figure 7), where TFs represented as “sources” and enhancer target genes represented as “targets” were constructed using visualization platform Gephi (<http://gephi.github.io/>). To connect LMX1A, LHX2 and EOMES with their targets (Extended Data Figure 8), same strategy was applied by restricting the initial set of TFs to only those three.

4C-seq data analysis. Aligned 4C data was further processed, filtered and visualized using Bioconductor package “Basic4Cseq”⁵⁸.

Mapping typical enhancers and super-enhancers using H3K27ac enhancer definitions. H3K27ac super-enhancers (SEs) and typical enhancers (TEs) in individual medulloblastoma samples were mapped using the ROSE2 software package described^{24,36} and available at <https://github.com/BradnerLab/pipeline>. A 12.5kb stitching window was used to connect proximal clusters of H3K27ac peaks into contiguous enhancer regions. These mappings identified on average ~600 SEs per sample.

Clustering medulloblastoma samples by SE patterns. Relationships between SE landscapes between samples were determined as in Chapuy et al., 2013²². First, we defined the union of all regions considered to be an SE in any individual primary sample and in three Group 3 cell lines. Next H3K27ac signal was calculated at each region and median normalized for each sample. Samples were hierarchically clustered based on similarity of patterns of median normalized H3K27ac enhancer signal as determined using pairwise Pearson correlations.

Mapping SEs and typical enhancers across medulloblastoma subgroups (subgroup enhancer mapping). In order to map and quantify enhancer regions for each medulloblastoma subgroup, we first mapped all enhancers in each individual sample within the group. Across a group, we used the union of all enhancer regions within group samples as the landscape of enhancers. Within this landscape, enhancers were ranked by average H3K27ac signal (area under curve) and classified as SEs or TEs as previously described. This produced SE and TE meta enhancer landscapes for WNT, SHH, Group 3, and Group 4 medulloblastoma with between 558 and 1,110 SEs called per group (Figure 4e). Locations for all SEs and TEs in each subgroup are provided in Supplemental Table S4.

Quantifying enhancer signal variance across samples at meta enhancer regions. To compare the dynamic range of SEs and TEs defined in each medulloblastoma subgroup, we quantified H3K27ac signal variance across samples. For SE and TE enhancer constituents (individual peaks of H3K27ac enrichment within broader enhancer domains) defined in each group, H3K27ac signal variance across samples as a fraction of the mean sample was calculated. The average H3K27ac signal variance across all SEs or TEs within a group is plotted in Extended Data Figure 5b.

Quantifying average H3K27ac signal across samples at subgroup SEs and typical enhancers. We sought to examine trends in H3K27ac signal across medulloblastoma samples at regions defined as SEs or TEs in each group. First we mapped H3K27ac

across all samples to enhancer constituents defined in each group. For each medulloblastoma sample, the average median normalized H3K27ac signal was plotted for SE and TE constituents respectively. For SEs and TEs defined in each group, the average sample H3K27ac signal is plotted with the mean and standard deviation shown as lines. This visualization enables a rapid assessment of H3K27ac variance within a group and of trends in H3K27ac signal for SEs and TEs defined in each group (Extended Data Figure 5d). For instance, enhancer constituents in Group 3 SEs tend to have high signal in Group 4.

Quantifying group ChIP-Seq signal at subgroup SEs and typical enhancers within and between groups. SEs have been shown to have higher H3K27ac and BRD4 signal density at constituents when compared to typical enhancers^{24,36}. To determine if these trends were observed at medulloblastoma enhancers, we calculated H3K27ac and BRD4 ChIP-Seq signal density across all samples at all regions defined as enhancers across groups (meta enhancers). In order to properly compare ChIP-Seq signal density between SEs and TEs, for each enhancer constituent, we first determined if it was considered part of an SE in one or more groups, and if so, these groups defined the “active group context” for that particular enhancer constituent. Groups in which the enhancer constituent showed no evidence of enhancer activity (SE or TE) were considered the inactive group context. For enhancer constituents considered only part of a TE in one or more groups, groups in which the enhancer constituent was classified as a TE were considered the active group context and all other groups were considered the inactive group context. For each SE or TE constituent, average H3K27ac or BRD4 signal density was calculated at all samples in the active group context or in the inactive group context. The distributions of H3K27ac or BRD4 signal for enhancer constituents classified by SE or TE status were plotted and the statistical significance of the difference in the mean was tested in the active or inactive group context using a Welch’s two-tailed *t* test (Extended Data Figure 5c).

Identifying group specific and conserved SEs. We developed a method to identify SEs that were conserved across all medulloblastoma subgroups as well as SEs that showed highly group specific patterns of enhancer activity. We first took as the SE landscape all regions identified as SEs in the meta subgroup enhancer mapping. To account for sample-to-sample variability in H3K27ac ChIP-Seq dynamic range, H3K27ac signal at enhancers in each medulloblastoma sample was rank transformed (Figure 4f). As each medulloblastoma sample contained on average ~600 SEs, enhancer regions with an average rank of 600 or better in each subgroup were considered conserved. To identify enhancers with group specific patterns of activity, we calculated a “group rank Z-score” that compared average signal in one group to average signal in other groups. Here we considered whether enhancers might show group specific patterns for WNT, SHH, Group 3, Group 4, and as well for groupings of WNT/SHH, and Group3/4. For each enhancer, this group rank Z-score was calculated for each group vs. other combination. Enhancers with a group rank Z-score > 1 (i.e. those whose mean rank within a group was > 1 standard deviation above the mean rank of all other samples) were considered group specific. To account for variability in enhancer ranks, only enhancers with a statistically significant difference in ranks (within group vs. all other samples, Welch’s two-tailed *t* test, p-Value < 0.01) were considered. Supplemental Table S4 contains all SE regions identified in medulloblastoma subgroups and their corresponding max group rank Z-score, p-Value, and classification.

Mapping H3K27ac enrichment at the MYC gene desert. To provide a developmental context for medulloblastoma MYC SEs, we mapped H3K27ac enrichment at the MYC locus. H3K27ac data was obtained from the Epigenome ROADMAP as in figure 1f. The 500kb region flanking the MYC SE No. 2 was divided into 5kb bins and each bin was tested for overlap with a H3K27ac peak in each ROADMAP sample. ROADMAP samples were hierarchically clustered by similarity of H3K27ac peak pattern at the MYC locus (Extended Data Figure 8g). Overlap with MYC SE No. 2 was found in 4/77 ROADMAP samples.

Calculating regulatory IN and OUT degree for all SE associated TFs. To quantify the interaction network of TF regulation, we calculated the IN and OUT degree of all SE associated TFs. The 92 SE associated TFs were those defined as either proximal to an SE (within 50kb) or the target of a differential SE enhancer element. For any given TF (TF_i) The IN degree was defined as the number of TFs with an enriched binding motif at the proximal SE of TF_i (Figure 5a). The OUT degree was defined as the number of TF associated SEs containing an enriched binding site for TF_i. Within any given SE, enriched TF binding sites were determined at putative nucleosome free regions (valleys) flanked by high levels of H3K27ac. Valleys were calculated using an algorithm adapted from Ramsey et al., 2010⁶⁰. In these regions, we searched for enriched TF binding sites using the FIMO⁵⁹ algorithm with TF position weight matrices defined in the TRANSFAC database⁵⁸. An FDR cutoff of 0.01 was used to identify enriched TF binding sites. Using this approach, we calculated IN and OUT degree for all SE associated TFs within the meta H3K27ac landscape (average of all samples) of each medulloblastoma subgroup. This approach resulted in an IN and OUT degree estimate for each SE associated TF in each medulloblastoma subgroup (Extended Data Figure 9c-e).

Identifying TF binding motifs for LMX1A, LHX2, and HLX. We sought to identify TF binding motifs for each TF in each subgroup. For each TF, we defined binding regions as the +/- 1,000bp flanking the enriched region summit (as defined using MACS 1.4.2 with a p-value cutoff of 1e-9). We took the union of all regions bound in a given subgroup (e.g. HLX bound regions in Group 3 samples) that overlapped an enhancer in that subgroup and did not overlap any ENCODE¹⁵ blacklist regions. We next took the top 10,000 discreet regions as ranked by average TF ChIP-Seq signal and used the +/- 100bp region flanking the region center as the input for *de novo* motif finding. *De novo* motif finding was performed using the MEME⁵⁹ suite using a 1st order background model and searching for motifs between 6 and 30bp in length. The top motif for each TF is displayed as a position weight matrix in Extended Data Figure 8i-l.

Visualizing TF regulatory networks. To visualize SE associated TF interactions in each subgroup, we ranked all SE associated TF by TOTAL degree (IN + OUT). We visualized the top 50% of SE associated TF in each subgroup as a network diagram with each node representing a SE associated TF, and with nodes colored and ordered by increasing TOTAL degree (Extended Data Figure 8e-h). Interactions between SE associated TF nodes were defined as a TF motif identified in the SE of a TF and are depicted as edges. For Group 3 and Group 4, edges validated by the presence of a TF ChIP-Seq peak are colored.

Clustering TFs by regulatory degree to identify and infer subgroup specific regulatory circuitry. To identify SE associated TFs with similar regulatory patterns likely to influence subgroup identity, we first normalized the TOTAL degree for each SE associated TF in each subgroup from 0 to 1. We then calculated the normalized TOTAL

degree for each SE associated TF in each subgroup. We filtered out all TFs with a max TOTAL degree across medulloblastomas of less than 0.7. We next clustered all remaining TFs by their TOTAL degree pattern. Hierarchical clustering was performed using a Euclidian distance metric and the resulting clustergram tree was cut at a distance of 0.5 to produce 26 individual clusters. Of these 26 clusters, 12 showed a median TOTAL degree > 0.7 in 1,2, or all 4 subgroups. Clusters with > 0.7 TOTAL degree in 3 subgroups were omitted for simplicity. TOTAL degree patterns of TFs in these 12 clusters are shown in Figure 5b. This filtering produced a list of 102 SE associated TFs, of which 71 had predicted interactions with one another. These 71 TFs fall into either conserved, subgroup specific, or dual subgroup clusters and together they comprise the inferred core regulatory circuitry of medulloblastoma subgroups. As in Extended Data Figure 8e-h, regulatory interactions between these core regulatory circuitry TFs are depicted in Figure 5c with Group 3 and Group 4 validated edges colored. A subset of this larger network containing the TFs HLX, LHX2, EOMES, and LMX1A is depicted in Figure 5f with ChIP-Seq validated edges drawn as solid lines and motif prediction edges drawn in dotted lines.

Quantifying protein-protein interactions of co-regulating SEs. We used the STRING interaction database⁶¹ to quantify protein-protein interaction frequencies of SE associated TFs with similar regulatory patterns. TF pairs were considered co-regulatory if they shared 50% of the same OUT degree edges. Interaction frequencies for co-regulatory pairs were compared to those from 10,000 randomly assigned pairs of TFs expressed in that subgroup (Extended Data Figure 9b).

Integration of TF ChIP-Seq occupancy into enhancer landscape and TF regulatory network. To determine the fraction of motif predicted edges with evidence of actual TF ChIP-Seq binding, we first took all predicted edges for HLX, LHX2, and LMX1A interacting SE associated with other TFs in Group 3 and Group 4. We validated all edges that contained a ChIP-Seq peak within the same enhancer as the predicted TF motif. The fraction of validated edges for each TF in each subgroup is shown in Extended Data Figure 8i-l.

Quantification of TF binding at Group 3 and 4 enhancers. To determine how Group 3 and Group 4 TF ChIP-Seq levels varied at Group 3 and Group 4 specific enhancers, we quantified TF ChIP-Seq signal at Group 3 and Group 4 enhancers. We first took the union of the top 1,000 enhancer regions as defined by H3K27ac signal in Group 3 and Group 4 (as in Extended Data Figure 3b). We identified as Group 3 and Group 4 specific enhancer regions with a $> \log_2 1.0$ absolute fold change between Group 3 and Group 4. We identified as conserved enhancer regions with a $< 0.05 \log_2$ absolute fold change between Group 3 and Group 4. We next identified all enhancer regions bound by LHX2 and HLX in Group 3 (G3 HLX and LHX2) or by LHX2 and LMX1A in Group 4 (G4 LMX1A and LHX2). TF ChIP-Seq occupancy in units of average area under the curve (AUC) were quantified at TF bound regions overlapping Group 3 specific, Group 4 specific, and conserved enhancer region (Figure 5e). Statistical differences in the means of the distributions of TF ChIP-Seq signal at different enhancer populations was determined using a Welch's two tailed t -test (Figure 5e).

Quantifying Group 4 TF gene expression changes in Dreher RL. To identify genes transcriptionally regulated by Lmx1a in the developing cerebellum, we isolated cerebellar uRL from wild type and Lmx1a^{-/-} embryos by laser capture microdissection. uRL was isolated from WT (n=3) and Lmx1a^{-/-} (n=3) embryos (~3000 cells/embryo) at e13.5, just

prior to abnormal RL regression in *Lmx1a*^{-/-} embryos. RNA was extracted using PicoPure RNA Isolation Kit (Arcturus) and hybridized to Illumina MouseRef8 v2 Expression BeadChips at the Johns Hopkins Array Core Facility. Next we identified all human TF genes with unambiguous mouse homologs that were detectably expressed in the WT mouse cerebellum (cut off of 100 arbitrary units). We subsequently quantified median normalized expression in WT or *Lmx1a*^{-/-} samples and calculated the log₂ fold-change for all TFs. We ranked the expression fold-change of all SE-associated TFs in medulloblastoma and plotted their log₂ fold change in *Lmx1a*^{-/-} vs. WT (Figure 6e). SE-associated TFs present in the Group 4 TF network (Extended Data Figure 8h) were colored in green. Lastly we summarized fold-changes between *Lmx1a*^{-/-} and WT samples for three classes of TFs: (i) all human TFs with expressed mouse homologs, (ii) medulloblastoma SE-associated TFs, and (iii) SE-associated TFs present in the Group 4 TF network. Statistical differences in the means of the distributions of TF expression fold-changes were determined using a Welch's two-tailed *t*-test (Figure 6f).

References:

- 1 Northcott, P. A., Dubuc, A. M., Pfister, S. & Taylor, M. D. Molecular subgroups of medulloblastoma. *Expert review of neurotherapeutics* **12**, 871-884, doi:10.1586/ern.12.66 (2012).
- 2 Northcott, P. A., Korshunov, A., Pfister, S. M. & Taylor, M. D. The clinical implications of medulloblastoma subgroups. *Nature reviews. Neurology* **8**, 340-351, doi:10.1038/nrneurol.2012.78 (2012).
- 3 Taylor, M. D. *et al.* Molecular subgroups of medulloblastoma: the current consensus. *Acta neuropathologica* **123**, 465-472, doi:10.1007/s00401-011-0922-z (2012).
- 4 Jones, D. T. *et al.* Dissecting the genomic complexity underlying medulloblastoma. *Nature* **488**, 100-105, doi:10.1038/nature11284 (2012).
- 5 Kool, M. *et al.* Genome sequencing of SHH medulloblastoma predicts genotype-related response to smoothened inhibition. *Cancer cell* **25**, 393-405, doi:10.1016/j.ccr.2014.02.004 (2014).
- 6 Northcott, P. A. *et al.* Medulloblastomics: the end of the beginning. *Nature reviews. Cancer* **12**, 818-834, doi:10.1038/nrc3410 (2012).
- 7 Northcott, P. A. *et al.* Enhancer hijacking activates GFI1 family oncogenes in medulloblastoma. *Nature* **511**, 428-434, doi:10.1038/nature13379 (2014).
- 8 Northcott, P. A. *et al.* Subgroup-specific structural variation across 1,000 medulloblastoma genomes. *Nature* **488**, 49-56, doi:10.1038/nature11327 (2012).
- 9 Pugh, T. J. *et al.* Medulloblastoma exome sequencing uncovers subtype-specific somatic mutations. *Nature* **488**, 106-110, doi:10.1038/nature11329 (2012).
- 10 Robinson, G. *et al.* Novel mutations target distinct subgroups of medulloblastoma. *Nature* **488**, 43-48, doi:10.1038/nature11213 (2012).
- 11 Batora, N. V. *et al.* Transitioning from genotypes to epigenotypes: why the time has come for medulloblastoma epigenomics. *Neuroscience* **264**, 171-185, doi:10.1016/j.neuroscience.2013.07.030 (2014).

- 12 Jones, D. T., Northcott, P. A., Kool, M. & Pfister, S. M. The role of chromatin remodeling in medulloblastoma. *Brain pathology* **23**, 193-199, doi:10.1111/bpa.12019 (2013).
- 13 Hovestadt, V. *et al.* Decoding the regulatory landscape of medulloblastoma using DNA methylation sequencing. *Nature* **510**, 537-541, doi:10.1038/nature13268 (2014).
- 14 Shlyueva, D., Stampfel, G. & Stark, A. Transcriptional enhancers: from properties to genome-wide predictions. *Nature reviews. Genetics* **15**, 272-286, doi:10.1038/nrg3682 (2014).
- 15 Consortium, E. P. An integrated encyclopedia of DNA elements in the human genome. *Nature* **489**, 57-74, doi:10.1038/nature11247 (2012).
- 16 Thurman, R. E. *et al.* The accessible chromatin landscape of the human genome. *Nature* **489**, 75-82, doi:10.1038/nature11232 (2012).
- 17 Roadmap Epigenomics, C. *et al.* Integrative analysis of 111 reference human epigenomes. *Nature* **518**, 317-330, doi:10.1038/nature14248 (2015).
- 18 Chapuy, B. *et al.* Discovery and characterization of super-enhancer-associated dependencies in diffuse large B cell lymphoma. *Cancer cell* **24**, 777-790, doi:10.1016/j.ccr.2013.11.003 (2013).
- 19 Zhang, Y. *et al.* Model-based analysis of ChIP-Seq (MACS). *Genome biology* **9**, R137, doi:10.1186/gb-2008-9-9-r137 (2008).
- 20 Loven, J. *et al.* Selective inhibition of tumor oncogenes by disruption of super-enhancers. *Cell* **153**, 320-334, doi:10.1016/j.cell.2013.03.036 (2013).
- 21 Kim, T. K. *et al.* Widespread transcription at neuronal activity-regulated enhancers. *Nature* **465**, 182-187, doi:10.1038/nature09033 (2010).
- 22 Cho, Y. J. *et al.* Integrative genomic analysis of medulloblastoma identifies a molecular subgroup that drives poor clinical outcome. *Journal of clinical oncology : official journal of the American Society of Clinical Oncology* **29**, 1424-1430, doi:10.1200/JCO.2010.28.5148 (2011).
- 23 Northcott, P. A. *et al.* Medulloblastoma comprises four distinct molecular variants. *Journal of clinical oncology : official journal of the American Society of Clinical Oncology* **29**, 1408-1414, doi:10.1200/JCO.2009.27.4324 (2011).
- 24 Kool, M. *et al.* Integrated genomics identifies five medulloblastoma subtypes with distinct genetic profiles, pathway signatures and clinicopathological features. *PloS one* **3**, e3088, doi:10.1371/journal.pone.0003088 (2008).
- 25 Jin, F. *et al.* A high-resolution map of the three-dimensional chromatin interactome in human cells. *Nature* **503**, 290-294, doi:10.1038/nature12644 (2013).
- 26 Pope, B. D. *et al.* Topologically associating domains are stable units of replication-timing regulation. *Nature* **515**, 402-405, doi:10.1038/nature13986 (2014).
- 27 Groschel, S. *et al.* A single oncogenic enhancer rearrangement causes concomitant EVI1 and GATA2 deregulation in leukemia. *Cell* **157**, 369-381, doi:10.1016/j.cell.2014.02.019 (2014).
- 28 Milde, T. *et al.* HD-MB03 is a novel Group 3 medulloblastoma model demonstrating sensitivity to histone deacetylase inhibitor treatment. *J Neurooncol* **110**, 335-348, doi:10.1007/s11060-012-0978-1 (2012).

- 29 Hallberg, B. & Palmer, R. H. Mechanistic insight into ALK receptor tyrosine kinase in human cancer biology. *Nature reviews. Cancer* **13**, 685-700, doi:10.1038/nrc3580 (2013).
- 30 Downen, J. M. *et al.* Control of cell identity genes occurs in insulated neighborhoods in mammalian chromosomes. *Cell* **159**, 374-387, doi:10.1016/j.cell.2014.09.030 (2014).
- 31 Hnisz, D. *et al.* Super-enhancers in the control of cell identity and disease. *Cell* **155**, 934-947, doi:10.1016/j.cell.2013.09.053 (2013).
- 32 Parker, S. C. *et al.* Chromatin stretch enhancer states drive cell-specific gene regulation and harbor human disease risk variants. *Proceedings of the National Academy of Sciences of the United States of America* **110**, 17921-17926, doi:10.1073/pnas.1317023110 (2013).
- 33 Whyte, W. A. *et al.* Master transcription factors and mediator establish super-enhancers at key cell identity genes. *Cell* **153**, 307-319, doi:10.1016/j.cell.2013.03.035 (2013).
- 34 Aruga, J. *et al.* Mouse *Zic1* is involved in cerebellar development. *The Journal of neuroscience : the official journal of the Society for Neuroscience* **18**, 284-293 (1998).
- 35 Grinberg, I. *et al.* Heterozygous deletion of the linked genes *ZIC1* and *ZIC4* is involved in Dandy-Walker malformation. *Nature genetics* **36**, 1053-1055, doi:10.1038/ng1420 (2004).
- 36 Rada-Iglesias, A. *et al.* A unique chromatin signature uncovers early developmental enhancers in humans. *Nature* **470**, 279-283, doi:10.1038/nature09692 (2011).
- 37 Gibson, P. *et al.* Subtypes of medulloblastoma have distinct developmental origins. *Nature* **468**, 1095-1099, doi:10.1038/nature09587 (2010).
- 38 Grammel, D. *et al.* Sonic hedgehog-associated medulloblastoma arising from the cochlear nuclei of the brainstem. *Acta neuropathologica* **123**, 601-614, doi:10.1007/s00401-012-0961-0 (2012).
- 39 Schuller, U. *et al.* Acquisition of granule neuron precursor identity is a critical determinant of progenitor cell competence to form Shh-induced medulloblastoma. *Cancer cell* **14**, 123-134, doi:10.1016/j.ccr.2008.07.005 (2008).
- 40 Yang, Z. J. *et al.* Medulloblastoma can be initiated by deletion of *Patched* in lineage-restricted progenitors or stem cells. *Cancer cell* **14**, 135-145, doi:10.1016/j.ccr.2008.07.003 (2008).
- 41 Fink, A. J. *et al.* Development of the deep cerebellar nuclei: transcription factors and cell migration from the rhombic lip. *The Journal of neuroscience : the official journal of the Society for Neuroscience* **26**, 3066-3076, doi:10.1523/JNEUROSCI.5203-05.2006 (2006).
- 42 Chizhikov, V. V. *et al.* *Lmx1a* regulates fates and location of cells originating from the cerebellar rhombic lip and telencephalic cortical hem. *Proceedings of the National Academy of Sciences of the United States of America* **107**, 10725-10730, doi:10.1073/pnas.0910786107 (2010).

- 43 Millonig, J. H., Millen, K. J. & Hatten, M. E. The mouse Dreher gene *Lmx1a* controls formation of the roof plate in the vertebrate CNS. *Nature* **403**, 764-769, doi:10.1038/35001573 (2000).
- 44 Gilbertson, R. J. Mapping cancer origins. *Cell* **145**, 25-29, doi:10.1016/j.cell.2011.03.019 (2011).
- 45 Byrd, J. C. *et al.* Targeting BTK with ibrutinib in relapsed chronic lymphocytic leukemia. *The New England journal of medicine* **369**, 32-42, doi:10.1056/NEJMoa1215637 (2013).
- 46 Hale, G. *et al.* Remission induction in non-Hodgkin lymphoma with reshaped human monoclonal antibody CAMPATH-1H. *Lancet* **2**, 1394-1399 (1988).
- 47 Hovestadt, V. *et al.* Robust molecular subgrouping and copy-number profiling of medulloblastoma from small amounts of archival tumour material using high-density DNA methylation arrays. *Acta neuropathologica* **125**, 913-916, doi:10.1007/s00401-013-1126-5 (2013).
- 48 Waszak, S. M. *et al.* Population Variation and Genetic Control of Modular Chromatin Architecture in Humans. *Cell* **162**, 1039-1050, doi:10.1016/j.cell.2015.08.001 (2015).
- 49 Bindea, G. *et al.* ClueGO: a Cytoscape plug-in to decipher functionally grouped gene ontology and pathway annotation networks. *Bioinformatics* **25**, 1091-1093, doi:10.1093/bioinformatics/btp101 (2009).
- 50 Brown, J. D. *et al.* NF-kappaB directs dynamic super enhancer formation in inflammation and atherogenesis. *Molecular cell* **56**, 219-231, doi:10.1016/j.molcel.2014.08.024 (2014).
- 51 Ramsey, S. A. *et al.* Genome-wide histone acetylation data improve prediction of mammalian transcription factor binding sites. *Bioinformatics* **26**, 2071-2075, doi:10.1093/bioinformatics/btq405 (2010).
- 52 Ni, T. T. *et al.* Conditional control of gene function by an invertible gene trap in zebrafish. *Proceedings of the National Academy of Sciences of the United States of America* **109**, 15389-15394, doi:10.1073/pnas.1206131109 (2012).
- 53 Haldipur, P. *et al.* Expression of Sonic hedgehog during cell proliferation in the human cerebellum. *Stem Cells Dev* **21**, 1059-1068, doi:10.1089/scd.2011.0206 (2012).
- 54 van de Werken, H. J. *et al.* 4C technology: protocols and data analysis. *Methods Enzymol* **513**, 89-112, doi:10.1016/B978-0-12-391938-0.00004-5 (2012).
- 55 Langmead, B., Trapnell, C., Pop, M. & Salzberg, S. L. Ultrafast and memory-efficient alignment of short DNA sequences to the human genome. *Genome biology* **10**, R25, doi:10.1186/gb-2009-10-3-r25 (2009).
- 56 John, S. *et al.* Chromatin accessibility pre-determines glucocorticoid receptor binding patterns. *Nature genetics* **43**, 264-268, doi:10.1038/ng.759 (2011).
- 57 Brown, J. D. *et al.* NF-kappaB Directs Dynamic Super Enhancer Formation in Inflammation and Atherogenesis. *Molecular cell*, doi:10.1016/j.molcel.2014.08.024 (2014).
- 58 Walter, C., Schuetzmann, D., Rosenbauer, F. & Dugas, M. Basic4Cseq: an R/Bioconductor package for analyzing 4C-seq data. *Bioinformatics* **30**, 3268-3269, doi:10.1093/bioinformatics/btu497 (2014).

- 59 Bailey, T. L. *et al.* MEME SUITE: tools for motif discovery and searching. *Nucleic acids research* **37**, W202-208, doi:10.1093/nar/gkp335 (2009).

Figure 1. The enhancer landscape of primary medulloblastoma.

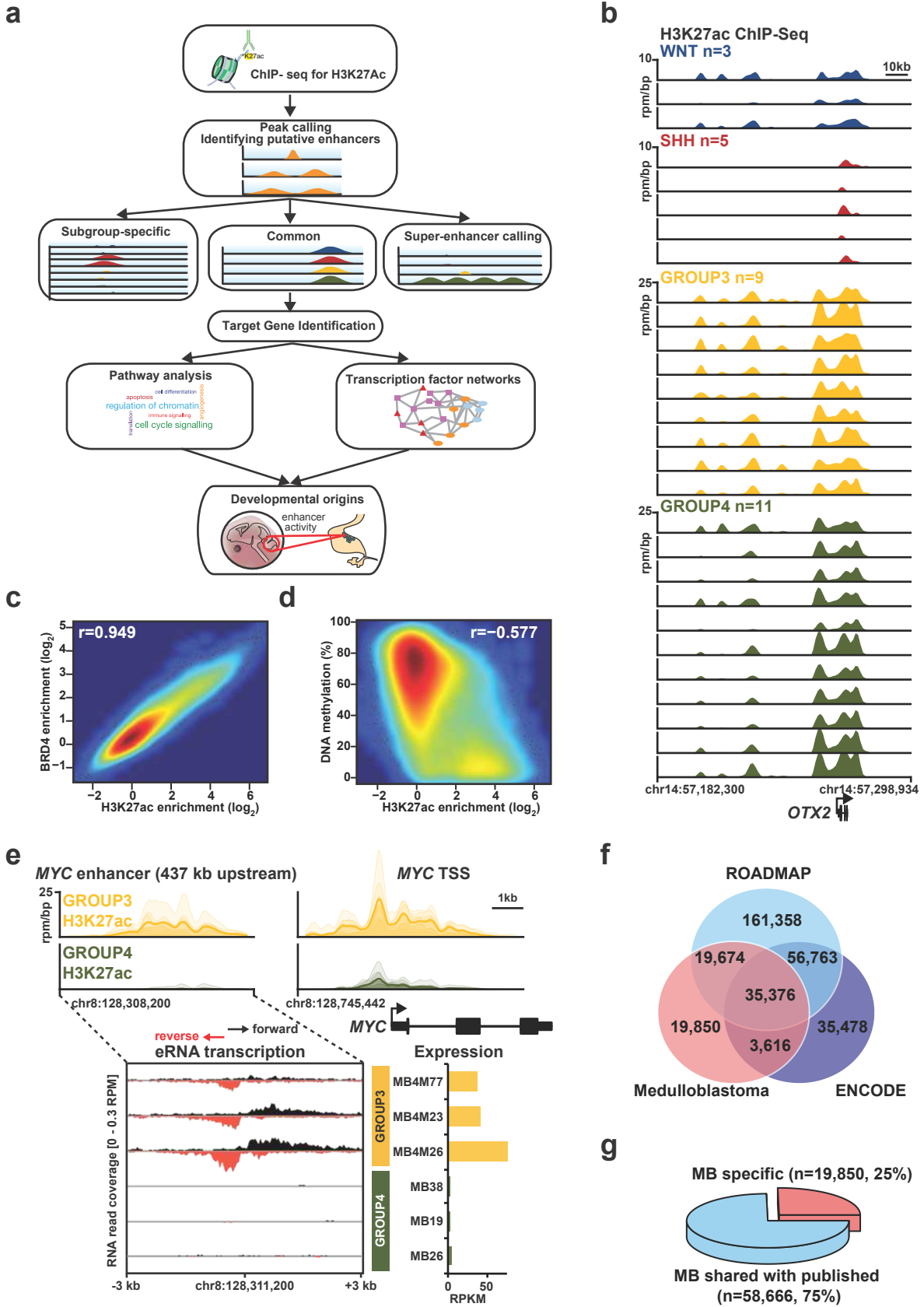


Figure 2. Differentially regulated enhancers and enhancer/gene assignments in medulloblastoma subgroups.

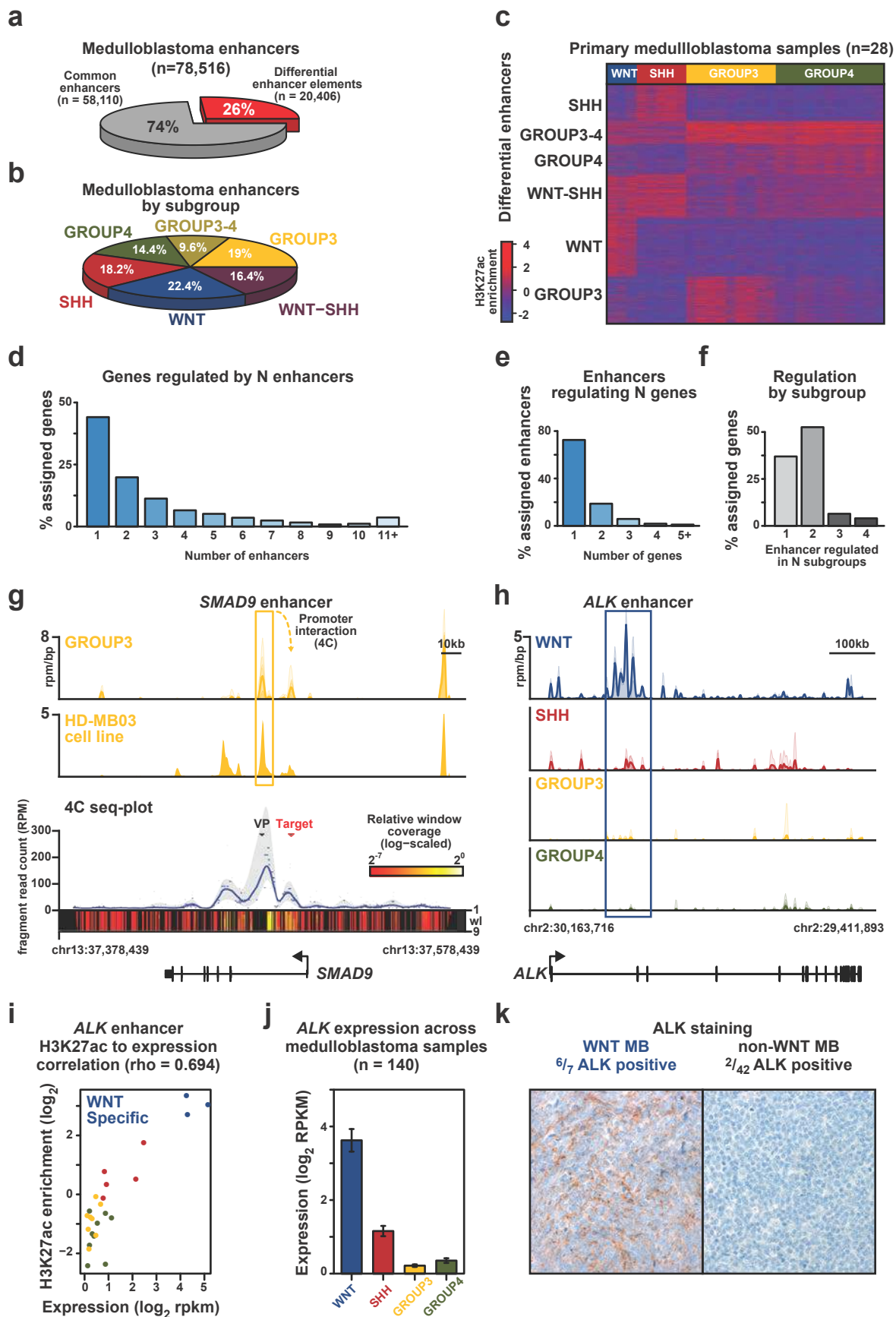


Figure 3. Medulloblastoma super-enhancers define subgroup-specific identity.

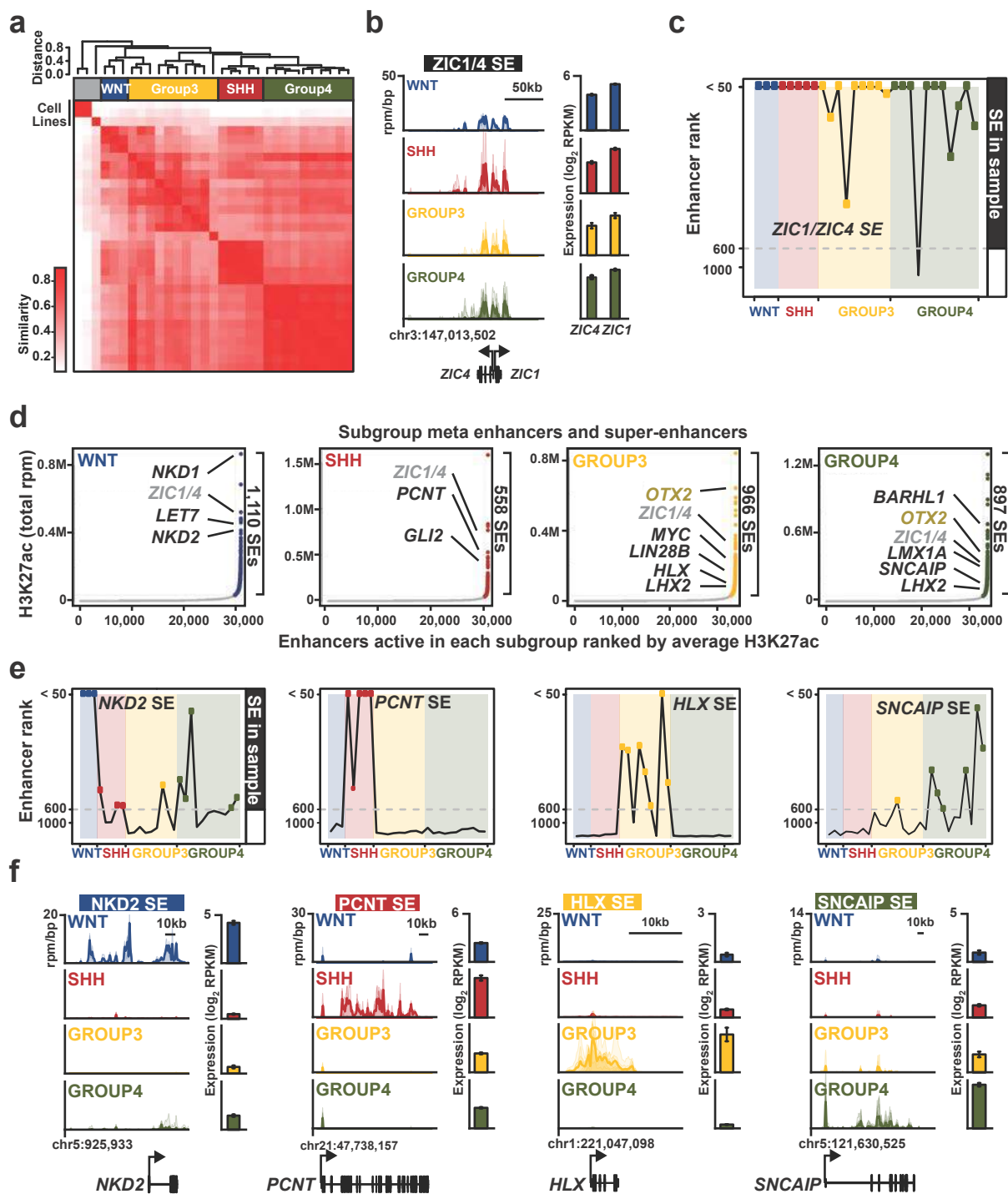


Figure 4. *In vivo* validation of Group 3 and Group 4 medulloblastoma super-enhancers.

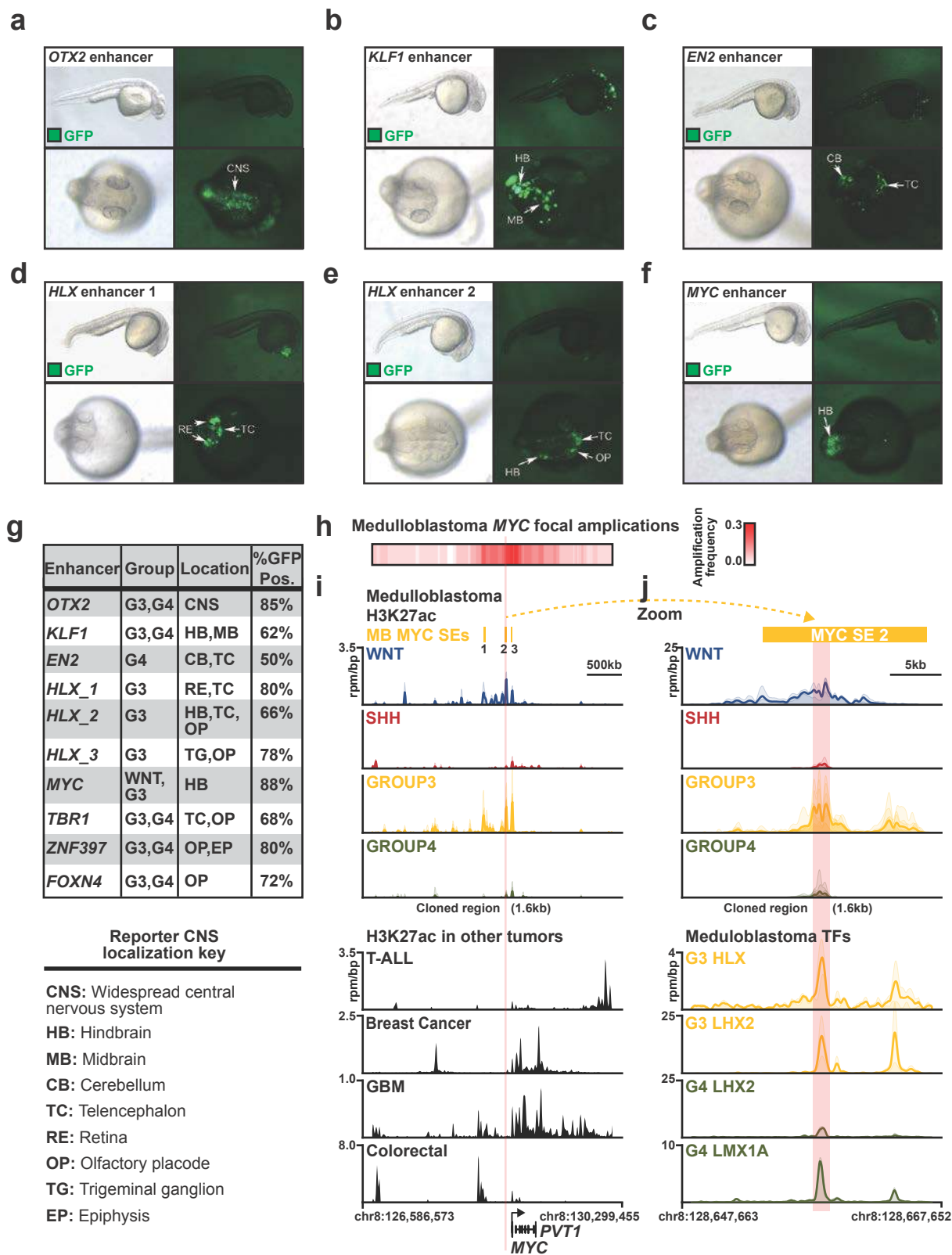


Figure 5. Super-enhancers define medulloblastoma regulatory circuitry.

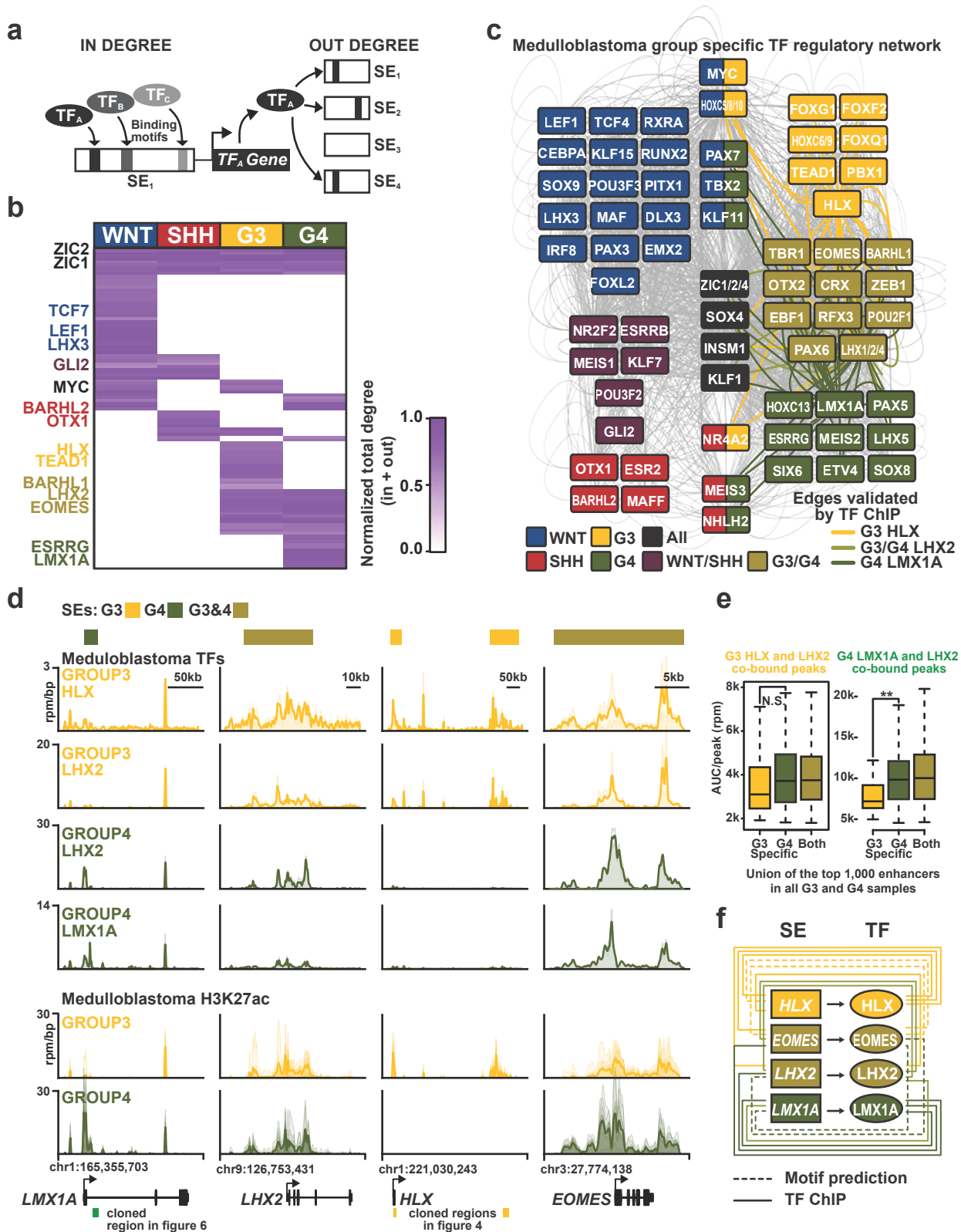
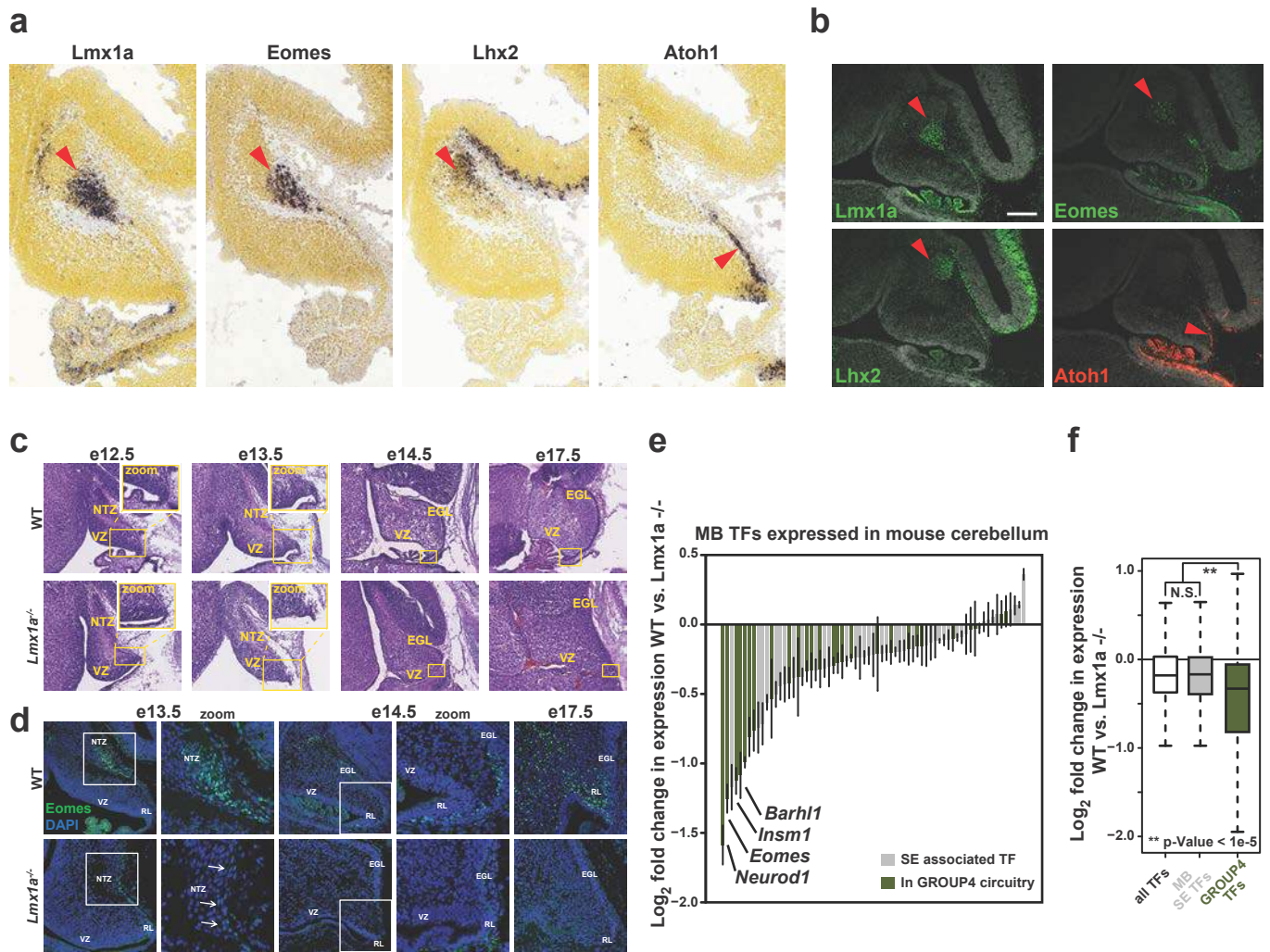
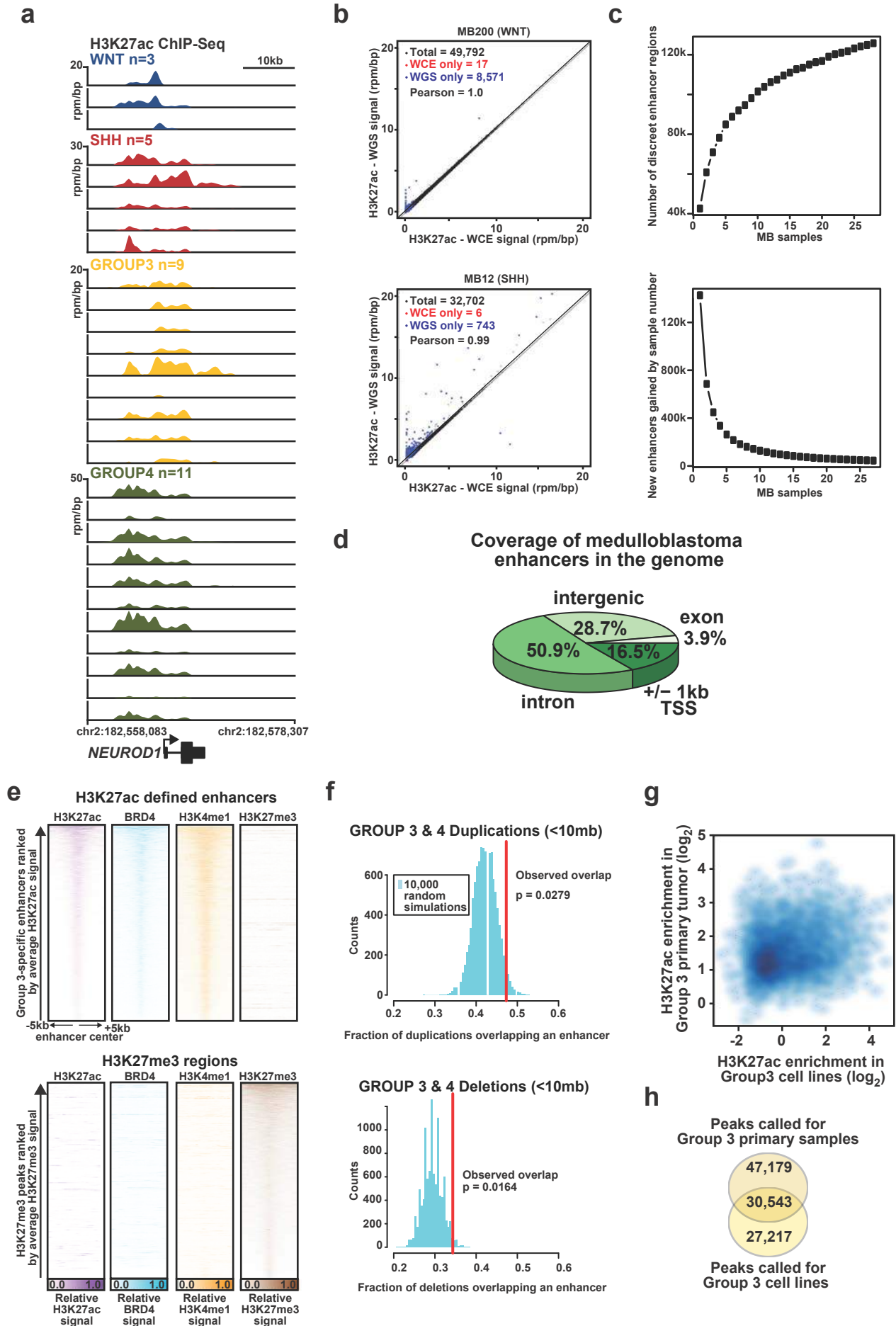


Figure 6. Master regulator transcription factors implicate Group 4 cellular origins.

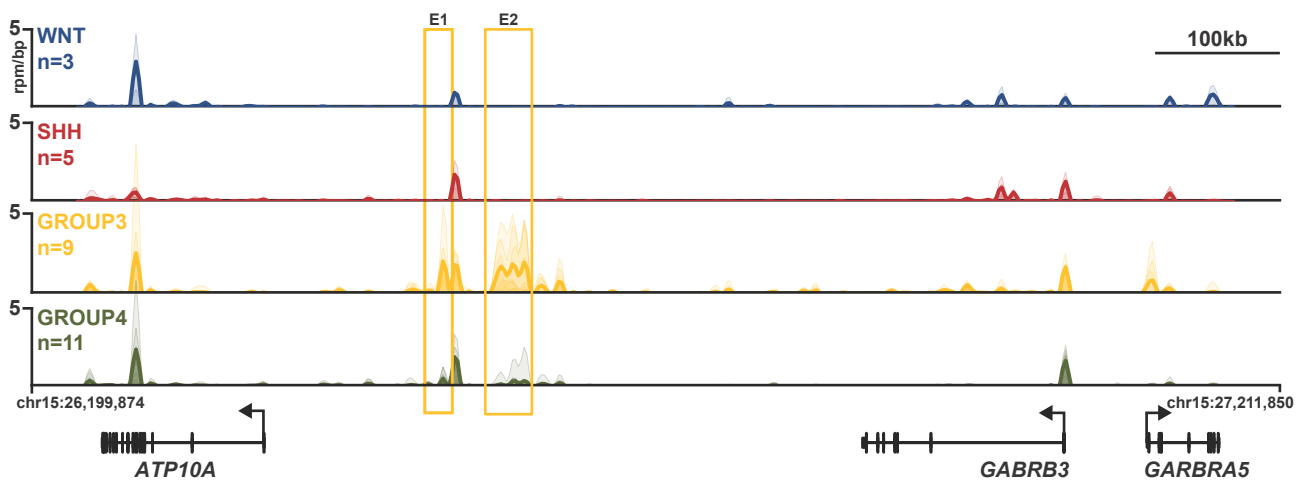


Extended Data Figure 1: Enhancer landscape of primary medulloblastoma.

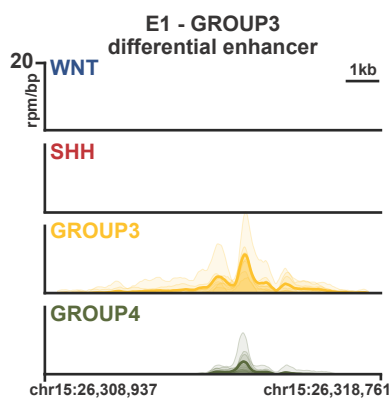


Extended Data Figure 2: Enhancer/gene assignments in medulloblastoma.

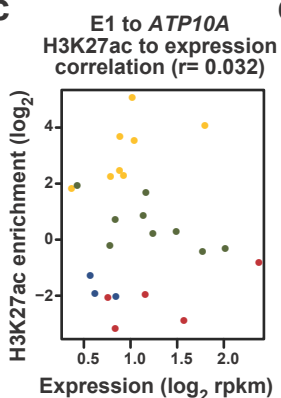
a



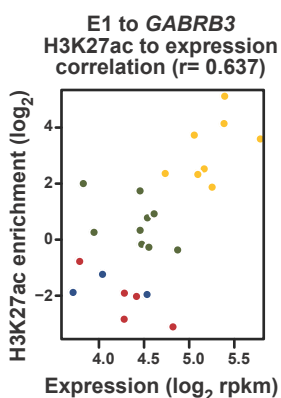
b



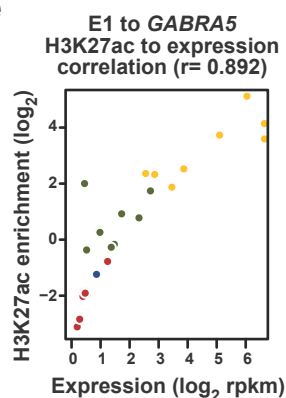
c



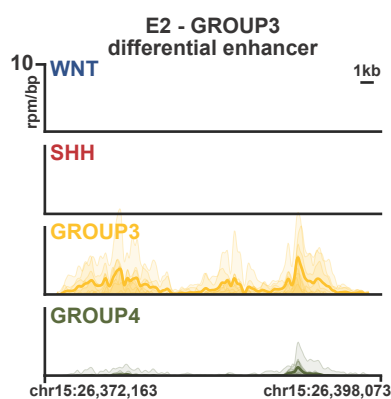
d



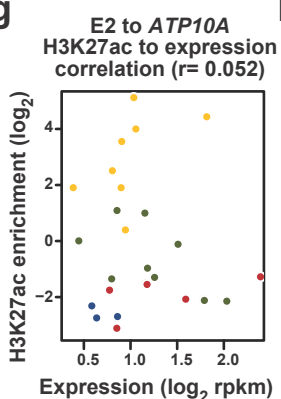
e



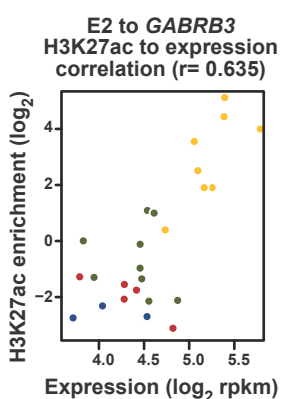
f



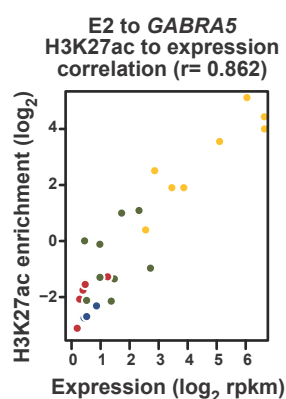
g



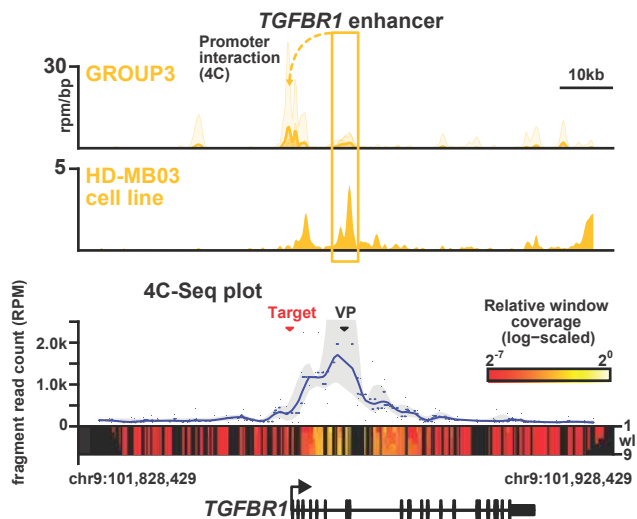
h



i

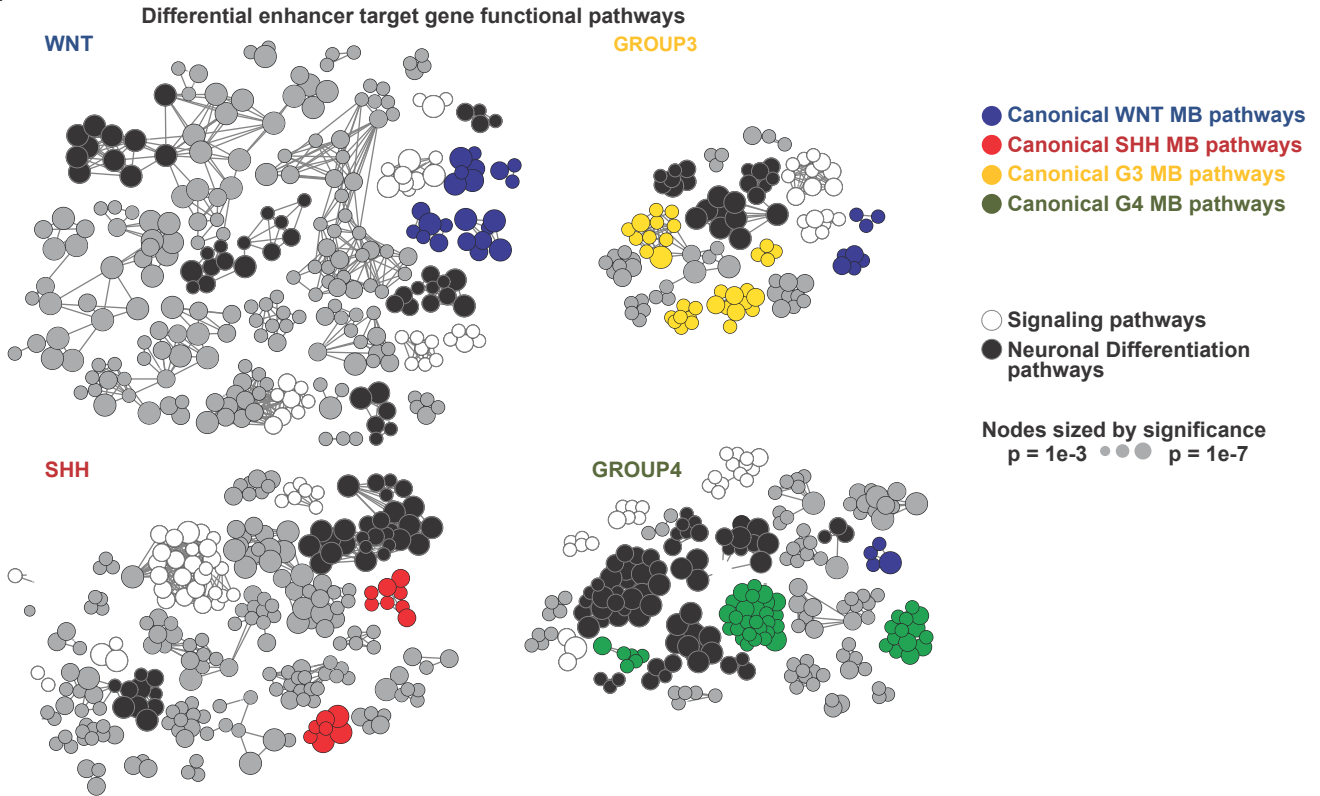


j

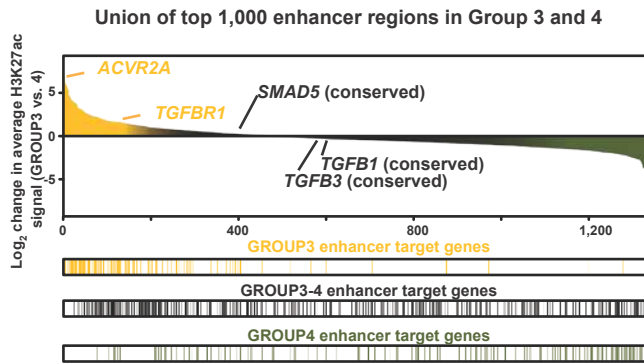


Extended Data Figure 3: Enhancer-driven TGF β activity in Group 3 medulloblastoma.

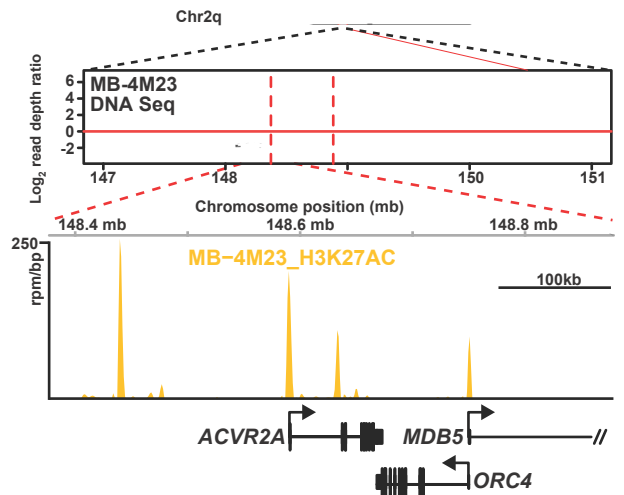
a



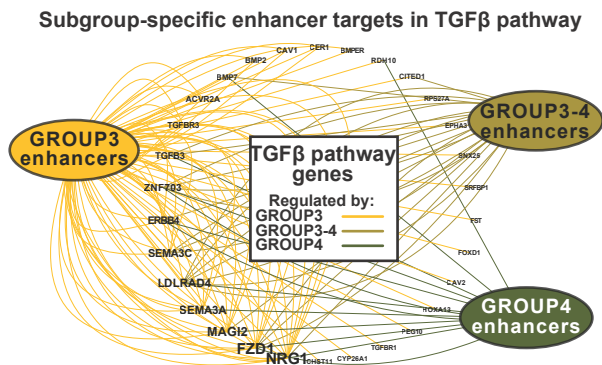
b



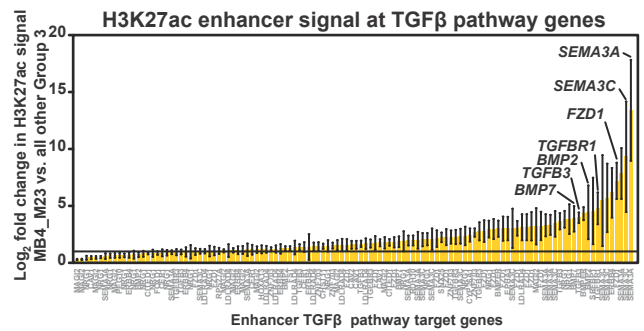
d



c

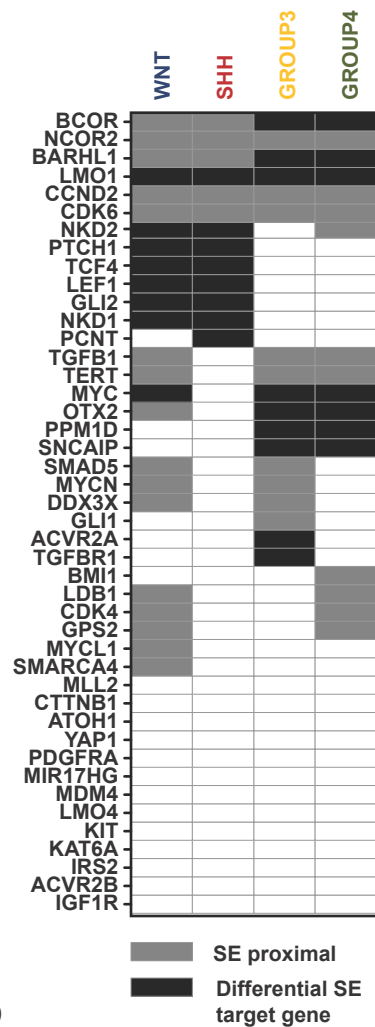


e

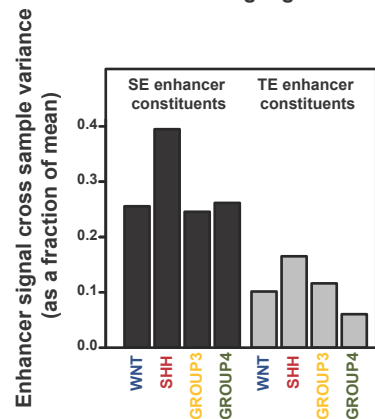


Extended Data Figure 4: Features of medulloblastoma super-enhancers.

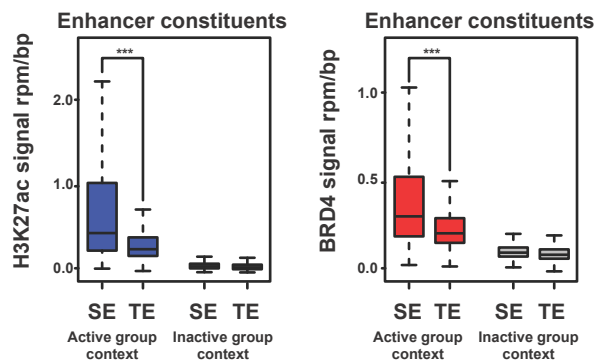
a



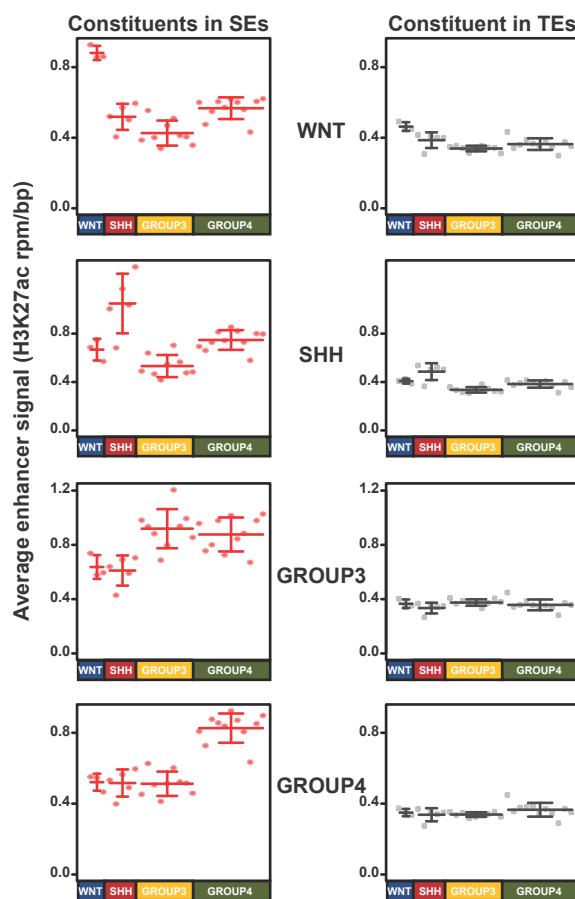
b



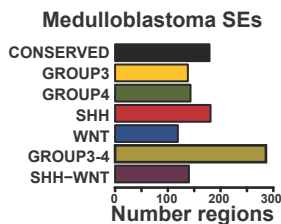
c



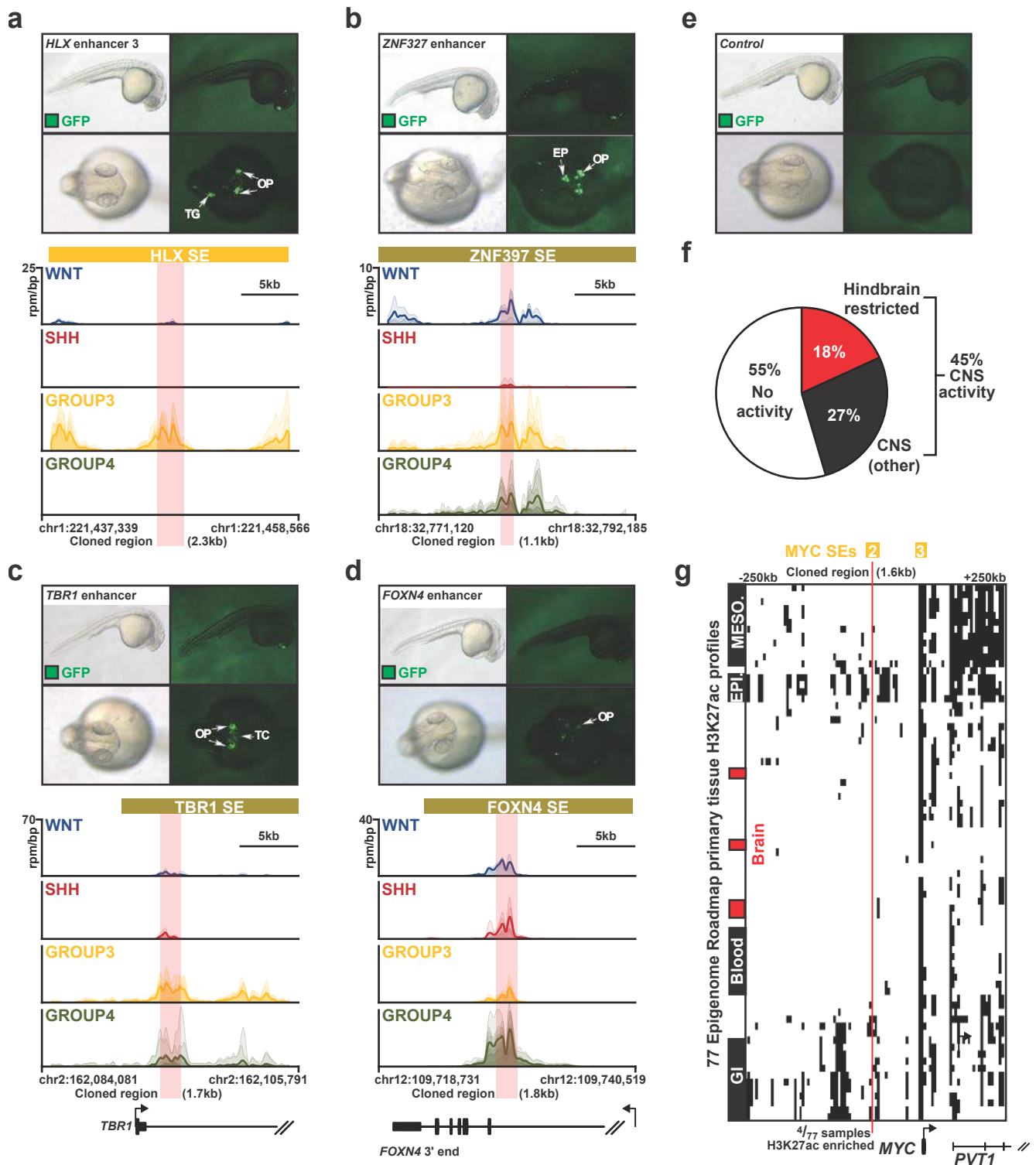
d



e

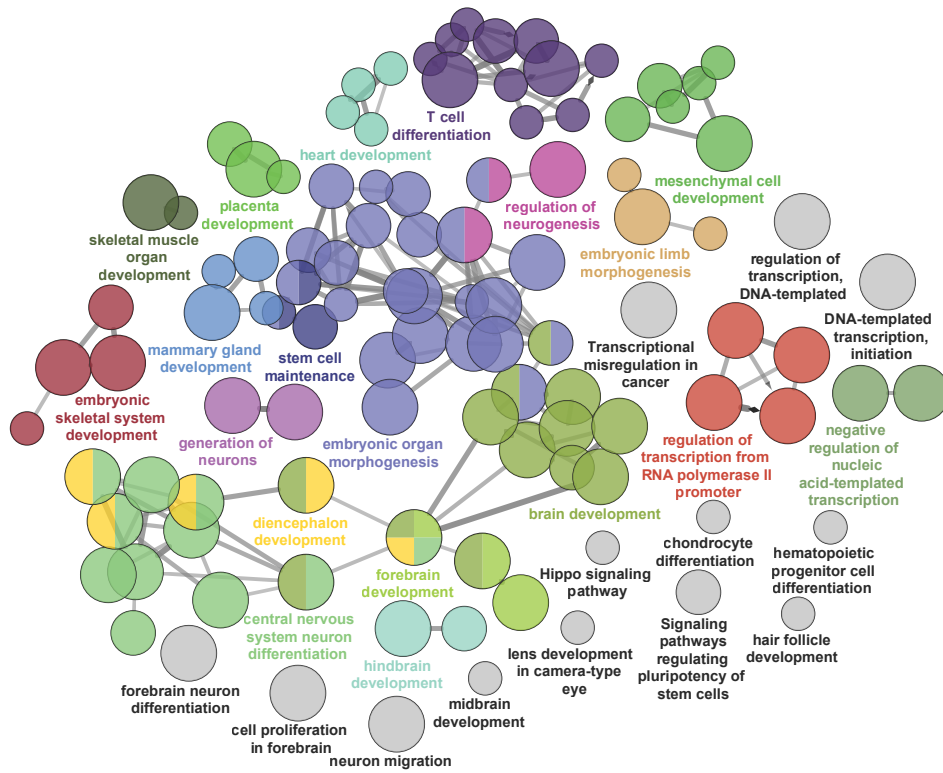


Extended Data Figure 5. *In vivo* validation of Group 3 and Group 4 medulloblastoma super-enhancers.

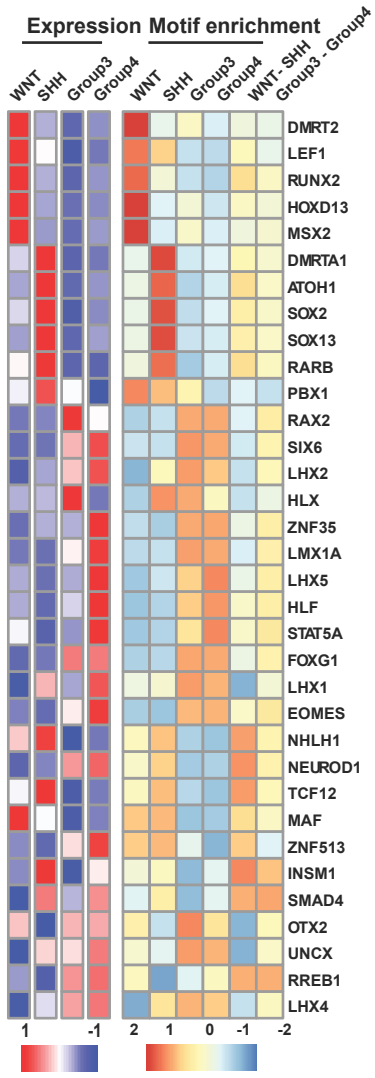


Extended Data Figure 6: Pathways regulated by super-enhancer associated transcription factors in medulloblastoma.

a

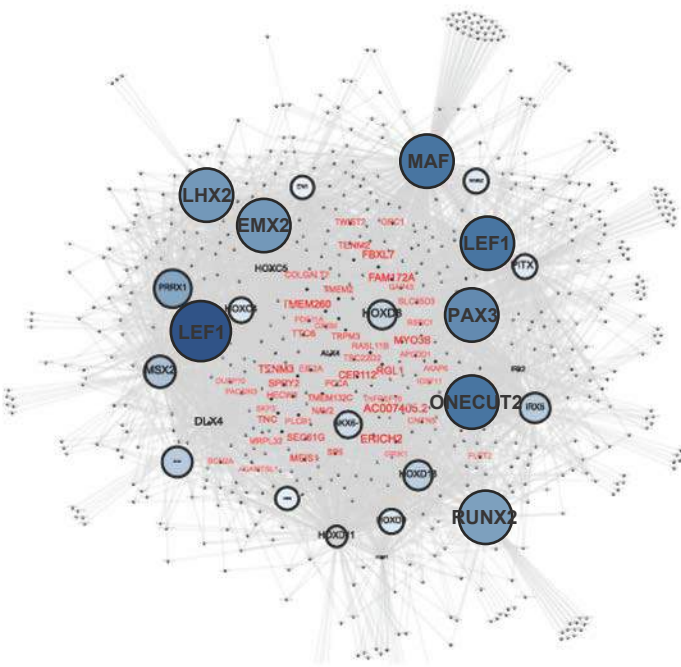


b

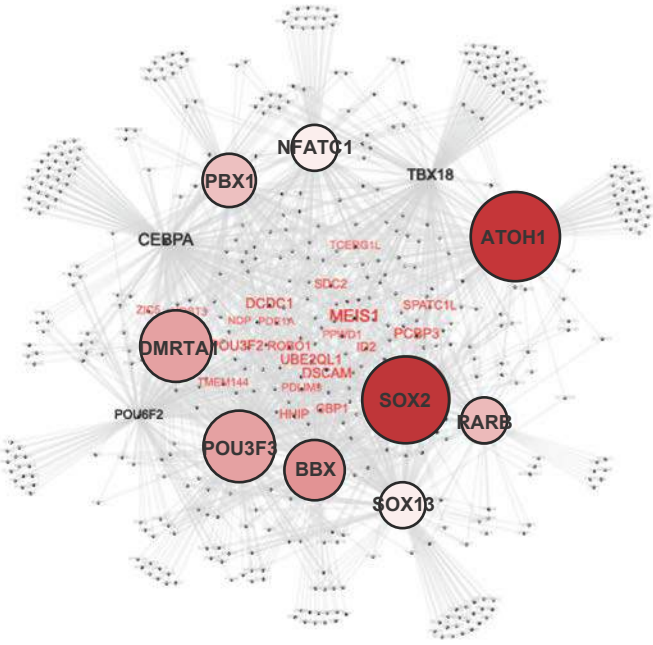


Extended Data Figure 7: Medulloblastoma subgroup-specific transcription factors and their associated target genes.

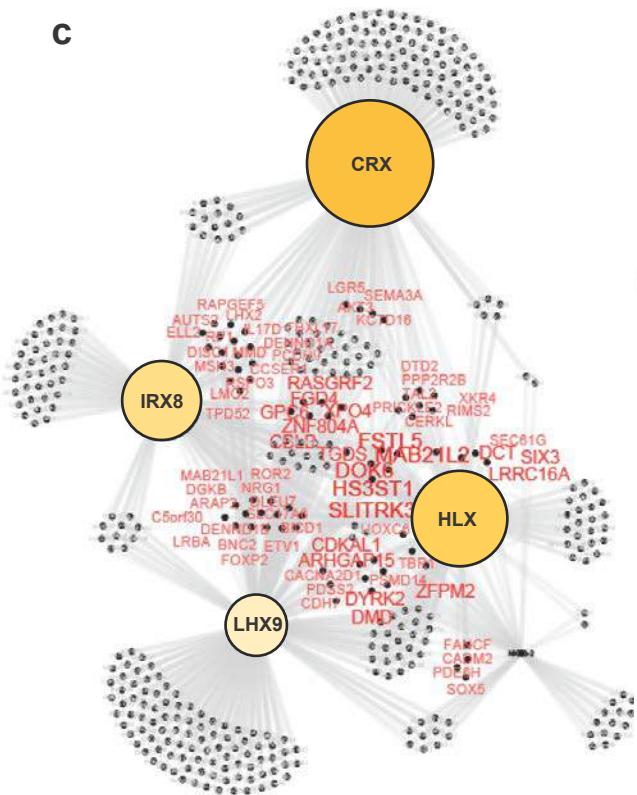
a



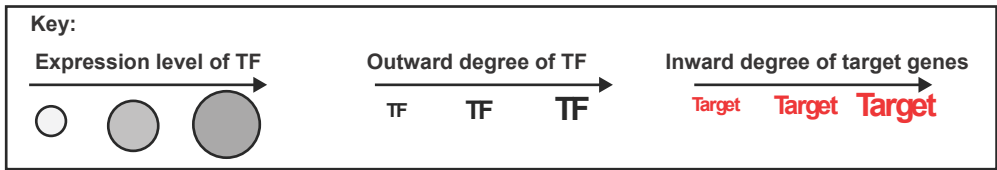
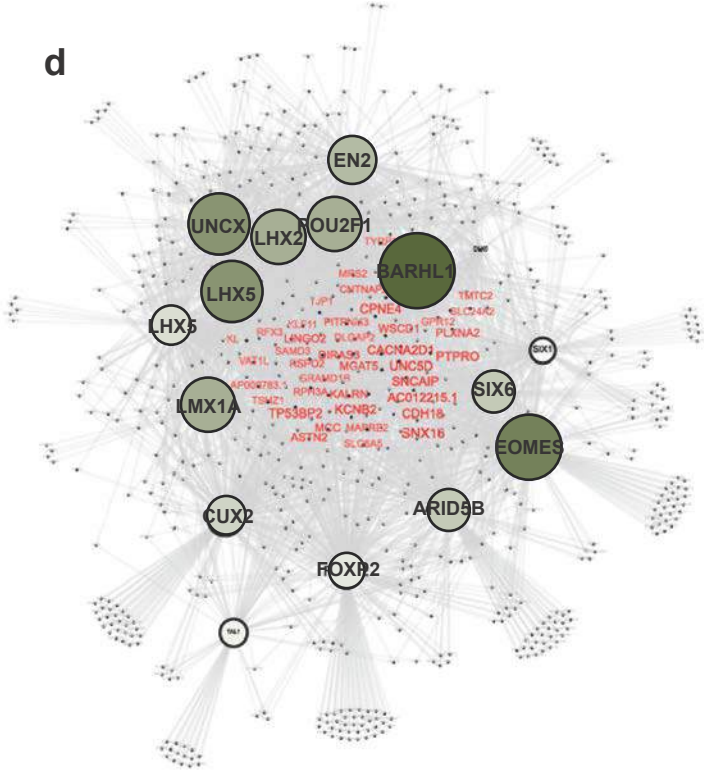
b



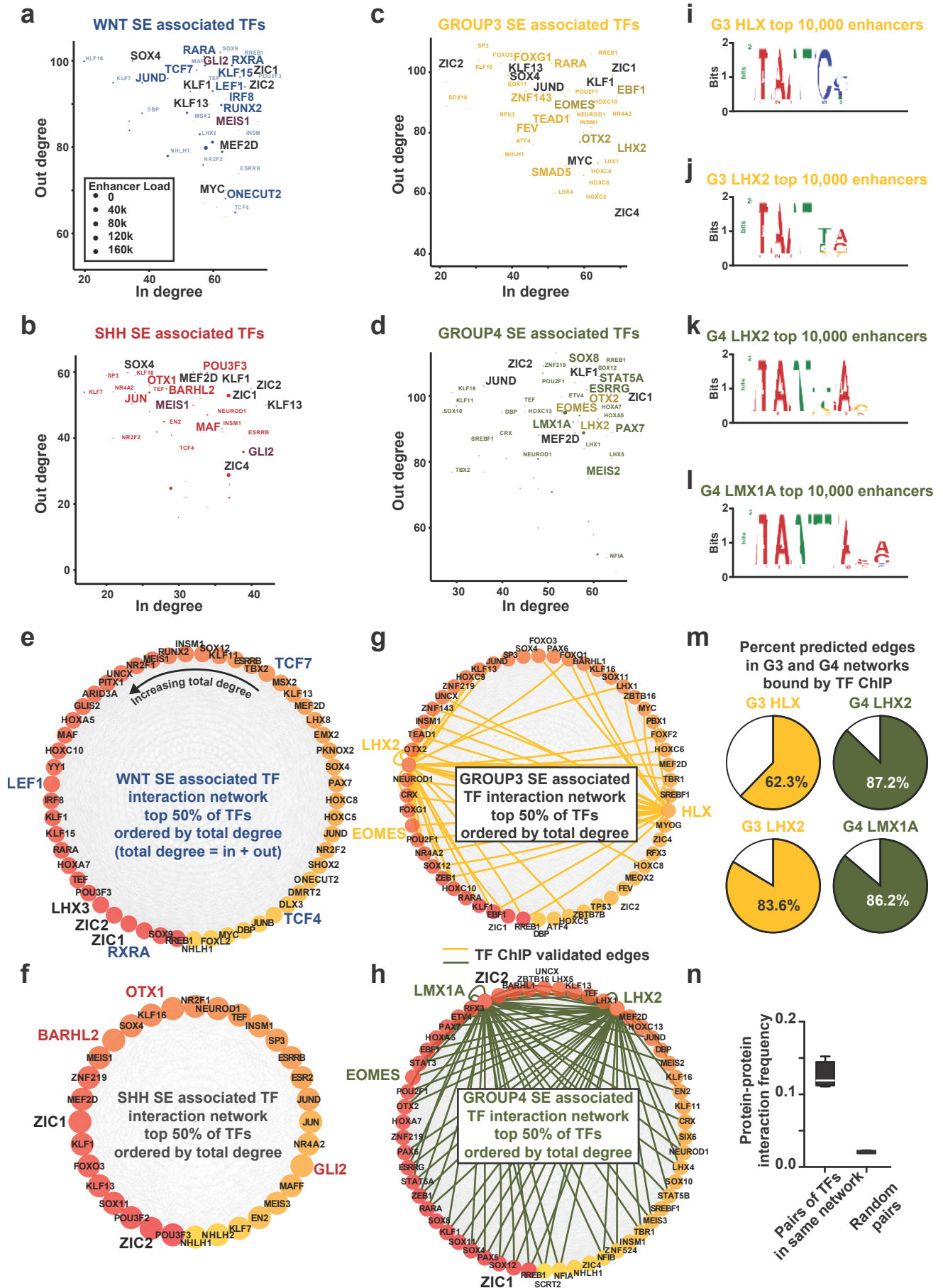
c



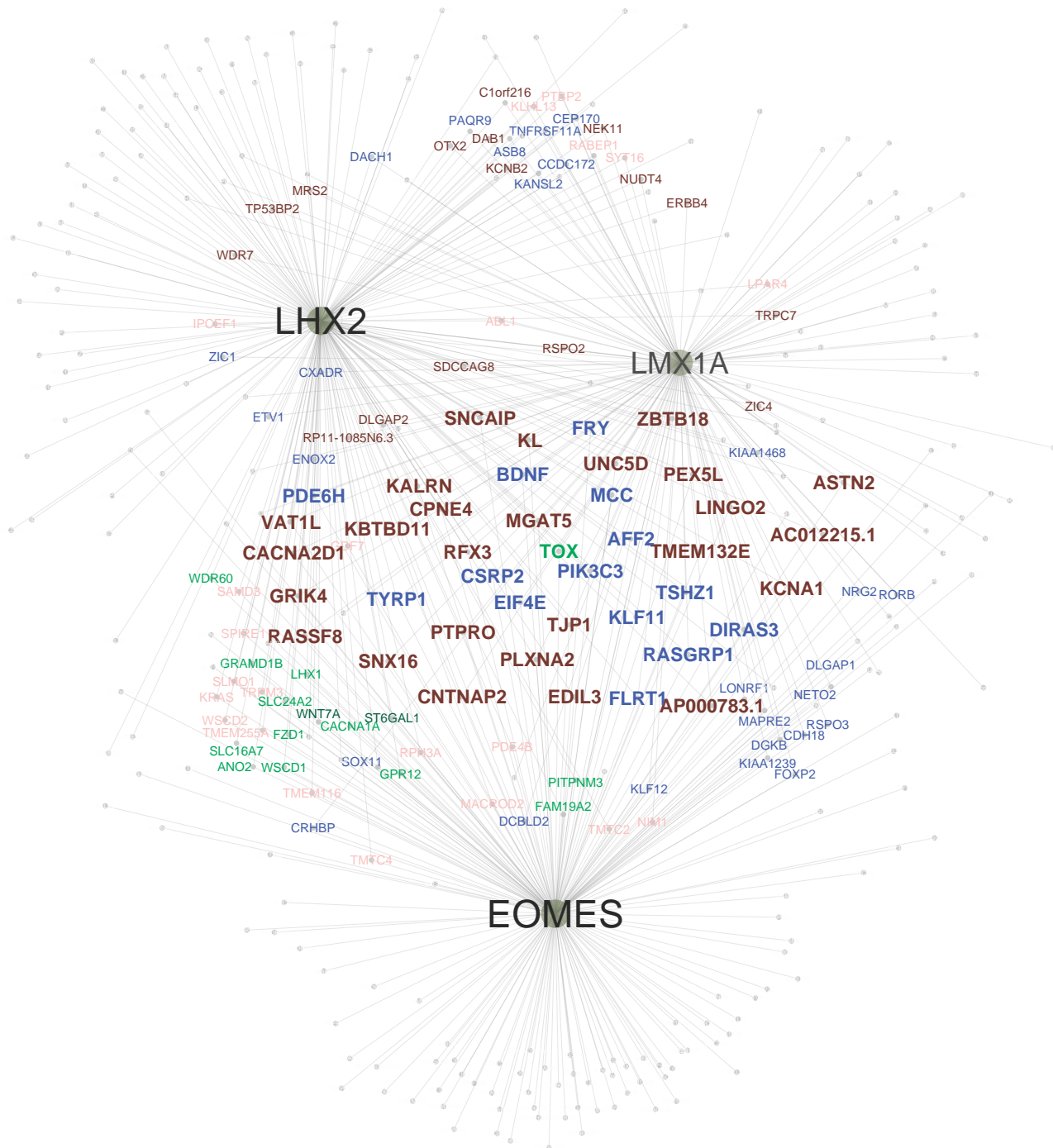
d



Extended Data Figure 8: Super-enhancers define medulloblastoma regulatory circuitry.



Extended Data Figure 9: LMX1A, EOMES and LHX2 are master transcriptional regulators of Group 4 medulloblastoma.



Target: Validated by both LMX1A and LHX2 ChIP
Target: Validated by only LMX1A ChIP
Target: Validated by only LHX2 ChIP
Target: Only prediction

Taming of the beast: shaping Myc-dependent amplification

Elmar Wolf¹, Charles Y. Lin², Martin Eilers¹, and David L. Levens³

¹Theodor Boveri Institute, Biocenter, and Comprehensive Cancer Center, University of Würzburg, Am Hubland, 97074 Würzburg, Germany

²Department of Medical Oncology, Dana Farber Cancer Institute, Harvard Medical School, Boston, MA 02115, USA

³Laboratory of Pathology, 10 Center Drive, Bethesda, MD 20892-1500, USA

Myc deregulation is a hallmark oncogenic event where overexpression of the transcription factor gives rise to numerous tumorigenic phenotypes. The complex consequences of Myc deregulation have prevented clear mechanistic interpretations of its function. A synthesis of recent experimental observations offers a consensus on the direct transcriptional function of Myc: when overexpressed, Myc broadly engages the established euchromatic cis-regulatory landscape of the cell, where the factor generally amplifies transcription. The level of Myc binding at target genes and the transcriptional output are differentially modulated by additional regulators, including Miz1. Targeting Myc oncogenic activity will require an understanding of whether amplification promotes tumorigenesis and the consequences of amplification in tumors adapted to oncogenic Myc.

Myc transcription in cancer

The intense interest in Myc proteins stems from their pervasive role in the genesis of human tumors. A large body of evidence has established that level of one out of three Myc proteins (c-Myc, N-Myc, or L-Myc) is enhanced and its expression released from its normally tight dependence on growth factors in a large fraction of all human tumors [1,2]. The three Myc genes are differentially expressed during development, but the proteins are functionally equivalent in most biological systems, allowing us to focus on c-Myc (called 'Myc' from here on) in this review [3]. Multiple experiments in transgenic models of human tumors show that this 'deregulated' expression of Myc proteins promotes tumorigenesis and that tumors generated by different oncogenes depend on elevated Myc levels [4]. Accordingly, several proof-of-principle studies suggest that targeting Myc proteins have considerable benefit for tumor therapy [5,6]. This hope awaits clinical confirmation, because therapies directed against Myc proteins have yet to enter the clinic. Myc proteins are nuclear proteins and, as such, may have several functions; however, there is consensus in the field that one major activity of Myc proteins is to regulate transcription [7]. This has

stimulated a vigorous debate about why Myc-dependent transcription is so important for tumorigenesis. Here, we review the current state of this debate.

The evolution of Myc

One of the best-understood Myc transcription factor networks is that of *Drosophila*. dMyc, a basic helix-loop-helix leucine zipper protein (bHLH-Zip), binds together with another bHLH-Zip protein, dMax, to target genes via a conserved sequence element termed an 'E-box' (CACGTG) and to activate transcription [8]. The dMyc antagonist dMnt, also pairs with dMax to repress transcription from the same DNA sequence [9]. Deletion of dMnt largely rescues the developmental defects of dMyc deletion, providing strong evidence that transcriptional activation is the critical biological function of dMyc [10]. Most target genes of dMyc and dMax encode proteins involved in RNA and protein synthesis [11]. Consistently, dMyc proteins stimulate cell growth, but not cell proliferation, and loss-of-function alleles show a 'minute' phenotype [8,12]. Transferring this model to mammalian tumorigenesis would suggest that the oncogenic activity of Myc is due to the deregulated and constitutive activation of its target genes. According to this model, sustained high levels of Myc in human tumors over-drive RNA biogenesis and protein translation, enabling growth factor-independent cell growth. Multiple observations are consistent with this model: for example, Myc-driven lymphomas, in contrast to their normal counterparts, rely on supraphysiological rates of protein translation to support growth [13].

Similar to *Drosophila* dMyc, mammalian Myc proteins, when dimerized with Max, are sequence-specific DNA-binding proteins that bind to E-boxes [7]. Unlike prokaryotic repressors that discriminate operator from nonoperator DNAs by approximately 10^{5-6} -fold, Max homodimers and, most likely, Myc/Max heterodimers have considerable affinity for variant E-boxes and even generic DNA [14]. Therefore, it is almost certain that Myc/Max heterodimers have non-negligible affinity for most promoters. Reflecting its continuum of association to targets, the intranuclear dynamics of Myc suggest engagement with intranuclear partners, indicating that Myc is globally distributed, is almost always bound directly or indirectly with chromatin, and is available to all active genes [15,16]. While broadly anticipated, there is currently only limited formal evidence that transcriptional activation is the critical oncogenic

Corresponding authors: Lin, C.Y. (Charles_lin@dfci.harvard.edu); Eilers, M. (martin.eilers@biozentrum.uni-wuerzburg.de); Levens, D.L. (levens@helix.nih.gov).

Keywords: Myc; cancer; transcription.

0962-8924/

© 2014 Elsevier Ltd. All rights reserved. <http://dx.doi.org/10.1016/j.tcb.2014.10.006>

function of Myc. One example is the finding that inactivation of Mga, a repressive partner protein of Max, occurs commonly, but mutually exclusively with focal amplification of the Myc gene in lung cancer, suggesting that Mga inactivation is pathologically equivalent to Myc overexpression in this entity [17].

Clues to how Myc regulates gene expression are provided in the list of co-activators it recruits to induce transcription: a conserved sequence in Myc (MycBoxII) binds the adaptor protein Transformation/transcription domain-associated protein (TRRAP) via TRRAP GCN5-containing histone acetylase complexes [18,19]. Myc also recruits the p300 histone acetylase and other histone-modifying enzymes to its target sites, although the requisite interaction surfaces on Myc are less well defined [20,21]. Myc also interacts with TATA box binding protein (TBP) [22] and the chromatin regulators Tip60 [23] and switch/sucrose nonfermentable (SWI/SNF) [24], and inhibits the H3 trimethyl K4 (H3K4Me3) demethylase dKDM5/LID [25]. The ability of Myc to interact with and recruit a multitude of general chromatin regulators is consistent with its global role in regulating chromatin structure because Myc activity has been broadly linked with large nuclei/nucleoli containing high levels of euchromatic and hyperacetylated chromatin [18,26].

Myc may also interact directly with the transcription apparatus. Most notably, the extreme amino-terminus of Myc binds cyclin T1 *in vitro* [27]. Cyclin T1 is part of the positive transcription elongation factor b (P-TEFb) elongation complex, which phosphorylates the C-terminal domain of RNA polymerase at serine 2 and thereby promotes the transition from promoter binding to productive elongation. The relevance of this finding stems from observations that Myc can stimulate transcription at a step after initiation of transcription and that RNA polymerase II accumulates in the body of transcribed genes after

activation of Myc [28–30]. Furthermore, ectopic expression of Myc globally enhances phosphorylation of RNA polymerase [30,31]. Together, these observations suggest that the release of RNA polymerase from a paused position is a key mechanism of transcriptional activation by Myc [30] (Figure 1). There is no doubt that other effectors of Myc remain to be defined. How Myc exploits these partners individually or in combination at any given promoter is not yet known.

The general amplifier model

The identification of Myc as a transcriptional activator raised the expectation that enumeration of the direct target genes of Myc would provide a list of critical downstream targets and biological processes that mediate the physiological and oncogenic functions of Myc. This expectation prompted a series of studies to identify the Myc-regulated genes by comparing RNA expression profiles and the genome-wide map of Myc-bound chromatin using microarray or next generation sequencing technology. Interrogation of a range of cell types surprisingly revealed mammalian Myc proteins at nearly all promoters in open chromatin [32]. This was not only true for genes transcribed by RNA polymerase II, but also for genes transcribed by RNA polymerases I and III (although rRNA promoters tend to bind less Myc compared with other promoters) [33,34]. For RNA polymerase II-transcribed genes, the presence of histone marks indicative of open chromatin, in particular H3K4Me3, highly correlated with Myc binding [35]. When overexpressed, Myc proteins also bound to many enhancers, again correlating with histone marks indicative of activity. Given that many genes encoding proteins involved in translation (e.g., ribosomal protein genes) are highly transcribed from promoters in CpG islands where E-boxes are more frequently found in an

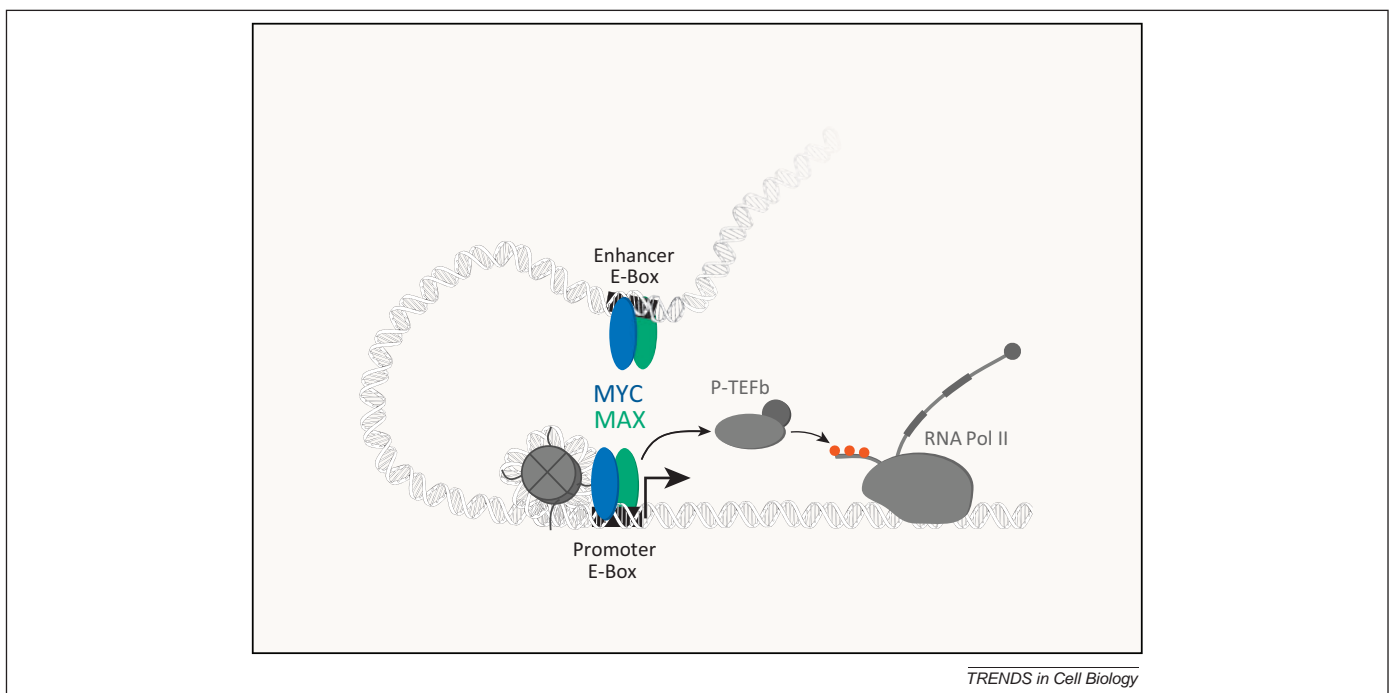


Figure 1. Schematic of transcription elongation promoting activity of MYC. MYC/MAX bind to E-box (CACGTG) sequences at enhancers and promoters and recruit the elongation factor complex positive transcription elongation factor b (P-TEFb), which promotes elongation in part by phosphorylating the C-terminal domain of RNA Polymerase II (RNA Pol II).

open chromatin conformation, these results parallel those obtained in *Drosophila*.

Collectively, these data have led to an exciting model in which Myc proteins act as general amplifiers that globally enhance transcription; the specificity and degree of amplification at individual genes is determined by the exact pattern of open promoters that pre-exists in a cell even before Myc activation [36,37]. In this model, the unique biological role of Myc stems from the ability to accelerate transcriptional activation (i.e., releasing a paused RNA polymerase from the promoter) rather than by specifying a particular program of gene expression [30]. Strong support for this model comes from the analysis of primary B cells [36]. Upon stimulation of resting B cells, Myc binds to all promoters of transcriptionally active genes in these cells and Myc binding follows the pattern of loading of RNA polymerase II that pre-exists in resting low Myc cells. In response to mitogen stimulation, there is a global increase in mRNA levels that depends on Myc, which has been confirmed by examining the mRNA levels of multiple individual genes. There are indications that the 'global amplifier' model operates not only in primary cells, but also in tumors. Comparing normal B cells with Myc-driven B cell lymphomas revealed a strong increase in total cellular mRNA content in lymphomas [38]. ChIP sequencing shows that Myc binds to 90% of all open promoters in lymphomas; an easy explanation might be that Myc broadly enhances expression of the genes to which it binds and this increases cellular mRNA content. Similarly, the comparison of human tumor cell lines with different Myc levels suggests that Myc-driven amplification accounts for differences in mRNA content between different tumor cells [37].

According to a strict amplifier model, the direct effect of Myc on promoters is always positive. The effect of Myc is not equally strong for each gene because promoters and relevant enhancers differ in their affinity for Myc: promoter binding dictates the differences in response. Moreover, the overall promoter response to Myc is not directly proportional to the amount Myc recruited there. Furthermore, at high and oncogenic levels, Myc 'invades' enhancers and promoters, enabling the pathological regulation of genes that bind little Myc at physiological levels [37–39]. Therefore, the general amplifier model can account for the observation that oncogenic levels of Myc regulate a specific set of genes in particular tumors [40]. The model can also account for apparent Myc-dependent repression. Specifically, if expression of most mRNAs is amplified and, therefore, if total mRNA content increases in a cell upon Myc stimulation, then the relative amount of mRNAs transcribed from genes that have low-affinity promoters and, thus, are poorly activated genes will decrease and, depending on the mode of normalization, these genes will appear repressed [41]. Hence, whether the general amplifier model can account for Myc-dependent repression is intimately tied to the question of whether Myc induces a general increase in cellular RNA levels and, by inference, whether cells grow as a result of Myc activation: if cells grow, seemingly repressed genes may in fact be low-affinity Myc targets that are relatively 'left behind' [41]. Myc drives both growth and proliferation of mammalian cells, unlike in *Drosophila* [42]. Given that cell proliferation and

division reduce cell size, some of the apparent Myc-dependent repression may reflect the postmitotic partition of cellular contents compared with nondividing cells; therefore, a complete description of amplification will be sensitive to cell cycle parameters. Furthermore, if Myc acts at transcription, then gauging Myc action from mRNA abundance is imprecise because mRNA synthesis becomes conflated with mRNA half-lives, and cell cycle parameters. Yet, this too becomes even more complicated because the factors that regulate mRNA stability and the cell cycle may themselves be important direct or indirect Myc targets.

An important aspect of the amplifier model is the postulate that, in any given cell type, all transcription initiating genes are potential targets of Myc: individual promoters differ quantitatively in their affinity for Myc, but no sharp cut-off discriminates Myc targets from nontargets. Occupancy at each promoter changes as Myc concentrations vary and this change defines the degree of the transcriptional response. We suggest that there is a continuum of activity as Myc flickers on and off of weakly bound, weakly expressed promoters, but stays longer or more frequently at high output promoters (Figure 2). This view of Myc as a general regulator capable of interacting with all active promoters has implications for the way that ChIP sequencing data need to be interpreted, because it suggests that cut-offs that are introduced by analysis (e.g., peak-calling) programs generate artificial distinctions between target and nontarget genes.

This quantitative view also suggests that, in some experimental settings, the response of some genes to Myc plateaus as occupancy by Myc at promoters and enhancers and corresponding transcriptional output is saturated. Whereas Myc abundance is low in most, but not all primary cells (luminal cells in mammary ducts are a notable exception), recent estimates for Myc in tumor cells appear high enough to allow the saturation of some promoters [37]. A recent study provides evidence that high-affinity promoters are Myc saturated in proliferating cells and, therefore, that further increases in Myc only increase occupancy and gene expression at low-affinity promoters [39]. As a result, gene expression patterns that discriminate cells with oncogenic Myc levels from normally proliferating cells are different from the gene expression changes that occur as Myc-levels increase during the physiological transition from quiescence to proliferation.

These considerations allow the conclusion that, even within the framework of the general amplifier model, the observed effects of Myc on gene expression depend on: (i) the precise Myc levels that are being compared; (ii) whether cells grow upon Myc activation; and (iii) the precise pattern of ongoing transcription that determines which genes are accessible to Myc.

Direct and indirect transcriptional repression

In many studies, almost as many genes are downregulated by Myc as are upregulated, evoking the notion that Myc can act as a repressor [38,43]. Setting aside pseudodownregulation arising from normalization issues (above), such downregulation can stem from a direct and context-dependent repressive function of Myc that is unmasked by factors bound locally at the regulatory sequences of

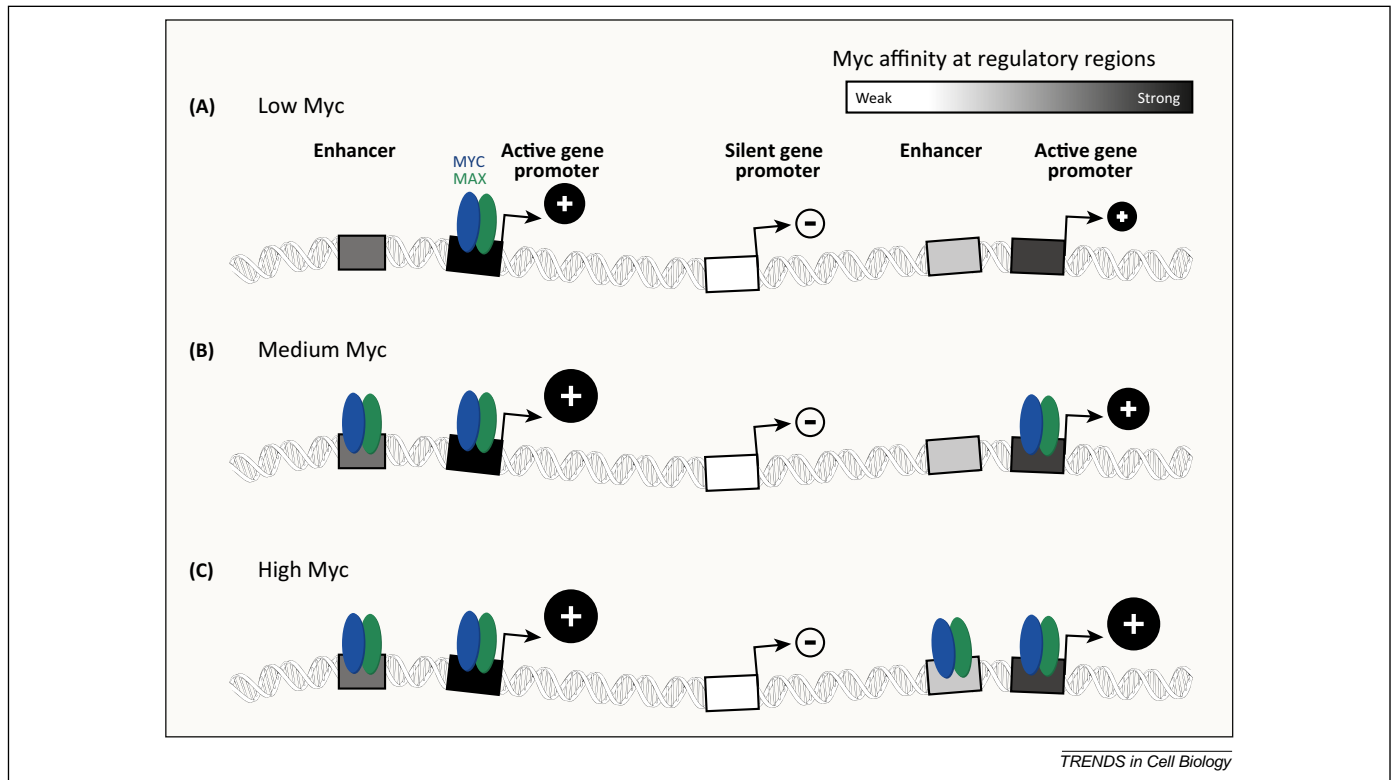


Figure 2. Schematic of MYC genomic binding at (A) low, (B) medium, and (C) high concentrations of the factor. *Cis*-regulatory elements (boxes) are shaded by their affinity for Myc. Myc transcriptional activity at genes is depicted as a circle sized by the impact of Myc.

particular target genes. For example, Myc blunts the induction of the cyclin-dependent kinase 4 inhibitor B (*CDKN2B*) and *CDKN1A* genes in response to transforming growth factor (TGF)- β signaling by a direct interaction with the Miz1 and Smad3 proteins at both promoters [44,45]. Alternatively, repression can be indirect; as a universal amplifier, Myc will increase the expression of repressive transcriptional and chromatin components. As repressors are upregulated, downregulation of sets of targets may ensue as the system seeks a new steady state. For example, Myc-upregulated phosphatase and tensin homolog (*PTEN*) inactivates Akt, which disinhibits enhancer of zeste homolog 2 (*Ezh2*), promoting widespread polycomb repressive complex 2 (*PRC2*)-mediated repression [46]. Furthermore, miRNAs, such as miR17-92 that represses SIN3 transcription regulator family member B (*Sin3b*), HMG-box transcription factor 1 (*Hbp1*), suppressor of variegation 4-20 homolog 1 (*Suv420h1*), and B cell translocation gene 1 (*Btg1*) to regulate chromatin structure as well as the apoptosis facilitator *Bim* [47], are repressive mediators of Myc action. Direct and indirect mechanisms may become entangled as feedforward and feedback arms of genetic circuits adjust to new conditions. In principle, the dynamics of the temporal profile of the transcriptome could help to discriminate direct from indirect regulation, because changes requiring newly synthesized protein intermediaries are expected to be delayed relative to the induction of Myc protein. However, few studies have had the temporal resolution to discriminate direct versus indirect targets. Given that they are translation independent, miRNAs and other noncoding RNAs are likely to act after only a brief delay. This rapid onset of activity is likely to

hinder the discrimination of the direct and indirect effects of Myc.

Shaping transcriptional amplification

Transcriptional amplification and cell growth induced by Myc cannot continue indefinitely and unopposed. Therefore, mechanisms must exist that adjust transcriptional amplification to available metabolic resources and that provide feedback from the physiological status of a cell to Myc activity. Consequently, supraphysiological levels of Myc would be expected to elicit either compensatory measures or, if they fail, promote cell death. As Myc saturates its strongest and most highly expressed sites (these being most likely to be physiological targets), it may pathologically spill over onto other promoters and enhancers, increasing their activity and overall cellular RNA production, provided that the cell can marshal sufficient resources to augment net transcription.

There is evidence for feedback mechanisms that limit Myc-dependent transactivation operating at both physiological and supraphysiological levels. The apoptosis elicited by overexpression provides an example of an upper-bound limit for Myc levels [48]. As another example, the ribosomal protein L11, encoded by a direct target gene of Myc, inhibits Myc-dependent transactivation and expression [49,50]. Supraphysiological levels of Myc induce expression of the Arf tumor suppressor protein, which in turn interacts with Myc and inhibits Myc-dependent transactivation [51,52]. One broadly acting mechanism that limits transcriptome amplification driven by supraphysiological Myc is the recruitment of the zinc finger protein Miz1 at many promoters [53]. In primary cells, and in the

absence of high levels of Myc, Miz1 is a highly sequence-specific transcription factor that activates a relatively small number of targets that share an extended consensus sequence and that control autophagy [54]. As Myc levels rise to supraphysiological levels, Miz1 joins Myc via a protein-protein interaction at a large fraction of promoters that then decreases output [39]. Miz1 is unstable and continuously degraded by the Huwe1 ubiquitin ligase [55]; upon inhibition of Huwe1, Miz1 broadly accumulates at Myc-bound promoters, blunts activation, and enhances repression by Myc [55,56]. Interestingly, the Arf protein binds to, and inhibits, Huwe1 and promotes association of Myc with Miz1 [57,58], strongly suggesting that Arf and Miz1 are part of a common stress response to oncogenic Myc levels.

A second mechanism that is likely to limit and shape Myc amplification is competition between Myc and other bHLH-Zip dimers for binding at E-boxes and perhaps at other sites (Figure 3). Myc-Max operates against Max homodimers as well as heterodimers of Max with repressive members of the bHLH-Zip family (Mxd1-4, Mnt, etc) [9–11]. The degree to which the levels of these other complexes alter the physical distribution and activity of Myc at E-box versus non-E-box promoters remains to be rigorously evaluated. The specialized regulation of these

other E-box-binding proteins (such as Mondo) have the capacity to tune the Myc response toward or away from cellular processes, such as metabolism [59] or circadian rhythms via coupling with proteins such as CLOCK [60].

Almost certainly, steady-state patterns of gene expression observed after Myc expression do not only reflect the direct action of Myc, but are also due to secondary effects of proteins or RNAs encoded by Myc target genes that feed back on gene expression [38]. In a rapidly growing cell, such as a B cell becoming activated from the naïve state, increasing synthesis of macromolecules is required to satisfy a growing demand for the transcription machinery and other components required to activate genes. Examples for such indirect effects are the induction of the Gen5 histone acetylase that mediates a global opening of chromatin upon Myc expression and enhanced expression of phosphoribosyl-pyrophosphate synthetase 2 (PRPS2), which promotes the enhanced nucleotide biosynthesis of Myc-driven tumors [18,26,61]. At the same time, rapid growth and enhanced global transcription may induce the redeployment of limiting components of the gene expression machinery to more or less active transcription start sites. Under conditions of limiting gene expression components, increasing Myc at strongly expressed promoters might recruit transcription

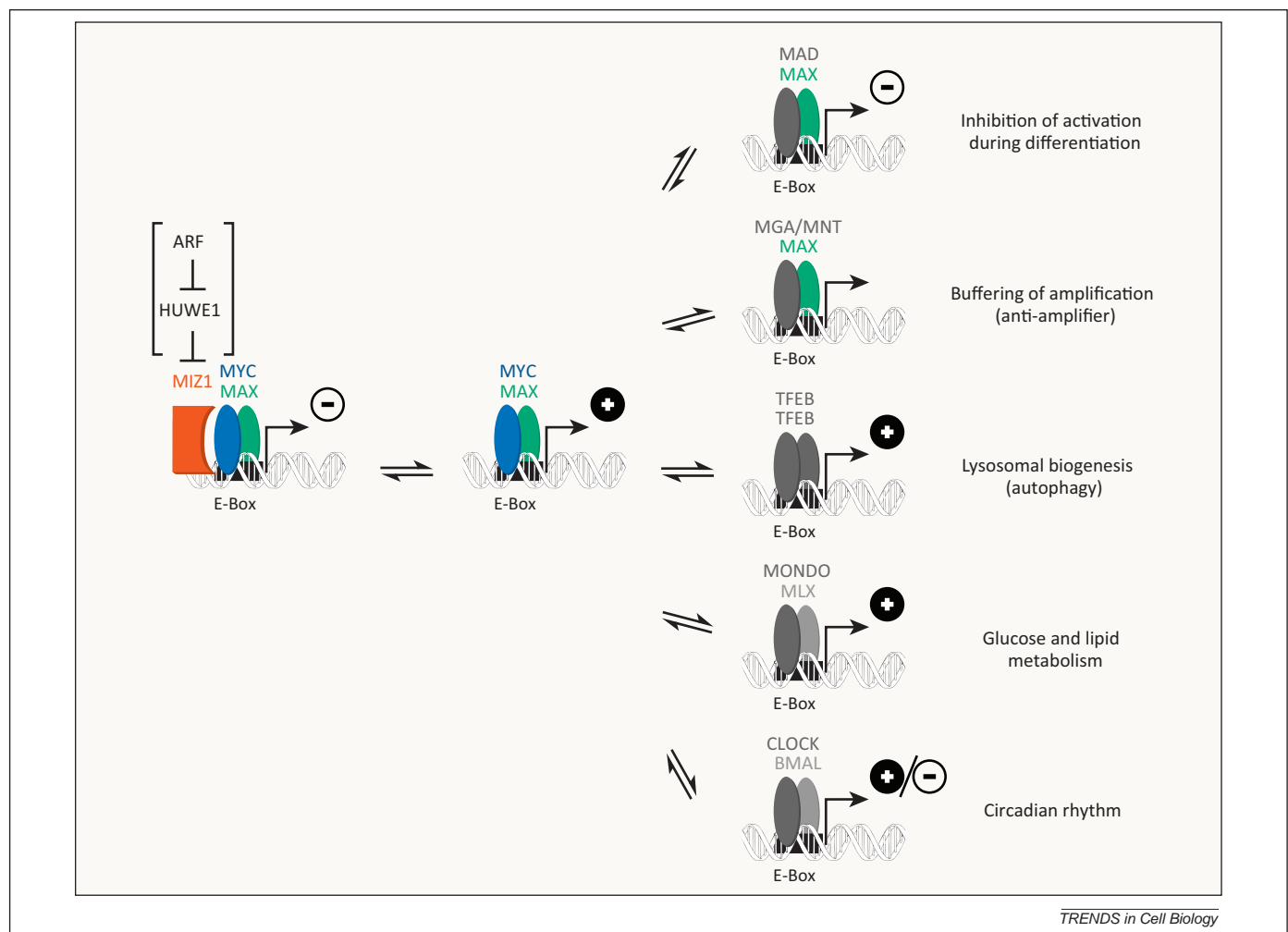


Figure 3. Schematic showing the dynamic occupancy of E-box sites by Myc and other transcriptional regulators. Multiple basic helix-loop-helix (bHLH) transcription factor pairings compete for binding at E-box sites. The net positive or negative transcriptional consequence of regulator binding at E-boxes is depicted. For definitions of abbreviations, please see the main text.

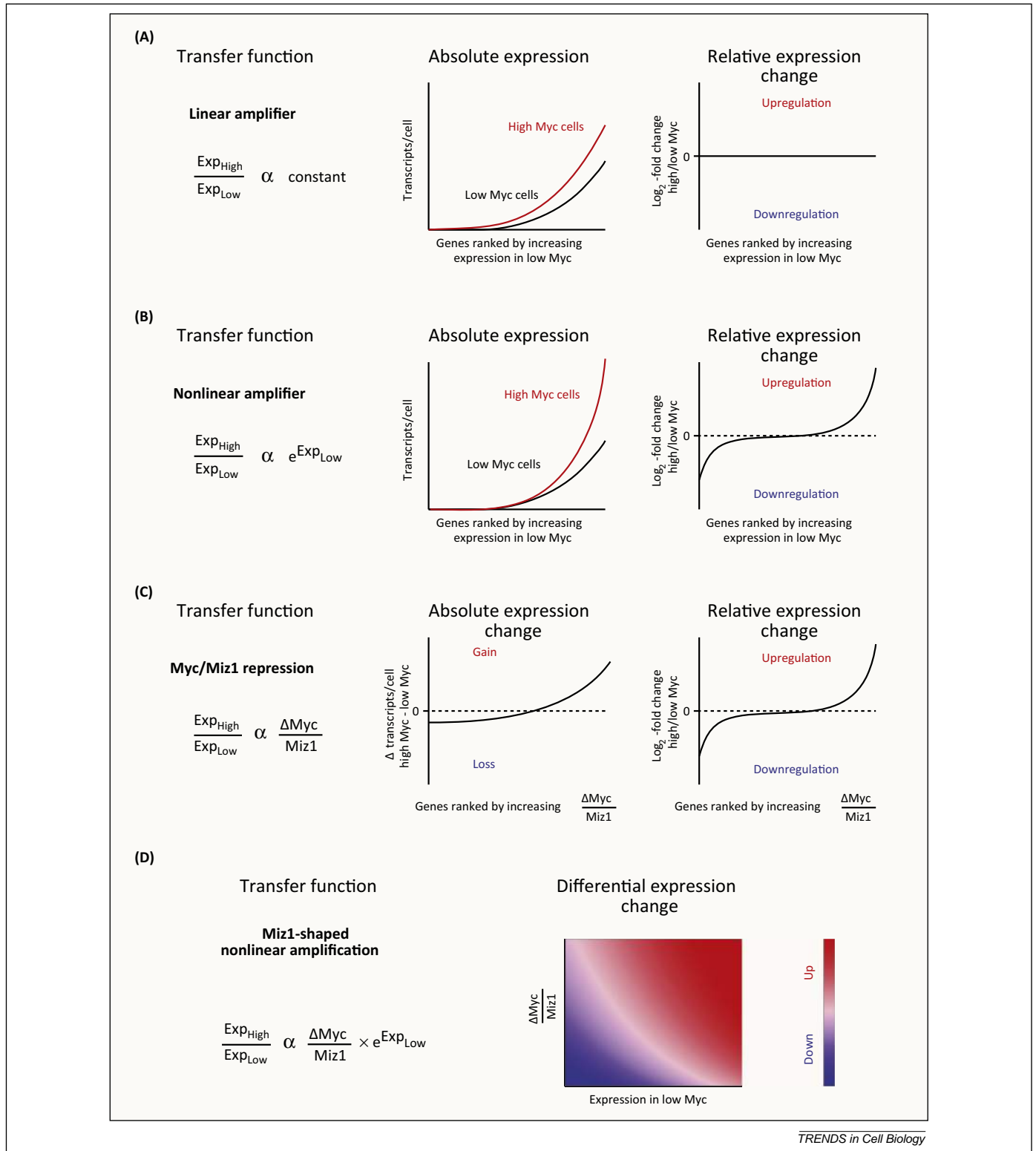


Figure 4. Schematic of Myc transfer functions. Transfer functions are shown providing the relation between expression changes at genes as a function of various parameters as measured either by absolute or relative change in expression. **(A)** A linear amplifier transfer function where the change in expression in high versus low Myc conditions is constant across all transcriptionally active genes. **(B)** A nonlinear amplifier transfer function where the change in expression in high versus low Myc conditions is proportional to the exponent of the expression in low Myc conditions. **(C)** A Myc/Miz1 repression transfer function where the change in expression is proportional to the ratio of ΔMyc binding divided by Miz1 binding. **(D)** A combined Miz1-shaped nonlinear amplifier model that combines the transfer functions in (B) and (C). A 2D heatmap is provided showing the relative change in expression as a function of both the ratio of ΔMyc binding divided by Miz1 binding (y-axis) and the initial expression in low Myc conditions (x-axis).

Review

machinery otherwise assigned to weakly transcribed genes. Such diversion would yield the upregulation of some genes with the downregulation of others. This repression by redistribution of the transcriptional machinery has been recently observed during nuclear factor (NF)- κ B activation in endothelial cells [62].

In principle, other mechanisms may act to counterbalance transcriptome amplification. For example, in yeast, rates of RNA synthesis and RNA degradation are coupled [63]. Mutations and strategies that alter the levels of one elicit compensatory changes in the other. Additional amplification counteracting pressures may arise from rate limiting levels of translation initiation in tumors. Notably, disruption of the translation initiation factor eukaryotic translation initiation factor 4 (eIF4F) is synthetic lethal in tumors with deregulated Myc, suggesting that the high levels of mRNA output need to be supported by high levels of protein expression, perhaps exposing an orthogonal vulnerability arising due to amplification [64]. For RNA levels to rise globally in response to MYC deregulation, these compensatory countermeasures may need to be defeated or overwhelmed.

Concluding remarks

Deregulated in tumors, Myc acts as a universal regulator of the pre-existing gene expression program of the cell. Whether amplification alone provides a sufficient oncogenic impulse or whether Myc-dependent repressive mechanisms are required for Myc-driven tumorigenesis warrants further investigation. Simply, as a universal regulator, mutations in other oncogenes and tumor suppressors must first specify particular genes to be turned on or off, and Myc then develops the new gene expression program. This model is also consistent with data in iPS reprogramming, where Myc overexpression increases the efficiency of an embryonic stem cell specifying Octamer 4/SRY (sex determining region Y)-box 2/Kruppel-like factor 4 (Oct4/Sox2/Klf4) transcription factors [65]. Alternatively, the pathways for growth, proliferation, apoptosis, and neoplastic metabolism do not scale linearly (i.e., increasing the components of these pathways drives them across thresholds that gate their activity as a step function). In this situation, malignant behavior would manifest as an emergent property explainable by the control theory (Box 1) and architecture of subsystems and networks whose components are upregulated by Myc.

Although predominantly an amplifier of transcription, context-specific conditions and constraints at individual genes modulate Myc transcriptional output and response. To elucidate the molecular mechanism of Myc-driven transcriptome amplification, a better description of its transfer function (the function describing how the Myc transcriptional effect depends on initial parameters at any gene; i.e., the input–output curve) will be required to account for its physiological and pathological activities. If proportional and linear, for example, all Myc targets will be upregulated equivalently, and any changes in the relative expression of particular genes would demand parallel changes in the levels of the gene-specific factors that differentially up- or downregulate these targets (Figure 4A). However, if the transfer function is nonlinear, as proposed in [66], then different zones across the expression spectrum will be

Box 1. Control theory

Control theory is a dynamic analysis of network behavior as modeled by the effect of inputs and their consequent feedback on system output. In engineering, this can describe how different components affect the output of a system. For instance, a compressor either boosts or dampens signal depending on initial input signal. A reverb module would apply a delay to an input signal before entering it back into the system, creating a recursive feedback loop. An amplifier increases signal by an amount relative to the initial input signal. In each of these examples, the transformations are surmised through the transfer function: a mathematical representation of the relation between input and output. Thus, a control theory analysis of Myc examines the consequence of adding Myc to the transcriptional system. The Myc transfer function describes the transcriptional output of Myc activity as a function of the initial transcription parameters.

disproportionately regulated. If highly expressed genes are preferentially amplified, then a Myc signature may emerge comprising genes that are highly expressed across many tissues (Figure 4B). Of course, such amplification cannot continue indefinitely and unopposed; supraphysiological levels of Myc are expected to elicit either compensatory measures or cell death (Figure 4C). Increasing amplification of all genes demands that the cell can marshal sufficient resources to augment net transcription. In the presence of limiting materials, the competition between promoters may modify the transfer function from one that supports only universal amplification to one that allows for repression at those promoters deprived of limiting factors that have been deployed to support the expression of other targets. In this scheme, repression (e.g., Miz1-dependent repression) reflects feedback control that responds to the unbalanced and excessive Myc-enforced expression of other targets (Figure 4D).

Universal activation by Myc does not preclude the functional emergence of preferred and, hence, specific targets. Moreover, the preferential up- or downregulation of specific genes that occurs as tumors achieve homeostasis in high Myc conditions may underlie the ability of Myc to act as one of the rare universal oncogenes capable of promoting tumorigenesis in a wide variety of tissues. Only when experiments challenge models that make quantitative, precise, and testable predictions will a durable consensus on the role of Myc emerge. Beyond having heuristic value as an organizing framework for diverse observations, the universal nonlinear amplifier model may yet account for quantitative differences in gene expression between cell states in health and disease.

References

- Dang, C.V. (2012) MYC on the path to cancer. *Cell* 149, 22–35
- Meyer, N. and Penn, L.Z. (2008) Reflecting on 25 years with MYC. *Nat. Rev. Cancer* 8, 976–990
- Kc, W. *et al.* (2014) L-Myc expression by dendritic cells is required for optimal T-cell priming. *Nature* 507, 243–247
- Gabay, M. *et al.* (2014) MYC activation is a hallmark of cancer initiation and maintenance. *Cold Spring Harb. Perspect. Med.* 4, a014241
- Soucek, L. *et al.* (2008) Modelling Myc inhibition as a cancer therapy. *Nature* 455, 679–683
- Soucek, L. *et al.* (2013) Inhibition of Myc family proteins eradicates KRas-driven lung cancer in mice. *Genes Dev.* 27, 504–513
- Eilers, M. and Eisenman, R.N. (2008) Myc's broad reach. *Genes Dev.* 22, 2755–2766
- Gallant, P. *et al.* (1996) Myc and Max homologs in *Drosophila*. *Science* 274, 1523–1527

- 9 Loo, L.W. *et al.* (2005) The transcriptional repressor dMnt is a regulator of growth in *Drosophila melanogaster*. *Mol. Cell. Biol.* 25, 7078–7091
- 10 Pierce, S.B. *et al.* (2008) *Drosophila* growth and development in the absence of dMyc and dMnt. *Dev. Biol.* 315, 303–316
- 11 Orian, A. *et al.* (2003) Genomic binding by the *Drosophila* Myc, Max, Mad/Mnt transcription factor network. *Genes Dev.* 17, 1101–1114
- 12 Johnston, L.A. *et al.* (1999) *Drosophila* myc regulates cellular growth during development. *Cell* 98, 779–790
- 13 Barna, M. *et al.* (2008) Suppression of Myc oncogenic activity by ribosomal protein haploinsufficiency. *Nature* 456, 971–975
- 14 Sauve, S. *et al.* (2007) The mechanism of discrimination between cognate and non-specific DNA by dimeric b/HLH/LZ transcription factors. *J. Mol. Biol.* 365, 1163–1175
- 15 Rosales, T. *et al.* (2013) Partition of Myc into immobile vs. mobile complexes within nuclei. *Sci. Rep.* 3, 1953
- 16 Izeddin, I. *et al.* (2014) Single-molecule tracking in live cells reveals distinct target-search strategies of transcription factors in the nucleus. *Elife* Published online June 12, 2014, <http://dx.doi.org/10.7554/eLife.02230>
- 17 The Cancer Genome Atlas Research Network (2014) Comprehensive molecular profiling of lung adenocarcinoma. *Nature* 511, 543–550
- 18 McMahon, S.B. *et al.* (2000) The essential cofactor TRRAP recruits the histone acetyltransferase hGCN5 to c-Myc. *Mol. Cell. Biol.* 20, 556–562
- 19 McMahon, S.B. *et al.* (1998) The novel ATM-related protein TRRAP is an essential cofactor for the c-Myc and E2F oncoproteins. *Cell* 94, 363–374
- 20 Ullius, A. *et al.* (2014) The interaction of MYC with the trithorax protein ASH2L promotes gene transcription by regulating H3K27 modification. *Nucleic Acids Res.* 42, 6901–6920
- 21 Vervoorts, J. *et al.* (2003) Stimulation of c-MYC transcriptional activity and acetylation by recruitment of the cofactor CBP. *EMBO Rep.* 4, 484–490
- 22 Hateboer, G. *et al.* (1993) TATA-binding protein and the retinoblastoma gene product bind to overlapping epitopes on c-Myc and adenovirus E1A protein. *PNAS* 90, 8489–8493
- 23 Frank, S.R. *et al.* (2003) MYC recruits the TIP60 histone acetyltransferase complex to chromatin. *EMBO Rep.* 4, 575–580
- 24 Cheng, S.W. *et al.* (1999) c-MYC interacts with IN1/hSNF5 and requires the SWI/SNF complex for transactivation function. *Nat. Genet.* 22, 102–105
- 25 Secombe, J. *et al.* (2007) The Trithorax group protein Lid is a trimethyl histone H3K4 demethylase required for dMyc-induced cell growth. *Genes Dev.* 21, 537–551
- 26 Knoepfler, P.S. *et al.* (2006) Myc influences global chromatin structure. *EMBO J.* 25, 2723–2734
- 27 Eberhardy, S.R. and Farnham, P.J. (2002) Myc recruits P-TEFb to mediate the final step in the transcriptional activation of the cad promoter. *J. Biol. Chem.* 277, 40156–40162
- 28 Eberhardy, S.R. and Farnham, P.J. (2001) c-Myc mediates activation of the cad promoter via a post-RNA polymerase II recruitment mechanism. *J. Biol. Chem.* 276, 48562–48571
- 29 Bouchard, C. *et al.* (2007) FoxO transcription factors suppress Myc-driven lymphomagenesis via direct activation of Arf. *Genes Dev.* 21, 2775–2787
- 30 Rahl, P.B. *et al.* (2010) c-Myc regulates transcriptional pause release. *Cell* 141, 432–445
- 31 Cowling, V.H. and Cole, M.D. (2007) The Myc transactivation domain promotes global phosphorylation of the RNA polymerase II carboxy-terminal domain independently of direct DNA binding. *Mol. Cell. Biol.* 27, 2059–2073
- 32 Chen, X. *et al.* (2008) Integration of external signaling pathways with the core transcriptional network in embryonic stem cells. *Cell* 133, 1106–1117
- 33 Gomez-Roman, N. *et al.* (2003) Direct activation of RNA polymerase III transcription by c-Myc. *Nature* 421, 290–294
- 34 Grandori, C. *et al.* (2005) c-Myc binds to human ribosomal DNA and stimulates transcription of rRNA genes by RNA polymerase I. *Nat. Cell Biol.* 7, 311–318
- 35 Guccione, E. *et al.* (2006) Myc-binding-site recognition in the human genome is determined by chromatin context. *Nat. Cell Biol.* 8, 764–770
- 36 Nie, Z. *et al.* (2012) c-Myc is a universal amplifier of expressed genes in lymphocytes and embryonic stem cells. *Cell* 151, 68–79
- 37 Lin, C.Y. *et al.* (2012) Transcriptional amplification in tumor cells with elevated c-Myc. *Cell* 151, 56–67
- 38 Sabo, A. *et al.* (2014) Selective transcriptional regulation by Myc in cellular growth control and lymphomagenesis. *Nature* 511, 488–492
- 39 Walz, S. *et al.* (2014) Activation and repression by oncogenic Myc shape tumour-specific gene expression profiles. *Nature* 511, 483–487
- 40 Yustein, J.T. *et al.* (2010) Induction of ectopic Myc target gene JAG2 augments hypoxic growth and tumorigenesis in a human B-cell model. *Proc. Natl. Acad. Sci. U.S.A.* 107, 3534–3539
- 41 Loven, J. *et al.* (2012) Revisiting global gene expression analysis. *Cell* 151, 476–482
- 42 Beier, R. *et al.* (2000) Induction of cyclin E-cdk2 kinase activity, E2F-dependent transcription and cell growth by Myc are genetically separable events. *EMBO J.* 19, 5813–5823
- 43 van Riggelen, J. *et al.* (2010) The interaction between Myc and Miz1 is required to antagonize TGFbeta-dependent autocrine signaling during lymphoma formation and maintenance. *Genes Dev.* 24, 1281–1294
- 44 Seoane, J. *et al.* (2001) TGFbeta influences Myc, Miz-1 and Smad2 to control the CDK inhibitor p15INK4b. *Nat. Cell Biol.* 3, 400–408
- 45 Staller, P. *et al.* (2001) Repression of p15INK4b expression by Myc through association with Miz-1. *Nat. Cell Biol.* 3, 392–399
- 46 Kaur, M. and Cole, M.D. (2013) MYC acts via the PTEN tumor suppressor to elicit autoregulation and genome-wide gene repression by activation of the Ezh2 methyltransferase. *Cancer Res.* 73, 695–705
- 47 Li, Y. *et al.* (2014) MYC through miR-17-92 suppresses specific target genes to maintain survival, autonomous proliferation, and a neoplastic state. *Cancer Cell* 26, 262–272
- 48 Evan, G.I. *et al.* (1992) Induction of apoptosis in fibroblasts by c-myc protein. *Cell* 69, 119–128
- 49 Dai, M.S. *et al.* (2007) Inhibition of c-Myc activity by ribosomal protein L11. *EMBO J.* 26, 3332–3345
- 50 Challagundla, K.B. *et al.* (2011) Ribosomal protein L11 recruits miR-24/miRISC to repress c-Myc expression in response to ribosomal stress. *Mol. Cell. Biol.* 31, 4007–4021
- 51 Qi, Y. *et al.* (2004) p19ARF directly and differentially controls the functions of c-Myc independently of p53. *Nature* 431, 712–717
- 52 Zindy, F. *et al.* (1998) Myc signaling via the ARF tumor suppressor regulates p53-dependent apoptosis and immortalization. *Genes Dev.* 12, 2424–2433
- 53 Wiese, K.E. *et al.* (2013) The role of MIZ-1 in MYC-dependent tumorigenesis. *Cold Spring Harb. Perspect. Med.* 3, a014290
- 54 Wolf, E. *et al.* (2013) Miz1 is required to maintain autophagic flux. *Nat. Commun.* 4, 2535
- 55 Inoue, S. *et al.* (2013) Mule/Huwe1/Arf-BP1 suppresses Ras-driven tumorigenesis by preventing c-Myc/Miz1-mediated down-regulation of p21 and p15. *Genes Dev.* 27, 1101–1114
- 56 Peter, S. *et al.* (2014) Tumor cell-specific inhibition of MYC function using small molecule inhibitors of the HUWE1 ubiquitin ligase. *EMBO Mol. Med.* Published online September 24, 2014, <http://dx.doi.org/10.15252/emmm.201403927>
- 57 Chen, D. *et al.* (2005) ARF-BP1/Mule is a critical mediator of the ARF tumor suppressor. *Cell* 121, 1071–1083
- 58 Herkert, B. *et al.* (2010) The Arf tumor suppressor protein inhibits Miz1 to suppress cell adhesion and induce apoptosis. *J. Cell Biol.* 188, 905–918
- 59 Diolaiti, D. *et al.* (2014) Functional interactions among members of the MAX and MLX transcriptional network during oncogenesis. *Biochim. Biophys. Acta* Published online May 22, 2014, <http://dx.doi.org/10.1016/j.bbagr.2014.05.016>
- 60 Kelleher, F.C. *et al.* (2014) Circadian molecular clocks and cancer. *Cancer Lett.* 342, 9–18
- 61 Cunningham, J.T. *et al.* (2014) Protein and nucleotide biosynthesis are coupled by a single rate-limiting enzyme, PRPS2, to drive cancer. *Cell* 157, 1088–1103
- 62 Brown, J.D. *et al.* (2014) NF- κ B directs dynamic super enhancer formation in inflammation and atherogenesis. *Mol. Cell* 56, 219–231
- 63 Sun, M. *et al.* (2013) Global analysis of eukaryotic mRNA degradation reveals Xrn1-dependent buffering of transcript levels. *Mol. Cell* 52, 52–62
- 64 Lin, C.J. *et al.* (2012) Targeting synthetic lethal interactions between Myc and the eIF4F complex impedes tumorigenesis. *Cell Rep.* 1, 325–333
- 65 Takahashi, K. and Yamanaka, S. (2006) Induction of pluripotent stem cells from mouse embryonic and adult fibroblast cultures by defined factors. *Cell* 126, 663–676
- 66 Levens, D. (2013) Cellular MYC economics: balancing MYC function with MYC expression. *Cold Spring Harb. Perspect. Med.* 3, a014233

Response and resistance to BET bromodomain inhibitors in triple-negative breast cancer

Shaokun Shu^{1,2*}, Charles Y. Lin^{1,2*}, Housheng Hansen He^{1,2,3,4,5*}, Robert M. Witwicki^{1,2*}, Doris P. Tabassum¹, Justin M. Roberts¹, Michalina Janiszewska^{1,2}, Sung Jin Huh^{1,2}, Yi Liang⁴, Jeremy Ryan^{1,2}, Ernest Doherty^{1,6}, Hisham Mohammed⁷, Hao Guo³, Daniel G. Stover^{1,2}, Muhammad B. Ekram^{1,2}, Guillermo Peluffo^{1,2}, Jonathan Brown^{1,2}, Clive D'Santos⁷, Ian E. Krop^{1,2}, Deborah Dillon^{1,8}, Michael McKeown^{1,2}, Christopher Ott^{1,2}, Jun Qi^{1,2}, Min Ni^{1,2}, Prakash K. Rao⁹, Melissa Duarte⁹, Shwu-Yuan Wu¹⁰, Cheng-Ming Chiang¹⁰, Lars Anders¹¹, Richard A. Young¹¹, Eric P. Winer^{1,2}, Antony Letai^{1,2}, William T. Barry^{2,3}, Jason S. Carroll⁷, Henry Long⁹, Myles Brown^{1,2,9}, X. Shirley Liu^{3,9,12}, Clifford A. Meyer^{1,2,3}, James E. Bradner^{1,2,12} & Kornelia Polyak^{1,2,9,12}

Triple-negative breast cancer (TNBC) is a heterogeneous and clinically aggressive disease for which there is no targeted therapy¹⁻³. BET bromodomain inhibitors, which have shown efficacy in several models of cancer⁴⁻⁶, have not been evaluated in TNBC. These inhibitors displace BET bromodomain proteins such as BRD4 from chromatin by competing with their acetyl-lysine recognition modules, leading to inhibition of oncogenic transcriptional programs⁷⁻⁹. Here we report the preferential sensitivity of TNBCs to BET bromodomain inhibition *in vitro* and *in vivo*, establishing a rationale for clinical investigation and further motivation to understand mechanisms of resistance. In paired cell lines selected for acquired resistance to BET inhibition from previously sensitive TNBCs, we failed to identify gatekeeper mutations, new driver events or drug pump activation. BET-resistant TNBC cells remain dependent on wild-type BRD4, which supports transcription and cell proliferation in a bromodomain-independent manner. Proteomic studies of resistant TNBC identify strong association with MED1 and hyper-phosphorylation of BRD4 attributable to decreased activity of PP2A, identified here as a principal BRD4 serine phosphatase. Together, these studies provide a rationale for BET inhibition in TNBC and present mechanism-based combination strategies to anticipate clinical drug resistance.

To explore non-oncogene addiction to BRD4 in breast cancer, we studied a series of BET bromodomain inhibitors (BBI) across breast cell lines reflecting transcriptionally defined breast cancer subtypes: luminal, HER2⁺ and TNBC^{2,10}, as well as MCF10A and MCF12A basal/mesenchymal immortalized mammary epithelial cells (Supplementary Table 1). Potent inhibitory effects were observed preferentially in TNBC lines, compared to more resistant luminal lines (Fig. 1a). Analysis of potency of drug response and subtype or known driver mutations identified the basal subtype as the only significant association ($P = 0.0475$) (Supplementary Table 1 and data not shown). BRD4 dependency was confirmed by RNA interference and phenocopied BBI (Extended data Fig. 1a–c). JQ1 or BRD4 knockdown induced growth inhibition and resulted in G1 arrest and apoptosis (Extended data Fig. 1d–g). Expression of factors described to mediate JQ1 effect (MYC) or required for TNBC growth (JAK2/STAT3) showed no clear association with JQ1 sensitivity (Extended data Fig. 1h and Extended Data Fig. 2a, b). JQ1 treatment of TNBC cells induced significant morphologic

changes consistent with induction of senescence, confirmed by β -galactosidase staining and luminal differentiation evidenced by changes in the expression of basal and luminal markers (Extended Data Fig. 2c, d and Fig. 1b).

Extending the translational significance of these findings, we evaluated the ability of JQ1 to inhibit tumour growth in murine TNBC xenografts. Two-week treatment efficiently inhibited established tumour growth from SUM159 and MDA-MB-231 lines, and patient-derived primary human TNBC xenografts (Fig. 1c and Extended Data Fig. 2e, f). Downregulation of BRD4 using two independent TET-inducible short hairpin RNAs produced even more pronounced effects, leading to complete tumour regression and failure to regrow even after discontinuing doxycycline treatment (Fig. 1c and Extended Data Fig. 2g). Evidence of BBI-induced basal-to-luminal differentiation was confirmed *in vivo* (Extended Data Fig. 2f, h).

Using integrated epigenomic analysis (Supplementary Table 2), we identified the direct transcriptional targets of BBI in TNBC. BBI binding was identified at active promoter and enhancer regions using ChemSeq¹¹ for biotinylated JQ1 (Bio-JQ1) enrichment and chromatin immunoprecipitation followed by sequencing (ChIP-seq) for acetyl-histone (H3K27ac) and BRD4 enrichment, with the three marks showing near perfect co-localization (Fig. 1d and Extended Data Fig. 3a). BBI efficiently displaced chromatin-bound BRD4 in treated SUM159 (Fig. 1e and Extended Data Fig. 3b) and in SUM149 cells (Extended Data Fig. 3c). To identify biologically relevant, direct targets of BBI in SUM159 and SUM149 cells, we quantified binding of Bio-JQ1 and BRD4 genome-wide and found strong enrichment at 219 and 159 super enhancers, respectively (Fig. 1f, Extended Data Fig. 3d and Supplementary Table 3)^{8,9,12,13}. Transcription factors with known roles in breast cancer, such as POU5F1B/MYC¹⁴ and HIF1 α ¹⁵, were evident among top super-enhancer-associated genes in both lines. Kinetic effects of JQ1 treatment on gene expression demonstrated preferential super-enhancer-associated gene downregulation (Fig. 1g and Extended Data Fig. 3e, f). Expression changes were observed within 3 h after JQ1 treatment and, as expected, more genes were significantly down- than upregulated (Extended Data Fig. 3g–j and Supplementary Table 4). Unsupervised Metacore¹⁶ analysis of JQ1 affected target pathways revealed downregulation of regulatory and effector genes in anti-apoptotic and JAK/STAT signalling pathways (Extended Data Fig. 3k).

¹Department of Medical Oncology, Dana-Farber Cancer Institute, Boston, Massachusetts 02215, USA. ²Department of Medicine, Brigham and Women's Hospital, and Department of Medicine, Harvard Medical School, Boston, Massachusetts 02115, USA. ³Department of Biostatistics and Computational Biology, Dana-Farber Cancer Institute, and Department of Biostatistics, Harvard School of Public Health, Boston, Massachusetts 02115, USA. ⁴Princess Margaret Cancer Center/University Health Network, Toronto, Ontario M5G1L7, Canada. ⁵Department of Medical Biophysics, University of Toronto, Toronto, Ontario M5G2M9, Canada. ⁶Harvard University, Cambridge, Massachusetts 02138, USA. ⁷Cancer Research UK, Cambridge Institute, University of Cambridge, Cambridge CB2 0RE, UK. ⁸Department of Pathology, Brigham and Women's Hospital, and Department of Pathology, Harvard Medical School, Boston, Massachusetts 02115, USA. ⁹Center for Functional Cancer Epigenetics, Dana-Farber Cancer Institute, Boston, Massachusetts 02215, USA. ¹⁰Simmons Comprehensive Cancer Center, Departments of Biochemistry and Pharmacology, University of Texas Southwestern Medical Center, Dallas, Texas 75390, USA. ¹¹Whitehead Institute for Biomedical Research, Cambridge, Massachusetts 02142, USA. ¹²Broad Institute, Cambridge, Massachusetts 02142, USA.

*These authors contributed equally to this work.

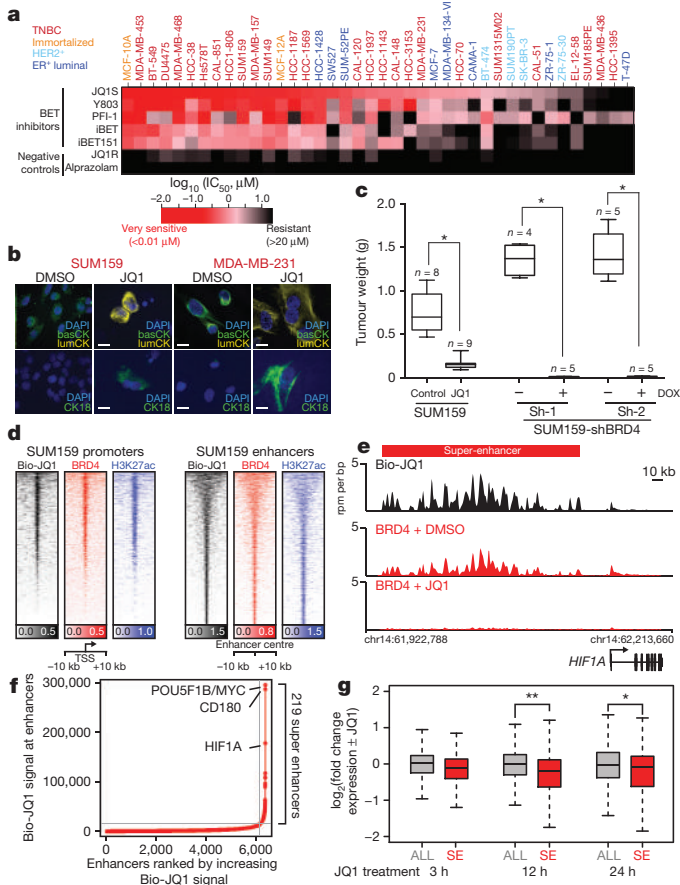


Figure 1 | Response to BBIs in breast cancer. **a**, Heat map of mean IC_{50} s of BBIs and inactive analogues in breast cell lines. Error bars represent s.e.m. **b**, Immunofluorescence of basal (basCK) and luminal (lumCK and CK18) cytokeratins in TNBC lines. Scale bars, 20 μ m. **c**, Box plots depicting xenograft weights; n indicates the number of mice per experiment. $*P < 0.0001$ (unpaired t -test). **d**, Heat map showing biotinylated JQ1 (Bio-JQ1), BRD4 and H3K27ac binding at transcription start site (TSS) and Bio-JQ1-bound enhancer regions. Each row represents a single genomic region (± 10 kb) from TSS or enhancer centre. Genomic occupancy is shaded by binding intensity in units of reads per million per base pair (rpm per bp). **e**, Genomic tracks depicting Bio-JQ1 and BRD4 with or without JQ1 in SUM159 cells at the *HIF1A* locus. x -axis, chromosome position with gene structures below; y -axis, genomic occupancy in units of rpm per bp; red bar, *HIF1A* super-enhancer. **f**, Plot of enhancers defined in untreated SUM159 cells ranked by increasing Bio-JQ1 signal (units rpm). Grey line marks cutoff discriminating typical from super-enhancers. **g**, Boxplots showing the \log_2 fold change in expression relative to control of either all active or super-enhancer (SE) associated genes upon JQ1 treatment. $**P < 10^{-5}$ (Welsh's t -test); $*P < 10^{-3}$ (Welsh's t -test).

These data support selective disruption of super-enhancer-associated genes by JQ1, leading to deregulation of coordinated transcriptional pathways involved in cell proliferation, invasion and survival.

Dissecting resistance to targeted therapy is critical to elucidate mechanisms of drug and target action, and to suggest approaches to treat or anticipate drug resistance in patients. Therefore, we established BBI-resistant TNBC cell lines by long-term culture of both SUM159 and SUM149 cells in escalating JQ1 doses. Low (0.5 μ M) and high (2.0 μ M) doses of JQ1 severely impaired proliferation of parental SUM159 and SUM149 lines, reducing viable cells after 6 days (Fig. 2a and Extended Data Fig. 3l). In contrast, JQ1-resistant cells (SUM159R and SUM149R) proliferated linearly, even in high JQ1 doses (20 μ M) (Fig. 2a and Extended Data Fig. 3l). BBI-resistance is not attributable to drug export, as MDR1 and other transporters are not transcriptionally upregulated (Extended Data Fig. 4a), co-incubation with MDR1

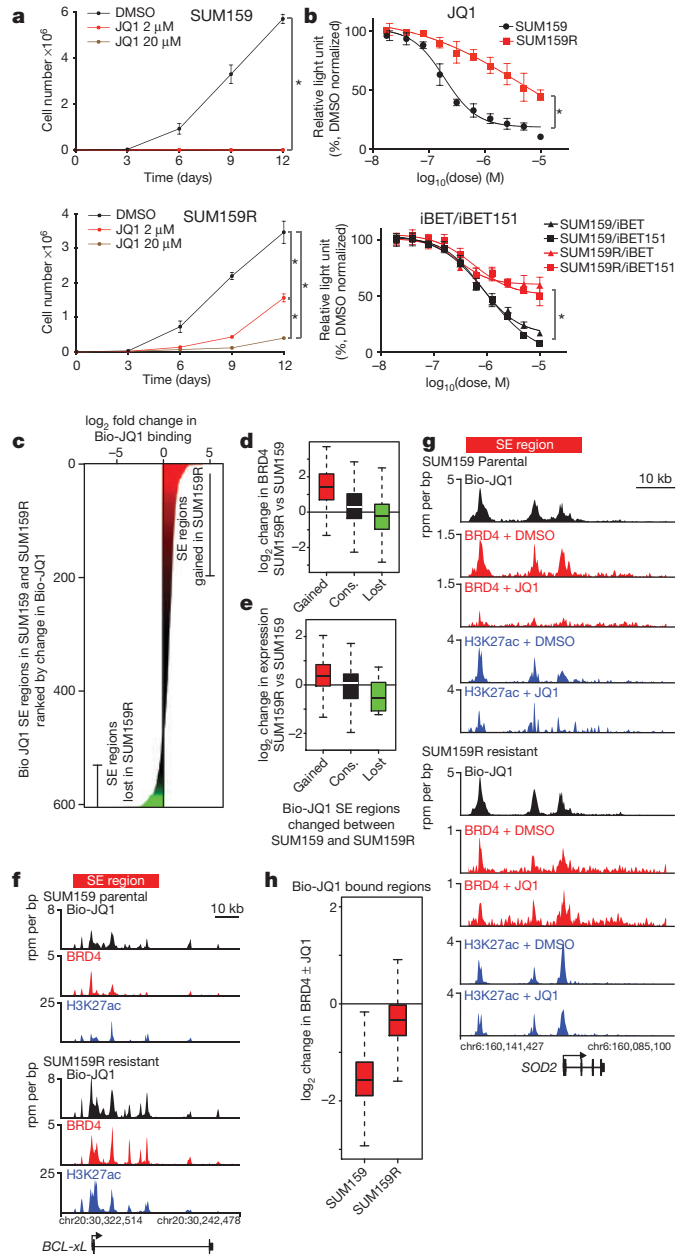


Figure 2 | Acquired BBI-resistance in TNBC. All error bars represent s.d., $n = 3$. **a**, Viable cell numbers after JQ1 treatment. $*P < 0.0001$ (two-way ANOVA). **b**, Cellular viability after treatment with BBIs. $*P < 0.0001$ (non-linear regression, extra sum-of-squares test). **c**, Genomic regions containing a super-enhancer in SUM159 or SUM159R cells ranked by \log_2 change in Bio-JQ1 genomic binding signal. x -axis, \log_2 fold change in Bio-JQ1 signal coloured by intensity of change. **d**, **e**, Boxplot showing the \log_2 fold change in BRD4 genomic occupancy (**d**) and gene expression (**e**) at regions with gained, conserved, or lost Bio-JQ1 binding in SUM159R versus SUM159 cells. **f**, **g**, Gene tracks depicting Bio-JQ1, BRD4, and H3K27ac at the *BCL-xL* (also known as *BCL2L1*; **f**) and *SOD2* (**g**) locus. The x -axis shows position along the chromosome with gene structures drawn below. The y -axis shows genomic occupancy in units of rpm per bp. **h**, Boxplot showing the \log_2 fold change in BRD4 genomic occupancy at regions bound by Bio-JQ1.

inhibitors (verapamil) had no effect (Extended Data Fig. 4b), and structurally divergent BBIs are equally inactive as JQ1 (Fig. 2b). Further support is provided by the equivalent chromatin engagement of BRD4 in sensitive and resistant cells, demonstrated by binding with Bio-JQ1 (Extended Data Fig. 4c). Notably, BBI-resistant TNBC cells retain sensitivity to compounds from orthogonal active drug classes, such as

CXCR2 and JAK2 inhibitors¹⁷, establishing specific resistance to BBIs (Extended Data Fig. 4d). Adaptive drug resistance was not attributable to outgrowth of a minor subpopulation of pre-existing resistant cells, as 10 independent single-cell-derived clones showed similar resistance profiles to pooled SUM159R cells (Extended Data Fig. 4e). Similar results were obtained *in vivo*, as SUM159R-derived xenografts were JQ1 unresponsive (Extended Data Fig. 4f). In all resistant TNBC populations studied, exome sequencing failed to identify alterations in BET bromodomain-encoding genes (for example, gatekeepers) or known driver genes (parallel pathway activation) (Supplementary Table 5).

Absent new genetic alterations, we explored the plausibility of an epigenomic mechanism of resistance. Differential enhancer analysis revealed a significant gain of super enhancers in resistant SUM159R cells (Fig. 2c and Supplementary Table 6). The gain of Bio-JQ1 super enhancers was associated with enrichment for BRD4 binding to these genomic loci (Fig. 2d) and increased transcription of associated genes (Fig. 2e). An upstream/intragenic region of H3K27ac at the BCL-xL locus featured prominently among top gained super enhancers in SUM159R (Fig. 2f), consistent with increased BCL-xL messenger RNA and protein expression in resistant cells (Supplementary Table 7, Extended Data Fig. 4g). Functionally, cells with acquired resistance to BBI featured a concordant switch in JQ1 anti-apoptotic response based on dynamic BH3 profiling^{18,19} (Extended Data Fig. 4h).

Observing emergent enhancers in resistant cells, we assessed whether BBI-resistant TNBC cells retained non-oncogene addiction to BRD4. Notably, we observed loss of SUM159R cell viability upon BRD4 knockdown (Extended Data Fig. 5a, b). Together these studies establish persistence of BRD4 addiction despite resistance to bromodomain inhibition, establishing the plausibility of bromodomain-independent recruitment of BRD4 to enhancers in BBI-resistant TNBCs. To test this hypothesis, we performed BRD4 ChIP-seq on sensitive and resistant cells with and without JQ1. JQ1 neither displaced BRD4 from chromatin in SUM159R (Fig. 2g), nor meaningfully influenced epigenome structure by H3K27ac ChIP-seq (Extended Data Fig. 5c–g). Notably, several luminal markers (FOXA1, CD24, and luminal cytokeratins) were elevated in SUM159R cells in cell culture and *in vivo* (Extended Data Fig. 5h, i), supporting a model whereby resistance arises via essential BRD4 recruitment to chromatin in a bromodomain-independent manner. Similar observations were made in SUM149R cells and in TNBC cells inherently resistant to JQ1 (Extended Data Fig. 3h–j; Extended Data Fig. 6a–d), suggesting a general mechanism of epigenomic resistance to BBI.

To disclose potential differences in BRD4-associated complexes between sensitive and resistant SUM159 cells, we performed quantitative proteomics using RIME (rapid immunoprecipitation mass spectrometry of endogenous proteins)²⁰ with and without JQ1. Analysis of BRD4-associated proteins identified relative enrichment of MED1 and BRD3 in JQ1-treated resistant cells (Fig. 3a, Extended Data Fig. 7 and Supplementary Table 8). BRD4 immunoprecipitation followed by immunoblot for MED1 and BRD3 revealed that JQ1 efficiently displaced BRD4 from MED1 in sensitive cells, but not in resistant cells (Fig. 3b), a result confirmed in SUM149R and BBI-resistant SUM149R, as well as inherently resistant TNBC and luminal lines (Extended Data Fig. 8a). Although elevated BRD3 abundance was observed in SUM159R, increased association of BRD4 and BRD3 was not confirmed by immunoblot (Fig. 3b). To assess functionally whether increased recruitment of BRD4 to chromatin by MED1 underlies resistance to JQ1, we expressed an exogenous bromodomain-inactivated mutant (BDmut) with concomitant knockdown of endogenous BRD4 (Extended Data Fig. 8b, c). Downregulation of endogenous BRD4 decreased cell growth both in parental and resistant cells, which was rescued by enforced expression of wild-type BRD4 (Fig. 3c). BDmut BRD4 expression failed to rescue parental SUM159 cells, but supported growth of JQ1-resistant SUM159R consistent with an evident bromodomain-independent mechanism of BRD4 recruitment (Fig. 3c). Next, we assessed the sensitivity of

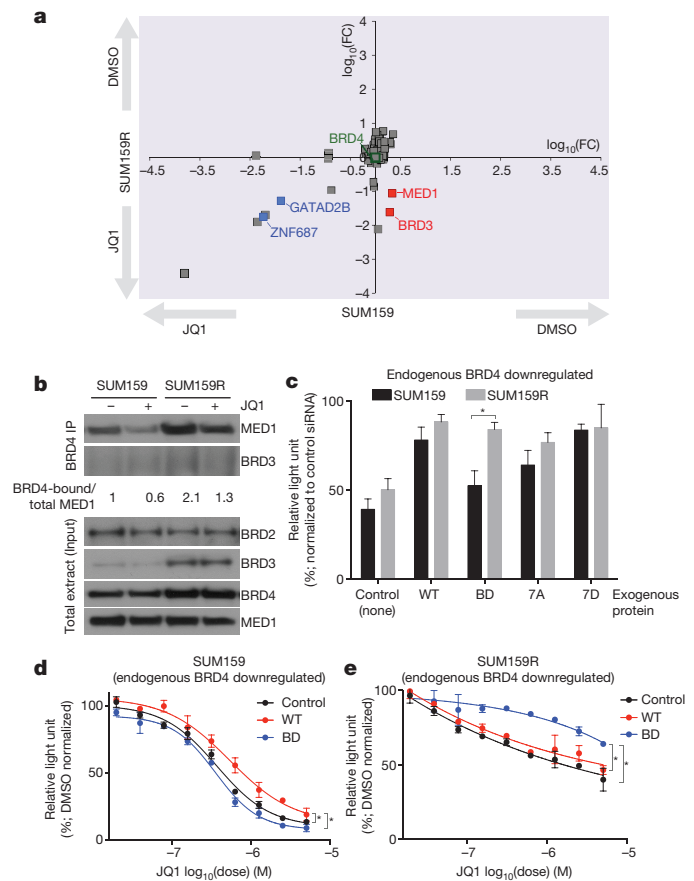


Figure 3 | Mechanism of BBI-resistance in TNBCs. All error bars represent s.d., $n = 3$. **a**, Plot depicting changes in BRD4-associated proteins in SUM159 and SUM159R cells following JQ1 treatment based on SILAC RIME. The axes represent \log_{10} of fold change (FC). **b**, Immunoblot analysis of BRD4 immunoprecipitates and total cell lysates in SUM159 and SUM159R cells. For gel source data, see Supplementary Fig. 1. **c**, Cellular viability of SUM159 and SUM159R cells expressing exogenous wild-type, BDmut, 7A and 7D mutant BRD4 with concomitant knockdown of endogenous BRD4. * $P = 0.04$ (paired *t*-test). **d**, **e**, Sensitivity of SUM159 (**d**) and SUM159R (**e**) cells expressing exogenous wild-type or BDmut BRD4 to JQ1 with concomitant knockdown of endogenous BRD4. * $P < 0.0001$ (non-linear regression, extra sum-of-squares test).

cells expressing BDmut BRD4 to JQ1, observing increased sensitivity to JQ1 in parental SUM159 cells exogenously expressing BDmut (Fig. 3d). In contrast, expression of BDmut BRD4 in SUM159R cells rescued the anti-proliferative effect of JQ1 (Fig. 3e), although this could partially be due to the slower growth of BDmut expressing cells. Together, these studies suggest BBI-resistance is associated with increased binding of BRD4 to MED1, in a bromodomain-independent manner unaffected by JQ1.

A recent study reported that the stability and nuclear localization of BRD4 is increased with phosphorylation by casein kinase II (CK2)²¹. To explore the contribution of BRD4 phosphorylation to BBI-resistance, we performed immunoblot analysis in parental and resistant cells and found a marked increase of phospho-BRD4 (pBRD4) in resistant cells (Fig. 4a and Extended Data Fig. 8d). Small-molecule inhibition of CK2 decreased BRD4 phosphorylation in SUM159 and SUM159R cells (Extended Data Fig. 8e). These results imply BRD4 hyperphosphorylation in resistant cells either owing to increased phosphorylation by CK2 or, alternatively, to decreased dephosphorylation by an as yet unidentified BRD4 phosphatase. We therefore first analysed CK2 activity in parental and resistant cells by performing pan-CK2 substrate immunoblots and detected no significant differences in CK2 activity (Extended Data Fig. 8f).

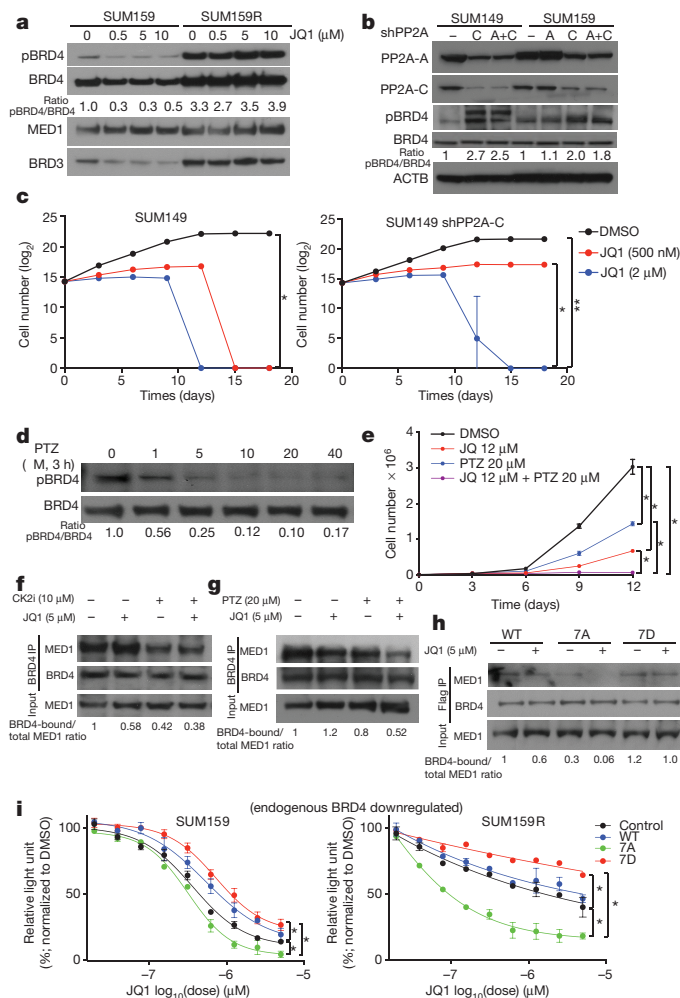


Figure 4 | Regulation and relevance of BRD4 phosphorylation. All error bars represent s.d., $n = 3$. **a**, Immunoblot for the indicated proteins following JQ1 treatment. **b**, Immunoblot for the indicated proteins after knockdown of PP2A A or C or both subunits. **c**, Viable cell numbers of JQ1-treated control and shPP2A-C expressing SUM149 cells. Left, $*P < 0.0001$ (two-way ANOVA); right, $*P = 0.0037$ and $**P = 0.0015$ (two-way ANOVA). **d**, Immunoblot of pBRD4 and BRD4 in SUM159R cells following phenothiazine (PTZ) treatment. **e**, Viable cell numbers of SUM159R cells treated with JQ1, phenothiazine or both compounds. $*P < 0.0001$ (two-way ANOVA). **f, g**, Immunoblot of BRD4 immunoprecipitates and total cell lysates of SUM159R cells after 3 h treatment with JQ1 and CK2i (**f**) and JQ1 and PTZ (**g**). **h**, Immunoblot of Flag-BRD4 (wild type or mutant) immunoprecipitates and total cell lysates after 3 h treatment with JQ1. **i**, JQ1 sensitivity of SUM159 and SUM159R cells expressing exogenous wild-type or mutant (7A, 7D) BRD4. $*P < 0.0001$ (non-linear regression, extra sum-of-squares test). For gel source data, see Supplementary Fig. 1.

Inactivation of the PP2A phosphatase tumour suppressor gene occurs commonly in breast cancer and is associated with therapy resistance²²; PP2A also often opposes CK2 function^{23,24}. Thus, we investigated whether PP2A may dephosphorylate BRD4 and whether decreased PP2A activity could lead to BBI resistance. Downregulation of PP2A catalytic subunit (*PPP2CA*) in SUM149 and SUM159 cells led to increased BRD4 phosphorylation, establishing PP2A as a previously unrecognized BRD4 phosphatase (Fig. 4b), further supported by pharmacologic inhibitors of PP2A that showed similar effects (Extended Data Fig. 8g). To strengthen the link between PP2A activity and BBI resistance, we tested the JQ1 sensitivity of SUM149 cells following the knockdown of PP2A C subunit and determined that downregulation of PP2A decreased JQ1 sensitivity (Fig. 4c). We have collaboratively reported phenothiazine compounds as activators of PP2A enzymatic

activity²⁵. Thus, we analysed pBRD4 levels in SUM159R, SUM149R and other cell lines after short-term treatment with phenothiazine (PTZ) and detected rapid dephosphorylation of BRD4 (Fig. 4d and Extended Data Fig. 8h). Combined treatment with PTZ and JQ1 overcame BBI resistance in SUM159R cells (Fig. 4e). To investigate the functional role of BRD4 hyperphosphorylation in BBI resistance, we analysed whether BRD4 phosphorylation influences MED1 binding. Indeed, SUM159R cells treated with CK2 inhibitor or PTZ both lead to decreased MED1 abundance in BRD4 immunoprecipitations, suggesting that pBRD4 binds MED1 more efficiently than BRD4 (Fig. 4f, g).

To functionally assess the role for BRD4 phosphorylation in BBI resistance and MED1 binding, we generated BRD4 constructs encoding mutants that cannot be phosphorylated by CK2 (7 serine to alanine substitutions; '7A mutant') or mimic constitutive phosphorylation (7 serine to aspartate substitutions; '7D mutant'). We first assessed the ability of these constructs to rescue effects of endogenous BRD4 knockdown in stable cell lines (Extended Data Fig. 8b, c). We observed expression of both 7D and 7A mutants supporting the growth of both parental SUM159 and JQ1-resistant SUM159R cells (Fig. 3c). Next, we analysed MED1 binding and subcellular localization of 7A and 7D mutants in the presence or absence of JQ1. We found that the 7A mutant displays weaker MED1 binding compared to wild-type BRD4 and completely dissociates after JQ1, whereas the 7D mutant seems to have higher affinity for MED1 that is unaffected by JQ1 treatment (Fig. 4h and Extended Data Fig. 8i). Lastly, we assessed the sensitivity of cells expressing 7A or 7D mutant BRD4 to JQ1. In parental SUM159 cells exogenously expressed 7D mutant BRD4 decreased sensitivity to JQ1, whereas the 7A mutant slightly increased sensitivity (Fig. 4i). In contrast, expression of 7A mutant BRD4 in SUM159R cells restored JQ1 sensitivity, whereas the 7D mutant showed a modest decrease. These results strongly support the hypothesis that hyperphosphorylation of BRD4 arises from decreased PP2A activity in BBI resistant cells, leading to increased binding of BRD4 to MED1, recruitment to chromatin and decreased responsiveness to bromodomain inhibition.

To explore the clinical relevance of phospho-BRD4 (pBRD4) in BET inhibitor-naïve TNBC, we performed immunofluorescence analysis of a tissue microarray (TMA) featuring of 89 patient-derived TNBC specimens. First, we validated the pBRD4 immunofluorescence assay by comparing xenografts derived from SUM159 and SUM159R cell lines and detected significantly higher pBRD4 in SUM159R cells (Extended Data Fig. 9a). We detected strong pBRD4 staining among a subset of TNBCs (Extended Data Fig. 9b, c), and variable staining overall that was not correlated with expression of the androgen receptor and basal cytokeratins (bCK; Extended Data Fig. 9d, e) and it was not significantly associated with disease outcomes (Supplementary Table 9 and Extended Data Fig. 9f).

To extend the translational relevance of our findings, we conducted synergy studies of JQ1 with molecules targeting BCL-xL (ABT737), a gained super-enhancer in SUM159R cells, and modulators of BRD4 phosphorylation, the CK2 inhibitor CX-4945 and the PP2A activator perphenazine (PPZ). We observed significant synergy between JQ1 and all three compounds studied (Extended Data Fig. 10), establishing a rationale for combination studies of BBI in TNBC to improve response and to anticipate BBI resistance.

BRD4 inhibition has demonstrated efficacy in disparate models of cancer in a rapidly expanding literature. Despite apparent resistance in the vast majority of tumour types, as we observed here in TNBC, mechanisms of BBI-resistance have not been mechanistically explained. As this research was in review, two studies reported moderate emergent resistance to BBI in murine AML associated phenotypically with a stem-like state and WNT pathway activation^{26,27}. Interestingly, in our study TNBCs with more basal/stem cell-like features and WNT pathway activation are more sensitive to BET inhibition, whereas resistant disease emerges as epigenomic adaptation to a more differentiated luminal phenotype. Our findings of persistent BET bromodomain dependency despite BBI resistance, as well as pBRD4 staining in

resistant disease should be studied in these murine AML models and further in human leukaemia.

Integrating approaches in epigenomics, proteomics and chemical biology, we provide an example of epigenomic drug resistance by an epigenetic mechanism, where in BBI-resistant cells, decreased PP2A activity leads to hyperphosphorylated BRD4, which binds more strongly to MED1, facilitating a bromodomain-independent chromatin recruitment mechanism. This research proposes putative combination strategies to anticipate and overcome BBI resistance, including pairing with BCL-xL inhibitors (for example, ABT-737) or CK2 inhibitors, and guides the development of second-generation BBIs that disrupt BET function via orthogonal biophysical or biochemical actions. More immediately, the robust efficacy observed in pre-clinical models supports the development of BET inhibition in TNBC alone, and in combination with mechanism-based targeted therapies.

Online Content Methods, along with any additional Extended Data display items and Source Data, are available in the online version of the paper; references unique to these sections appear only in the online paper.

Received 12 November 2014; accepted 3 December 2015.

Published online 6 January 2016.

- Vaz-Luis, I. *et al.* Outcomes by tumor subtype and treatment pattern in women with small, node-negative breast cancer: a multi-institutional study. *J. Clin. Oncol.* **32**, 2142–2150 (2014).
- Lehmann, B. D. *et al.* Identification of human triple-negative breast cancer subtypes and preclinical models for selection of targeted therapies. *J. Clin. Invest.* **121**, 2750–2767 (2011).
- Metzger-Filho, O. *et al.* Dissecting the heterogeneity of triple-negative breast cancer. *J. Clin. Oncol.* **30**, 1879–1887 (2012).
- Puissant, A. *et al.* Targeting MYCN in neuroblastoma by BET bromodomain inhibition. *Cancer Discov.* **3**, 308–323 (2013).
- Delmore, J. E. *et al.* BET bromodomain inhibition as a therapeutic strategy to target c-Myc. *Cell* **146**, 904–917 (2011).
- Filippakopoulos, P. *et al.* Selective inhibition of BET bromodomains. *Nature* **468**, 1067–1073 (2010).
- Belkina, A. C. & Denis, G. V. BET domain co-regulators in obesity, inflammation and cancer. *Nature Rev. Cancer* **12**, 465–477 (2012).
- Chapuy, B. *et al.* Discovery and characterization of super-enhancer-associated dependencies in diffuse large B cell lymphoma. *Cancer Cell* **24**, 777–790 (2013).
- Hnisz, D. *et al.* Super-enhancers in the control of cell identity and disease. *Cell* **155**, 934–947 (2013).
- Burstein, M. D. *et al.* Comprehensive genomic analysis identifies novel subtypes and targets of triple-negative breast cancer. *Clin. Cancer Res.* **21**, 1688–1698 (2015).
- Anders, L. *et al.* Genome-wide localization of small molecules. *Nature Biotechnol.* **32**, 92–96 (2014).
- Lovén, J. *et al.* Selective inhibition of tumor oncogenes by disruption of super-enhancers. *Cell* **153**, 320–334 (2013).
- Whyte, W. A. *et al.* Master transcription factors and mediator establish super-enhancers at key cell identity genes. *Cell* **153**, 307–319 (2013).
- Hayashi, H. *et al.* The *OCT4* pseudogene *POU5F1B* is amplified and promotes an aggressive phenotype in gastric cancer. *Oncogene* **34**, 199–208 (2015).
- Semenza, G. L. HIF-1 mediates metabolic responses to intratumoral hypoxia and oncogenic mutations. *J. Clin. Invest.* **123**, 3664–3671 (2013).
- Bessarabova, M. *et al.* Functional synergies yet distinct modulators affected by genetic alterations in common human cancers. *Cancer Res.* **71**, 3471–3481 (2011).
- Marotta, L. L. *et al.* The JAK2/STAT3 signaling pathway is required for growth of CD44⁺CD24⁻ stem cell-like breast cancer cells in human tumors. *J. Clin. Invest.* **121**, 2723–2735 (2011).
- Ryan, J. & Letai, A. BH3 profiling in whole cells by fluorimeter or FACS. *Methods* **61**, 156–164 (2013).
- Montero, J. *et al.* Drug-induced death signaling strategy rapidly predicts cancer response to chemotherapy. *Cell* **160**, 977–989 (2015).
- Mohammed, H. *et al.* Endogenous purification reveals GREB1 as a key estrogen receptor regulatory factor. *Cell Reports* **3**, 342–349 (2013).
- Wu, S. Y., Lee, A. Y., Lai, H. T., Zhang, H. & Chiang, C. M. Phospho switch triggers Brd4 chromatin binding and activator recruitment for gene-specific targeting. *Mol. Cell* **49**, 843–857 (2013).
- Rincón, R. *et al.* PP2A inhibition determines poor outcome and doxorubicin resistance in early breast cancer and its activation shows promising therapeutic effects. *Oncotarget* **6**, 4299–4314 (2015).
- Westermarck, J. & Hahn, W. C. Multiple pathways regulated by the tumor suppressor PP2A in transformation. *Trends Mol. Med.* **14**, 152–160 (2008).
- Eichhorn, P. J., Creighton, M. P. & Bernards, R. Protein phosphatase 2A regulatory subunits and cancer. *Biochim. Biophys. Acta* **1795**, 1–15 (2009).
- Gutierrez, A. *et al.* Phenothiazines induce PP2A-mediated apoptosis in T cell acute lymphoblastic leukemia. *J. Clin. Invest.* **124**, 644–655 (2014).
- Rather, P. *et al.* Transcriptional plasticity promotes primary and acquired resistance to BET inhibition. *Nature* **525**, 543–547 (2015).
- Fong, C. Y. *et al.* BET inhibitor resistance emerges from leukaemia stem cells. *Nature* **525**, 538–542 (2015).

Supplementary Information is available in the online version of the paper.

Acknowledgements We thank D. Silver and members of the Polyak and Bradner laboratories for their critical reading of this manuscript and useful discussions. We thank G. Brown for help with creating the word cloud figures. This work was supported by the NIH DF/HCC SPORE in Breast Cancer CA168504 (K.P., E.P.W., I.E.K., D.D., W.T.B., and J.E.B.), CA080111 (K.P. and M.B.), and CA103867 (C.M.C.), Susan G. Komen Foundation (S.S.), CPRIT RP110471 and RP140367 (C.M.C.), Welch Foundation (C.M.C.), US Department of Defense CDMRP BC122003 (S.X.L.) and CA120184 (C.Y.L.), Princess Margaret Cancer Foundation (H.H.H.), Canada Foundation for Innovation and Ontario Research Fund CF132372 (H.H.H.), NSERC discovery grant RGPIN-2015-04658 (H.H.H.), and the Harvard Ludwig Center for Cancer Research (J.E.B., M.B. and K.P.).

Author Contributions S.S. performed cell culture, xenograft, ChIP-seq, and RNA-seq experiments, and data analyses. C.Y.L. and C.A.M. performed genomic data analyses. H.H.H. helped with ChIP-seq and RNA-seq experiments and data analyses. R.M.W. performed cell culture, ChIP-seq experiments and data analyses. J.M.R. performed synergy studies. D.P.T. helped with immunofluorescence staining. M.J. and S.J.H. helped with confocal microscopy and image quantification. Y.L. helped with BRD4 ChIP-seq. M.B.E. and G.P. helped with cell cycle studies. E.D. helped with generating and testing BRD4 mutants. J.B. and L.A. performed Chem-seq. H.M., C.D. and J.S.C. conducted proteomic experiments and data analyses. C.O. and M.M. performed drug sensitivity screens. J.Q. synthesized BBI compounds. M.N. generated shRNA constructs. D.D., I.E.K. and E.P.W. generated the TMA and linked to clinical data. H.G., D.G.S. and W.T.B. performed TMA and statistical analyses. J.R. and A.L. performed BH3 profiling and data analyses. C.-M.C. and S.-Y.W. provided phospho-BRD4 antibody. P.K.R. and M.D. generated RNA-seq libraries. K.P. supervised with help from J.E.B., X.S.L., M.B., R.A.Y. and H.L. All authors helped to design the study and write the manuscript.

Author Information RNA-seq, ChIP-seq, and Chem-seq data have been deposited in the NCBI GEO database with the accession number GSE63584. Reprints and permissions information is available at www.nature.com/reprints. The authors declare competing financial interests: details are available in the online version of the paper. Readers are welcome to comment on the online version of the paper. Correspondence and requests for materials should be addressed to K.P. (kornelia_polyak@dfci.harvard.edu) or J.E.B. (james_bradner@dfci.harvard.edu).

METHODS

No statistical methods were used to predetermine sample size. The experiments were not randomized, and the investigators were not blinded to allocation during experiments and outcome assessment.

Cell lines and breast tumour tissues. Breast cell lines were obtained from the ATCC and S. Ethier (SUM series). Cells were cultured in media recommended by the provider, their identity was confirmed by STR analysis, and they were regularly tested for mycoplasma. Breast tumour samples were collected using protocols approved by the DF/HCC Institutional Review Board, informed consent was obtained from all patients. Tumours were minced with razor blades and digested with stirring for 3–4 h at 37 °C in DMEM/F12 with 2 mg ml⁻¹ BSA, 2 mg ml⁻¹ collagenase type IV, and 2 mg ml⁻¹ hyaluronidase. After digestion, cells were filtered through 500-µm mesh, washed in DMEM/F12 with 5% FBS, frozen in DMEM/F12 with 5% FBS and 10% DMSO, and stored in liquid nitrogen for subsequent xenograft studies. PDX IDC50 was derived from a primary tumour of highly invasive metaplastic TNBC resistant to chemo and radiation therapy leading to the rapid death of the patient. Exome sequencing of the tumour and xenograft identified numerous mutations including heterozygous frameshift mutation in *PTEN* (chr10_89701964-89701964_A) and *CDH1* chr16_67400242-67400242_C). PDX EL-12-58 was derived from a liver metastasis of a heavily pretreated basal-like TNBC, Oncopanel mutation testing identified homozygous mutations in *BRCA2* (p.S1970*), *TP53* (p.I232fs), *TSC2*, *FLT3*, and *ROS1*, and lower frequency mutations in *RAD21*, *JAK3*, *ARID1B*, *ARID1A*, *KDM6A*.

High-throughput screening of BET bromodomain inhibitors in breast cell line panel. We tested a panel of compounds (synthesized in the Bradner laboratory) in 40 human breast cell lines in a 384-well format at 2,000 cells per well using a semi-automated screen essentially as described⁵. Cell viability at 72 h was evaluated using ATPlite (Perkin Elmer).

Synergy studies. SUM149, SUM149R, SUM159, and SUM159R cells were seeded in sterile, white, opaque 384-well microtitre plates (Thermo), using an automated dispensing system (BioTek EL406), at 1,000 cells per well in 50 µl of media. Drugs were delivered in DMSO by robotic pin transfer with a JANUS workstation (100 nl) to achieve a matrix of pairwise dose–response incubations of each compound, each pair having eight replicates. Following 72 h of incubation, ATP levels were determined for treated cells and vehicle controls (ATPlite, PerkinElmer). Data were normalized to vehicle controls. Combination indices were determined using the median-effect principle of Chou & Talalay²⁸ (CalcuSyn Software). Isobologram plots were generated with GraphPad Prism software. Points represent paired values of drug concentrations assessed for synergism. The diagonal line signifies drug additivity. Points above the line represent antagonistic drug combinations, and those below the line represent synergistic drug combinations. Synergy assays were performed in triplicates and repeated 2–3 times.

Xenograft assays. For xenograft assays 5–6-weeks old female CrTac:NCr-Foxn1^{tmu} and NOD.Cg-Prkd^{scid} Il2rg^{tm1Sug}/JicTac mice were purchased from Taconic. Tumours were induced by bilateral orthotopic mammary fat pad injection of 1 × 10⁶ cells in 50% Matrigel (BD Biosciences) in DMEM/F12 or Medium 171 (except for IDC50-X cells, which were injected with 3% FBS and 4 mg ml⁻¹ collagen gel in Medium 171). Animal experiments were conducted following protocol 11-023 approved by the Dana-Farber Cancer Institute Animal Care and Use Committee. For all the xenograft studies, the sample size of each group (5–10 mice) is indicated in the figures. We performed pilot experiments using a few (5–10) mice per group followed by larger studies if needed to reach statistical significance and repeated experiments to ensure reproducibility. Due to the nature of the performed experiments, no randomization and no blinding was used as it was deemed unfeasible. However, the resulting tumours were analysed in a blinded manner. Mice were administered JQ1 (50 mg per kg, daily), vehicle only (control) for 14 days beginning at day 14 (SUM159), or doxycycline at day 21 (SUM159-shBRD4) after injection. Mice were euthanized and tumours evaluated 28 and 60 days after injection of parental and TET-inducible shBRD4-expressing SUM159 cells into mammary fat pads.

Cellular viability, senescence, MDR and BH3 profiling assays. Cell viability and growth assays (Figs 1a, 2a,b, 3d,e, 4c,i, Extended Data Figs 1a,b, 3i, 4d,e,g,h, 10), cycle, apoptosis, and MDR assays were performed in triplicates and repeated 2–3 times. For cell proliferation assays, cells were plated at 500 cells per well in 96-well plates and treated the next day with inhibitors, DMSO or doxycycline (500 ng). Cells were cultured at 37 °C with 5% CO₂ in the media described-above, and cell viability was measured using CellTiter-Glo three days after treatments. For cell growth assays, cells were plated at 5,000 (SUM159) or 20,000 (SUM149) cells per well in 6-well plates and treated the next day with inhibitors. Cells were counted every three days by cell counter. Cellular apoptosis was analysed with an APC AnnexinV/7AAD Apoptosis Detection kit (BD Pharmingen). AnnexinV/7AAD assessments and cell cycle graphics were generated using FlowJo software V7.6.1 for Windows (Tree Star). Senescence Beta-gal staining was performed using

Senescence β-Galactosidase staining kit from Cell Signaling. Briefly, after JQ1 treatment (500 nM) for 72 h, SUM159 and MDA-MB-231 cells were fixed by fixative solution for 15 min, followed by β-galactosidase solution incubation overnight at 37 °C. The staining was checked under microscope for the development of blue colour. Multi-Drug Resistance Assay was performed with MDR assay kit from Cayman Chemical (600370). Briefly, SUM159 and SUM159R cells were treated with JQ1 or DMSO for 30 min in SUM medium. Verapamil was used as a positive control at 1:1,000 dilution. Calcein AM/Hoechst Dye staining solution was added after that and cells were incubated at 37 °C for 15 min. The cells were analysed by fluorescent microscope and FACS.

Cell cycle analysis was performed 72 h after JQ1 treatment or BRD4 down-regulation with doxycycline using propidium iodide (PI) staining. Cells were resuspended in 1 ml of growth medium supplemented with 2 µg ml⁻¹ PI (Life Technologies) as final concentration. After 60 min at 37 °C in the dark, analysis was performed on a FACS AriaII cytometer (BD Biosciences). The cell cycle was plotted as histogram after excluding doublets. Cell synchronization Procedure. SUM159 cells were treated with nocodazole (200 ng ml⁻¹) for 12 h and then cells were tapped to detach from the plates. After washing twice with PBS, cells were replated with or without JQ1 in collagen coated plates. Cells were collected at 0, 3, 6, 12 h time point for FACS and immunoblot analysis. Dynamic BH3 profiling was performed using the JC-1 plate method as previously described^{18,19}. Briefly, 2.5 × 10⁵ cells were seeded in T25 flasks in the presence of 500 nM or 5 µM JQ1 for 72 or 96 h. Cells were trypsinized, suspended in MEB (150 mM mannitol, 10 mM HEPES, 50 mM KCl, 5 mM succinate, 20 µM EDTA, 20 µM EGTA, 0.1% protease-free BSA, pH 7.5 ± 0.1), and 1–2 × 10⁴ cells were added in 15 µl of MEB to each well of a 384 well Fluotrac 200 plate containing 15 µl per well of either peptides at 2 × final concentration, buffer only, or 50 µM alamethicin in MEB supplemented with 2 µM JC-1, 10 mM 2-mercaptoethanol, 20 µg ml⁻¹ oligomycin, and 50 µg ml⁻¹ digitonin. Fluorescence at emission 590 ± 10 nm and excitation 545 ± 10 nm was recorded at 5 min intervals at 32 °C. The area under each curve was normalized to the alamethicin and buffer controls as:

$$\% \text{ Depolarization} = 1 - \frac{(\text{AUC}_{\text{sample}} - \text{AUC}_{\text{alamethicin}})}{(\text{AUC}_{\text{buffer}} - \text{AUC}_{\text{alamethicin}})}$$

Delta priming was calculated per peptide treatment as: Delta Priming = (Depolarization Treated) – (Depolarization Untreated). Positive delta priming indicates an increase in priming due to treatment and an increased potential for apoptosis at later time points.

Immunofluorescence staining and image and statistical analysis of tissue microarrays. Antibodies used for immunofluorescence were CK18 (Dako, M7010), CK17 (Dako, M7046), HMW CK (Dako, M0630), LMW CK (Dako, M0631), CD44 (NeoMarkers, MS-668-P1), CD24 (NeoMarkers, MS-1279-P1), p-STAT3 (Cell Signaling, 9145S), VIM (Dako, M073501), CDH1 (BD Biosciences, 610181), Flag (Sigma, F1804), BrdU (Roche, 11170376001), pBRD4 (a gift from C. M. Chiang), and androgen receptor (Cell Signaling, 5153S). Immunofluorescence experiments were performed in cultured cells or in whole sections of formalin-fixed paraffin embedded (FFPE) xenograft tumours. The staining was performed as described²⁹. Antibody dilutions were as follows: p-STAT3 (1:25), CD44 (1:100), CD24 (1:100), CK18 (1:200), CK17 (1:200), HMW CK (1:100), LMW CK (1:100), VIM (1:100), CDH1 (1:100), Flag (1:50), BrdU (1:200), pBRD4 (1:200), and androgen receptor (1:50). The Dana-Farber Breast Cancer Tissue Microarray (TMA) consists of primary TNBC samples from approximately 83 patients who underwent definitive breast surgery at Brigham and Women's Hospital between 1 January 1997 and 31 December 2005. Formalin-fixed, paraffin-embedded breast cancers were collected from the archives of the Department of Pathology at Brigham and Women's Hospital. Best blocks and best areas for coring were identified and selected by a breast pathologist (DD) to represent different area of the tumour. Results of immunohistochemical studies for oestrogen (ER) and progesterone receptor (PR) and HER2 and FISH assay results for HER2 were extracted from pathology reports. TMA construction was carried out in the Dana-Farber/Harvard Cancer Center Tissue Microarray Core Facility. Three 0.6 mm cores were taken from different marked areas in each case and placed into a recipient block using a manual arrayer (Beecher Instruments). Specimens are arrayed in triplicate. Participants signed consent for research use of tissue and the linking of tumour specimens to clinical follow-up. Clinical data on these patients was collected retrospectively at first presentation, at 4, 9, 18, 30, and 42 months, and annually thereafter. After 9.3 years median follow up, 24 recurrences and 14 deaths have been recorded. The data elements are the following: staging, tumour pathology, diagnostic and follow-up tests performed, treatments administered (surgery, radiation and systemic therapy), and recurrence. Although the patients in this cohort were not treated as part of a clinical trial protocol, they were treated relatively uniformly as per Dana-Farber clinical practice guidelines. This serves to minimize confounding due to treatment heterogeneity. The TMA was stained with pBRD4 (1:200) antibody and imaged manually on Yokagawa spinning disc confocal microscope. Three images were taken per each core for 240 out of 267 cores, for the remaining

27 one or two images were taken due to tissue loss or low tumour content. Image analysis was performed with ImageJ software macro (code available upon request). Phospho-BRD4 staining mean intensity was calculated per individual nucleus within an image. The mean intensity per image was normalized to nuclei count. For clinical outcome analysis patients were dichotomized as 'High'/Low pBRD4 by median intensity (Supplementary Table 9). Disease outcomes were evaluated in 83 of 89 TMA samples (3 were not TNBC by definitive pathology, 2 did not have clinical data available, one was a repeat biopsy on a patient). Recurrence-free survival (RFS) was defined as the interval from the date of initial surgical resection to the date of recurrence (local or distant), or date of last known contact if the patient was alive and has not recurred. RFS and overall survival were estimated using the Kaplan–Meier product-limit method, with hazard ratios and 95% confidence intervals from a univariate Cox proportional hazard model.

siRNAs and lentiviral shRNA and expression constructs. For siRNA transfection cells were plated at 2,000 cells per well in 96-well plates and cultured at 37 °C with 5% CO₂ in the media. The next day, cells were transfected in triplicate with siGENOME SMARTpools for the genes of interest or “Non-Targeting siRNA” controls using DharmaFECT 1 (Dharmacon). The sequences of the siRNAs in the SMARTpools are listed in Supplementary Table 10. Cell viability was measured using CellTiter-Glo (Promega) three days after transfections, with the effects of each siRNAs treatment on each cell line compared to the effects of no siRNAs.

TET-inducible pLKO-TET-ON lentiviral constructs were packaged by co-transfection of the lentiviral hairpin containing plasmid pLKO.1 and the helper plasmids pCMV-dR8.91 and pMD2.G-VS.V-G into HEK293T cells using Lipofectamine (Life Technologies). Following transduction via spinoculation for 30 min at 1,000g and selection with 1 µg ml⁻¹ puromycin for 72 h (Sigma, St. Louis, MO), knockdown efficacy was determined by western blotting and cells were seeded for proliferation assays as described above. Sequences of shRNAs used are listed in Supplementary Table 10.

Full length BRD4 in pCDNA3 was a gift from Dr. French at Brigham and Women's Hospital, Harvard Medical School. Mutations of BRD4 BD1 (N140A) and BD2 (N433A) bromodomains, 7A and 7D mutants were generated using a Quickchange Multi Site-Directed Mutagenesis Kit (Agilent Technologies) using primers listed in Supplementary Table 10 and subsequently verified by sequencing.

Immunoblotting and immunoprecipitation experiments. Cells were lysed five days after transfection with siRNAs in RIPA buffer. Proteins were resolved in SDS-polyacrylamide gels (4–12%) and transferred to PVDF membranes by using a Tris-glycine buffer system. Membranes were blocked with 5% milk powder in 0.1% Tween20 in PBS (PBS-T) for 1 h at room temperature followed by incubation with primary antibodies at 1:1,000 dilution in 2.5% milk PBS-T. For immunoprecipitation, nuclear extracts were prepared as follow: 1 × 10⁷ cells were resuspended in 5 ml buffer A: 10 mM Tris pH 7.9, 1.5 mM MgCl₂, 10 mM KCl, 0.05% NP-40, 1 mM DTT, and protease and phosphatase inhibitors. Cells were incubated on ice for 15 min and gently vortexed every 5 min. After centrifugation at 2,000g for 5 min, pellets were suspended in 0.3 ml buffer B (20 mM Tris pH 7.9, 25% glycerol, 0.42 M NaCl, 1.5 mM MgCl₂, 1 mM KCl, 0.5% NP40, 0.2 mM EDTA, 1 mM DTT, and protease and phosphatase inhibitors) and incubated for 5 min on ice. After centrifugation of the lysates at 14g for 10 min at 4 °C, supernatant was diluted with 0.6 ml buffer A, and added NP-40 to final 0.5% and treated with DNase I. The samples were then incubated at 4 °C overnight with BRD4 or Flag antibodies at 1:100 dilution and immunoprecipitates were collected on Dynabeads Protein G for 2 h. Beads were washed with buffer B containing 150 mM NaCl and 0.5% NP-40 three times and then resuspended in gel loading buffer. Immunoblotting and immunoprecipitation experiments were repeated 2–3 times.

Antibodies and inhibitors. Antibodies used for immunoblotting, immunoprecipitation and ChIP-seq were as follows: BRD4 (Bethyl, A301-985A), MED1 (Bethyl, A300-793A), BRD3 (Bethyl, A302-368A), BRD2 (Bethyl, A302-583A), MYC (Santa Cruz, sc764), p-STAT3 (Cell Signaling, 9145S), STAT3 (Cell Signaling, 4904), p-STAT5 (Cell Signaling, 9351), p-JAK2 (Cell Signaling, 3771), CYCLIN D1 (Cell Signaling, 2922), p-H3 (Cell Signaling, 12201), CK2 substrate (Cell Signaling, 8738), PP2A-A (Cell Signaling, 2039), PP2A-C (Cell Signaling, 2038) and p-BRD4 was a gift from C. M. Chiang. Antibodies used for ChIP-seq were BRD4 (Bethyl) histone H3K27ac (Abcam, ab4729). CXCR2 inhibitor (239819) and CK2 inhibitor (218860) were from CalBiochem, JAK2 inhibitor (Ruxolitinib, INCB018424), MEK inhibitor (GSK1120212, S2673), ABT-737 (s1002), and PI3K inhibitor (BKM120, S2247) were from Selleckchem, phenothiazine (1525707) and perphenazine (1511000) were from Sigma-Aldrich. Inhibitor treatment for immunoblot analyses was conducted for 3 h.

SILAC-RIME Experiments and data analysis. SUM159 and SUM159R cells were grown in R/K-deficient SILAC DMEM (paa; E15-086), 10% dialysed serum (Sigma-Aldrich; F0392), and supplemented with 800 µM L-lysine ¹³C₆/¹⁵N₂ hydrochloride and 482 µM L-arginine ¹³C₆/¹⁵N₄ hydrochloride (Cambridge Isotope

laboratory) for “heavy”-labelled media or 800 µM L-lysine ¹²C₆/¹⁴N₂-hydrochloride and 482 µM L-arginine ¹²C₆/¹⁴N₄ hydrochloride for “light”-labelled media. After SILAC labelling, RIME was performed as described²⁰. Word clouds for Extended Data Fig. 7 were generated using R version 3.1.0 and the R package “wordcloud” version 2.5. The size of the tag reflects the square root of the MASCOT score of the protein (the choice of square root is arbitrary, but visually appealing). Experiments were filtered against the Contaminant Repository for Affinity Purification Mass Spectrometry Data³⁰, considering any protein which occurs in at least 20 negative control experiments to be contamination, hence removed from the data set. Refseq protein IDs provided by the contaminant repository were converted to Uniprot IDs found in the mass spec experiments using mappings from the Bioconductor package “org.Hs.eg.db”, version 2.14 (Carlson M. org.Hs.eg.db: Genome wide annotation for Human. R package version 3.0.0). SILAC RIME experiments were performed in duplicates and repeated 2–3 times.

In vitro Chem-seq, ChIP-seq, and RNA-seq. Chem-seq was performed essentially as described¹¹. ChIP-seq: SUM159 and SUM159R cells (4 × 10⁷) were grown in SUM Medium. The media were then removed and replaced with media containing 1% formaldehyde (EM grade; tebu-bio) and crosslinked for 8 min. Crosslinking was quenched by adding glycine to a final concentration of 0.2 M. The cells were washed with ice-cold PBS, harvested in PBS, and the cell pellet was washed with PBS. The nuclear fraction was extracted by first resuspending the pellet in 10 ml of LB1 buffer (50 mM HEPES-KOH (pH 7.5), 140 mM NaCl, 1 mM EDTA, 10% glycerol, 0.5% NP-40 or Igepal CA-630, and 0.25% Triton X-100) for 10 min at 4 °C. Cells were pelleted, resuspended in 10 ml of LB2 buffer (10 mM Tris-HCl (pH 8.0), 200 mM NaCl, 1 mM EDTA, and 0.5 mM EGTA), and mixed for 5 min. Cells were pelleted and resuspended in 300 µl of LB3 buffer (10 mM Tris-HCl (pH 8), 100 mM NaCl, 1 mM EDTA, 0.5 mM EGTA, 0.1% Na-deoxycholate, and 0.5% N-lauroylsarcosine) and sonicated in a Covaris sonicator for 10 min. A total of 30 µl of 10% Triton X-100 was added, and lysate was centrifuged for 10 min at 20,000 rcf to purify the debris. The supernatant was then incubated with 100 µl of Dynabeads Protein G (Life Technologies, 10003D) prebound with 20 µg BRD4 antibody (Bethyl, A301-985A), and immunoprecipitation (IP) was conducted overnight in the cold room. The beads were washed ten times in 1 ml of RIPA buffer and twice in 100 mM ammonium hydrogen carbonate (AMBIC) solution. DNA was eluted in elution buffer (50 mM Tris-HCl pH 8, 10 mM EDTA, and 1% SDS). Cross-links were reversed overnight at 65 °C. RNA and protein were digested with 0.2 mg ml⁻¹ RNase A for 2 h followed by 0.2 mg ml⁻¹ Proteinase K for 1 h. DNA was purified with phenol-chloroform extraction and ethanol precipitation. Libraries for Illumina sequencing were prepared following the Rubicon ThruPLEX-FD kit for 10–12 cycles.

RNA-seq: SUM159 and SUM159R were incubated in biological duplicates for 3, 12 and 24 h with 500 nM of JQ1 or DMSO treatment. Total RNA was extracted using the standard Qiagen RNeasy kit (74106). RNA concentrations were measured and quality controlled on a Bioanalyzer, RNA-Seq libraries were made using Illumina True-Seq RNA kits using the Sciclone NGSx workstation.

All RNA-seq and ChIP-seq experiments were performed in duplicates.

Genomic data analyses. *Accessing data generated in this manuscript.* All ChIP-seq, Chem-seq, and RNA-seq data generated in this publication can be found online associated with GEO Publication Reference ID GSE63584 (www.ncbi.nlm.nih.gov/geo/). Supplementary Table 2 lists all sequencing data sets and their corresponding GEO GSM accession IDs.

Gene sets and annotations. All analysis was performed using RefSeq (NCBI37/HG19) human gene annotations.

RNA-seq data processing and gene expression quantification. All RNA-Seq data sets were aligned to the transcriptome using Tophat2³¹ (version 2.0.11) using the Illumina igenomes NCBI37/HG19 UCSC transcriptome build retrieved from <http://ccb.jhu.edu/software/tophat/igenomes.shtml>. Alignments were performed using default parameters. Transcript expression quantification was performed using Cufflinks³² (version 2.2.0) with default parameters to generate gene expression values in units of FPKM.

ChIP-seq and Chem-seq data processing. All ChIP-seq and Chem-seq data sets were aligned using Bowtie2³³ (version 2.2.1) to build version NCBI37/HG19 of the human genome or build version NCB37/MM9 of the mouse genome. Alignments were performed using the following criteria: -k 1, with all other parameters set to default. These criteria preserved only reads that mapped uniquely to the genome without any mismatches.

Calculating read density. We calculated the normalized read density of a ChIP-seq or Chem-seq data set in any region using the Bamliquidator (version 0.9) read density calculator (<https://github.com/BradnerLab/pipeline/wiki/bamliquidator>). Briefly, ChIP-Seq reads aligning to the region were extended by 200 bp and the density of reads per base pair (bp) was calculated. The density of reads in each region was normalized to the total number of million mapped reads producing read density in units of reads per million mapped reads per bp (rpm per bp).

Identifying ChIP-seq and Chem-seq enriched regions. We used the MACS version 1.4.2 (Model based analysis of ChIP-Seq)³⁴ peak finding algorithm to identify regions of ChIP-Seq enrichment over background. A *P* value threshold of enrichment of 1×10^{-9} was used for all data sets. The GEO accession number and background used for each data set can be found in the accompanying Supplementary Table 2.

Creating heat map representations of ChIP-seq occupancy. Heat maps of ChIP-seq occupancy for various factors were created as described³⁵. Heat maps were created for the ± 10 kb region flanking all transcription start sites (TSS) or for the ± 10 kb region flanking all TSS distal BET bromodomain bound enhancers. Each row plots a specific TSS or enhancer region. Rows are ranked by peak occupancy of BET bromodomains as determined by Bio-JQ1 Chem-seq signal (Fig. 1d).

Correlating BRD4 and H3K27ac occupancy to Bio-JQ1. Occupancy of BRD4 and H3K27ac was correlated to Bio-JQ1 occupancy at all regions of Bio-JQ1 enrichment in SUM159 cells. Pearson correlation statistics are shown (Extended Data Fig. 3a). To quantify changes in BRD4 or H3K27ac occupancy upon JQ1 treatment, all Bio-JQ1 enriched regions were ranked in SUM159 cells and then binned ($n = 10$). Corresponding boxplots of BRD4 or H3K27ac log₂ fold change with or without JQ1 are shown for each bin (Extended Data Fig. 3b).

Mapping enhancers and super-enhancers using Bio-JQ1 occupancy or BRD4. Enhancers and super enhancers (SEs) were mapped using the ROSE software package described^{12,13} and available at (http://younglab.wi.mit.edu/super_enhancer_code.html). In SUM159 and SUM159R cells, Bio-JQ1 Chem-Seq enriched regions were used to map enhancers and super enhancers (Fig. 1f). In SUM149 cells, BRD4 ChIP-seq enriched regions were used to map enhancers and super enhancers (Extended Data Fig. 3a). Enhancers are defined as regions of Bio-JQ1 binding not contained in promoters.

Quantifying changes in gene expression of super enhancer proximal genes. Genes within 50 kb of super enhancer in SUM159 or SUM149 were identified and filtered for expression status (>1 FPKM expression in any sample), and filtered to remove non poly-adenylated transcripts (for example, microRNAs). For SUM159, log₂ fold changes in gene expression at super-enhancer-associated genes or all expressed genes was compared at 3, 12, and 24 h post JQ1 treatment (Fig. 1g). For SUM149, comparisons were made at 12 h post JQ1 treatment (Extended Data Fig. 3f). The statistical significance of differences between distributions of changes was also assessed using a Welch's two-tailed *t* test.

Identifying differentially expressed genes upon JQ1 treatment. To identify genes differentially regulated by JQ1 treatment in SUM159 or SUM149 cells, all genes with a >1 log₂ fold change in expression were ordered by fold change at 24 h with or without JQ1 for SUM159 or at 12 h with or without JQ1 for SUM149. The log₂ row median normalized fold change for each gene is displayed as a heat map in Extended Data Fig. 3g for SUM159 and in Extended Data Fig. 3h for SUM149. For subsequent gene set and pathway analysis, SUM159 genes with consistent and statistically significantly altered expression were selected using a Welch's two-tailed *t* test between DMSO and JQ1 treated expression values at 12 and 24 h. A *P* value cutoff of 0.01 was applied (Extended Data Fig. 3k).

Identifying gained/lost super enhancers between SUM159 and SUM159R. Super enhancer differential regions were defined as in Brown *et al.* 2014³⁶. Briefly, in order to quantify changes in super-enhancers between two conditions, background subtracted ChIP-Seq signal was calculated at the set of all enhancer regions considered super in at least one condition. Gained/lost super-enhancers were determined as those with a greater than log₂ fold change signal in either direction. The log₂ fold change in Bio-JQ1 occupancy at all rank ordered super-enhancer-containing regions is shown in Fig. 2c. Super enhancer regions were classified as either gained, conserved, or lost. Gained/lost regions were classified as those with >1 log₂ fold change in either direction. Conserved regions were classified as those with <0.25 log₂ fold change in either direction. The log₂ fold change in either BRD4 or proximal (within 50 kb of region) gene expression is shown in Extended Data Fig. 5d–f.

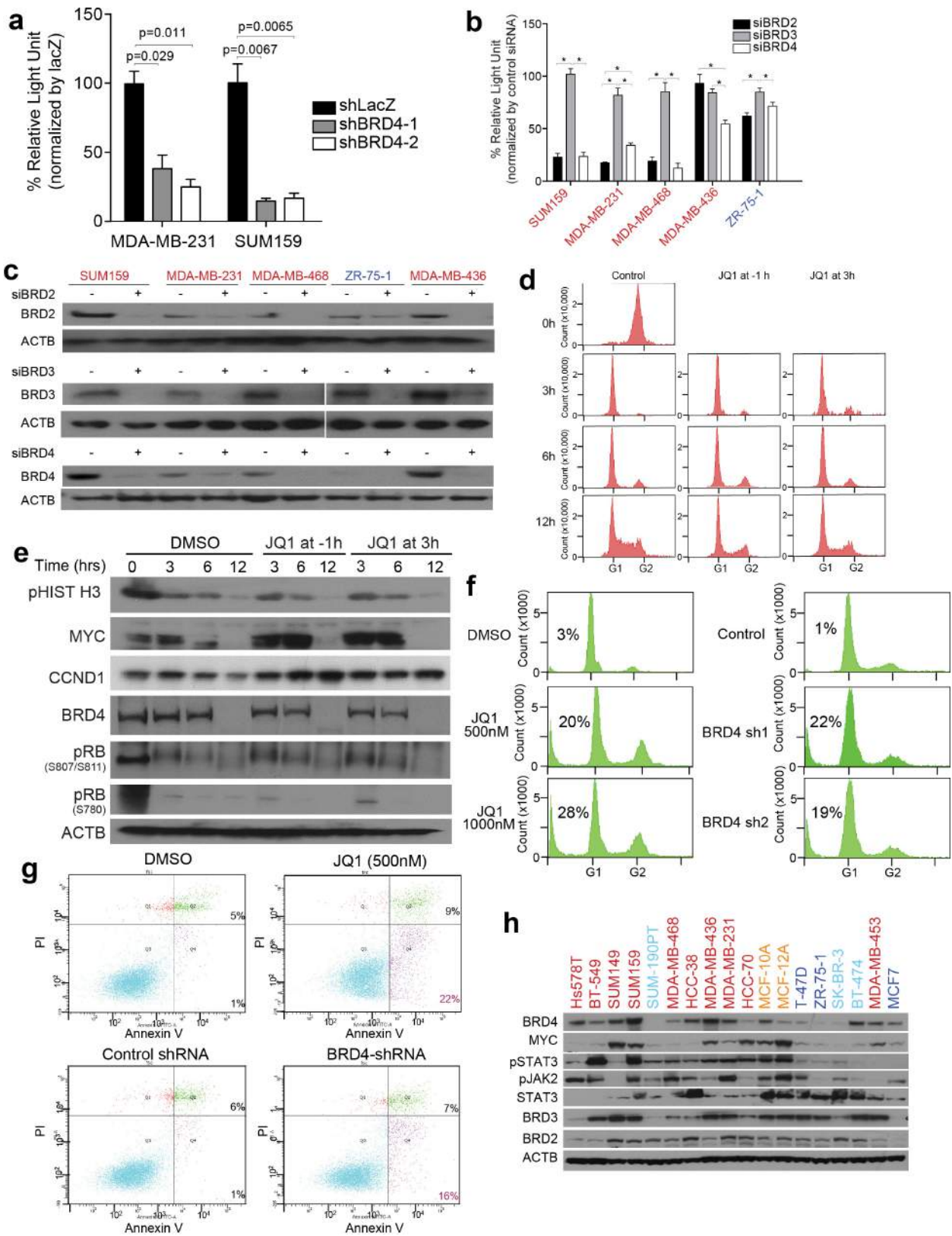
Quantifying changes in BRD4 and H3K27ac occupancy upon JQ1 treatment in either SUM159 or SUM159R cells at Bio-JQ1 regions. Log₂ fold changes in BRD4 or H3K27ac were quantified at Bio-JQ1 enriched regions in their respective cell line and shown in Extended Data Fig. 5c.

Quantifying changes in BRD4 and H3K27ac as a function of Bio-JQ1 or BRD4 occupancy. Bio-JQ1 enriched regions in SUM159 or BRD4 enriched regions in SUM149 were ranked by increasing levels and then distributed into 10 bins. Log₂ fold changes in BRD4 or H3K27ac were quantified in each bin of regions and displayed as a box plot (Extended Data Fig. 3b, c).

Quantifying changes in BRD4 occupancy upon JQ1 treatment in all TNBC. Log₂ fold changes in BRD4 upon JQ1 treatment were quantified at BRD4 enriched regions in each respective cell line Extended Data Fig. 6c.

All code related to genomic and transcriptome analysis can be found at <https://github.com/BradnerLab/TNBC>.

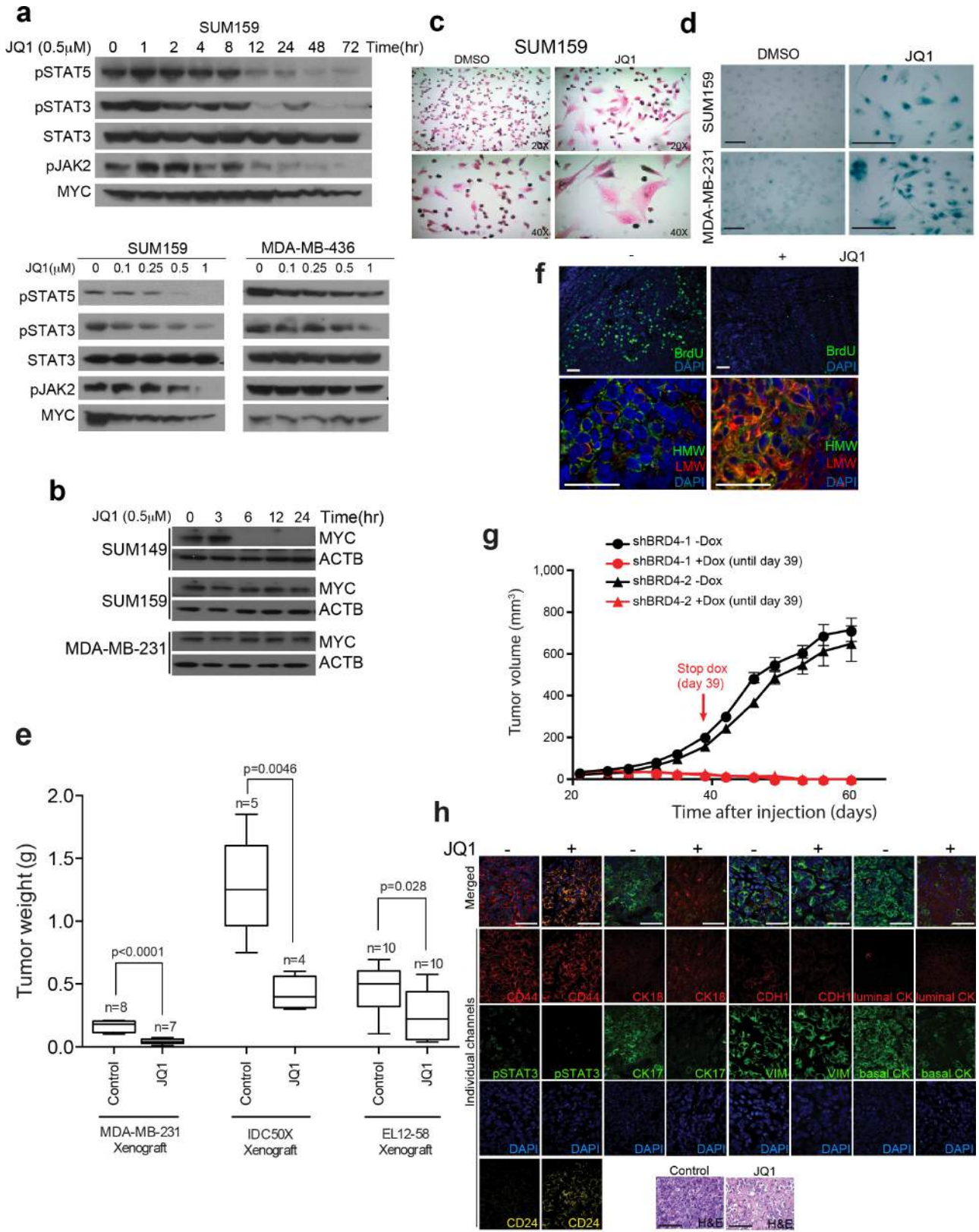
28. Chou, T. C. & Talalay, P. Quantitative analysis of dose-effect relationships: the combined effects of multiple drugs or enzyme inhibitors. *Adv. Enzyme Regul.* **22**, 27–55 (1984).
29. Choudhury, S. *et al.* Molecular profiling of human mammary gland links breast cancer risk to a p27⁺ cell population with progenitor characteristics. *Cell Stem Cell* **13**, 117–130 (2013).
30. Mellacheruvu, D. *et al.* The CRAPome: a contaminant repository for affinity purification-mass spectrometry data. *Nature Methods* **10**, 730–736 (2013).
31. Trapnell, C., Pachter, L. & Salzberg, S. L. TopHat: discovering splice junctions with RNA-Seq. *Bioinformatics* **25**, 1105–1111 (2009).
32. Trapnell, C. *et al.* Transcript assembly and quantification by RNA-Seq reveals unannotated transcripts and isoform switching during cell differentiation. *Nature Biotechnol.* **28**, 511–515 (2010).
33. Langmead, B., Trapnell, C., Pop, M. & Salzberg, S. L. Ultrafast and memory-efficient alignment of short DNA sequences to the human genome. *Genome Biol.* **10**, R25 (2009).
34. Zhang, Y. *et al.* Model-based analysis of ChIP-Seq (MACS). *Genome Biol.* **9**, R137 (2008).
35. Lin, C. Y. *et al.* Transcriptional amplification in tumor cells with elevated c-Myc. *Cell* **151**, 56–67 (2012).
36. Brown, J. D. *et al.* NF- κ B directs dynamic super enhancer formation in inflammation and atherogenesis. *Mol. Cell* **56**, 219–231 (2014).



Extended Data Figure 1 | See next page for figure caption.

Extended Data Figure 1 | BET bromodomain proteins and cell growth in TNBCs. All error bars represent s.d., $n = 3$. **a**, Cellular viability of SUM159 and MDA-MB-231 cells expressing TET-inducible BRD4-targeting or lacZ shRNAs. P values indicate statistical significance of the observed differences (paired t -test). **b**, Cellular viability four days after transfection of siRNAs targeting BET bromodomain proteins. *indicate statistical significance (paired t -test) of the marked differences as follows. SUM159: siBRD2 versus siBRD3, $P = 0.002$; siBRD3 versus siBRD4, $P = 0.0006$, MDA-MB-231: siBRD2 versus siBRD3, $P = 0.006$; siBRD2 versus siBRD4, $P = 0.002$; siBRD3 versus siBRD4, $P = 0.016$, MDA-MB-468: siBRD2 versus siBRD3, $P = 0.0009$; siBRD3 versus siBRD4, $P = 0.0055$, MDA-MB-436: siBRD2 versus siBRD4, $P = 0.002$; siBRD3 versus siBRD4, $P = 0.015$, ZR-75-1: siBRD2 versus siBRD3, $P = 0.0169$; siBRD3 versus siBRD4, $P = 0.007$. **c**, Immunoblot analysis of BET bromodomain proteins four days after siRNA transfection.

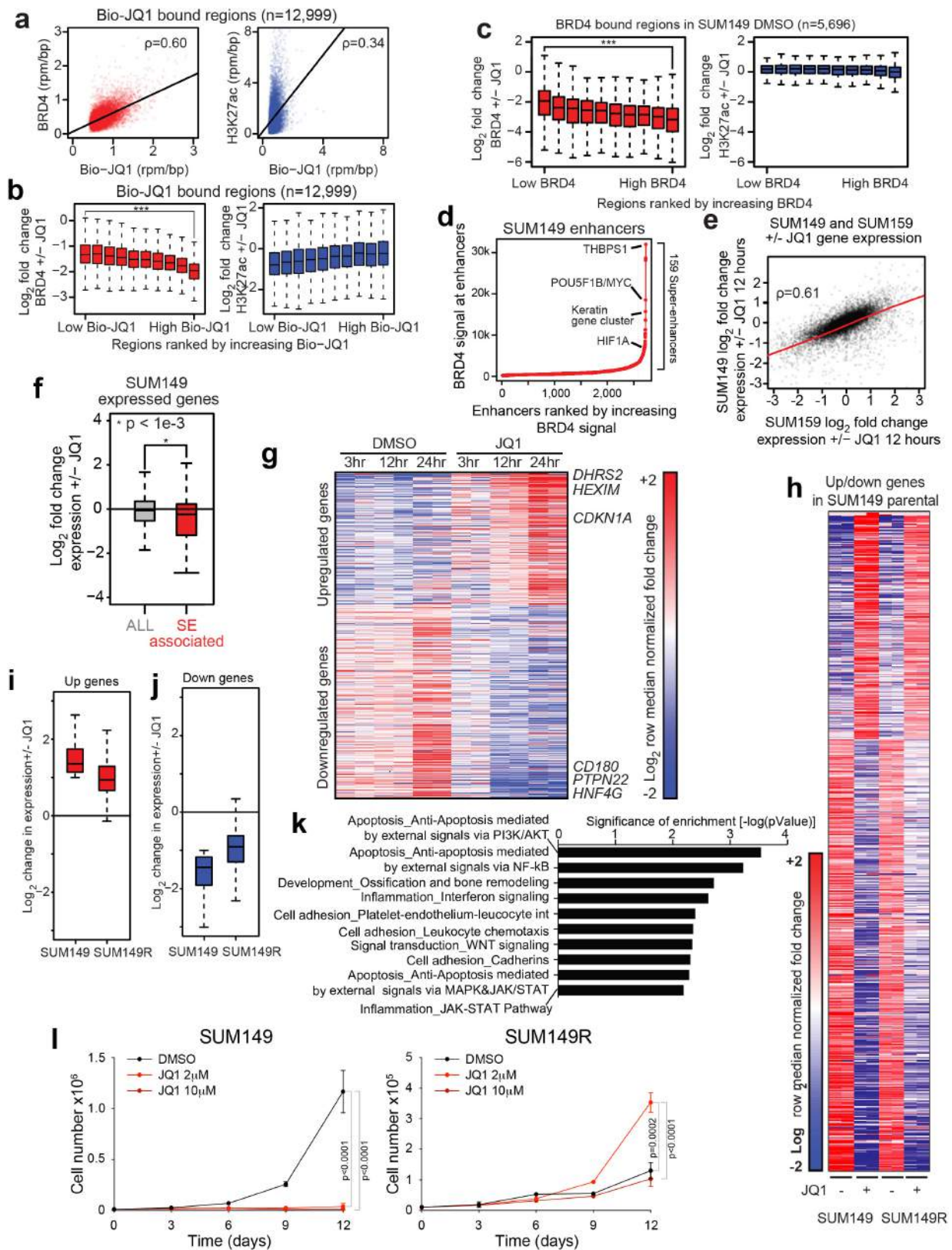
d, Cell cycle profile of SUM159 cells synchronized in G2/M with 100 ng ml^{-1} nocodazole followed by replating to fresh medium with DMSO or JQ1 (500 nM) added at -1 h or at 3 h after release. Cells were collected at different time points (0, 6, 12 h) after release. **e**, Immunoblot analysis of the indicated proteins at different time points (0, 3, 6, 12 h) after release of SUM159 cells synchronized with 100 ng ml^{-1} nocodazole followed by replating to fresh medium with DMSO or JQ1 (500 nM) added at 1 h before or 3 h after release. **f**, Cell cycle analysis of SUM159 cells following 72 h treatment with JQ1 (500 nM) or downregulation of BRD4 using TET-inducible shRNAs. **g**, Annexin V staining of SUM159 cells following 72 h treatment with JQ1 (500 nM) downregulation of BRD4 using TET-inducible shRNAs. All error bars represent s.e.m. **h**, Immunoblot analysis of the indicated proteins in a panel of breast cell lines; colour scheme as in **a**. For gel source data, see Supplementary Fig. 1.



Extended Data Figure 2 | See next page for figure caption.

Extended Data Figure 2 | Response to BBIs in TNBCs. **a**, Immunoblot analysis of the indicated proteins at different time points following JQ1 treatment (500 nM) in SUM159 cells (top) and at different JQ1 doses for 24 h treatment in SUM159 and MDA-MB-436 cells (bottom). **b**, Immunoblot analysis of the indicated proteins at different time points following JQ1 treatment (500 nM) in SUM149, SUM159 and MDA-MB-231 cells. **c**, Haematoxylin and eosin staining of SUM159 cells after 3 days of JQ1 treatment. **d**, Senescence β -galactosidase staining of SUM159 and MDA-MB-231 cells after 3 days of JQ1 treatment. Scale bars, 100 μ m. **e**, Box plots depict the weights of xenografts 30 days after injection of MDA-MB-231 (2×10^6) and IDC50X (2×10^5) cells into inguinal mammary fat pads of NOG mice; *n* indicates the number of mice per experiment. *P* values indicate statistical significance of the observed differences (unpaired *t*-test). Error bars represent s.e.m. Mice were administered JQ1 (50 mg per kg, daily) or vehicle only (control) for 14 days beginning at day 16 (MDA-MB-231) or 10 (IDC50X) after injection (after tumours reached palpable size). For EL12-58X PDX, mice were implanted

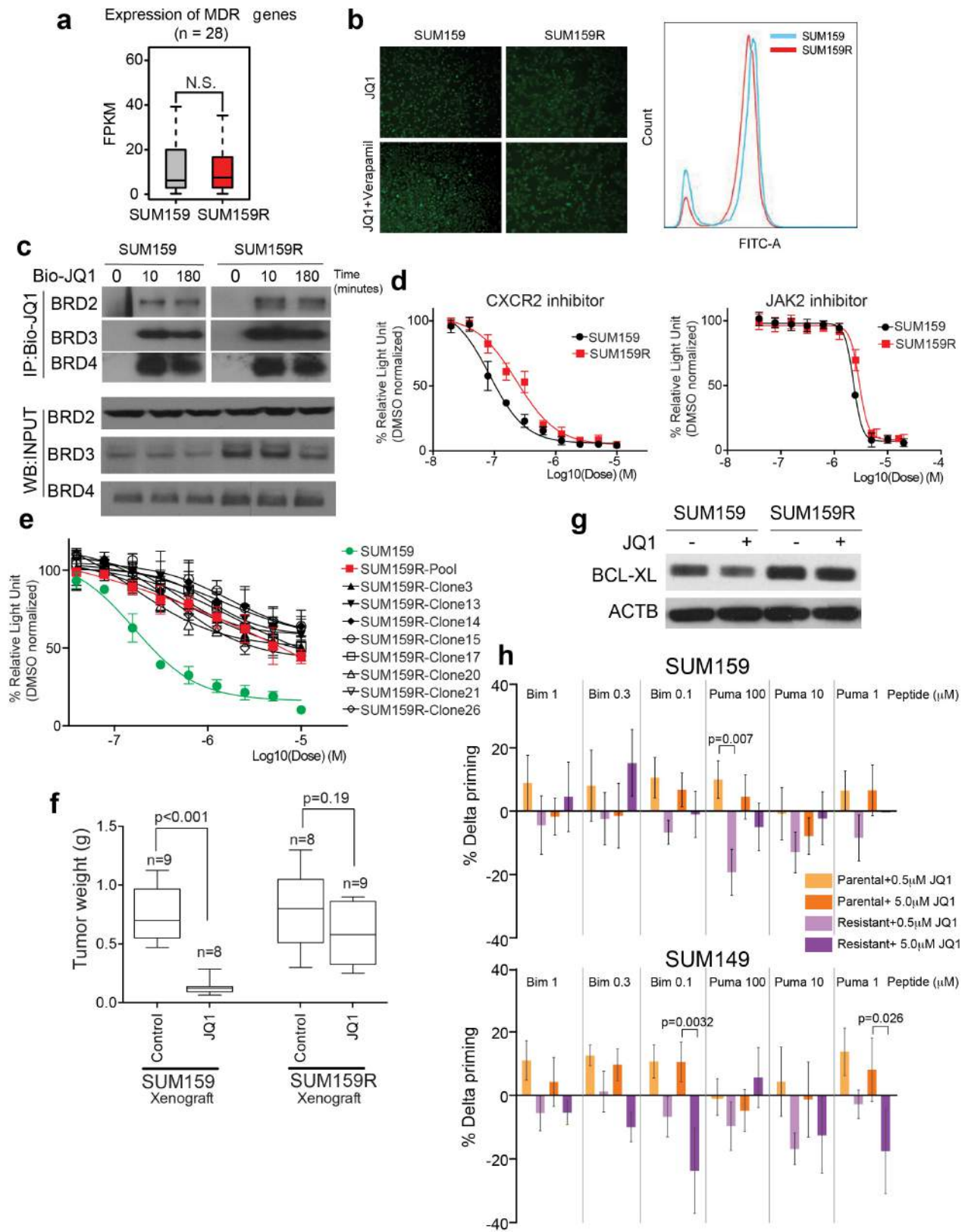
with pieces of tissue measuring $1 \times 3 \times 3$ mm into the inguinal mammary fat pads and were administered daily JQ1 (50 mg per kg) for 14 days beginning at day 21 after injection (after tumours reached palpable size). **f**, Bromodeoxyuridine (BrdU) and luminal low (Low MW CK) and basal high (High MW CK) molecular weight cytokeratin staining of EL12-58 xenograft with or without JQ1 treatment. Scale bars, 50 μ m. **g**, Tumour volume of SUM159 cells expressing TET-inducible BRD4-targeting shRNAs. Mice were administered doxycycline or vehicle only (control) for 39 days beginning at day 21 after injection (after tumours reached palpable size). Error bars represent s.d., *n* = 4 (shBRD4-1 experiment) and *n* = 5 (shBRD4-2 experiment). **h**, Haematoxylin and eosin staining and immunofluorescence analysis of basal (basal cytokeratin, cytokeratin 17, pSTAT3, and CD44) and luminal (luminal cytokeratin, cytokeratin 18, and CD24) markers in SUM159 xenografts with or without JQ1 treatment. Scale bars, 100 μ m for haematoxylin and eosin and 50 μ m for immunofluorescence, respectively. For gel source data, see Supplementary Fig. 1.



Extended Data Figure 3 | See next page for figure caption.

Extended Data Figure 3 | SUM149 JQ1 response. **a**, Scatter plots showing the relationship between the genomic binding of BRD4 and Bio-JQ1 (left) or H3K27ac and Bio-JQ1 (right) at all Bio-JQ1 enriched bound regions. Units of genomic occupancy are in rpm per bp. A simple linear regression is drawn in black. Pearson correlation statistics are also shown. **b**, Boxplots showing the \log_2 fold change in BRD4 with or without JQ1 (left) or H3K27ac with or without JQ1 (right) at Bio-JQ1 bound regions in SUM159. The 12,999 Bio-JQ1 regions are ranked by increasing Bio-JQ1 binding and divided into 10 separate bins (displayed from left to right). The statistical significance of the difference in the mean BRD4 \log_2 fold change between the weakest and strongest Bio-JQ1 bound region bins is shown (Welch's *t*-test; ****P* value $< 1 \times 10^{-10}$). **c**, Boxplots showing the \log_2 fold change in BRD4 with or without JQ1 (left) or H3K27ac with or without JQ1 (right) at BRD4 bound regions in SUM149. The 5,696 BRD4 bound regions are ranked by increasing background subtracted BRD4 binding and divided into 10 separate bins (displayed from left to right). The statistical significance of the difference in the mean BRD4 \log_2 fold change between the weakest and strongest BRD4 bound region bins is shown (Welch's *t*-test; ****P* value $< 1 \times 10^{-10}$). **d**, Ranked plots of enhancers defined in untreated SUM149 cells ranked by increasing BRD4 signal (units rpm). Enhancers are defined as regions of BRD4 binding not contained in promoters. The cutoff discriminating typical from super-enhancers is shown as a dashed grey line. Enhancers associated with TNBC characteristic genes are highlighted. **e**, Scatter plots showing the relationship between the \log_2 fold change in gene expression upon 12 h JQ1 treatment in SUM149 (*y*-axis) and SUM159 (*x*-axis). A simple linear regression is drawn in red. The Pearson correlation statistic is also

shown. **f**, Boxplots showing the \log_2 fold change in expression relative to DMSO control of either all active genes or super-enhancer (SE)-associated upon 12 h JQ1 treatment. The statistical significance of the difference in expression change between all active genes and super-enhancer-associated genes is shown by a Welch's *t*-test **P* value $< 1 \times 10^{-3}$). **g**, Heat map showing the expression of genes that are up or down regulated by JQ1 versus DMSO after 24 h treatment. Each row shows the expression of a single gene in either DMSO or JQ1 treated cells at 3, 12, and 24 h after treatment. Expression values are coloured according to fold change relative to the median for each row. Genes are ordered by fold change with or without JQ1 24 h after treatment. **h**, Heat map showing the expression of genes that are up or down regulated by JQ1 versus DMSO after 12 h treatment in SUM149 and SUM149R cells. Each row shows the expression of a single gene in either DMSO or JQ1 treated cells at 12 h after treatment. Expression values are coloured according to fold change relative to the median for each row. Genes are ordered by fold change with or without JQ1 12 h after treatment in SUM149 cells. **i**, **j**, Boxplots showing the \log_2 fold change in expression at genes that are up- (**i**) or down- (**j**) regulated by JQ1 versus DMSO after 12 h of treatment in parental SUM149 cells. \log_2 fold change in expression is shown for either parental SUM149 (left) or resistant SUM149R (right) cells. **k**, Top signalling pathways affected by JQ1-induced gene expression changes in SUM159 cells. **l**, Viable cell numbers of SUM149 (left) and SUM149R (right) treated with different doses of JQ1 (2 μ M, 10 μ M). Error bars represent s.d., *n* = 3. *P* values indicate statistical significance of the observed differences (two-way ANOVA with Bonferroni multiple comparison correction).

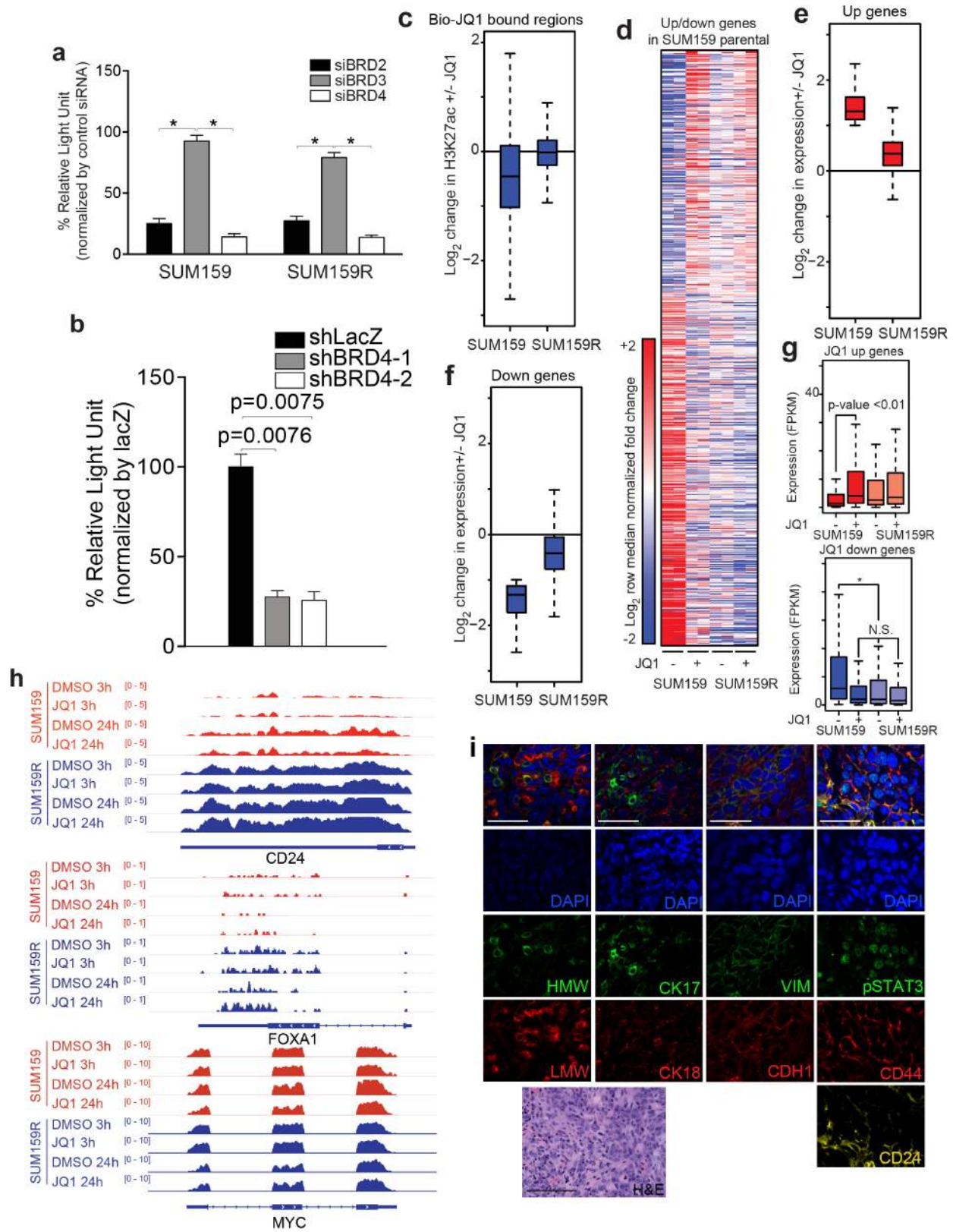


Extended Data Figure 4 | See next page for figure caption.

Extended Data Figure 4 | Characterization of SUM159R cells.

a, Expression of ABC transporters in SUM159 and SUM159R cells. The expression of 29 ABC transporters was analysed based on RNA-seq data on the two cell lines. **b**, Assay for MDR (multi drug resistance) pumps in SUM159 and SUM159R cells treated with JQ1 alone or together with verapamil based on microscopic examination (left) and FACS (right) of cells labelled with fluorescent MDR substrate. **c**, Immunoprecipitation analysis of Biotinylated JQ1 (Bio-JQ1) in SUM159 and SUM159R cells with JQ1 treatment at different time points following immunoblot for the indicated proteins. **d**, Cellular viability of SUM159 and SUM159R cells treated with CXCR2 and JAK2 inhibitors. Error bars represent s.d., $n = 3$. **e**, Cellular viability of SUM159, and pool and single cell clones of SUM159R cells treated with different doses of JQ1. Error bars represent s.d., $n = 3$. **f**, Tumour weight of xenografts derived from SUM159 and

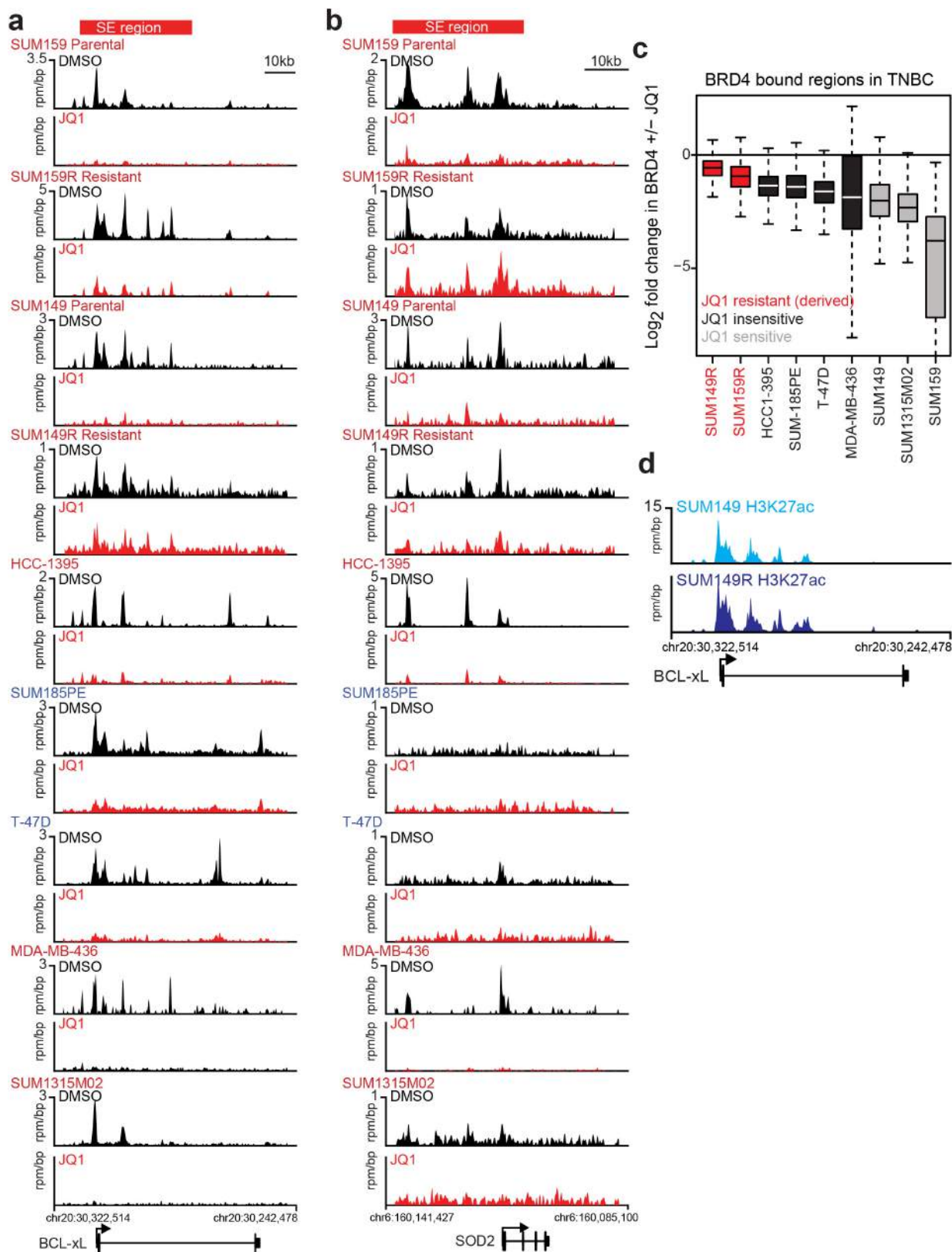
SUM159R cells. Mice were administered JQ1 for 14 (SUM159) and 30 (SUM159R) days beginning at day 14 and 26, respectively, after injection. *P* values indicate statistical significance of the observed differences (unpaired *t*-test). Error bars represent s.e.m. **g**, Immunoblot analysis of BCL-XL expression in SUM159 and SUM159R cells before and after JQ1 3 h treatment (500 nM). **h**, Dynamic BH3 profiling reveals inverse apoptotic response to JQ1 in SUM149R and SUM159R cells. In parental lines JQ1 increases priming relative to untreated cells indicating an increase in apoptotic propensity. In resistant lines JQ1 reduces priming indicating greater resistance to apoptosis relative to untreated cells. *P* values indicate statistical significance of the observed differences (two-way ANOVA). Error bars represent s.e.m., $n = 5$. For gel source data, see Supplementary Fig. 1.



Extended Data Figure 5 | See next page for figure caption.

Extended Data Figure 5 | BRD4 binding in SUM159R cells. **a**, Cellular viability of SUM159 and SUM159R cells transfected with siRNAs targeting bromodomain proteins. *indicate statistical significance (paired *t*-test) of the marked differences as follows: SUM159: siBRD2 versus siBRD3, $P = 0.013$, siBRD3 versus siBRD4, $P = 0.0154$ and SUM159R: siBRD2 versus siBRD3, $P = 0.0159$, siBRD2 versus siBRD4, $P = 0.0048$; siBRD3 versus siBRD4, $P = 0.0068$. **b**, Cellular viability of SUM159R cells expressing TET-inducible BRD4-targeting or lacZ shRNAs. All error bars represent s.e.m. *P* values indicate statistical significance of the observed differences (unpaired *t*-test). **c**, Boxplot showing the \log_2 fold change in H3K27ac genomic occupancy at regions bound by Bio-JQ1 in parental SUM159 or resistant SUM159R cells. **d**, Heat map showing the expression of genes that are up or down regulated by JQ1 versus DMSO after 24 h treatment in parental SUM159 cells. Each row shows the expression of a single gene in either DMSO or JQ1 treated cells at 24 h after treatment in SUM159 cells (left four columns) or SUM159R cells (right four columns). Expression values are coloured according to fold change relative to the median for each row. Genes are ordered by fold change with or without JQ1 24 h after treatment. **e**, **f**, Boxplots showing the \log_2 fold change in expression at genes that are up- (**e**) or down- (**f**) regulated by JQ1

versus DMSO after 24 h of treatment in parental SUM159 cells. \log_2 fold change in expression is shown for either parental SUM159 or resistant SUM159R cells. **g**, Boxplots showing expression of genes that are up or down regulated by JQ1 versus DMSO after 24 h of treatment in parental SUM159 cells. Expression is shown in DMSO and JQ1-treated conditions in units of FPKM for either parental SUM159 (left) or resistant SUM159R (right) cells. The statistical significance of the difference between gene expression distributions for SUM159 DMSO and JQ1 treated cells is shown ($P < 0.01$). The difference between all other distributions are considered non significant (NS). The statistical significance of the difference between SUM159 DMSO gene expression distribution and all other distributions is shown ($*P$ value $< 1 \times 10^{-3}$). The difference between all other distributions are considered non significant. **h**, Examples of luminal and basal cell-specific genes, and MYC in SUM159 and SUM159R cells. RNA-seq tracks are shown. **i**, Haematoxylin and eosin staining and immunofluorescence analysis of luminal (CK18 and LMW) and basal (CK17 and HMW) cytokeratins and luminal (VIM and CD24) and basal (CDH1, CD44, and pSTAT3) cell markers in SUM159R xenografts. All error bars represent s.e.m. Scale bars, 100 μm for haematoxylin and eosin and 50 μm for immunofluorescence, respectively.



Extended Data Figure 6 | JQ1 response in other breast cancer cell lines.

a, b, Gene tracks depicting BRD4 + DMSO and BRD4 + JQ1 in multiple TNBC cells at the *BCL-xL* (**a**) or *SOD2* (**b**) gene loci. The *x*-axis shows position along the chromosome with gene structures drawn below. The *y*-axis shows genomic occupancy in units of rpm per bp. The *BCL-xL* and *SOD2* super-enhancers are shown as a red bar at the top. **c**, Box plots showing the log₂ fold change in BRD4 occupancy with or without JQ1 for

all BRD4 bound regions in each cell line for multiple TNBC. Cell lines are ordered by their JQ1 (IC₅₀) and coloured by their sensitivity. **d**, Gene tracks depicting H3K27AC occupancy at the *BCL-xL* locus in SUM149 parental (top, light blue) or SUM149R resistant (bottom, dark blue) cells. The *x*-axis shows position along the chromosome with gene structures drawn below. The *y*-axis shows genomic occupancy in units of rpm per bp. All error bars represent s.e.m.

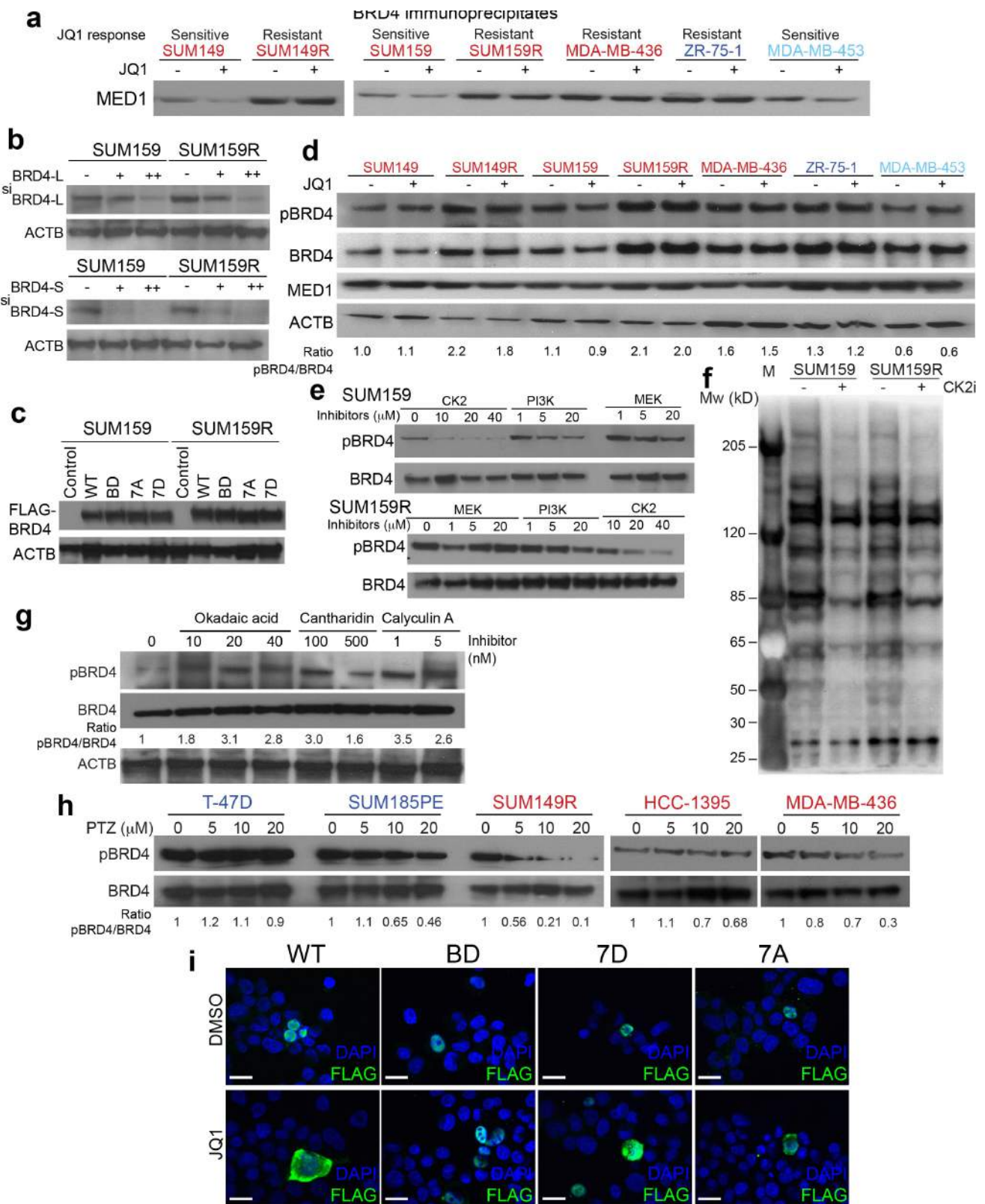
SUM159



SUM159R

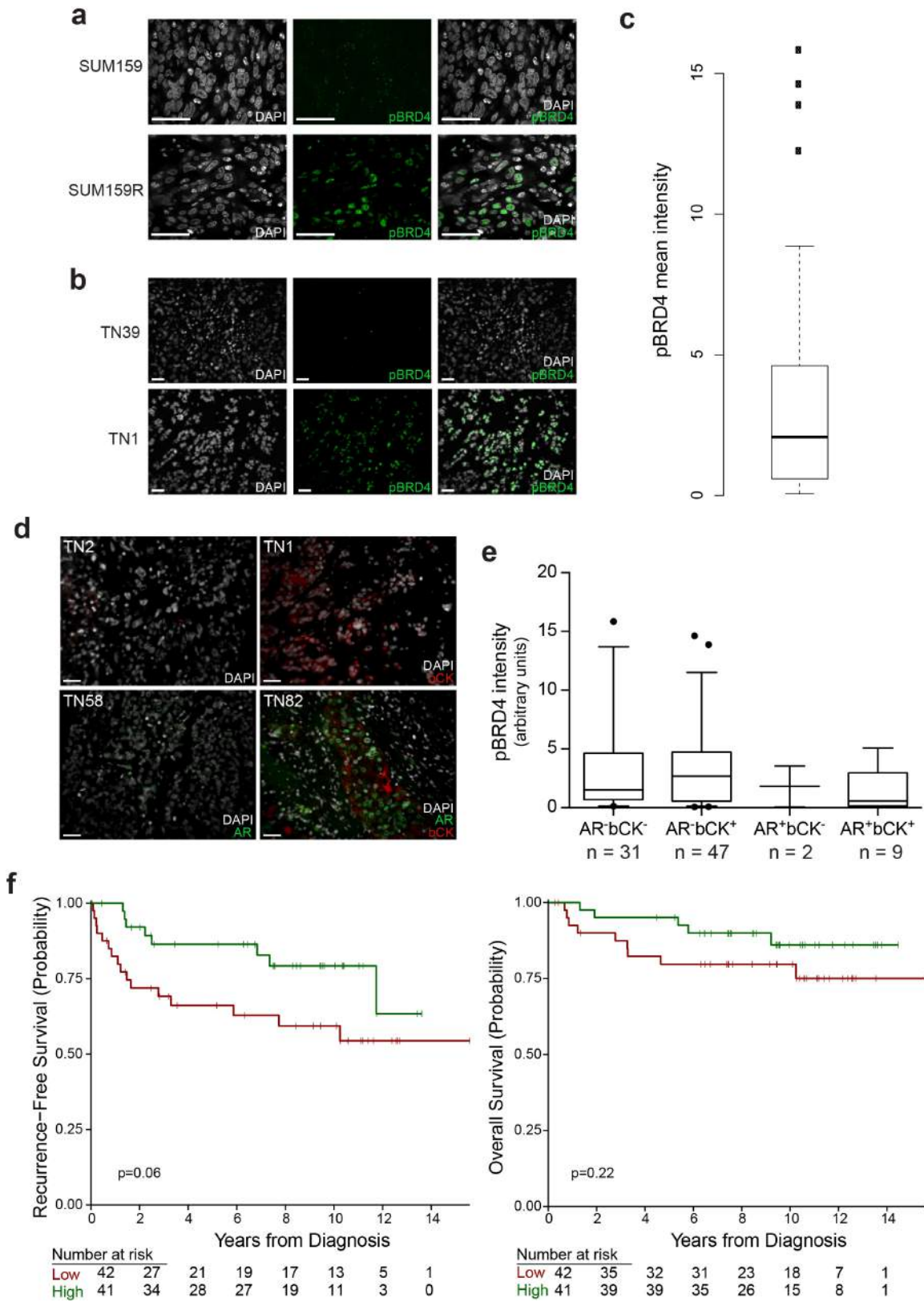


Extended Data Figure 7 | Word clouds depicting BRD4-associated proteins identified in RIME analysis.



Extended Data Figure 8 | Mechanism of BBI-resistance. **a**, Immunoblot analysis of BRD4 immunoprecipitates for MED1 in the indicated cell lines with or without JQ1 treatment (5 μM, 3 h). **b**, Immunoblot analysis of long (BRD4L) and short (BRD4S) forms of BRD4 after transfection of siRNAs. **c**, Immunoblot analysis of the indicated exogenously expressed Flag-tagged BRD4 proteins in SUM159 and SUM159R cells. **d**, Immunoblot analysis of phospho-BRD4 (pBRD4) and BRD4 in SUM159 and SUM159R cells treated with the indicated doses of CK2, PI3K, and MEK inhibitors for 2 h. **e**, Immunoblot analysis of pBRD4, BRD4, MED1 and ACTB in the indicated cell lines with or without JQ1 treatment. **f**, Immunoblot analysis

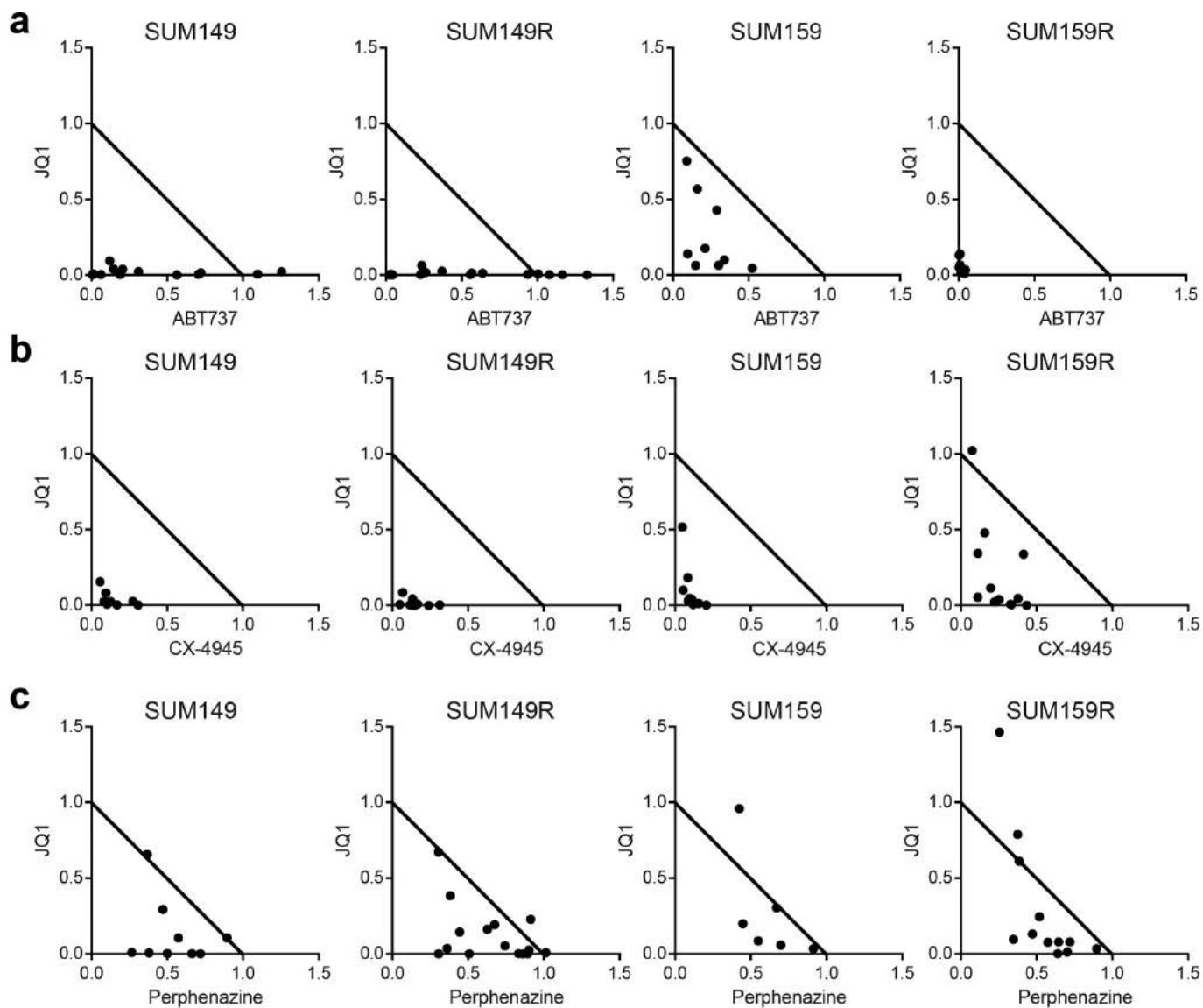
of CK2 substrates in SUM159 and SUM159R cells following CK2 inhibitor (CX-4945, 10 μM) 3 h treatment. **g**, Immunoblot analysis of pBRD4 and BRD4 in SUM149 cell line treated with different doses of the indicated PP2A inhibitors for 3 h. ACTB was used as loading control. **h**, Immunoblot analysis of pBRD4 and BRD4 in the indicated cell lines treated with different doses of phenothiazine for 6 h. **i**, Immunofluorescence analysis of exogenous Flag-tagged BRD4 proteins (WT, BD, 7D and 7A) in SUM159 cells with or without JQ1 treatment (5 μM, 3 h). Scale bars, 20 μm. For gel source data, see Supplementary Fig. 1.



Extended Data Figure 9 | See next page for figure caption.

Extended Data Figure 9 | Phospho-BRD4 levels in xenografts and primary TNBC samples. **a**, Immunofluorescence analysis of phospho-BRD4 (pBRD4) in SUM159 parental and SUM159R xenografts showing that resistance is associated with higher pBRD4 levels. **b**, Examples of pBRD4 immunofluorescence in patient tumours depicting variability among different TNBC samples. Scale bars, 50 μ m. **c**, Mean intensity of phospho-BRD4 (pBRD4) in tissue samples from 83 patients with early-stage triple negative breast cancer (TNBC). **d**, Examples of androgen receptor and basal cytokeratin (bCK, HMW CK) immunofluorescence in TNBC samples. Scale bars, 50 μ m. **e**, Box plot depicting pBRD4 signal intensity in TNBCs tumours with the indicated androgen receptor and bCK expression patterns. None of the differences among groups were

significant (ANOVA test $P = 0.5413$ and Dunnett's multiple comparisons test was not significant). **f**, Kaplan–Meier estimates of disease-free survival (DFS) and overall survival (OS) in TNBC subgroups using a median-split of pBRD4 intensity. Disease outcomes were evaluated in 83 of 89 TMA samples. Patients with low pBRD4 had a worse overall prognosis with a five-year RFS of 66.2% (95% confidence interval (CI) 52.7–83.1%), compared to an RFS of 86.4% (95% CI 76.0–98.3%) among patients with high pBRD4 (HR = 2.3, 95% CI 0.98–5.4, $P = 0.06$). However, with this small sample size this difference did not reach statistical significance, nor did a ratiometric (twofold) consideration of pBRD4 status and overall survival (HR = 2.0, 95% CI 0.67–5.9, $P = 0.22$).



Extended Data Figure 10 | Overcoming BBI-resistance. a–c, Synergy studies of JQ1 with ABT737 (BCL-x1 and BCL-2 inhibitor) (a), CX-4945 (CK2 inhibitor) (b) and perphenazine (PP2A activator) (c). Points represent paired values of drug concentrations assessed for synergism.

The diagonal line signifies drug additivity. Points above the line represent antagonistic drug combinations, and those below the line represent synergistic drug combinations.

Author Queries

Journal: **Nature**

Paper: **nature16508**

Title: **Response and resistance to BET bromodomain inhibitors in triple-negative breast cancer**

Query Reference	Query
1	<p>AUTHOR: A PDF proof will be produced on the basis of your corrections to this preproof and will contain the main-text figures edited by us and the Extended Data items supplied by you (which may have been resized but will not have been edited otherwise by us).</p> <p>When you receive the PDF proof, please check that the display items are as follows (doi:10.1038/nature16508): Figs 0 (black & white); 1–4 (colour); Tables: None; Boxes: None; Extended Data display items: 10.</p> <p>Please check the edits to all main-text figures (and tables, if any) very carefully, and ensure that any error bars in the figures are defined in the figure legends. If you wish to revise the Extended Data items for consistency with main-text figures and tables, please copy the style shown in the PDF proof (such as italicising variables and gene symbols, and using initial capitals for labels) and return the revised Extended Data items to us along with your proof corrections.</p>
Web summary	<p>BET inhibitors that target bromodomain chromatin readers such as BRD4 are being explored as potential therapeutics in cancer; here triple-negative breast cancer cell lines are shown to respond to BET inhibitors and resistance seems to be associated with transcriptional changes rather than drug efflux and mutations, opening potential avenues to improve clinical responses to BET inhibitors.</p>

Author: Please check the wording of the following statement, which will appear online only.

J.E.B. and R.A.Y. are founders of Syros Pharmaceuticals, J.E.B. is the founder of Tensha Therapeutics. K.P. receives research support from and is a consultant for Novartis Oncology.

For Nature office use only:

Layout	<input type="checkbox"/>	Figures/Tables/Boxes	<input type="checkbox"/>	References	<input type="checkbox"/>
DOI	<input type="checkbox"/>	Error bars	<input type="checkbox"/>	Supp info	<input type="checkbox"/>
Title	<input type="checkbox"/>	Colour	<input type="checkbox"/>	Acknowledgements	<input type="checkbox"/>
Authors	<input type="checkbox"/>	Text	<input type="checkbox"/>	Author contribs	<input type="checkbox"/>
Addresses	<input type="checkbox"/>	Methods	<input type="checkbox"/>	COI	<input type="checkbox"/>
First para	<input type="checkbox"/>	Received/Accepted	<input type="checkbox"/>	Correspondence	<input type="checkbox"/>
		AOP	<input type="checkbox"/>	Author corr	<input type="checkbox"/>
		Extended Data	<input type="checkbox"/>	Web summary	<input type="checkbox"/>
				Accession codes link	<input type="checkbox"/>